Reconfigurable Multi-Carrier Transmitters and their Application in Next Generation Optical Networks

Prajwal Doddaballapura Lakshmijayasimha

B. Eng., M. Sc.

A dissertation submitted in fulfilment of
the requirements for the award of Doctor
of Philosophy (Ph.D.)
to the

School of Electronic Engineering
Dublin City University

Supervisor: Dr. Prince M. Anandarajah (DCU)

External Supervisor: Dr. Aleksandra
Kaszubowska-Anandarajah
(Trinity College Dublin)

February 2022

Declaration

I hereby certify that this material, which I now submit for assessment on the programme of study leading to the award of Doctor of Philosophy is entirely my own work, and that I have exercised reasonable care to ensure that the work is original, and does not to the best of my knowledge breach any law of copyright, and has not been taken from the work of others save and to the extent that such work has been cited and acknowledged within the text of my work.

Signed:

ID No.: 17212388

Date: 21/02/2022

To Amma, Appa, Ajji
and Prakruthi

Every brilliant experiment, like every great work of art, starts with an act of imagination."

– Jonah Lehrer

Acknowledgements

Table of Contents

List of Figures

List of Tables

List of Acronyms

APD	Avalanche Photodiode
A-RoF	Analog - Radio over Fibre
ASE	Amplified Spontaneous Emission
AWG	Arrayed Waveguide Grating
BBU	Baseband processing units
BER	Bit Error Rate
BtB	Back-to-back
BW	Bandwidth
C-band	Conventional band
CDM	Carrier Density Modulation
CIR	Circulator
CLP	Comb Line Power
CLSR	Comb Line Suppression Ratio
CO-OFDM	Coherent Optical Orthogonal Frequency Division Multiplexed
C-RAN	Centralised or Cloud Radio Access Network
CW	Continuous Wave
CWDM	Coarse Wavelength Division Multiplexed
DAC	Digital-to-Analog Converter
DCF	Dispersion Compensation Fibre
DCI	Data Centre Interconnect
DCN	Data Centre Network
Demux	Demultiplexer
DFB	Distributed Feed Back
DM	Discrete Mode
DMT	Discrete Multi-Tone
DP-QPSK	Dual Polarisation Quadrature-Phase Shift Keyed
DSF	Dispersion Shifted Fibre
DSP	Digital Signal Processing
DWDM	Dense Wavelength Division Multiplexed
EBPF	Electrical Band Pass Filter
EDFA	Erbium Doped Fibre Amplifier
EI-GSL	Externally Injected Gain Switched Laser
EML	Externally Modulated Laser
EOM	Electro Optic Modulation
ESA	Electrical Spectrum Analyser
EVM	Error Vector Magnitude
FM	Frequency Modulated
FMF	Few Mode Fibre
FM-MCF	Few Mode Multi Core Fibre

FP	Fabry-Pérot
FPGA	Field Programmable Gate Array
FSR	Free Spectral Range
FWM	Four Wave Mixing
GSL	Gain Switched Laser
HD-FEC	Hard Decision Forward Error Correction
HNLF	Highly Non-Linear Fibre
ICI	Inter Channel Interference
IF	Intermediate Frequency
IM	Intensity Modulation
IM/DD	Intensity Modulation Direct Detection
IoT	Internet of Things
IPTV	Internet Protocol Television
ISO	Isolator
ITU-T	International Telecommunication Union
KPI	Key Performance Index
L-band	Long wavelength band
LiNb03	Lithium Niobate
LO	Local Oscillator
MIL-GSL	Mutually Injection Locked Gain-switched Laser
MLL	Mode Locked Laser
MMF	Multi-Mode Fibre
mmW	Millimetre Wave
MRR	Micro Ring Resonator
MS	Master-Slave
MZM	Mach-Zehnder Modulator
NRZ	Non-Return to Zero
N-WDM	Nyquist-WDM
OBPF	Optical Band Pass Filter
OCNR	Optical Carrier to Noise Ratio
ODL	Optical Delay Line
OFC	Optical Frequency Comb
OIL	Optical Injection Locking
OOK	On Off keyed
OSA	Optical Spectrum Analyser
OSNR	Optical Signal to Noise Ratio
PAM	Pulse Amplitude Modulation
PC	Polarisation Controller
PD	Photodetector
PDM	Polarisation Division Multiplexed
PIC	Photonic Integrated Circuit
PM	Phase Modulation
PMF	Polarisation Maintaining Fibre

PPG	Pulse Pattern Generator
PRBS	Pseudo Random Binary Sequence
PS	Phase Shifter
PSK	Phase Shift Keyed
QAM	Quadrature Amplitude Modulation
QSPF-DD	Quad Small Form-factor pluggable Double Density
RBW	Resolution Bandwidth
RF	Radio Frequency
RIN	Relative Intensity Noise
ROP	Received Optical Power
RRC	Root Raised Cosine
RRU	Remote Radio Unit
RTS	Real Time Oscilloscope
SBVT	Sliceable Bandwidth Variable Transmitter
SDM	Space Division Multiplexed
SE	Spectral Efficiency
SSMF	Standard Single Mode Fibre
SMSR	Side Mode Suppression Ratio
SOA	Semiconductor optical amplifier
SOH	Silicon-Organic Hybrid
SSB PN	Single Side Band Phase noise
SSC	Spot Size Converter
TEC	Thermo Electric Cooler
THz	Tera Hertz
TL	Tunable Laser
UDWDM	Ultra-Dense Wavelength Division Multiplexed
UF-OFDM	Universal Filtered Orthogonal Frequency Division Multiplexed
VBW	Video Bandwidth
VCO	Voltage Controlled Oscillator
VCSEL	Vertical Cavity Surface Emitting Laser
VOA	Variable optical attenuator
WDM	Wavelength Division Multiplexed
WSS	Wavelength Selective Switch
5G+	Fifth Generation and beyond

Reconfigurable Multi-Carrier Transmitters and their Application in Next Generation Optical Networks

By: <u>Prajwal Doddaballapura Lakshmijayasimha</u>

Abstract

With the advent of new series of Internet services and applications, future networks will have to go beyond basic Internet connectivity and encompass diverse services including connected sensors, smart devices, vehicles, and homes. Today's telecommunication systems are static, with pre-provisioned links requiring an expensive and time-consuming reconfiguration process. Hence, future networks need to be flexible and programmable, allowing for resources to be directed, where the demand exists, thus improving network efficiency. A cost-effective solution is to utilise the legacy fibre infrastructure more efficiently, by reducing the size of the guard bands and allowing closer optical carrier spacing, thereby increasing the overall spectral efficiency. However, such a scheme imposes stringent transmitter requirements such as frequency stability, which would not be met with the incumbent laser-array based transmitters. An attractive alternative would be to employ an optical frequency comb (OFC), which generates multiple phase correlated carriers with precise frequency separation. The reconfigurability of such a multi-carrier transmitter would enable tuning of channel spacing, number of carriers and emission wavelengths, according to the dynamic network demands.

This research thesis presents the work carried out, in the physical layer, towards realising reconfigurability of an optical multi-carrier transmitter system. The work focuses on an externally injected gain-switched laser-based OFC (EI-GSL), which is a particular type of multi-carrier source. Apart from the detailed characterisation of GSL OFCs, advances to the state of the art are achieved via comb expansion, investigating new demultiplexing methods and system implementations. Firstly, two novel broadband GS-OFC generation techniques are proposed and experimentally demonstrated. Subsequently, two flexible and compact demultiplexing solutions, based on micro-ring resonators and laser based active demultiplexers are investigated. Finally, the application of a reconfigurable multi-carrier transmitter, employed in access and data centre networks, as well as analog-radio over fibre (A-RoF) distribution systems, is experimentally demonstrated.

1. Introduction

The advent of internet communication revolutionised the world and has become embedded in every aspect of our day-to-day activities, by redefining how we interact with others, work, or do business. The internet and its services are facilitated by optical fibre communications, which represents the true backbone of modern high-capacity communication systems. It is supported by a web of interconnected optical network segments, connecting the entire world, i.e.: the long haul/core network, carrying large, aggregated data over thousands of kilometres through terrestrial or submarine fibres; metro network, providing optical interconnection between core and access (with the span of around 200 km); and finally, the 'last mile' access networks that connect the end-user (several kilometres).

Over the last decade, the global demand for data traffic has increased in an unprecedented manner and is expected to reach 4.8 Zettabytes per year by 2022, as predicted in Figure 1.1(a) [1]. This continuing growth is mainly fuelled by bandwidth-hungry applications like high-definition TV, internet protocol television (IPTV), online gaming, , cloud computing, social media applications, etc. In addition, due to the impact of the Covid-19 outbreak, the optical network experienced an unanticipated global traffic spike of at least 30% (Figure 1.1 (b)) [2], [3]. This surge in the need for bandwidth was driven by remote working, digitalisation of economic infrastructures, video conferences, online lecturing, etc. All these traffic requirements have put a huge strain on the existing optical networks, further exacerbating the "capacity crunch", a situation where the optical networks carryings the world's data traffic, are running out of capacity. To cope with the increasing bandwidth demand, the number of channels in wavelength division multiplexing (WDM) networks has been increased by reducing the channel spacing to achieve dense WDM

(DWDM), along with an increasing baud rate per channel. However, the conventional capacity scaling approaches are reaching their limit and may struggle to support innovative next-generation applications. Therefore, next-generation optical networks are required to employ novel capacity scaling solutions that can provide an increased capacity, performance, and able to respond to dynamic traffic conditions and requirements.

Exabytes per Month

(a)

% Increase in Total Traffic
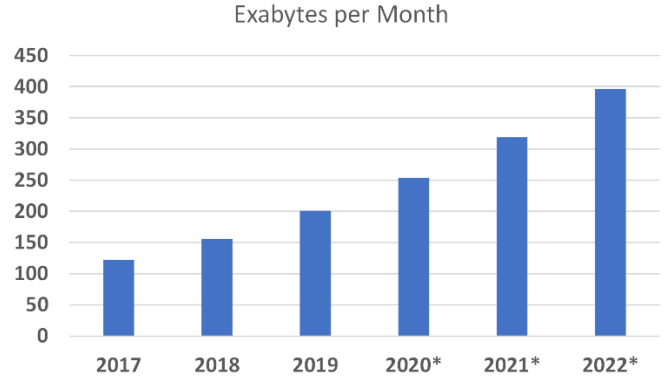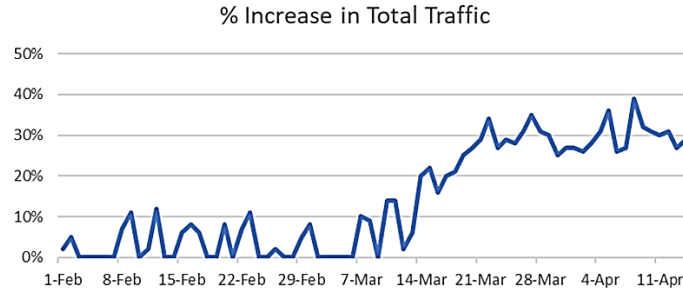
(b)

Figure 1.1 (a) Global data traffic volume during 2017-2022 as predicted in 2019, (b) percentage of global traffic increased between February and April 2020 due to the Covid-19 pandemic lockdown. [1], [3].

One such effective capacity scaling approach is to reduce the size of the guard band and allow closer channel spacing to utilise the available spectrum more effectively, thus increasing the data throughput. To achieve this, the existing optical networks should evolve towards responsive reconfigurable optical systems that operate on flex-grid or gridless architecture. Such networks should also support network-level programmability to swiftly tune (typically <few ms) [4] the physical layer parameters, such as the number

2

of carriers, carrier spacing, emission wavelength, baud rate, system reach, etc., according to the dynamic network demand. Thus, to truly realise such a reconfigurable optical network, an optical transmitter with a high degree of flexibility is crucial. While the flex-grid architecture has the potential to deliver improved spectral utilisation, it also introduces several stringent optical carrier requirements such as the frequency stability of the carriers, which could not be met by the currently employed array of lasers. An attractive solution is to employ a multi-carrier transmitter based on an optical frequency comb (OFC), which generates a series of precisely spaced and phase correlated optical carriers. This outstanding frequency stability between channels, allows closer channel spacing by alleviating the need for guard band, thus achieving the promised superior spectral efficiency. Hence, to realise the next-generation reconfigurable optical network, an OFC-based transmitter that can tune its physical transmission parameters is essential.

This work focuses on the technological advancement of physical layer reconfigurability such as the development of a reconfigurable OFC-based transmitter and compatible sub-systems such as tunable demultiplexers. Amongst the various OFC generation schemes reported in the literature, this thesis focuses on an externally injected gain-switched laser (EI-GSL) technique due to its simplicity, flexibility, and cost-effectiveness. Several key advances to the state-of-the-art technology were accomplished, with the primary focus of enhancing the feasibility of the proposed reconfigurable GSL OFC-based transmitter for application in next-generation access, data centre networks, and analog-radio over fibre (A-RoF) distribution systems.

The structure of this thesis is as follows:
Chapter 1 describes the evolution of optical fibre communications networks as well as the current state-of-the-art. The challenges that next-generation optical networks may face to improve their capacity are outlined and several effective capacity scaling approaches are introduced. Particular attention is given to reconfigurable optical networks enabled by an OFC as a multicarrier source, which is the focus of this work. In addition, some of the main physical layer considerations and implementational challenges of the reconfigurable

optical network are discussed. The chapter concludes by highlighting the motivation and main contributions of this thesis work.

Chapter 2 introduces various semiconductor-based OFC generation approaches, including mode-locked lasers, Kerr effect in microring resonators, electro-optic modulation, and gain-switched lasers. A brief review of their suitability as a multi-carrier source in next-generation reconfigurable optical networks is discussed. Amongst others, the gain-switched laser is chosen as the OFC generation technique of study in this thesis due to its attractive features, which includes dynamic and continuous tuning of channel spacing and central emission wavelength, with desirable noise (intensity and phase) properties.

Chapter 3 focuses on the realisation of reconfigurable multicarrier sources by addressing the limited GSL spectral bandwidth issue, which hampers its commercial employability. Thus, two novel GSL laser-based generation and expansion architectures are proposed and experimentally demonstrated in this chapter. The generated expanded OFC is then fully characterised in terms of its spectral bandwidth, noise properties (intensity and phase), and tunability (channel spacing and emission wavelengths).

Chapter 4 examines two reconfigurable demultiplexer solutions that are necessary to filter out closely spaced individual comb lines before encoding the data. The first approach is based on a microring resonator, which can be dynamically tuned using a field-programmable gate array (FPGA) in conjunction with a digital to analog converter (DAC). Using this method, a real-time reconfigurable GSL based transmitter system is demonstrated. The second approach uses an active demultiplexer based on optical injection locking (OIL), which offers functionalities of tunable demultiplexing, ultra-low noise amplification and modulation, all with a single device.

Chapter 5 presents the experimental implementation of the GSL transmitter system employing an active demultiplexer as a direct modulator. The system performance is firstly evaluated for on-off-keying (OOK) and subsequently extended to 4-QAM and 16-QAM discrete multitone modulation. The impact of adjacent unsuppressed tones and cross channel interference on the system performance, are also analysed.

Chapter 6 proposes the usage of the active demultiplexers in series and cascade configuration, to filter out two comb lines that are then used to generate tunable mmW frequencies for A-RoF distribution. Detailed characterisation of the mmW signals in terms of stability, amplitude fluctuations, single-sideband phase noise, etc. are performed, highlighting the superior mmW signal generation. Furthermore, the optical linewidth independence of the cascaded demultiplexer (dual-stage active demultiplexer) is investigated by generating mmW signal by considering two linewidth OFC sources and experimentally realised a tunable mmW signal A-RoF distribution system and compared their performance as a function of optical linewidths.

Chapter 7 concludes the thesis and summarises the main contributions of this study. Finally, some potential future research directions and system implementations are discussed.

1.1 Evolution of Optical Fibre Communication Systems

Optical fibre communication systems, a pioneering innovation that facilitated today's internet and the plethora of services, have their origin dating to the first fibre transmission demonstration in 1977 [5]. Early use of the technology for data communication yielded data rates of 45 Mb/s transmitted over tens of kilometres [6]. This has since increased by more than five orders of magnitude to recent record demonstrations of 319 Tb/s transmissions over 3001 km [7]. In this section, a brief evolution of the optical fibre communication systems is outlined, which can be classified into distinct generations, dictated by the technological advancements to increase in the bit rate (B) and transmission distance (L) product ($B{\times}L$), as depicted in Figure 1.2.
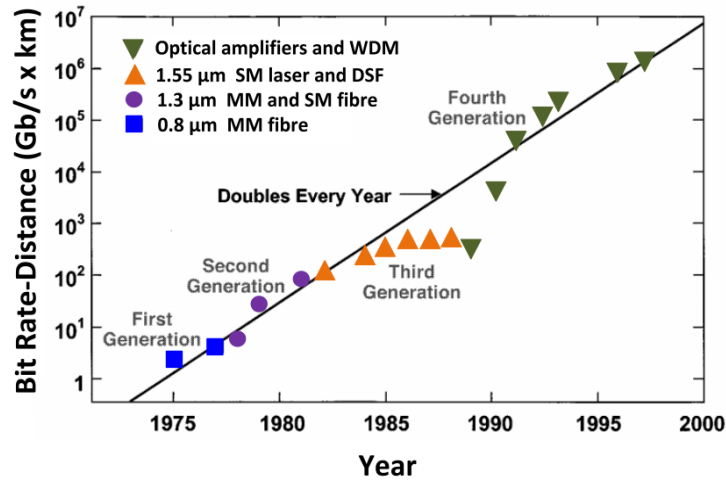
Figure 1.2 Evolution of optical communication system ($B{\times}L$) throughout 1975 to 2000 [6]. MM: multimode; SM: single-mode; DSF: dispersion-shifted fibre; WDM: wavelength division multiplexing.

During the late 1970s, the development of GaAs semiconductor lasers, operating near 0.8 µm wavelength range (the 1st communication window), led to the first-generation optical systems. Such systems offered data rates of 45 Mb/s, with a repeater spacing of up to 10 km over multimode fibre (MMF) [6]. The advent of InGaAsP lasers and detectors, operating near the 1.3 µm region (the 2nd communication window), allowed system designers to take advantage of the reduced fibre loss at this wavelength (<1 dB/km). The maximum transmission speed demonstrated was 44.7 Mb/s up to 23 km and 274 Mb/s

over 7.5 km without repeaters [8]. However, the system reach was improved but limited due to dispersion in MMF. This led to an increased interest in employing a single-mode fibre (SMF) that exhibits minimal chromatic dispersion around the 1.3 µm window. By 1987, the optical systems carrying data rates up to 1.7 Gb/s, with repeater spaced by 50 km, were commercially available [6]. In the third generation, the operating wavelength again moved to a 1.5 µm window to benefit from low silica losses, typically 0.2 dB/km. However, the implementation slowed down, as observed in Figure 1.2 (orange triangles) due to larger chromatic dispersion at 1.5 µm [9]. This led to the development of dispersion-compensation fibre (DCF), with the dispersion coefficient having an opposite sign to that of a standard single-mode fibre (SSMF). The $B{\times}L$ was then enhanced by employing a single longitudinal laser along with DCF, transmission rates of 2.5 Gb/s over 100 km were achieved [10], [11]. Furthermore, the quest for high capacity and longer reach systems received a boost with the advent of the Erbium-doped fiber amplifier (EDFA) and wavelength division multiplexing (WDM) [12], [13]. These innovations led to the fourth generation and transformed optical communications, doubling the $B{\times}L$ every year (Figure 1.2, green triangles) leading to the first long-haul data transmission, in 1991, achieving 2.5 Gb/s over 21,000 km [14].

1.1.1 Wavelength division multiplexing

Wavelength division multiplexing is a well-known capacity scaling approach that allows multiple data streams to be multiplexed and transmitted together over a single optical fibre. The generic WDM architecture, as illustrated in Figure 1.3, comprises an array of discrete lasers emitting at distinct wavelengths. Each wavelength represents an individual optical channel that can be modulated with different data signals either directly or externally (only external modulation is shown in Figure 1.3). The modulated data channels are then multiplexed and transmitted over a single SSMF. The frequency separation between two wavelengths in WDM is known as channel spacing. It accounts for the data bandwidth and the guard band to prevent cross-channel interference (due to frequency drift of laser or non-ideal response of the demultiplexer). Current DWDM systems, as standardised by International Telecommunication Union (ITU-T), operate on

a 50 GHz channel spacing in the conventional (C) band [15]. The inset in Figure 1.3 illustrates multiple data channels fitting on the 50 GHz grid DWDM architecture.
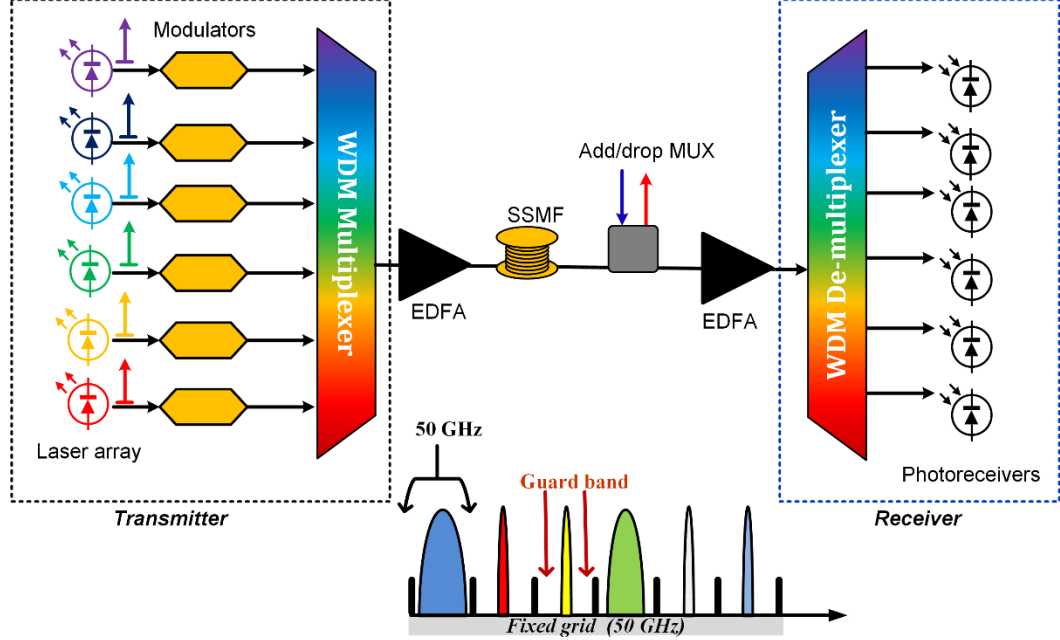
Figure 1.3 Basic WDM transmitter and receiver architecture. Inset depicts the data channels on ITU-T 50 GHz DWDM grid.

The spectral utilisation of the WDM transmission system is indicated by a metric known as *spectral efficiency (SE)*. It is defined as the ratio of the aggregate system capacity C_{sys} to the system bandwidth B_{sys}, which is equivalent to the ratio of bit rate per channel R_{ch} to the frequency spacing F_{ch} between the WDM channels [16],

$$SE = \frac{C_{sys}}{B_{sys}} = \frac{R_{ch}}{F_{ch}} \tag{1.1}$$

It is measured in b/s/Hz and shows how well the available fibre bandwidth is being utilised. The first commercial WDM system implemented in 1995, consisted of 8 WDM channels on a 200 GHz Coarse WDM grid, carrying data at a bit rate of 2.5 Gb/s with a SE of 0.0125 b/s/Hz and with regenerators after every 360 km of fibre [17]. In the following decade, with the technological advancements (lasers and modulator characteristics, filter bandwidths, etc.), the channel count and the bit rate per channel

increased to 80 channels on a 50 GHz grid with 10 Gb/s, 40 Gb/s, and 100 Gb/s per wavelength [18] achieving a SE of 0.2 b/s/Hz. Achieving long transmission distances at data rates exceeding 10 Gb/s using basic on-off keying (0s and 1s), is prohibitive due to the chromatic dispersion impairments inherent in the fibre medium [19]. In order to satisfy the growing need for higher capacity, the network operators turned towards complex modulation formats in conjunction with coherent detection [20], which enabled encoding data on intensity and phase. In addition, multiplexing using the two polarisation states of the carrier enabled a further increase in the data rate per channel. Currently, commercial 40 Gb/s and 100 Gb/s (per wavelength) systems using dual polarisation quadrature-phase modulation (DP-QPSK) on a 50 GHz grid with a SE of 2 b/s/Hz (for 100 Gb/s) are commercially available [21], [22].

1.1.2 State of the art: towards 400 Gbps and beyond

In the last few years, the global internet traffic has been increasing exponentially with no sign of abating, putting enormous pressure on the existing optical network. While the state-of-the-art 100 Gb/s coherent systems are commercially deployed in long-haul links, the anticipated 40% annual growth in data demand over the next few years, will cause the existing optical networks to struggle. To provision for future demands, optical networks should advance towards supporting per-channel data rates of 400 Gb/s, 1 Tb/s, and beyond. However, scaling current networks to cater for higher data rates poses a few different challenges. Current 100 Gb/s/λ/pol. DWDM systems on a 50 GHz ITU-T grid, could accommodate a maximum capacity of around 8 Tb/s with an SE of 2 b/s/Hz. However, a 400 Gb/s per wavelength would require an SE of at least 8 b/s/Hz on the fixed grid, which needs a high optical signal-to-noise ratio (OSNR). However, such OSNR requirements with current systems would result in a shorter reach. To further increase the OSNR, a high optical power source is required, which increases the cost and complexity and the maximum launch power is limited by the fibre nonlinearities.
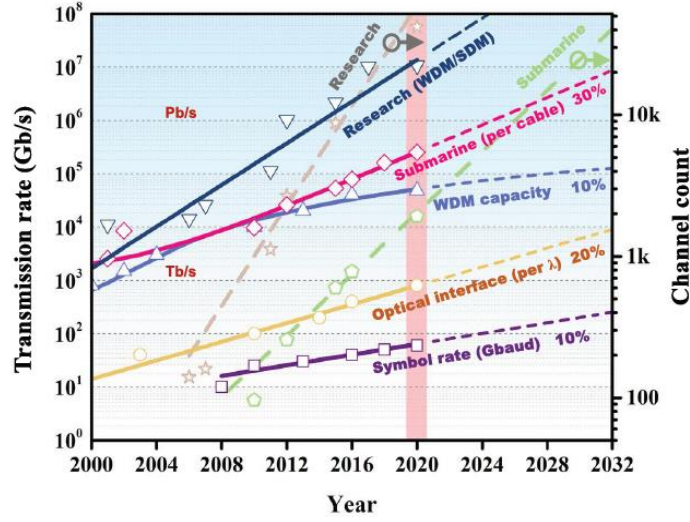
Figure 1.4 Evolution and state-of-the-art of optical fibre communication system capacity (aggregate rates) during 2000-2020. Here, WDM: wavelength division multiplexing, SDM: space-division multiplexing, λ: wavelength [24].

Therefore, moving forward industries and research communities have actively considering various alternative solutions, which will be discussed in section 1.2. Figure 1.4 shows the recent evolution of bit rates of state-of-the-art and future research aspects of optical communication systems. Amongst many, two prominent research aspects that are considered to effectively scale optical systems are superchannel transmission on existing legacy single-mode fibre and space division multiplexing employing novel multi-core or few-mode fibres. Some of the recent notable achievements include Huawei's demonstration of 800 Gb/s per wavelength superchannel transmission over 1100 km of SSMF [25]; OFC based 12 Tb/s superchannel realisation with SE > 10 b/s/Hz and transmission over 1000 km of SSMF [25]; OFC based 10 Pb/s SDM system over 13 km of 38-core 3-mode fibre [26], and many more.

1.2 Capacity Scaling Approaches
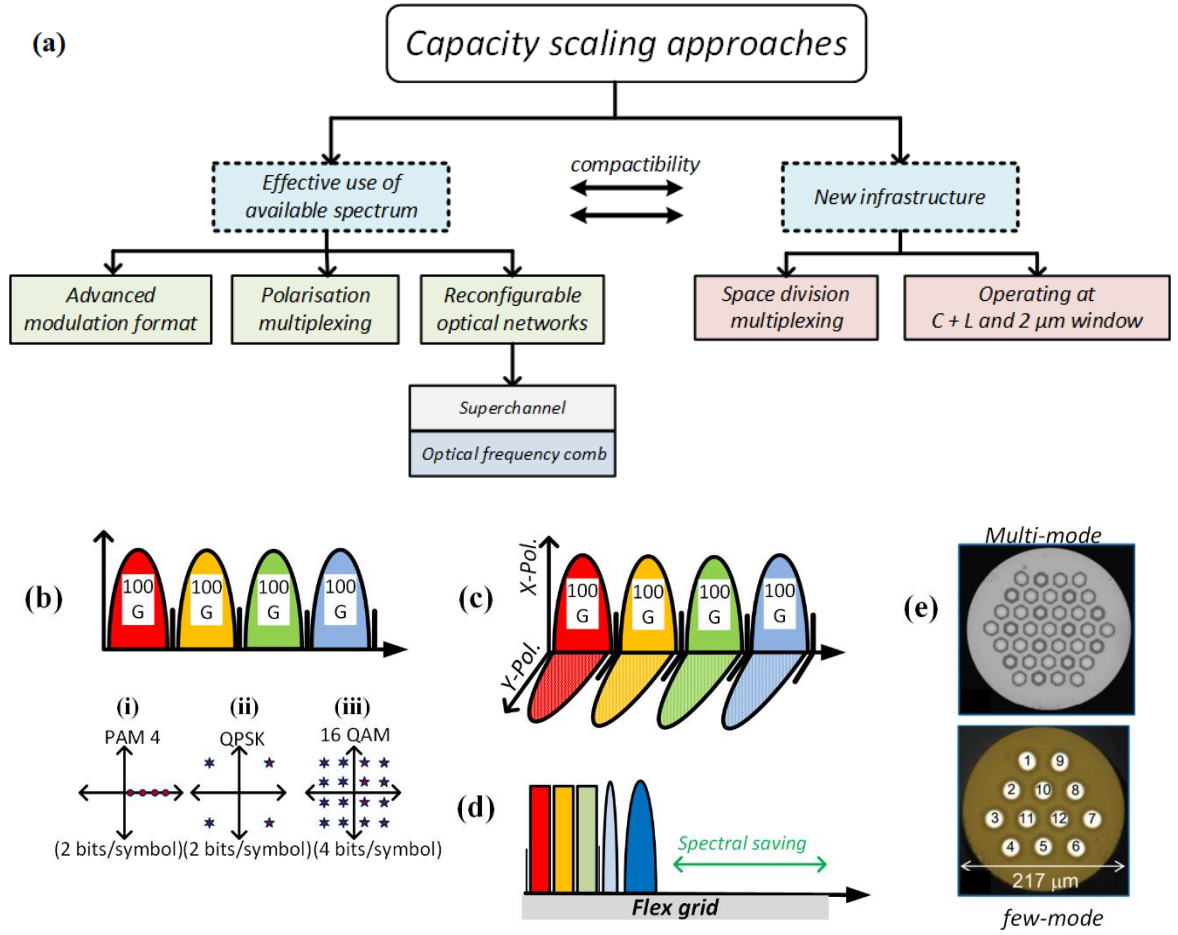
Figure 1.5 (a) Various capacity scaling approaches, capacity scaling on a fixed grid using (b) advance modulation format, (c) two polarisation states, (d) spectral savings by employing flex grid architecture, (e) realisation of space division multiplexing employing multi-mode and few-mode fibres. Insets (i)-(iii) illustrate the constellation diagram of PAM 4, QPSK, and 16- QAM respectively. (Only depiction, not drawn to scale)

To meet the incessant demand for traffic and facilitate next-generation applications, the optical network has to scale its capacity. This can be achieved by (1) effective use of available spectrum and resource and (2) transition towards SDM or exploring new transmission windows as shown in Figure 1.5 (a). The latter would require infrastructural changes of the entire network. This thesis focuses on investigating a reconfigurable optical network, which falls into the first category. Firstly, achieving the finer granular grid (flex grid) UDWDM avoids wastage of spectrum (compared to the fixed grid). Secondly,

adjusting the modulation format and bandwidth allocation based on the demands of the individual channels, such networks not only effective use the available spectrum and satisfy the growing demand using legacy fibre but will also be compatible with potential new infrastructure. In this section, a brief overview of some of the capacity scaling approaches is presented.

1.2.1 Advanced modulation formats

The basic capacity scaling approach is to encode more bits per symbol to reduce the bandwidth occupied by data. This can be achieved by employing advanced modulation formats, which encode information in amplitude, phase of the light. The simplest way is to encode multiple bits using several amplitude levels. Such a modulation scheme is known as pulse amplitude modulation or PAM-N, where N is the number of amplitude levels. For instance, PAM 4 uses 4 distinct level amplitudes, which encodes 2 bits/symbol, thus doubling the capacity compared to a traditional OOK system. The spectral efficiency can be further improved by employing quadrature amplitude modulation (QAM), where data can be encoded on both multi-level amplitude and phase together. Usually, it is denoted as m-QAM, where m is the overall number of symbols. The constellation diagram of 16-QAM, where each symbol carries 4 bits of information, is shown in inset iii, Figure 1.5. Similarly, 32 QAM or 64 QAM can be achieved by encoding 5 bits and 6 bits per symbol, respectively.

1.2.2 Polarisation division multiplexing

The SE can be further improved by exploiting two orthogonal states of polarisation to encode data individually and such a technique is called polarisation division multiplexing (PDM). Usually, PDM is employed with higher-order PSK or QAM to increase the transmission capacity by a factor of 2 [27] and is the technique that enabled the industrial deployment of 100 Gb/s system using 25 Gbaud PM-QPSK systems on the current DWDM ITU-T grid. However, it requires polarisation diverse coherent reception and digital signal processing to account for the time-varying nature of the polarisation states [28]. The scaling capability of advanced modulation formats is limited by the increased noise sensitivity (reduction in the distance between the constellation points). As a result,

such systems require a higher OSNR and low phase noise/narrow optical linewidth optical source [29]. For example, the transition from QPSK to 16 QAM doubles the spectral efficiency but requires 3.7 dB higher OSNR [30], while moving from 16 QAM to 256 QAM means that the OSNR requirement goes up by 8.8 dB [29]. Such a high OSNR requirement is prohibitive as increasing the optical power launched into fibre is limited (due to the adverse nonlinear effects), requires complex DSP and upsurges the power consumption [31], [32].

1.2.3 Reconfigurable / elastic optical networks

Another capacity scaling approach is to employ a new spectrally efficient network paradigm called reconfigurable/elastic optical networks [33], [34]. It utilises the available spectrum effectively, firstly by reducing the size of the guard band to allow closer spacing and accommodating a larger number of WDM channels. Secondly, such networks are capable of dynamically adjusting their transmission parameters, such as the number of carriers, channel separation, modulation formats, according to the incoming traffic requirements. Consequently, the resources are effectively utilised by dynamically allocating the spectrum on-demand. Thus, the realisation of such a fast reconfigurable optical network is very attractive and is the focus of this thesis. The concept of reconfigurable optical networks is discussed in detail in the next section.

1.2.4 Spectral efficient transmission techniques

The capacity of the optical network can also be effectively scaled by realising spectrally efficient "superchannels". It refers to the closely spaced multiple optical carriers or sub-channels that are (i) encoded with higher-order modulation formats (thus, improved SE) and multiplexed together, (ii) transmitted and routed together towards a common receiver site through the same optical link [35]–[37]. As previously discussed, the advent of a higher modulation format, where data is encoded utilising the combination of intensity, phase, of the optical carrier, increased the network capacity significantly. However, the legacy WDM fixed grid architecture with a slot of 50 GHz, is not spectrally efficient as these high order modulation formats will result in smaller channel occupancy than the allotted spectrum. Figure 1.6 (a) illustrates a 1Tb/s WDM system with 10 carriers, each

carrying 100 Gb/s employing PM-16 QAM on the fixed 50 GHz grid. As such signals would occupy a carrier width of ~37 GHz, 25% of the available spectrum is wasted as guard band [38]. A superchannel alleviates the spectral wastage by densely packing the channels employing spectral efficient transmission schemes such as Nyquist WDM, Co-OFDM. An example illustration of such 1 Tb/s superchannel comprising the same 10 carriers PM-16 QAM superchannel, is depicted in Figure 1.6 (b). The subchannels are spectrally shaped employing Nyquist filtering to reduce the spectral bandwidth of each channel to ~12.5 GHz and packed tightly with a guard band of 500 MHz, thus increasing the overall spectral efficiency by ~74% (Nyquist filtering and reduced guard band) [38].
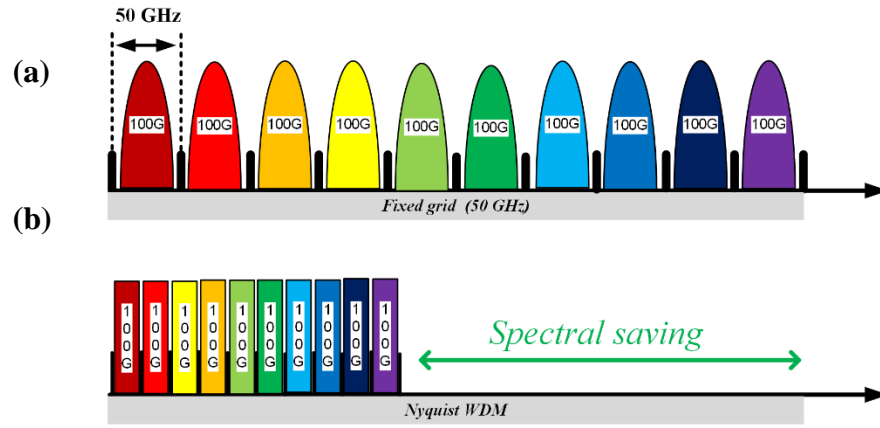
Figure 1.6 1Tb/s system employing (a) existing fixed 50 GHz grid, (b) Nyquist WDM, with sub-channel spacing ~12.5 GHz. (only depiction, not drawn to scale)

Superchannel transmission relies on improving the SE of the WDM system by packing the data channels as close as possible [34], [35]. However, minimising the channel spacing could lead to inter-channel interference (ICI). Pre-filtering can be used at the transmitter, to avoid ICI in the frequency domain, however, this may lead to inter-symbol interference (ISI) in the time domain. Hence, to minimise the ICI and ISI and improve the SE, transmission techniques such as Nyquist-WDM (N-WDM) and coherent optical orthogonal frequency division multiplexing (CO-OFDM) are used.

The concept behind *Nyquist-WDM* [40], [41], can be simply explained by considering the shaping of each sub-carrier to be rectangular. Hence, the channels can be densely packed to occupy a minimum bandwidth confining to Nyquist ISI criteria that ensures ISI-free

transmission. Typically, a root-raised cosine (RRC) filter is applied to realise a rectangular shape (at the transmitter) [42]. For Nyquist pulse shaping, the sharpness of the spectral filtering is dictated by the roll-off factor, β, where $0 < β ≤ 1$, as illustrated in Figure 1.7 (a) and (b). Then, a certain number of such narrow sub-carriers are then tightly packed, with a reduced guard band, to realise a superchannel. Hence, N-WDM improves the overall SE by minimising the sub-carrier spectral occupancy and the size of the guard bands between them. However, this poses stringent requirements in terms of frequency stability of the transmitter to avoid frequency drift and ICI.
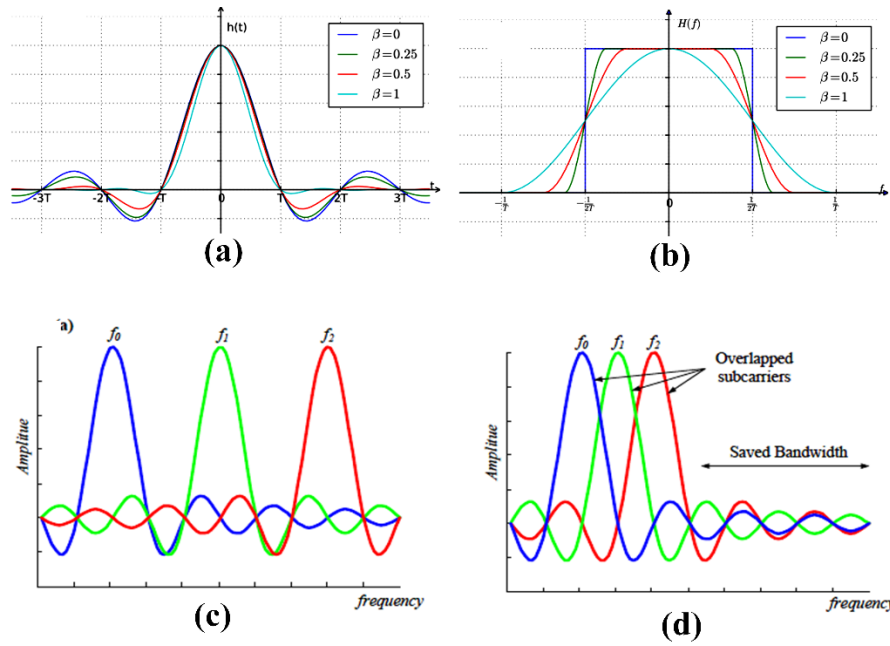
Figure 1.7 Illustration of (a) raised-cosine pulse in the time domain (b) frequency response of raised-cosine pulse [42] (c) non-overlapped subcarriers, (d) CO-OFDM subcarriers.

While N-WDM prevents ICI by ensuring spectral separation between channels, *CO-OFDM* [40] increases the SE by allowing the neighbouring channels to overlap. The ICI interference is minimised by ensuring mutual orthogonality between subcarriers, as depicted in Figure 1.7 (d). From the time domain perspective, CO-OFDM transmits ideal rectangular pulses with a duration equal to a symbol period. Nevertheless, it requires optical sub-carriers that are frequency locked with constant channel separation (equals to symbol rate) and time-aligned symbols on all subcarriers. Furthermore, a strong phase

correlation between the sub-carriers can reduce the OFDM crosstalk at the receiver by the cancellation of the correlated phase noise and reduce the DSP complexity [43].

1.2.5   Space division multiplexing

The commercially used transmission medium in optical communications, thus far, has been limited to a single waveguide (core and cladding) per fibre (SSMF). Hence, in the recent past, there has been interest in exploring the process of multiplexing in the spatial dimension, which is called space-division multiplexing (SDM) [25], [34]–[37]. The concept of SDM refers to incorporating multiple independent physical transmission channels through the use of novel fibres structures. These include multi-core (MCF) and few-mode fibres (FMF) or at times a combination of both, as shown in Figure 1.5 (e). The most attractive SDM realisation is the few-mode multi-core fibre (FM-MCF), which combines the benefits of both MCF and FMF and increases the system capacity ($B \times L$). Several Pb/s SDM system demonstrations have been reported, which includes a recent OFC-based 10.66 Pb/s transmission over 13 km of a 38-core 3-mode fibre with an SE of 1158.7 b/s/Hz [44]. However, the practical realisation of SDM systems is mainly hampered by the impact of inter-core, crosstalk and requires DSP algorithms to compensate for such transmission impairments. Furthermore, such technology may be most suitable for greenfield deployments as the cost of replacing the existing fibre infrastructure to accommodate the SDM system can be prohibitive. Overall, the realisation of SDM could be considered as an effective capacity scaling approach but necessitates significant technological advancement in the future.

1.2.6   Other wavelength bands (C + L and 2 µm windows)

The usable communication spectrum and transmission capacity are mainly limited by the bandwidth of optical amplifiers such as EDFAs (typically covers the conventional (C) band ~1530-1565 nm). However, a lot of recent research focusing on extending the bandwidths of optical amplifiers to the C (1530-1565 nm) + L band (1565-1625 nm) has opened the potential of employing a wider C + L transmission window [46]. The potential of using a new operating wavelength around the 2 µm wavelength region is also being given attention by the research community [47]. Nevertheless, the commercial

deployment of such technologies still needs significant advancement in order to realise components and devices operating at such wavelengths and do so cost-efficiently.

1.3 Reconfigurable Optical Networks
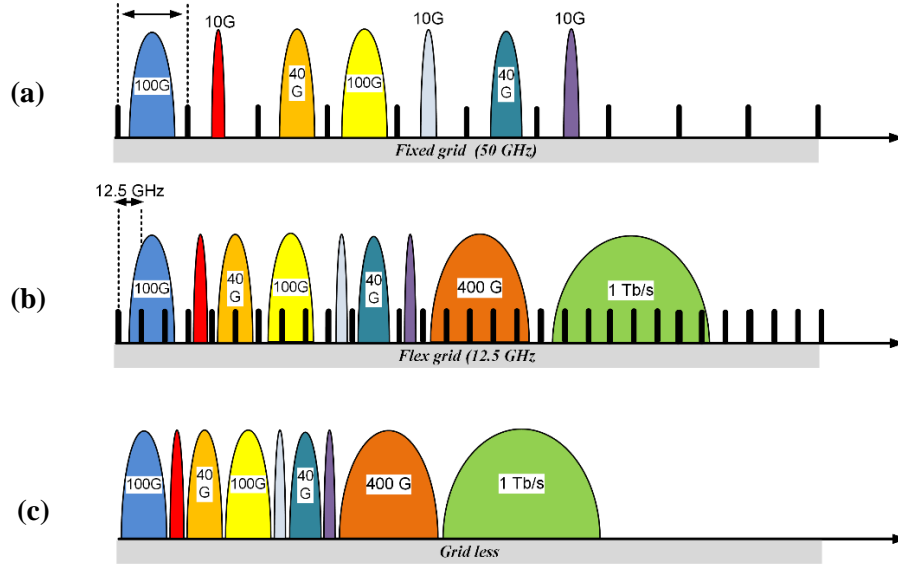
Figure 1.8 Spectral utilisation in a network employing (a) existing fixed 50 GHz grid, (b) flex grid with a granularity of 12.5 GHz and (c) gridless architecture. (Only depiction, not drawn to scale)

With the existing fixed ITU grid architecture, the entire available spectrum (C-band) is divided into 50 GHz frequency slots. Each channel is assigned to a particular spectral slot independent of the data rate. The current state-of-the-art 100 Gb/s systems are compatible with the existing static 50 GHz ITU grid but going towards 400 Gb/s would be too broad to fit within the frequency slot. It would require the use of a higher-order modulation format (limits the system reach) or the concatenation of two 50 GHz slots (results in large spectral wastage). The latter approach could be limited by the design specifications of other elements such as optical switches, which are intended for fixed grid requirements. The major drawback of the fixed ITU grid is the spectral inefficiency, as frequency slots are assigned regardless of the transmitted data rate, as shown in Figure 1.8 (a). Let us assume, three individual channels carrying 10 Gb/s OOK (channel occupancy of 20 GHz + guard band of 10 GHz), 40 Gb/s DP-QPSK (channel occupancy of 25 GHz + guard band of 10 GHz), and 100 Gb/s (channel occupancy of 37.5 GHz + guard band of 10

GHz). Including the guard bands, the spectral occupancy of these three channels sums up to 112.5 GHz while the allocation would be 3 spectral slots taking up the bandwidth of 150 GHz (3×50) thereby resulting in a spectral wastage of 40% (due to fixed channel spacing regardless of data rate).

The spectral efficiency can be improved by adopting a finer (more granular) flex grid architecture, where frequency slot size is reduced to 12.5 or 6.25 GHz, as per the ITU-T recommendation G 694.1 [47], G 872 [15], respectively. A frequency slot is usually defined in reference to the nominal central frequency $f_n = 193.1\,THz + n \times 6.25$ GHz, where 193.1 THz is the ITU-T "anchor frequency" and n is the integer number of slots. This means the centre frequency can be moved in steps of 6.25 GHz. The amount of optical spectrum is defined by the slot-width, which is a multiple of 12.5 GHz. The finer frequency slot of 12.5 GHz would support 400 Gb/s, 1 Tb/s data rate, and beyond by aggregating multiple 12.5 GHz channel slots, as illustrated in Figure 1.8 (b) and (c). For optimum utilisation of spectral resources and to adapt to even higher data rates, flex grid architectures could eventually transition towards gridless architecture.

However, transitioning to a finer grid to achieve better SE would not be sufficient on its own, as the internet data traffic not only increases in volume but also becomes more dynamic. The dynamic variations in the traffic manifests itself as changes in volume (e.g., between night and day), and in location (business vs. residential areas). Figure 1.9 (a) illustrates a static 200 Gb/s system usage over 24 hours of the day for a particular connection [33]. As seen in the graph, there are both idle periods, where the connection is under-utilised. Similarly, Figure 1.9 (b) depicts the data traffic pattern in a business district (blue plot), which shows peak demand during the day/working hours, and a residential area (dotted red), which experiences higher volumes of traffic during the evening hours. However, assigning a fixed capacity to these two areas does not account for this variation, which results in suboptimal utilisation of the resources. With the static legacy network, the network operators cannot re-allocate non-utilised resources to other connections during idle periods or allocate additional resources during high-activity periods.
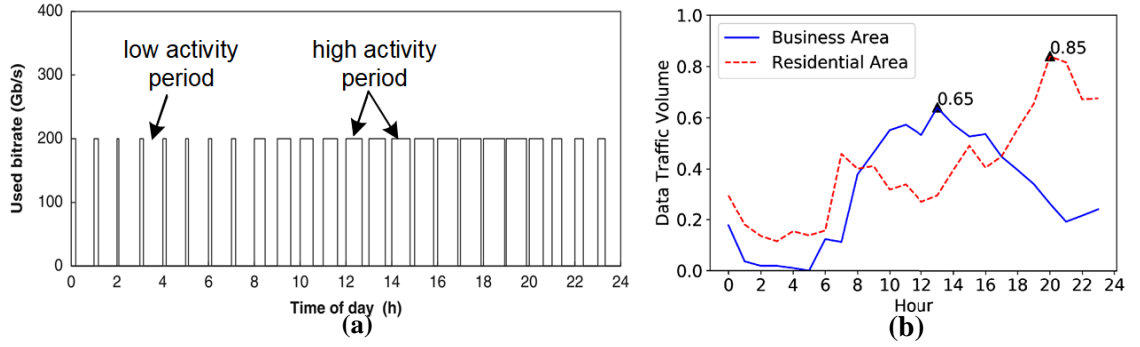
Figure 1.9 (a) Static 200 Gb/s data usage of an optical connection during the time of day [32], (b) data traffic pattern in different areas: business and residential area [44].

To reap the full benefits of the flex grid approach, the optical network should evolve towards a new flexible data rate and resource-efficient network. Such a network paradigm is referred to as a reconfigurable/elastic optical network, which can dynamically adjust its resources, according to the live traffic requirements. For instance, if the traffic demands 100 Gb/s over 400 km, then reconfigurable transceiver may dynamically choose closer channel spacing and employ an advanced modulation format such as DP-16 QAM, which will occupy only 25 GHz of the spectrum. On the other hand, if the same traffic needs to reach over 1500 km, a DP-QPSK modulation would be chosen, sacrificing the spectral efficiency for lower OSNR requirements (extended reach) [33].

1.3.1 Reconfigurable optical networks requirements

To fully envision a reconfigurable optical network, several technological considerations and optimisations need to be considered across physical, control, and network layers. A truly reconfigurable and responsive network would require a dynamic, software-controllable architecture that is not only confined to control and data plane but also to physical layer components, to use the available resources and infrastructure most effectively.

1.3.1.1 *Physical layer considerations*

Flexibility in the physical layer is the key building block of reconfigurable optical networks for next-generation spectral efficient systems. Some of the vital technological aspects are (1) *reconfigurable transceivers* and (2) *reconfigurable optical switches*. The

characteristics and the degree of flexibility of these elements determine the overall performance of the optical connections.
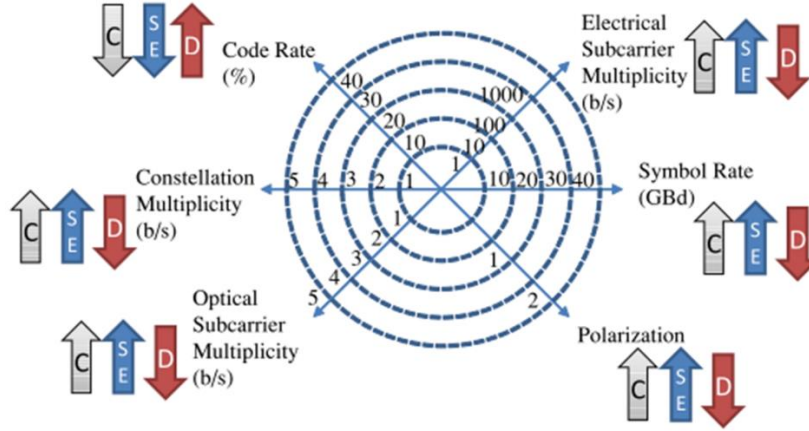
Figure 1.10 Degrees of freedom of a reconfigurable transceiver [46]. Here, C: capacity, SE: spectral efficiency, D: optical reach distance.

Reconfigurable transceivers: To evaluate the physical level connection, several performance metrics such as effective capacity, transparent reach, spectral efficiency, and tunability are considered [33], [49], [50]. A reconfigurable transceiver is able to effectively tune and optimise the above-mentioned metrics to meet dynamic traffic conditions. Figure 1.10 exemplifies the flexibility of a transceiver, where various transmission parameters can be simultaneously adjusted, to achieve the desired performance.

- The effective capacity of the system can be increased either by increasing the baud rate/symbol rate or by using a higher-order modulation format. It can be doubled by employing polarisation multiplexing, which enables the transmission of individual data signals in both X and Y polarisation states of light. While these approaches increase the SE and capacity of the network, they limit the system reach, by requiring a higher OSNR. The reach could be extended by increasing the code rate (error correction code bits), at the expense of a reduced information rate and the complexity of the receiver [49].

- The spectral efficiency and capacity can be further improved by employing multicarrier transmission techniques such as N-WDM, CO-OFDM, etc. As previously discussed, Tb/s data rates can be accomplished by creating a superchannel, comprising several lower-speed subcarriers. Increasing the number of subcarriers would lead to a linear increase in the system capacity, but also reduce the reach due to cross channel interference. An ideal reconfigurable transmitter would exhibit most, if not all of the above-mentioned degrees of flexibility, coupled with a short reconfigurability time and standardised control interface to interact with the higher networking layers.

Reconfigurable optical switches: To obtain the benefit of reconfigurable transceivers, firstly, it is necessary to migrate from the existing fixed to flex grid architecture. As discussed in the previous section, the finer granularity improves the SE and supports different frequency slots to be packed tightly or combined to achieve the desired data rate. However, the adaption of the finer grid could be hindered by the other network elements such as optical switches. Thus, an upgrade of optical switches to the variable channel spacing, with a minimal penalty (due to filter shape imperfections) is crucial. The trade-off between the filter passband characteristics (flat top), the number of filtering stages and SE also needs to be considered [48]–[52].

This thesis work focuses on the reconfigurability of the physical layer for next-generation optical networks. The advanced higher network and control plane configuration and optimisations are beyond the scope of this thesis.

1.3.2   Optical multicarrier transmitter

An optical multicarrier transmitter is a key enabler of the reconfigurable optical network. The degree of flexibility of a multi-carrier source dictates the overall reconfigurability of the network connection. Hence, in order for a multicarrier source to be considered as a transmitter, it needs to portray certain characteristics such as high spectral purity (low noise characteristics), frequency stability, and the ability to rapidly tune the number of carriers, emission wavelength and carrier spacing. In this section, some of the multicarrier

source solutions are outlined and evaluated for their suitability in future reconfigurable optical networks.

1.3.2.1 Bank of lasers
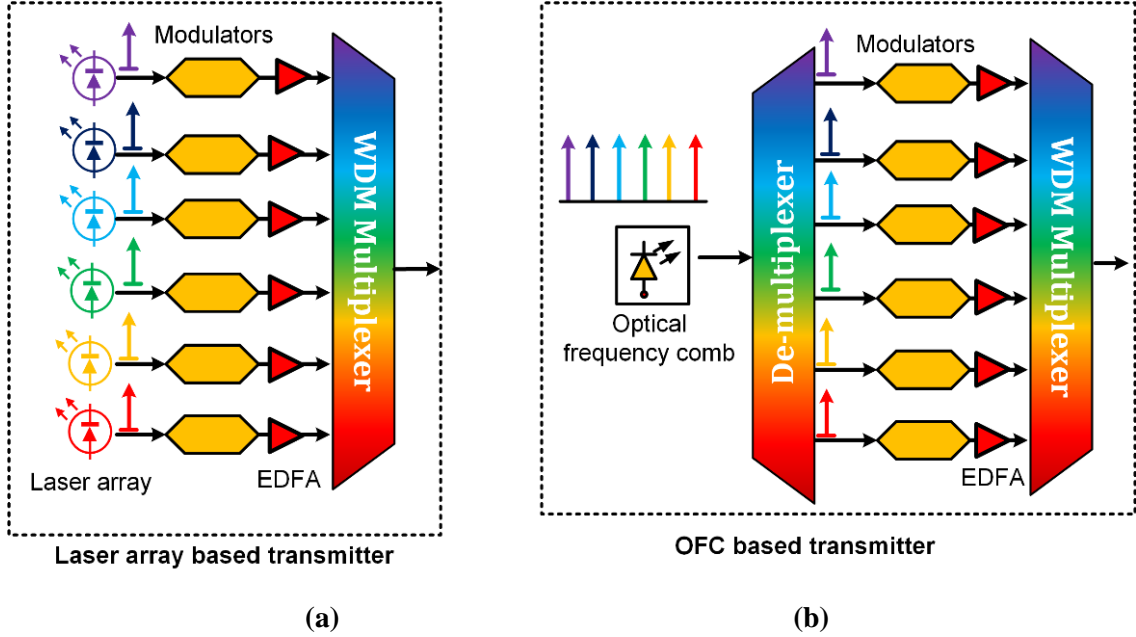
Figure 1.11 Laser array-based multi-carrier transmitter architecture, (b) optical frequency comb-based multi-carrier transmitter architecture.

Standard telecommunication lasers in the form of an integrated laser array are widely used as optical sources in existing WDM systems. The laser-based WDM multicarrier transmitter system is as depicted in Figure 1.11 (a). Each laser within the bank is tuned to emit at a discrete wavelength in order to set them apart by the desired frequency spacing. It is important to note that, in this thesis, wavelength is used to represent absolute values and frequency to represent the differences (which are usually small). However, the major drawback is that these lasers struggle to provide fixed channel separation, as each laser suffers from an arbitrary drift in their emission wavelength over time, causing undesirable cross channel interference. To avoid such interference, a large guard band must be introduced between adjacent channels. Although, some commercial transponders may employ wavelength lockers to reduce the frequency drift whilst incurring additional cost and complexity. However, the wavelength lockers may still fail to operate at a finer

granularity (<12.5 GHz), which would counter any SE gains from moving to flex grid. In addition, tuning of the frequency spacing involves changing the wavelength of all lasers, which increases the complexity of the operation. Hence, the frequency drift may hinder their application in high-capacity superchannel transmission techniques like N-WDM, CO-OFDM.

1.3.2.2 *Optical frequency comb*

One attractive solution is to employ an optical frequency comb (OFC) as an optical multi-carrier source. It can provide multiple carriers originating from a single device that can replace an array of lasers, as depicted in Figure 1.11 (b). An OFC source generates a series of equidistant tones that exhibit excellent frequency stability and a high degree of phase correlation between them. This precise frequency separation between adjacent tones/channels, enables a reduction in the size of the guard band, allowing closer channel spacing and improving spectral efficiency. Other features of an OFC that would make it an ideal candidate to be employed as a reconfigurable transceiver include:

- *Reconfigurability:* many OFC generation techniques offer a tunability of the number of comb lines, channel spacing, emission wavelength, etc. This allows reconfigurability of transmission parameters according to the dynamic traffic requirements
- *Fast reconfiguration:* an OFC (based on the generation technique used) could provide a fast tuning of the number of subcarriers and channel spacing. As a result, these transmission parameters are expected to be reconfigured rapidly [33].
- *Reduced inventory, cost, and power consumption:* A single OFC can replace an array of discrete lasers, requiring a single thermal and wavelength stabilisation subsystem. Thus, the employment of an OFC reduces the size, cost and power consumption.

1.3.3 OFC implementation challenges

While an OFC offers several advantages over the laser array solution, several challenges need to be met prior to their adoption in commercial systems. These include:

- *Development of a simple and flexible OFC source:* Several semiconductor baser OFC generation schemes are being actively investigated in the research world [53]–[59]. However, not every OFC generation technique is simple and offers the desired level of flexibility. Each scheme has its pros and cons, which will be discussed in detail in chapter 2. Therefore, the development of a simple, flexible OFC, which can generate high purity optical carriers with excellent tunability is considered crucial. Further simplification could be achieved if the OFC were to be fully integrated with other functional components, into a single chip. Such integration would render added benefits of small size, low cost and energy efficiency

- *Tunable demultiplexing stage (at transmitter):* An OFC-based transmitter system requires a demultiplexer to separate individual comb lines prior to data encoding. The demultiplexing becomes a major challenge when the channel spacing is to be reconfigured from a large granularity (100/50 GHz) to a finer granularity (12.5/6.25 GHz). The existing commercially available solutions fail to meet these disparate bandwidths needs due to their limited bandwidth resolution. Therefore, designing a tunable OFC demultiplexer with high bandwidth resolution, low loss and cost, can be considered to be a major challenge.

- *Asymmetric channel spacing*: Another challenge that needs to be addressed is how to achieve asymmetric channel spacing when an OFC generates a series of equidistant carriers. This would be a critical feature when realising highly spectral efficient grid-less architecture in the near-future.

- *Amplification stages:* In an OFC, the average output power of a single laser is distributed among multiple lines resulting in each of the tones exhibiting a low output power. This is exacerbated by the use of demultiplexers that further add to the losses with average insertion losses of 5-6 dBs. Hence, optical amplifiers are required, which results in reduced OSNR, higher cost and increased complexity of the system.

- *Spectral purity, robustness, and long-term stability:* OFC lines are expected to portray spectral purity (intensity and phase) and offer long-term stability and robustness in terms parameters such as comb line power, channel separation, and comb line suppression ratio.

- *Development of tunable filter (at the receiver site):* To reap the full benefit (i.e., SE) of OFC, it is essential to develop a bandwidth tunable filter that can separate reduced guard band signal at the receiver site without introducing filtering impairments.

1.3.4 Thesis Main Contributions
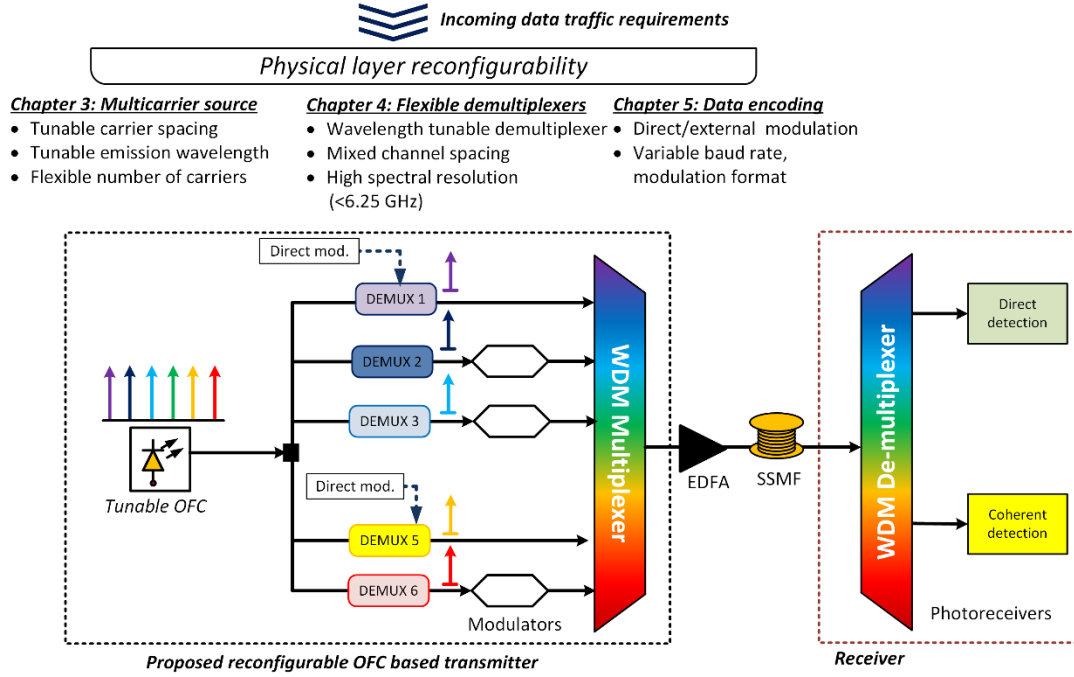
Figure 1.12 Schematic of proposed reconfigurable GSL comb-based transmitter system

This thesis investigates potential solutions to the OFC implementation challenges mentioned in section 1.3.3 and aims to contribute to enhancing the suitability of OFC-based reconfigurable transmitters for application in next-generation high-capacity networks. The reconfigurable OFC-based transmitter architecture envisioned in this work is illustrated in Figure 1.12. It comprises a reconfigurable gain-switched laser (the OFC generation technique chosen in this work) based OFC, which generates the desired number of optical carriers and possesses the ability to swiftly tune its channel spacing and emission wavelength. The OFC is followed by a tunable active demultiplexer that supports asymmetric channel spacing and offers multiple functionalities including a tunable demultiplexer (channel spacing and wavelength), low noise amplifier, power equaliser and a direct modulator. Depending upon the incoming traffic requirements (such

as data rate, connection reach), the number of OFC carriers, channel spacing, modulation (direct or external) can be efficiently reconfigured. Furthermore, the architecture lends itself to photonic integration thus reducing the size, cost, and energy consumption.

The main contributions of this thesis are:

❖ ***Development of a reconfigurable OFC-based multi-carrier transmitter:*** Two novel reconfigurable GS-OFC expansion schemes are experimentally demonstrated, providing an increase of the OFC spectral bandwidth by a factor of 3. The first approach is based on a mutually injection-locked GSL to generate an expanded OFC that offers an expansion in the number of carriers and channel spacing without the need to re-optimise the gain switching settings. The second architecture entails multiple GS-OFCs that are combined, and phase correlated with the aid of four-wave mixing in a semiconductor optical amplifier. The wavelength tunability feature of the proposed expanded OFC is validated by tuning over 30 nm across the C-band. A comprehensive characterisation of the expanded OFCs is performed, including phase noise/linewidth, relative intensity noise, and phase correlation. The results achieved show that both architectures lend themselves to photonic integration and are well suited for employment as transmitters in reconfigurable optical networks.

❖ ***Investigation of tunable demultiplexers:*** Two potential tunable demultiplexers (a) microring resonator (b) active demultiplexer based on optical injection locking are investigated. The first solution where the MRR is used as a tunable demultiplexer to demonstrate the first, real-time FPGA-controlled reconfigurable OFC-based transmitter (OFC + demultiplexer). This serves as a proof-of-principle experiment and validates the potential realisation of a software-defined reconfigurable optical network employing a GSL source. The second approach employs a semiconductor laser as a multi-functional active demultiplexer to select and amplify the desired comb line with a suppression ratio > 30 dB and output power of 8 dBm (delivering between 30 and 40 dB of gain). This multi-functionality is highlighted by demonstrating tunable demultiplexing of individual lines across the comb and for channel spacing varying from MHz to GHz. Furthermore, the power equalisation features are also illustrated

by using comb lines that sit 10 dB below the spectral peak of the OFC. This OFC expansion scheme increases the number of comb lines that can be used for data transmission by a factor of 1.7. Finally, a thorough characterisation of injection locking parameters such as comb line power, detuning frequency, and their impact on the demultiplexed phase noise of the signal and the achieved suppression of unwanted comb tones is investigated.

❖ *Demonstration of OFC-based transmission systems*: First demonstrations of an OFC-based transmission system employing a single device (active demultiplexer) to perform OFC demultiplexing, amplification, and direct modulation is carried out. Performance evaluation of such a system, utilising various modulation formats, is also undertaken. Firstly, a two-channel 10.7 Gb/s OOK system for short-reach applications is realised, and error-free data transmission over 3 km is achieved. Then, a 4-channel transmitter, employing 4-, 16-QAM discrete multitone (DMT) signals is used to achieve aggregate data rates of 100 Gb/s (8×12.5 Gb/s) and 200 Gb/s (8×25 Gb/s), respectively. A bit error ratio (BER) below the 7% hard-decision forward error correction (HD-FEC) limit is achieved for all channels (within 20 dB from the spectral peak) for transmission over 40 and 25 km of SSMF. Furthermore, the impact of suppression ratio/adjacent channel crosstalk on the system performance is experimentally investigated and the impact of low injection power on the chirp induced on the laser (due to direct modulation) is studied by building a simulation model using the virtual photonics incorporated transmission maker (VPI-TM) tool.

❖ *Active demultiplexer enabled linewidth tolerant tunable mmW signal generation:* Two novel mmW signal generation and A-RoF distribution enabled by active demultiplexer in parallel and cascade are demonstrated. The proposed solutions inherit all the benefits of the active demultiplexer (filter-amplify-modulate) and the latter configuration possesses a unique property that renders the quality of the generated signal to be tolerant to the optical linewidth of the comb. This is verified by employing two different OFC linewidths (3.1 MHz and 30 kHz) and obtaining a low single-sideband phase noise value ($-99 \ dBc/Hz$, at 10kHz offset), regardless of the

OFC used. In addition, a complete A-RoF system is realised by transmitting a directly modulated 64-QAM universal filtered orthogonal frequency division multiplexed (UF-OFDM) and DMT data signals at 29.5, 38 GHz, 61 GHz over 25 km of SSMF. In all the cases, optimum performance is achieved with BER and error vector magnitude (EVM) recorded below the HD-FEC limit. Furthermore, the system performance was evaluated as a function of OFC linewidth for dual-stage active demultiplexer (active demultiplexer in cascaded form). The two orders of magnitude increase in OFC linewidths induces only a 0.1 dB penalty (at HD-FEC), demonstrating the linewidth tolerance feature. Finally, a case study of an A-RoF distribution system is presented, to illustrate the benefits of the proposed scheme, in terms of power budget and the number of RRU's that can be served using a single OFC.

1.4 References

[1]   M. Nowell, "Cisco VNI Forecast update and forecast: 2017-2022," *Cisco White paper*, 2019. [Online]. Available: https://www.ieee802.org/3/ad_hoc/bwa2/public/calls/19_0624/nowell_bwa_01_190624.pdf (accessed Feb. 12, 2020).

[2]   ITU, "Economic Impact of COVID-19 Report of an Economic Experts Roundtable," *ITU-D Policy and Regulation*, 2020. [Online]. Available: https://www.itu.int/en/ITU-D/Regulatory-Market/Pages/Events2020/EconomicRoundTable/home. (accessed Sept. 3, 2021).

[3]   T. Bienkowski, "COVID-19 Network Traffic Patterns: A Worldwide Perspective from Our Customers," *Netscout*, 2020. [Online]. Available: https://www.netscout.com/blog/Network-Traffic-in-the-Age-of-COVID-19. (accessed Sept. 3, 2021).

[4]   V. López, L. Velasco, "Elastic Optical Networks Architectures, Technologies, and Control", Springer Publishing Company, 2016

[5]   I. Jacobs, "Atlanta fiber system experiment: Overview," *in The Bell System Technical Journal,* vol. 57, no. 6, pp. 1717–1721, 1978, DOI: 10.1002/j.1538-7305.1978.tb02121.x.

[6]   G. P. Agrawal, "Fiber-Optic Communications Systems", *Third Edition Wiley* 2002. DOI: 10.1002/9780470611388.

[7]   NICT, "Demonstration of World Record: 319 Tb/s Transmission over 3,001 km with 4-core optical fiber," *NICT press release*, 2021. [Online]. Available: https://www.nict.go.jp/en/press/2021/07/12-1.html. (accessed Jan. 5, 2019).

[8]   K. Ogawa, E. L. Chinnock, D. Gloge, P. Kaiser, S. R. Nagel, and S. J. Jang, "System experiments using 1.3 μm LEDs," *Electronics Letters*, vol. 17, no. 2, pp. 71–72, 1981. DOI: 10.1049/el:19810051

[9]   T. Miya, Y. Terunuma, T. Hosaka, and T. Miyashita "Ultimate low-loss singlemode fiber at 1.55 μm," *Electronics Letters*, vol. 15, no. 4, pp. 106-108, 1979.

[10]   A. H. Gnauck, B. L. Kasper, R. A. Linke, R. W. Dawson, T. L. Koch, T. J. Bridges, E. G. Burkhardt, R. T. Yen, D. P. Wilt, J. C. Campbell, K. C. Nelson, and L. G. Cohen, "4-Gbit/s transmission over 103 km of optical fibre using a novel electronic multiplexer/demultiplexer," *Journal of Lightwave Technology*, vol. 3, no. 5, pp. 1032–1035, 1985.

[11]   S. Mohrdiek, "10-Gb/s standard fiber transmission using directly modulated 1.55-μm quantum-well DFB lasers," *IEEE Photonics Technology Letters*, vol. 7, no. 11, pp. 1357–1359, 1995, DOI: 10.1109/68.473497.

[12]   R. Mears, L. Reekie, I. M. Jauncey, and D. Payne, "Low-noise erbium-doped fibre amplifier operating at 1.54μm," *Electronics Letters*, vol. 23, no. 19, pp. 1026–1028, 1987.

[13] E. Desurvire, J. R. Simpson, and P. C. Becker, "High-gain erbium-doped traveling-wave fiber amplifier," *Optics letters*, vol. 12, no. 11, pp. 888–890, 1987.

[14] N. S. Bergano, J. Aspell, C. R. Davidson, P. R. Trischitta, B. M. Nyman, and F. W. Kerfoot, "Bit error rate measurements of 14,000 5 Gbit/s fiber-amplifier transmission system using circulating loop," *Electronics Letters*, vol. 27, no. 21, pp. 1889–1890, 1991.

[15] ITU-T, "Architecture of Optical Transport Networks, Recommendation G.872," *ITU-T Recommendations*, 2012. [Online]. Available: https://www.itu.int/rec/T-REC-G.872. (accessed Jun. 3, 2019).

[16] P. J, Winzer, D. T. Neilson, A. R. Chraplyvy, N. B. Labs, and H. Road, "Fiber-optic transmission and networking : the previous 20 and the next 20 years*," Optics Express,* vol. 26, no. 18, pp. 24190–24239, 2018, DOI: 10.1364/OE.26.024190.

[17] H. Kogelnik, "On optical communication: reflections and perspectives," in *2004 European Conference on Optica; communication (ECOC)*, pp. Mo1.1.1, 2004.

[18] M. Birk, L. Raddatz, D. Fishman, S. Woodward, and P. Magill, "Field Trial of End-to-End OC-768 Transmission Using 9 WDM Channels over 1000km of Installed Fiber," *Conference on Optical Fiber Communication, Technical Digest Series*, vol. 86, pp. 290–291, 2003, DOI: 10.1109/ofc.2003.1247664.

[19] T. Foggi, E. Forestieri, G. Colavolpe, and G. Prati, "Maximum-likelihood sequence detection with closed-form metrics in OOK optical systems impaired by GVD and PMD," *Journal of Lightwave Technology*, vol. 24, no. 8, pp. 3073–3087, 2006, DOI: 10.1109/JLT.2006.876898.

[20] G. Li, "Recent advances in coherent optical communication," *Advances in Optics and Photonics*, vol. 1, no. 2, pp. 279-307, 2009, DOI: 10.1364/aop.1.000279.

[21] A. K. Mishra, "Evolution of Optical Fiber Technologies," *white paper: Sterlite Tech*, 2012. [Online]. Available: https://www.stl.tech/optical-interconnect-products/optical-fibre/pdf/Evolution_Optical_Fiber.pdf. (accessed Dec. 23, 2019).

[22] P. J. Winzer, "Beyond 100 G Ethernet" *IEEE Communications Magazine,* vol. 48, no. 7, pp. 26-30, 2010. DOI:10.1109/MCOM.2010.5496875

[23] R. J. Essiambre, G. J. Foschini, P. J. Winzer, G. Kramer, and B. Goebel, "Capacity Limits of Optical Fiber Networks," *Journal of Lightwave Technology*, vol. 28, no. 4, pp. 662–701, 2010, DOI: 10.1109/JLT.2009.2039464.

[24] W. Shi, Y. Tian, and A. Gervais, "Scaling capacity of fiber-optic transmission systems via silicon photonics," *Nanophotonics*, vol. 9, no. 16, pp. 4629–4633, 2020, DOI: 10.1515/nanoph-2020-0309.

[25] M. Mazur, M-G. Suh, A. Fülöp, J. Schröder, V. Torres-Company, M. Karlsson, K. J. Vahala, and P. A. Andrekson, "High Spectral Efficiency Coherent Superchannel Transmission with Soliton Microcombs," *Journal of Lightwave Technology*, vol. 39, no. 13, pp. 4367–4373, 2021, DOI: 10.1109/JLT.2021.3073567.

[26] N. Yoshikane and T. Tsuritani, "Recent Progress in Space-Division Multiplexing Optical Network Technology," *2020 24th International Conference on Optical Network Design and Modeling, ONDM 2020*, pp. 12–15, 2020. DOI: 10.23919/ONDM48393.2020.9133031.

[27] H. Sun, K.-T. Wu, and K. Roberts, "Real-time measurements of a 40 Gb/s coherent system," *Optics Express*, vol. 16, no. 2, pp. 873, 2008, DOI: 10.1364/oe.16.000873.

[28] K. Kikuchi, "Coherent Optical Communications: Historical Perspectives and Future Directions," in *High Spectral Density Optical Communication Technologies*, Springer, Berlin, Heidelberg, 2010. DOI: https://doi.org/10.1007/978-3-642-10419-0_2.

[29] R.-J. Essiambre, G. Kramer, P. J. Winzer, G. J. Foschini, B. Goebel, "Capacity limits of optical fiber networks," *Journal of Lightwave Technology*, vol. 28, no. 4, pp. 662–701, 2010.DOI: 10.1109/JLT.2009.2039464

[30] P. J. Winzer, "High-Spectral-Efficiency Optical Modulation Formats," *Journal of Lightwave Technology*, vol. 30, no. 24, pp. 3824–3835, 2012.
DOI: 10.1109/JLT.2012.2212180

[31] J. M. Yates, J. P. R. Lacey, M. P. Rumsewicz, and M. A. Summerfield, "Performance of networks using wavelength converters based on four-wave mixing in semiconductor optical amplifiers," *Journal of Lightwave Technology*, vol. 17, no. 12, pp. 2419–2427, 1999, DOI: 10.1109/50.762892.

[32] J. F. T. Zami, B. Lavigne, O. B. Pardo, S. Weisser, J. David, M. Le Monnier, "31.2-Tb/s real time bidirectional transmission of 78x400 Gb/s interleaved channels over C band of one 90-km SMF span," in *Optical Fiber Communication Conference (OFC) and National Fiber Optic Engineers Conference (NFOEC)*, 2018, p. W1B.5.

[33] V. López, L. Velasco, "Elastic Optical Networks Architectures, Technologies, and Control", *Springer Publishing Company,* 2016.

[34] G. Zhang, M. de Leenheer, A. Morea, and B. Mukherjee, "A survey on OFDM-based elastic core optical networking," *IEEE Communications Surveys and Tutorials*, vol. 15, no. 1, pp. 65–87, 2013, DOI: 10.1109/SURV.2012.010912.00123.

[35] X. Liu, "Evolution of Fiber-Optic Transmission and Networking toward the 5G Era," *iScience*, vol. 22, pp. 489–506, 2019, DOI: 10.1016/j.isci.2019.11.026.

[36] S. Chandrasekhar, X. Liu, B. Zhu, and D. W. Peckham, "Transmission of a 1.2-Tb/s 24-carrier no-guard-interval coherent OFDM superchannel over 7200-km of ultra-large-area fiber," in *35th European Conference on Optical Communication*, pp. 1-2, 2009.

[37] X. Liu and S. Chandrasekhar, "Superchannel for next-generation optical networks", in *2014 Optical Fiber Communications Conference and Exhibition,* pp. M2F.3, 2014. DOI: 10.1364/OFC.2014.M2G.3.

[38] G. Bennett, "Superchannels to the rescue!," *Press release*, 2012. [Online]. Available: e. (accessed Jun 1, 2020).

[39] S. Chandrasekhar and X. Liu, "OFDM based superchannel transmission technology," *Journal of Lightwave Technology*, vol. 30, no. 24, pp. 3816–3823, 2012, DOI: 10.1109/JLT.2012.2210861.

[40] G. Bosco, "Spectrally efficient transmission: A comparison between Nyquist-WDM and CO-OFDM approaches," in *2012 Advanced Photonics Congress*, pp. SpW3B.1, 2012, DOI: 10.1364/sppcom.2012.spw3b.1.

[41] P. Guan, K. M. Røge, H. C. H. Mulvad, M. Galili, H. Hu, M. Lillieholm, T. Morioka, and L. K. Oxenløwe, "All-Optical Ultra-High-Speed OFDM to Nyquist-WDM Conversion Based on Complete Optical Fourier Transformation," *Journal of Lightwave Technology*, vol. 34, no. 2, pp. 626–632, 2016, DOI: 10.1109/JLT.2015.2495188.

[42] WikiWand, "Raised-Cosine Filter", 2020. [Online]. Available: http://www.wikiwand.com/en/ Raised-cosine filter. (accessed April 21, 2020).

[43] G. Bosco, A. Carena, V. Curri, P. Poggiolini and F. Forghieri, "Performance limits of Nyquist- WDM and CO-OFDM in high-speed PM-QPSK systems," IEEE Photonics Technology Letters, vol. 22, no.15, pp. 1129–1131, 2010.

[44] G. Rademacher, B. J. Puttnam, R. S. Luís, J. Sakaguchi, W. Klaus, T. A. Eriksson, Y. Awaji, T. Hayashi, T. Nagashima, T. Nakanishi, T. Taru, T. Takahata, T. Kobayashi, H. Furukawa, and N. Wada "10.66 Peta-Bit / s Transmission over a 38-Core-Three-Mode Fiber," in *2020 Optical Fiber Communications Conference and Exhibition*, pp. Th4C.5, 2020.

[45] G. Rademacher, R. S. Lu, B. J. Puttnam, and R. Ryf, S. van der Heide, T. A. Eriksson, N. K. Fontaine, H. Chen, R-J. Essiambre, Y. Awaji, H. Furukawa, and N. Wada "172 Tb / s C + L Band Transmission over 2040 km Strongly Coupled 3-Core Fiber," in *2020 Optical Fiber Communications Conference and Exhibition*, pp. Th4C.5, 2020.

[46] F. Gunning and B. Corbett, "Time to Open the 2-μm Window?," *Optics & Photonics News*, vol. 30, no. 3, pp. 42-47, 2019

[47] ITU-T, "Spectral Grids for WDM Applications: DWDM Frequency Grid, Recommendation G.694.1," *ITU-T Recommendations*, 2012. [Online]. Available: https://www.itu.int/rec/T-REC-G.694.1/. (accessed Jun. 3, 2019).

[48] L. Chen, D. Yang, D. Zhang, C. Wang, J. Li, and T. M. T. Nguyen, "Deep mobile traffic forecast and complementary base station clustering for C-RAN optimization," *Journal of Network and Computer Applications*, vol. 121, no. July, pp. 59–69, 2018, DOI: 10.1016/j.jnca.2018.07.015.

[49] M. Imran, P. M. Anandarajah, A. Kaszubowska-Anandarajah, N. Sambo, and L. Poti, "A Survey of Optical Carrier Generation Techniques for Terabit Capacity Elastic Optical Networks," *IEEE Communications Surveys and Tutorials*, vol. 20, no. 1, pp. 211–263, 2018, DOI: 10.1109/COMST.2017.2775039.

[50] M. Jinno, H. Takara, B. Kozicki, Y. Tsukishima, Y. Sone, and S. Matsuoka, "Spectrum-efficient and scalable elastic optical path network: Architecture, benefits, and enabling

technologies," *IEEE Communications Magazine*, vol. 47, no. 11, pp. 66–73, 2009, DOI: 10.1109/MCOM.2009.5307468.

[51]   O. Gerstel, M. Jinno, A. Lord, and S. J. Ben Yoo, "Elastic optical networking: A new dawn for the optical layer?," *IEEE Communications Magazine*, vol. 50, no. 2, pp. 12–20, 2012, DOI: 10.1109/MCOM.2012.6146481.

[52]   S. Talebi, F. Alam, I. Katib, M. Khamis, R. Salama, and G. N. Rouskas, "Spectrum management techniques for elastic optical networks: A survey," *Optical Switching and Networking*, vol. 13, no. 2, pp. 34–48, 2014, DOI: 10.1016/j.osn.2014.02.003.

[53]   T. Habruseva, S. O. Donoghue, N. Rebrova, F. Kéfélian, S. P. Hegarty, and G. Huyet, "Optical linewidth of a passively mode-locked semiconductor laser," *Optics Letters*, vol. 34, no. 21, pp. 3307–3309, 2009.

[54]   R. G. M. P. Koumans and R. van Roijen, "Theory for passive mode-locking in semiconductor laser structures including the effects of self-phase modulation, dispersion, and pulse collisions," *IEEE Journal of Quantum Electronics*, vol. 32, no. 3, pp. 478–492, 1996, DOI: 10.1109/3.485400.

[55]   M. Zhang, B. Buscaino, C. Wang, A. Shams-Ansari, C. Reimer, R. Zhu, J. M. Kahn, and M. Lončar, "Broadband electro-optic frequency comb generation in a lithium niobate microring resonator," *Nature*, vol. 568, no. 7752, pp. 373–377, 2019, DOI: 10.1038/s41586-019-1008-7.

[56]   T. Herr, K. Hartinger, J. Riemensberger, C. Y. Wang, E. Gavartin, R. Holzwarth, M. L. Gorodetsky, and T. J. Kippenberg "Universal formation dynamics and noise of Kerr-frequency combs in microresonators," *Nature Photonics*, vol. 6, no. 7, pp. 480–487, 2012, DOI: 10.1038/nphoton.2012.127.

[57]   Y. K. Chembo, "Kerr optical frequency combs: Theory, applications and perspectives," *Nanophotonics*, vol. 5, no. 2, pp. 214–230, 2016, DOI: 10.1515/nanoph-2016-0013.

[58]   R. Zhou, S. Latkowski, J. O'Carroll, R. Phelan, L. P. Barry, and P. Anandarajah, "40nm wavelength tunable gain-switched optical comb source," *Optics Express*, vol. 19, no. 26, pp. B415–B420, 2011, DOI: 10.1364/OE.19.00B415.

[59]   P. M. Anandarajah, S. P. Ó Dúill, R. Zhou, and L. P. Barry, "Enhanced Optical Comb Generation by Gain-Switching a Single-Mode Semiconductor Laser Close to Its Relaxation Oscillation Frequency," *IEEE Journal of Selected Topics in Quantum Electronics*, vol. 21, no. 6, pp. 592–600, 2015, DOI: 10.1109/JSTQE.2015.2456751.

2. Optical Frequency Comb as a Multicarrier Transmitter

The advent of optical frequency combs (OFCs) is considered one of the most important breakthroughs in the field of photonics [1]–[7]. In the past decade, OFCs have been extensively studied and become an attractive solution in diverse applications such as spectroscopy [8, 9], ranging [10], atomic clock [11], steganography [12], spectrally efficient optical communication networks [13]–[16], millimetre and terahertz generation [17], [18], and many more. As discussed in the previous chapter, OFCs gained a lot of attention in the field of optical fibre communications due to its outstanding stability of its free spectral range. Hence, the OFC can serve as an alternative solution to the existing laser array, for deployment in next-generation optical networks employing spectrally efficient modulation formats [7], [16], [19].

In this chapter, a brief overview of the OFC and the desired characteristics it needs to portray for it to be considered employable as a flexible transmitter, are presented. Then, some of the prominent semiconductor-based OFC generation schemes are discussed and their suitability in reconfigurable optical networks are studied.

2.1 Optical Frequency Comb Source

An optical frequency comb source generates a series of phase correlated optical carriers with fixed frequency separation. An illustration of an OFC source and its` spectral output

is shown in Figure 2.1. OFCs are usually described by carrier spacing (f_r), which is known as the free spectral range (FSR), and their emission frequency (f_0). The multiple comb lines in the optical frequency domain correspond to the train of ultra-short optical pulses in the time domain, with a repetition rate $\tau_r = 1/f_r$. The temporal pulse width signifies the spectral bandwidth of the OFC i.e., the narrower the pulse, the broader the OFC spectral width. An OFC can be represented in the (a) optical frequency domain, (b) time domain, and (c) RF domain (showing the beat tones generated by optoelectronic conversion of an OFC), as shown in Figure 2.2.

Optical Frequency Comb
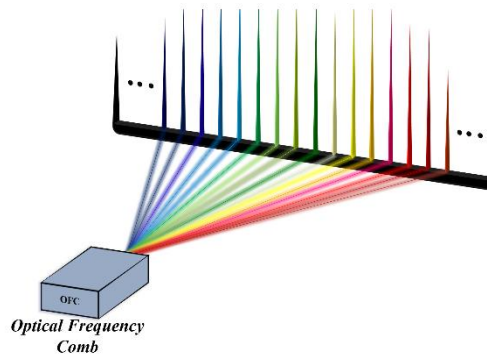
Figure 2.1 Illustration of the OFC source emitting a series of optical carriers.
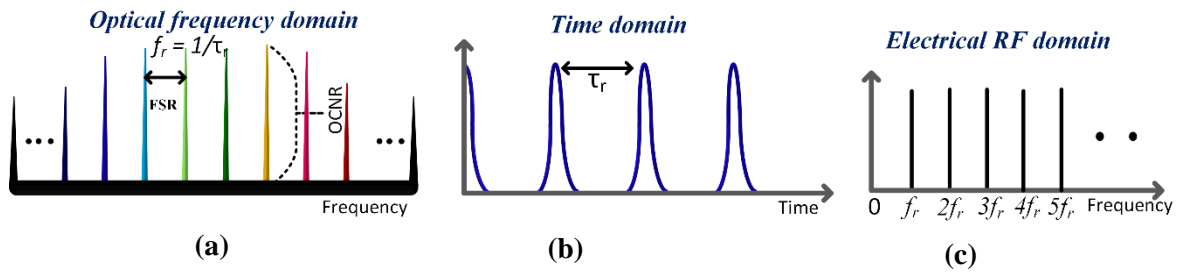
Figure 2.2 OFC representation in (a) optical frequency, (b) time, and (c) radio frequency (RF) domains. Here, FSR: free spectral range, OCNR: optical carrier to noise ratio.

For applications in high-capacity reconfigurable optical networks, an OFC is expected to portray certain spectral characteristics and flexibility features. The most important of them are outlined below:

- *Large spectral bandwidth:* an OFC with a large number of comb lines, with specified frequency spacing, is desirable as it provides a large number of optical carriers thus replacing multiple individual lasers.

- *Tunable channel spacing:* The optical carrier spacing should be tunable. As the occupied data bandwidth is proportional to the baud rate, the OFC channel spacing must be rapidly tuned according to the required modulation format and baud rate.

- *Tunable emission wavelength*: It implies the tuning of the central emission wavelength of the comb. This enables a dynamic spectrum allocation to take advantage of the unused bandwidth slots.

- *Spectral flatness:* It refers to the optical power level variation between the comb lines, which in turn determines the number of comb tones that can be used for the transmission. Generally, a 3 dB excursion from the spectral peak is considered to be acceptable for near-uniform performance, avoiding the need for power equalisation before modulation.

- *Optical power per comb line*: High power levels of individual comb lines is highly attractive. This reduces the need for multiple optical amplification stages, thus reducing complexity, cost, and power consumption.

- *Noise properties:* A low relative intensity noise (RIN) and phase noise are highly desirable [20], [21]. RIN is the random intensity fluctuation of the optical carriers and is usually measured as dB/Hz. The current IEEE standard for Ethernet 802.3 specifies the RIN better than -132 and -136 dB/Hz for 200 and 400 Gb/s systems. Phase noise is a random frequency fluctuation leading to the broadening of the spectral tone [21]. This can also be referred to as optical linewidth. It affects the systems employing phase and hybrid amplitude-phase modulation schemes (M-PSK, M-QAM) and can limit the maximum achievable baud rate. For example, the linewidth requirement for 10 Gbaud QPSK is 4.1 MHz, whereas for 16-QAM is 1.4 MHz [22].

- *Optical carrier to noise ratio (OCNR):* A large OCNR is desirable. This criterion serves as a signal-to-noise ratio when considering each optical tone as a carrier.

- *Phase correlation:* A high degree of phase correlation between the comb lines is attractive. It can reduce the DSP complexity at the receiver [22] and allow for the use of an OFC as a multi-wavelength local oscillator in a coherent system [24].

In addition to the above-mentioned characteristics, an OFC to be employed as a multi-carrier transmitter is also expected to deliver long-term stable operation in terms of frequency, and power. The OFC generation architecture should be feasible for photonic integration thereby reducing the size, cost and energy consumption of the entire transmitter.

2.2 Semiconductor Based OFC Generation Techniques

In this section, some of the most prominent semiconductor-based OFC generation schemes are outlined and their suitability as a multi-carrier transmitter in future reconfigurable networks discussed.

2.2.1 Mode-locked lasers

A mode-locked laser (MLL) is the most popular ultra-short pulse generation technique, which was initially demonstrated in 1964 [25]. The term "mode-locking" refers to the process of introducing phase synchronisation or locking between the longitudinal modes in a semiconductor laser cavity [26], [27]. When the longitudinal modes are phase-locked, they will constructively and periodically interfere, resulting in a generation of periodic short optical pulses with a repetition rate (τ_r) equal to the round-trip time of the cavity. Correspondingly, a series of optical frequency comb lines are generated in the frequency domain, with a fixed frequency spacing of $f_r = 1/\tau_r$, as depicted in Figure 2.3 (b). A theoretical understanding of the MLL can be understood from [28], while the recent advances and versatile applications can be found in [6], [29], [30].
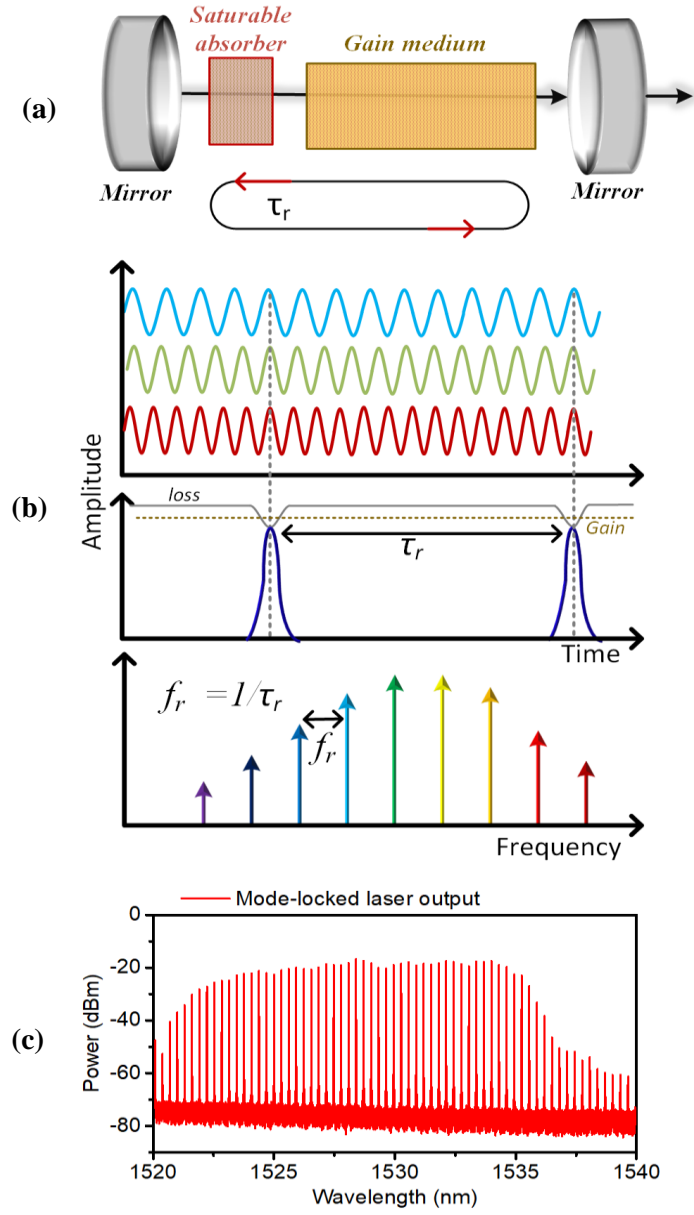
Figure 2.3 (a) Schematic of a passively mode-locked laser, (b) illustration of pulse and OFC generation, (c) optical spectrum of Q-dash mode-locked laser output with FSR of ~ 42 GHz. Illustrative diagrams are redrawn from [28].

Mode-locking can be achieved using various laser structures and methods. They can be classified into passive, active and hybrid [32], [33]. Passively mode-locked lasers depend on a non-linear phenomenon to induce mode-locking. It may comprise of an inter-cavity, intensity-dependent loss element, called a saturable absorber, as shown in Figure 2.3 (a) or a specific quantum structure (well, dash, dot) designed to enhance third-order optical

nonlinear interactions (such as FWM) inside the cavity [34], [35]. The process of mode-locking can be explained as follows. With an increase in the intensity of the incident light, the absorption profile of the saturable absorber decreases until it saturates and then becomes transparent for a small period. During this period, the gain overcomes the losses (Figure 2.3 (b)) and emits a pulse [31]. As the longitudinal modes within the gain region start to lase at the same time, they begin with the phases that are correlated i.e., mode-locked. This repetitive process of selective amplification of high-intensity peaks and absorption of low-intensity light leads to the emission of a train of short pulses. In active mode-locking, an active component such as a modulator is used instead of a passive component. The modulator is driven by an external signal, whose frequency is equal to the longitudinal mode spacing (cavity length). This modulates the cavity losses periodically, stimulating laser turn on and off sequence, resulting in the emission of ultra-short pulses [26]. Hybrid mode-locking refers to a case where both passive (through saturable absorber) and active (modulating cavity losses) mode-locking are present at the same time in the same laser [36].

2.2.1.1   *Mode-locked laser as a reconfigurable OFC source*

A MLL generates a broadband comb and is well-known for its compactness and energy efficiency (passive MLLs). The optical spectrum of the Q-dash MLL with an FSR of ~ 42 GHz, spanning over 15 nm is shown in Figure 2.3 (c). The detailed characterisation of this device can be found in [37]. Several experimental demonstrations of a photonic integrated MLL [36] and its use in data transmission systems are reported in [38]–[41].

However, several features of MLLs hinder their employability in next-generation reconfigurable networks. First and foremost, the frequency spacing between the comb line is dictated by the cavity length of the MLL i.e., frequency spacing is fixed. Thus, the FSR cannot be tuned to adjust to the dynamic network demands and requirements. Some of the other shortcomings are (i) sophisticated and complex cavity design, (ii) relatively large optical linewidths (in MHz range) [32] unless external injection (at the cost of reduced comb bandwidth) or a feed-forward heterodyne scheme is used [40], (iii) mode-partition noise resulting in large RIN (typically below −120 dB/Hz) [41], and (iv) long term

stability issues [33]. These shortcomings make them not suitable for future flexible optical networks.

2.2.2 Kerr optical frequency comb

A Kerr comb, based on the non-linear interaction (i.e.: cascaded four-wave mixing (FWM) in high Q microring resonators [44], [45]) is another popular type of frequency comb generation technique. In principle, it consists of a single tunable continuous wave (CW) laser and a microring resonator, as depicted in Figure 2.4 (a). Kerr OFCs typically span a few THz with line spacing in order of tens to hundreds of GHz, as in Figure 2.4 (c) [46].

The formation of the wideband comb can be briefly explained as follows [45]: a strong pump is injected into the ring resonator, which evokes an optical Kerr effect that changes the resonator's refractive index proportionally to the pump intensity. As a result, the pump signal generates new frequency components through degenerate FWM [45], where two photons from the pump signal are annihilated to produce two new photons one up-shifted and one down-shifted from the pump frequency by the same amount. If the frequencies of the pump and the newly generated FWM components (signal and idler) coincide with micro-resonator cavity modes (grey lines, Figure 2.4 (b)), the nonlinear process is enhanced, leading to an efficient cascaded FWM. As a result, a frequency comb with an FSR of Δ and phase correlated with the pump signal is generated. Such a comb is referred to as the "primary comb". However, the number of comb tones is limited and their power drops exponentially with the distance from the pump (inset (ii), Figure 2.4 (b)). Next, the "sub-comb" evolves around primary comb lines via degenerative or non-degenerative processes with line a spacing of 'δ', matching the resonator mode spacing, as seen in (inset (iii), Figure 2.4 (b)). Eventually, sub-combs merge with the primary comb to form a wide comb, where δ is a sub-harmonic of Δ within some margin or frequency mismatch $\Delta - \delta$ (usually in the MHz range [44]), as depicted in (inset (iv), Figure 2.4 (b)). This mismatch has to be compensated by active comb synchronisation ($\Delta - \delta$ reduced to 0) [47] to obtain a soliton comb state [48]. The recent advances in the Kerr comb are reported in [4], [49], [50].
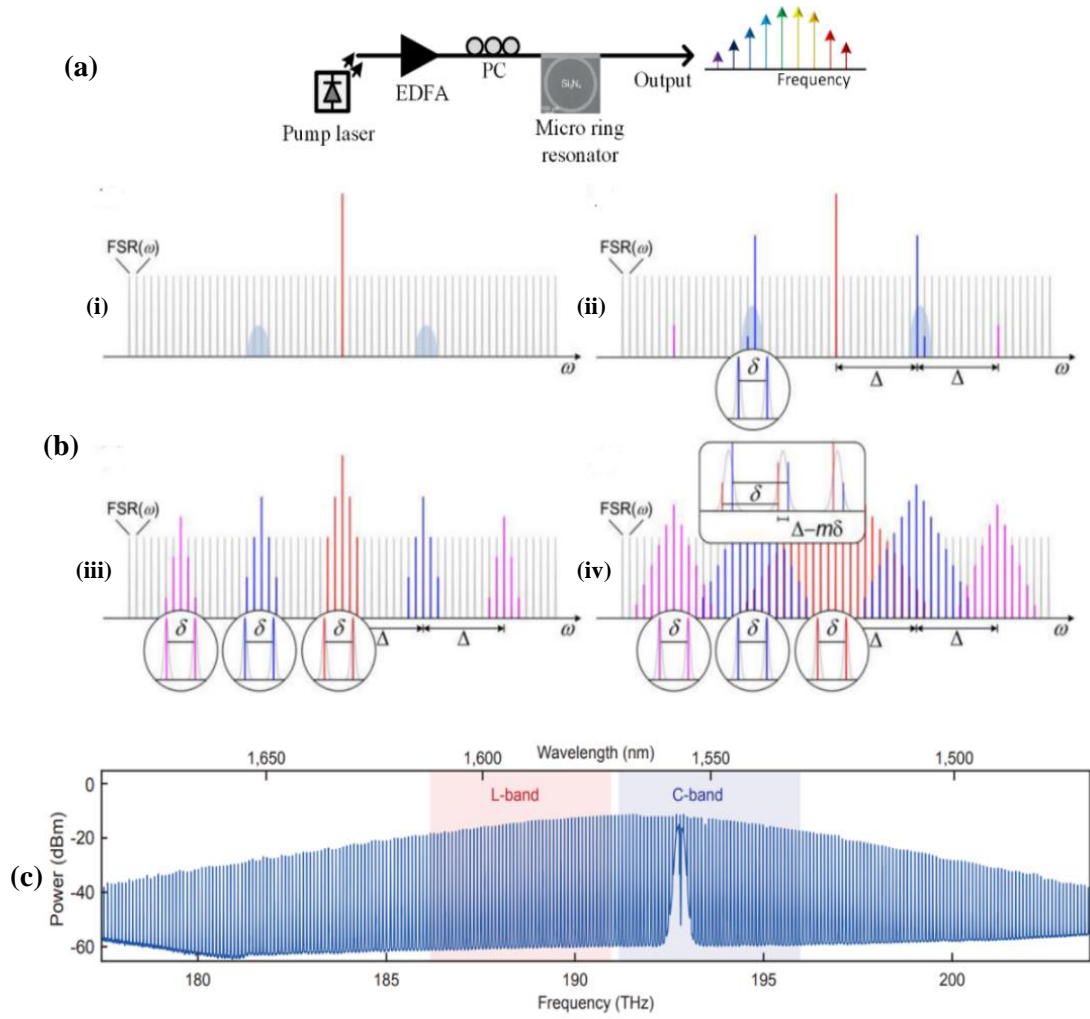
Figure 2.4. (a) Schematic of Kerr comb generation scheme, (b) formation of Kerr comb depicting primary and sub-combs, (c) optical spectrum of Kerr comb spanning over C + L band with FSR ~100 GHz. Adapted from [46]. Here, EDFA: Erbium-doped fibre amplifier, PC: polarisation controller. FSR: free spectral range.

2.2.2.1 *Kerr comb as a reconfigurable OFC source*

The Kerr OFC can be a compact and photonically integrable solution. Depending on the dispersion profile of the resonator and the pumping scheme, the method is capable of generating a broadband comb with a good OCNR, and mutually coherent low phase noise lines. The ultra-broad bandwidth of the Kerr OFC attracted a lot of attention, resulting in several high-capacity (tens of Tb/s) WDM systems demonstrations in the last few years [51], [52]. Nevertheless, the method requires sophisticated comb synchronisation, tuning, and feedback control loop mechanism for stable long-term operation [50], [51].

Furthermore, Kerr based combs require very high pump power (in the order of 30 dBm [51]), which can be difficult to realise as a photonic integrated circuit. Several pump power reduction techniques have been investigated [52], [53] recently, but they further complicate the overall structure of the device. More importantly, the comb line spacing is fixed and is dictated by the size of the resonator cavity. This is a critical shortcoming of the Kerr frequency comb that hinders its employability as a reconfigurable multi-carrier source in future flexible optical networks.

2.2.3 Electro-optic modulator

An electro-optic modulator (EOM) based OFC is generated by modulating (phase, amplitude, or a combination) a continuous wave (CW) laser with the aid of single or multiple modulators. The modulators are driven by large sinusoidal signals to generate multiple sidebands around the CW laser frequency, thus resulting in the generation of an OFC. EOM combs are reconfigurable in terms of their FSR, which can be tuned by changing the frequency of the modulating signal. The maximum FSR and the number of comb lines generated (spectral bandwidth) are determined by the bandwidth of the modulator and the modulation index. Furthermore, the noise properties of the comb lines are predominantly dictated by the CW laser, with an additional contribution from the RF source, and amplifiers used. The details of EOM comb generation methods and recent advances are reported in [3], [5], [58].

EOM-based combs can be realised in various configurations as reported [56], [59]–[62]. These include a single-phase modulator (PM) or cascaded PM, hybrid MZM and PM, dual-drive MZM and PM, and so on. The basic form of the EOM comb is a single-phase modulator driven with a signal with amplitude equal to multiples of V_π, where V_π is the half-wave voltage to attain a π phase shift. The output signal can be written as [62],

$$E_0(t) = A(t)e^{j(\omega_o t + \phi(t) + \beta \sin \Omega t)} \tag{2.1}$$

where the input CW laser electric field is $A(t). e^{j(\omega_o t + \phi(t))}$. A is the amplitude, ω_o, ϕ are the emission frequency and phase of the signal, respectively. β and Ω are the amplitude and modulation frequency of the RF signal. The modulation amplitude $\beta = \pi \frac{V}{V_\pi}$, defines

the modulation index. Usually, an EOM generates a limited number of comb lines and exhibits amplitude variations. The EOM comb can be expanded by the Jacobi-Anger expansion to express the multi-carriers as [61],

$$E_0(t) = \sum_{n=-\infty}^{\infty} A(t)J_n(\beta)e^{j(\omega_o t+\phi(t)+n\Omega t)} \tag{2.2}$$

Here, J_n is the nth order Bessel function and β determines the overall comb bandwidth.
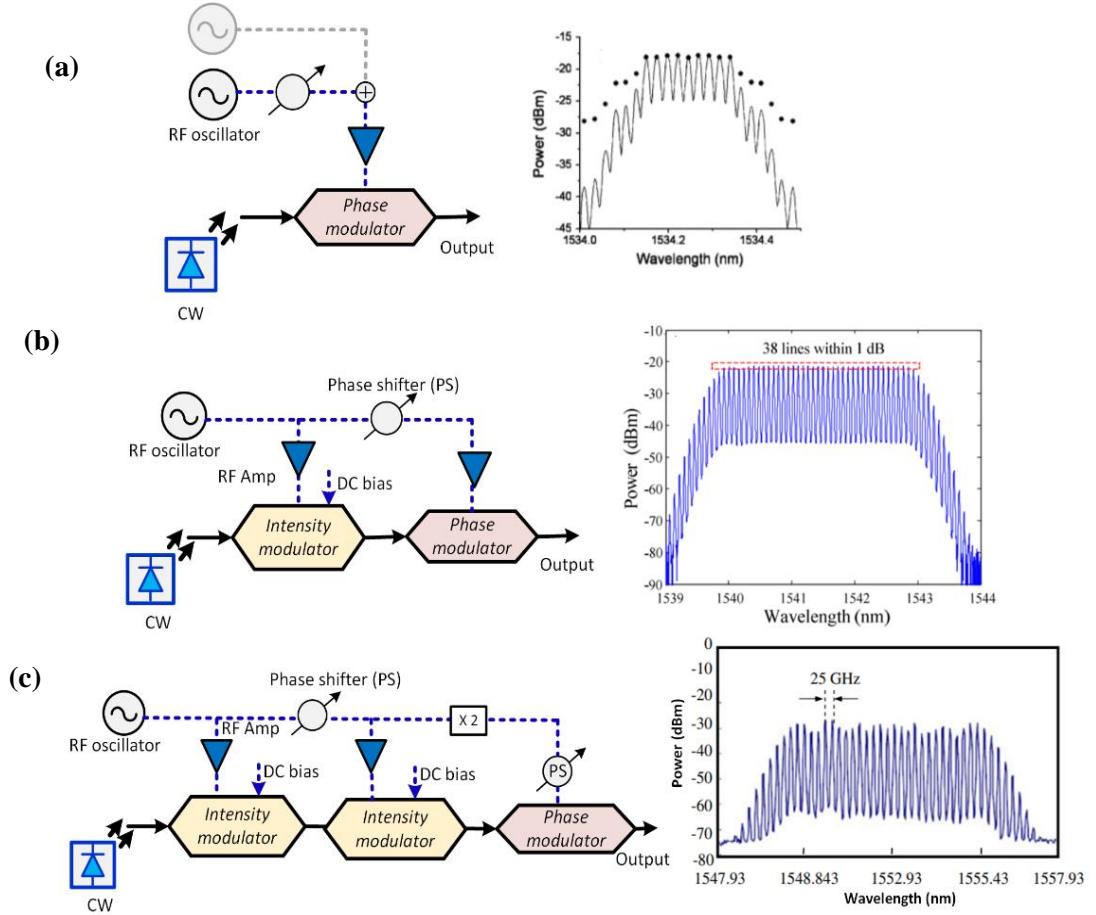
Figure 2.5 Schematics of the EOM comb generation employing (a) single phase modulator (PM) [55], (b) intensity modulation (IM) and PM [56] , (c) cascaded IM and PM [57].

Furthermore, better spectral flatness can be achieved by driving a phase modulator with the combination of two sinusoidal signals or employing a dual-drive MZM in tandem with a phase modulator, or by creating a fibre ring cavity with a modulator loop [61] [56]. Amongst several configurations, the combination of intensity modulators and phase

modulators is considered the most balanced configuration in terms of tuning, complexity, and comb spectral bandwidth [3], [62].

2.2.3.1 *EOM frequency comb as a reconfigurable OFC source*

Although EOM combs are limited in spectral bandwidth compared to the previously discussed OFC techniques, they offer a large degree of freedom in terms of FSR and emission wavelength tunability. They also generate highly coherent tones with phase noise determined by the characteristics of the CW source used. Finally, an EOM (depending on the material used) architecture lends itself to photonic integration. Several demonstrations of high-capacity WDM networks employing EOM combs have been reported [58], [61]. Generally, to achieve spectrally broad and flat comb, a series of cascaded modulators are employed. This translates into large insertion losses (typical insertion losses of a LiNbO$_3$ IM modulator ~ 5-6 dB per device) and needs amplification stages, which in turn degrades the achievable OCNR of the comb lines and more importantly increases the cost and footprint. In addition, as LiNbO$_3$ modulators suffer from inherent bias drifts, operating a set of cascade modulators [64] leads to stability-related issues. Recently, EOM OFC with Silicon-Organic Hybrid (SOH) based modulator, generating 7 comb lines with 40 GHz FSR was demonstrated [65]. However, the insertion loss of the device was ~21 dB, and thus comb lines exhibited low OCNR and low power per line (-27 to -17 dBm) [65]. Furthermore, InP-based push-pull modulators integrated with tunable laser is demonstrated to generate 29 comb lines (FSR of 10 GHz) [66]. Though the EOM combs offer reconfigurability, their implementation in future optical networks could be hampered by the above-mentioned drawbacks and complexity.

2.2.4 Gain-switched laser OFC

Gain-switched laser (GSL) [67]–[73], a popular short pulse generation scheme, entails the use of DC-biased semiconductor laser that is directly modulated with a large RF signal. The frequency of the modulating signal determines the FSR of the OFC. The GSL based OFC has attracted a lot of attention mainly due to its simplicity and cost-effectiveness. It generates correlated comb lines with a high OCNR, as well as offers FSR and emission wavelength tunability. Hence, in this thesis, the gain-switched laser is chosen as the OFC

generation technique. The following section provides a detailed description of the GSL OFC and a variant called the externally injected GSL OFC. Subsequently, its operation, characteristics, and suitability for employment in a reconfigurable optical network are discussed.

2.3 Gain-Switched Lasers

The gain-switching process involves the direct modulation of a semiconductor laser and can be theoretically understood by using a set of nonlinear rate equations, which defines the relationship between the carrier (N) and photon densities (S), and phase (ϕ) within the laser cavity. The rate equations for single-mode semiconductor laser (without considering the gain compression effect) can be written as, [68], [74]

$$\frac{dN}{dt} = \frac{I(t)}{eV} - R(N) - g(N - N_{tr})S + F_N(t) \tag{2.4}$$

$$\frac{dS}{dt} = g\Gamma(N - N_{tr})S - \frac{S}{\tau_p} + \beta BN^2 + F_S(t) \tag{2.5}$$

$$\frac{d\phi}{dt} = \frac{1}{2}\Gamma\alpha_H g(N - N_{tr}) - \frac{1}{\tau_p} + F_\theta(t) \tag{2.6}$$

Where, $I(t) = I_{bias} + I_r \sin(2\pi f_r t)$ is a time-varying bias current applied (gain-switching signal), e is the electronic charge, V is the volume of an active region, g is the gain constant, N_{tr} is carrier density at transparency, S is the photon density, Γ denotes confinement factor, τ_p is the photon lifetime, β denotes spontaneous emission factor coupling into the lasing mode, B is the bimolecular recombination coefficient, and α_H, denotes linewidth enhancement factor. The stochastic terms F_N, F_S, F_θ represent Langevin noise sources due to random carrier recombination induced amplified spontaneous noise into the lasing mode. R(N) is the rate of recombination consisting of non-radiative, bimolecular, and Auger recombination and is given by $R(N) = AN + BN^2 + CN^3$ [74]. The intuitive meaning of the above rate equations can be explained as follows.

Equation (2.4)   *Carrier density evolution with time*. The first term defines the contribution of the bias current applied to the laser, whereas the

45

second term gives the rate of carrier recombination due to spontaneous emission. The third term represents the decay of the carriers by recombination due to stimulated emission.

Equation (2.5)   *Photon density evolution with time*. The first term describes the number of photons created due to stimulated emission. It depends on the carrier density and losses in the cavity. The second term denotes the optical losses in the laser cavity, characterised by photon lifetime. The third term represents the part of spontaneously emitted photons that are coupled into the laser output.

Equation (2.6)   *Phase evolution with time*. The first term indicates the laser phase evolution due to stimulated emission, while the second term represents the influence of spontaneous emission.
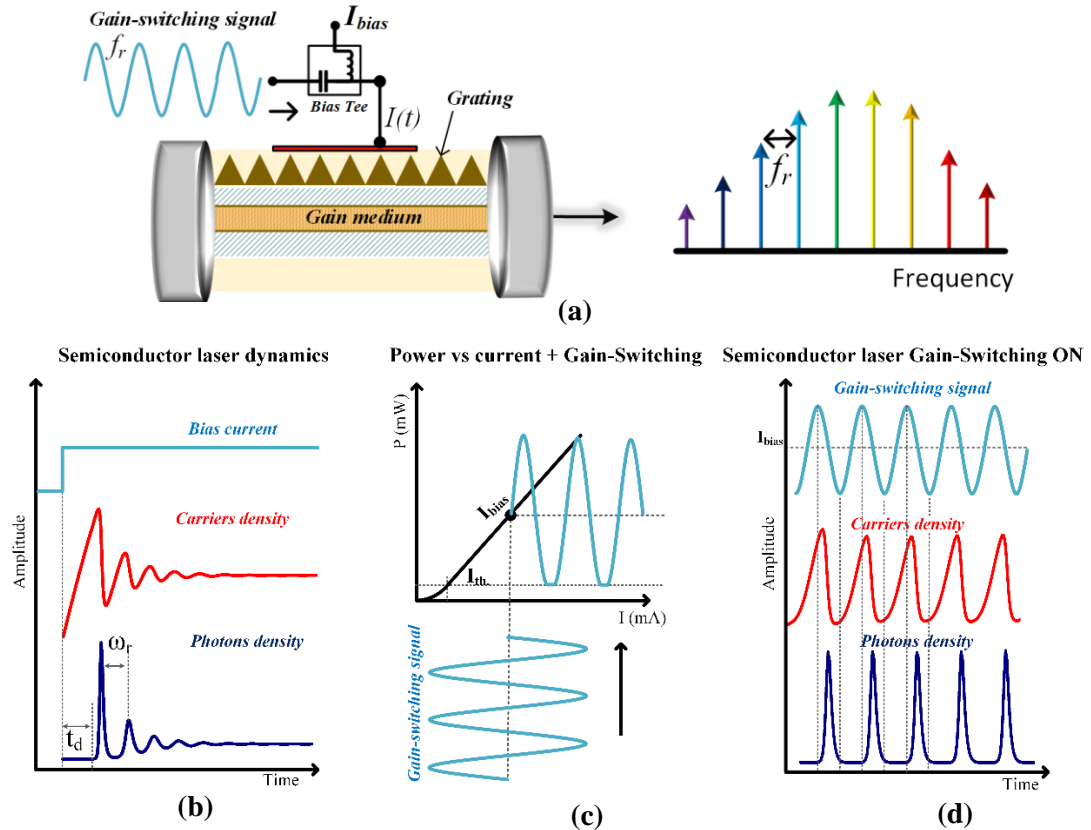
Figure 2.6. Illustration of (a) gain-switched semiconductor laser, (b) laser dynamics when a step bias current is applied, (c) power vs bias current when a laser is gain-switched, (d) laser dynamics when gain-switched.

An illustration of the gain-switching of a semiconductor laser is shown in Figure 2.6. The notion of gain-switching is to directly modulate a laser with a large RF signal that excites only the first relaxation oscillation spike at the onset of the laser operation and truncates the subsequent peaks. Periodic repetition of this process results in the generation of optical pulses. To understand the process of gain-switching, two laser turn-on dynamics are considered, when $I(t) = I_{bias}$ and $I_{bias} + I_r sin(2\pi f_r t)$, where I_r and f_r are the amplitude and frequency of the gain-switching signal. Figure 2.6 (b) illustrates the semiconductor laser dynamics when $I(t) = I_{bias}$, whereas Figure 2.6 (c) shows typical power vs bias current plot under gain-switching conditions. The laser dynamics when gain-switched are illustrated in Figure 2.6 (d).

Laser operation mode	*Description*
Laser turn ON state $I(t) = I_{bias}$	The step input bias current I_{bias} well above the threshold current is applied to the laser. As a result, the carrier and photon density start to build up and portray a transient damped oscillation response before reaching a steady state.
Gain-switched laser $I(t) = I_{bias} + I_r sin(2\pi f_r t)$	A large-amplitude, usually sinusoidal, signal in conjunction with the I_{bias}, is applied to the laser. This time-varying bias current creates dynamic carrier density fluctuations inside the laser cavity. While bias current increases (from trough to crest), it builds up the carrier density. The photon density starts to grow once the carrier density reaches its threshold and lasing starts. Then, the photon population increases rapidly and depletes the carrier density. This in turn leads to a reduction in the photon density, creating an optical pulse. As the bias current decreases (crest to trough), it prevents any further build-up of the carrier density, thereby preventing subsequent relaxation oscillation spikes. This process repeats periodically leading to the generation of a

train of optical pulses and correspondingly an optical frequency comb.

The first notable GSL OFC experimental demonstration was reported in 2009 and was followed by extensive studies [68]–[70], [75]–[77]. The typical experimental setup of gain-switched OFC generation is shown in Figure 2.7 (a). A single-mode laser is driven with a 10 GHz sinusoidal amplified (+18 dBm) signal in conjunction with a DC bias (65 mA, $\sim 5 \times I_{th}$ ($bias\ threshold$)). The output OFC with an FSR of 10 GHz, consisting of 4 lines within 3 dB from the spectral peak, portraying an OCNR of 40 dB (within 20 MHz resolution) is as shown in Figure 2.7 (b).
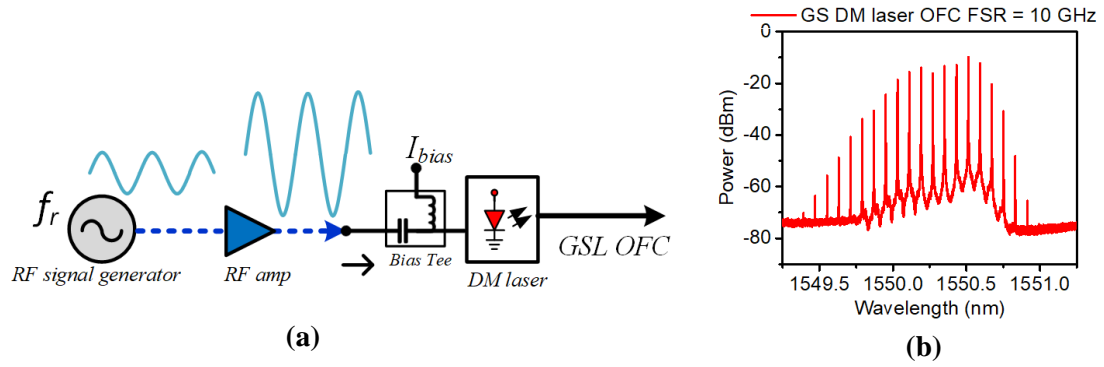
Figure 2.7. (a) Experimental setup of a gain-switched laser, (b) optical spectrum of resultant GS OFC with an FSR of 10 GHz. The optical spectrum is recorded at 20 MHz OSA resolution.

The gain-switched laser is the simplest comb generation technique and offers significant advantages in terms of compactness, precise FSR tunability and cost-efficiency. The average power per comb line is better than the EOM comb (no lossy components) and emission wavelength can be tuned via temperature and bias current within the standard laser tuning range (~2 nm). The main drawback of the technique is the limited modulation bandwidth/frequency response of most commercially available semiconductor lasers, which dictates the maximum achievable FSR and number of comb lines. Some of the other GSL shortcomings include a large frequency chirp due to the time-varying carrier density [69]. In addition, as the laser is continuously driven below the threshold level on each gain-switching cycle, spontaneous emission contribution tends to result in large

values of phase noise and temporal jitter [69]. These limitations may limit the employability of the GSL OFC as a transmitter in systems that employ advanced modulation formats. To overcome these drawbacks, external optical injection from a spectrally pure master laser (low optical linewidth) can be employed. Such a configuration is referred to as an externally injected gain-switched OFC.

2.3.1 Externally injected gain-switched OFC

An externally injected gain-switched laser (EI-GSL), employs a master-slave configuration, comprising a slave laser that is gain-switched and a spectrally pure master laser that is used for the injection. The use of the optical injection locking (OIL) provides several advantages such as increased modulation response and bandwidth enhancement [74], improved noise property through the transfer of spectral properties from the master to the slave laser [79], [80], single-mode operation (in case of multi-mode slave laser), and frequency chirp reduction [78], [81].

Optical injection refers to the process of injecting coherent photons from the master laser into the cavity of the slave, where two optical fields may couple, undergo several nonlinear interactions (such as beating, FWM) or become locked to the master, such state is referred as injection-locked. The latter implies the phenomenon under which the slave is frequency and phase-locked to the master laser, inheriting its phase and frequency characteristics. The nonlinear phenomena are dictated by the detuning frequency (Δf), defined as the frequency difference between master (f_{inj}) and the slave (f_S) and by the injection power ratio $K_{inj} = (\frac{P_{inj}}{P_{slave}})$, where P_{inj} and P_{slave} are the injected optical power from the master, and total emission power of the slave laser (in its free-running state), respectively. To attain stable OIL, the Δf must be within locking range $\Delta f_{locking}$ given by [81] :

$$\Delta f_{locking} = \Delta f_{max} - \Delta f_{min} \tag{2.7}$$

$$-k_C\sqrt{1+\alpha_H}\sqrt{\frac{P_{inj}}{P_{slave}}} = \Delta f_{min} < \Delta f < \Delta f_{max} = k_C\sqrt{\frac{P_{inj}}{P_{slave}}} \tag{2.8}$$

where k_C is the coupling co-efficient describing the rate at which photons are coupled or injected into the slave cavity and α_H is the linewidth enhancement factor.

An EI-GSL OFC can be mathematically described by modifying the rate equations in eq. 2.4 and 2.5, to account for optical injection. A detailed analysis of injection locking (theoretical and experimentally) can be found in [68], [69], [78]–[83]. The modified rate equations can be written as [68],

$$\frac{dN}{dt} = \frac{I(t)}{eV} - R(N) - g(N - N_{tr})S + F_N(t) \tag{2.9}$$

$$\frac{dS}{dt} = g\Gamma(N - N_{tr})S - \frac{S}{\tau_p} + \beta BN^2 + 2k_c\sqrt{S_{inj}S}\cos(\phi - \phi_{inj}) + F_S(t) \tag{2.10}$$

$$\frac{d\phi}{dt} = \frac{1}{2}\Gamma\alpha_H g(N - N_r) - k_c\sqrt{\frac{S_{inj}}{S}}\sin(\phi - \phi_{inj}) - \Delta f + F_\theta(t) \tag{2.11}$$

where k_c is the injection coupling coefficient, S_{inj} is the injected photon density, Δf is the detuning frequency, ϕ and ϕ_{inj} represent the phase of the slave and master lasers, respectively.

2.3.2   EI-GSL comb generation

To generate an EI-GSL OFC, the experimental setup from Figure 2.7 is modified to include a narrow linewidth semiconductor-based tunable laser as a master. The new set-up diagram is shown in Figure 2.8 (a). The resultant OFC with an FSR of 10 GHz, consisting of 8 comb lines (within a 3 dB window from the spectral peak) with OCNR > 50 dB, is as shown in Figure 2.8 (b). The increase in the number of comb lines visible by comparing Figure 2.7 (b) and Figure 2.8 (b), can be attributed to the modulation bandwidth enhancement due to external optical injection. One of the salient features of the EI-GSL OFC generation is that any commercially available semiconductor-based single-mode or multimode laser can be used for comb generation.

(a)

(b)
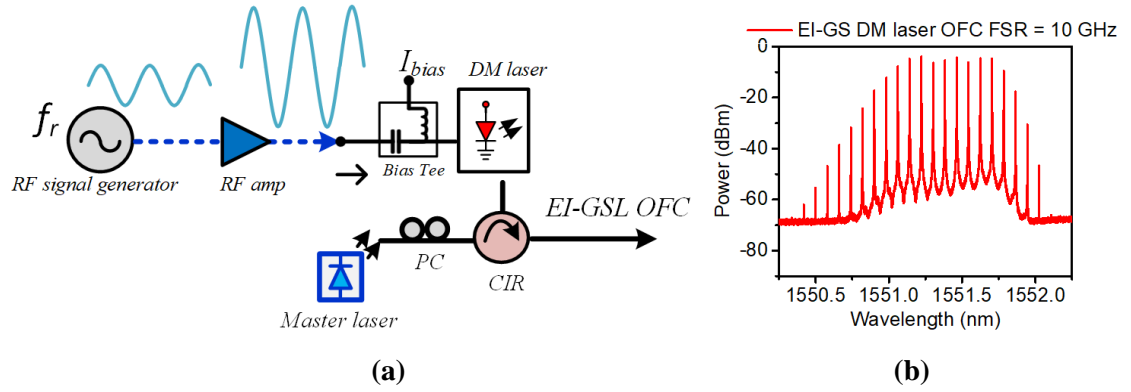
Figure 2.8. (a) Experimental schematic of externally injected gain-switched laser (GS frequency of 10 GHz), (b) resultant optical spectrum of EI-GS DM laser OFC with an FSR of 10 GHz.

Figure 2.9 (a)-(c) illustrates the optical spectra of a standard DFB laser in free-running (CW), GSL and EI-GSL configurations. The free-running laser, biased at ~53 mA ($\sim 5.I_{th}$), is gain switched with an amplified 6.25 GHz sinusoidal signal (~25 dBm). The gain-switched spectrum in Figure 2.9 (b) does not show any discernible comb lines due to a large timing jitter introduced by the gain-switching [69] However, with the introduction of optical injection, a continuous flow of photons from the master laser locks the phase of the successive pulses and introduces a pulse-to-pulse coherence. This results in the generation of distinguishable comb lines as shown in Figure 2.9 (c). The optical injection parameters such as frequency detuning (Δf) and injection power (K_{inj}) play a crucial role in terms of spectral and noise properties of the EI-GSL. Using a negative detuning ($\Delta f < 0$), where the injection frequency is lower than that of the slave laser (in its free running state), favours the enhanced resonance peak and generation of a "flat-top comb", at the expense of less effective transfer of the phase characteristics, as investigated in [14]. On the other hand, when the detuning is positive ($\Delta f > 0$), the modulation bandwidth enhancement is improved but less pronounced resonance peak, resulting in a narrower comb, but with spectral properties closely reflecting those of the master laser. Therefore, the optimisation of optical injection parameters, based on the application, is essential.
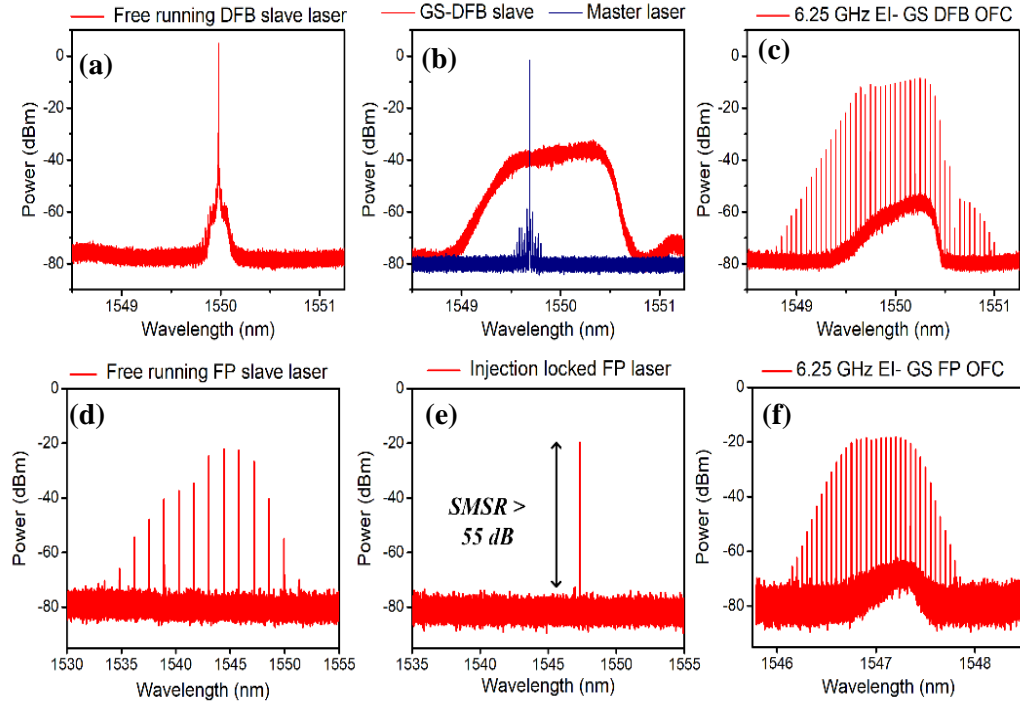
Figure 2.9. Optical spectrum of EI-GSL OFC generation process (a)-(c) single mode DFB laser (DFB), (d)-(e) multi-mode FP laser.

Correspondingly, a multimode laser such as a Fabry-Pérot (FP) can also be used for EI-GSL OFC generation. Figure 2.9 (d)-(e) shows the spectra of a multi-mode FP laser in free running (CW), under OIL, and in an EI-GSL configuration. The spectrum of the FP laser with a mode spacing of ~1.2 nm is shown in Figure 2.9 (d). The single-mode operation of the FP is achieved by injection locking the desired longitudinal mode, which suppresses the gain in other modes (as seen in Figure 2.9 (e)). Such an externally injection locked FP can then be gain-switched, resulting in the OFC, as depicted in Figure 2.9 (f). Each longitudinal mode can be selected via injection locking and an EI-GSL OFC can be generated around each longitudinal mode to achieve wavelength tunability across the C band.

2.3.2.1 *Externally injected gain-switched laser as a reconfigurable OFC source*

In the last two decades, the EI-GSL OFC has been extensively studied for various applications and some of the notable demonstrations include: (i) the realisation of a superchannel transmitter employing spectrally efficient schemes such as CO-OFDM [15],

coherent Nyquist WDM [84]; (ii) directly modulated DMT or pulse amplitude modulation (PAM)-4 for data centre interconnects [85], [86] (iii) dual-comb gas sensing spectroscopy [9]; (iv) soliton generation [54]; (v) absolute distance measurement [84], (vi) analog radio-over-fiber distribution [18], [88] (vii) steganography [12] and many more. Some of the salient characteristics of the EI-GSL OFC that make them an ideal candidate for versatile applications in next-generation reconfigurable optical networks are briefly discussed here.

i.   *Simple and cost-effective:* An EI-GSL OFC is based on direct modulation and requires a low component count and no sophisticated or bespoke fabrication. They employ mature, well-established commercially available single-mode (DM, DFB [70], VCSELs [89]) or multimode (FP [76]) lasers.
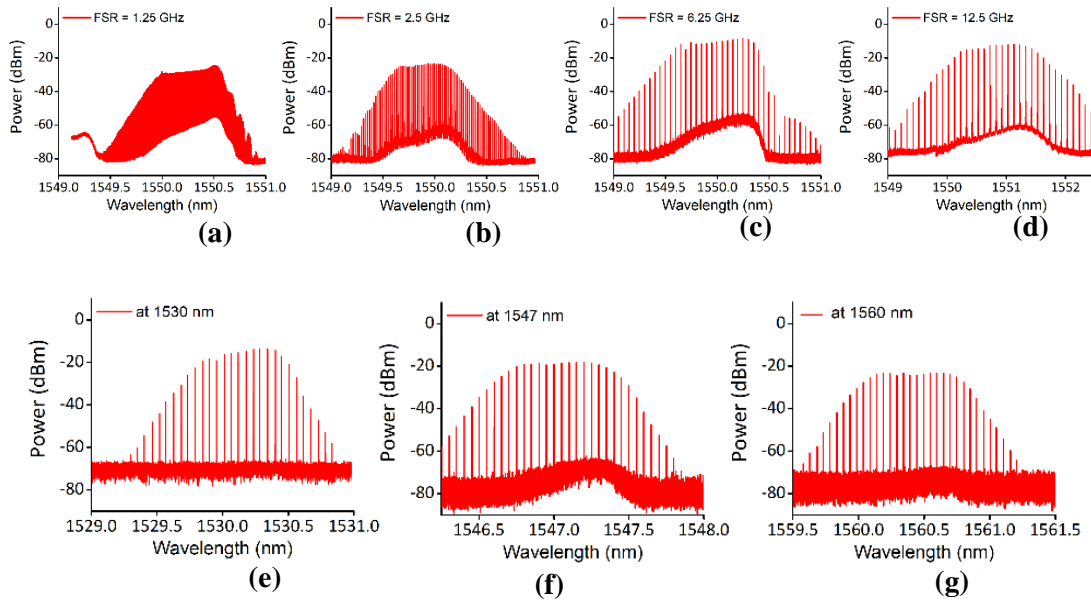
Figure 2.10. Optical spectra highlighting EI-GSL OFC tunability features (a)-(d) FSR tunability from 1.25 to 12.5 GHz, (d)-(e) discrete wavelength tunability from 1530-1560 nm.

ii. *Tunability:* EI-GSL OFCs offer a high level of tunability in terms of comb lines spacing and emission wavelength. The FSR of the comb can be easily tuned by changing the frequency of the gain-switching signal (RF source). As an example, Figure 2.10 (a)-(d), shows an EI-GSL OFC with an FSR varying from 1.25 to 12.5 GHz. FSRs exceeding 30 GHz have also been demonstrated [90]. Furthermore, sub-

GHz comb spacing can be achieved by gain-switching using an electrical pulse rather than a sinewave [91] or employing a comb densification approach [92]. The latter will be discussed in chapter 3. Continuous emission wavelength tuning can be accomplished by adjusting the temperature and bias conditions of the slave laser, while the discrete wavelength tuning can be achieved using multimode lasers (e.g., FP), as shown in Figure 2.10 (e) - (h).
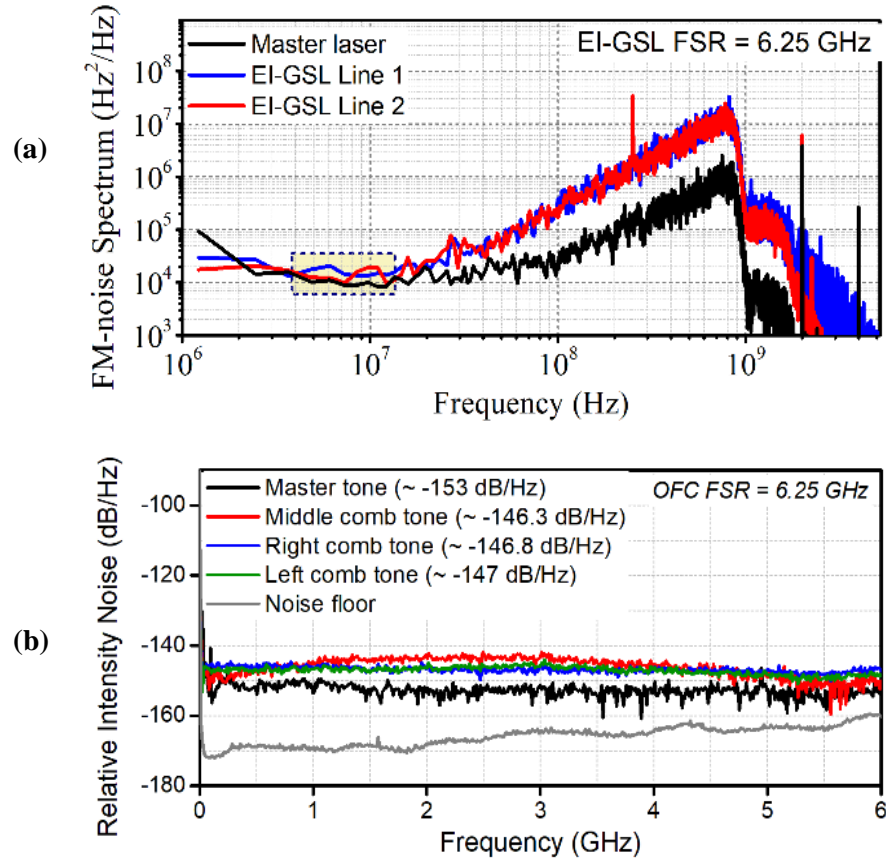
Figure 2.11 Noise characteristics of master laser and EI-GSL OFC lines (a) FM-phase noise spectrum, (b) relative intensity noise.

iii. *Noise characteristics:* EI-GSL OFC lines portray the noise characteristics of the master laser used. This applies to both the phase and relative intensity noise (RIN) of a specific line as shown in Figure 2.11. An example of the FM noise spectrum of the master laser and EI-GSL comb lines is shown in Figure 2.11 (a). The measured linewidths are less than < 30 kHz, clearly demonstrating the comb line inherits the

phase noise of the master laser. Furthermore, the comb line exhibits extremely low RIN better than −140 dB/Hz, as depicted in Figure 2.11 (b). Such a low RIN can be attributed to external optical injection reducing the carrier and photon fluctuations inside the slave cavity. The noise characteristics of the comb lines are investigated in detail and discussed in chapter 3. The resultant narrow linewidth and RIN are extremely attractive in a high-capacity system, where advanced modulation formats are used.
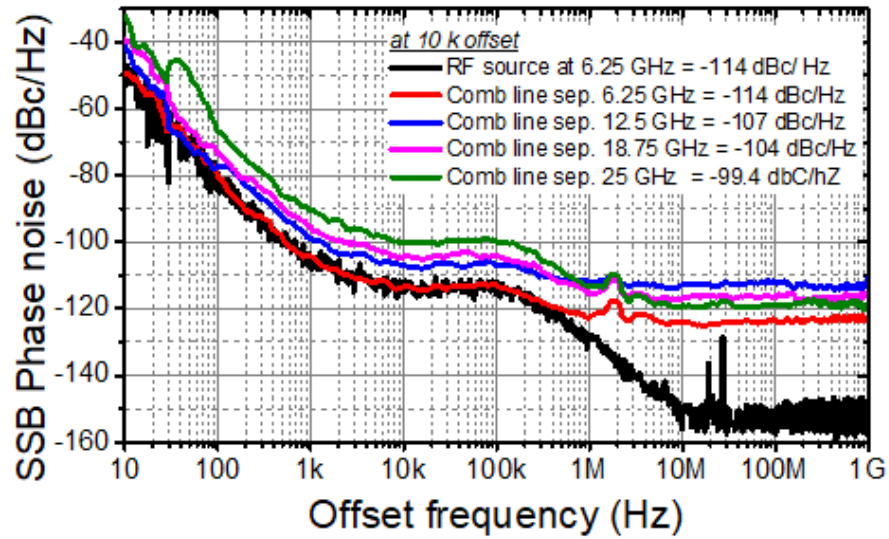
Figure 2.12. SSB phase noise measurement of the EI-GSL OFC lines demonstrating a high degree of phase correlation between them.

iv.   *Phase correlation:* The EI-GSL comb lines portray a high degree of phase correlation between them, which can be verified by examining the single-sideband phase noise (SSB-PN) of their beat tone. Figure 2.12 shows the results of an SSB-PN measurement on a 6.25 GHz signal obtained by mixing two EI-GSL OFC tones on a photodiode. From the plot, it can be seen that an SSB-PN better than −114 dBc/Hz is obtained at a 10 kHz offset frequency. Thus, EI-GSL OFC lines are ideal for the realisation of low phase noise mmW/THz signal.

v.   *Photonic integration.* The master and slave laser configuration required for the EI-GSL OFC generation lends itself to photonic integration, which allows for a further

reduction in size and cost. In recent years, several two-section Figure 2.13 (a)) [93] and four-section (Figure 2.13 (b)) EI-GSL OFCs [94] have been successfully demonstrated highlighting the potential of an EI-GSL OFC to be adopted commercially due to their cost-effectiveness.
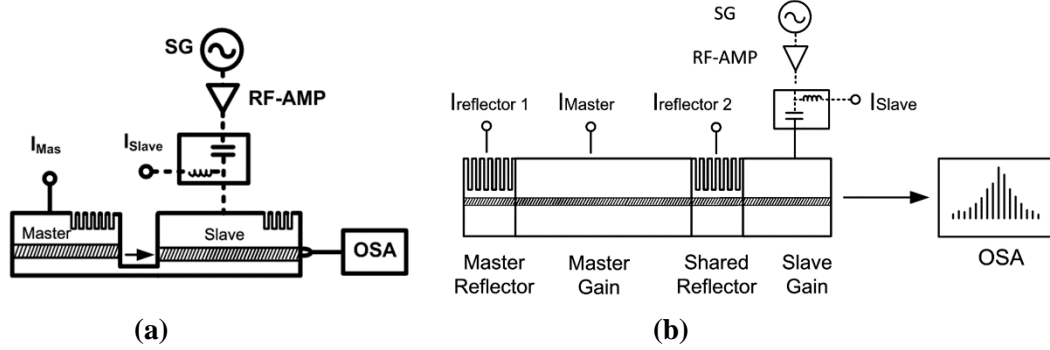
Figure 2.13. Photonic integrated EI-GSL OFC (a) two-section, (b) four-section devices [88], [84].

The above-mentioned merits (flexibility, excellent noise properties) render the EI-GSL OFC to be a highly attractive multi-carrier transmitter that could be employed in next-generation optical networks. However, as mentioned earlier, the commercial adoption of this technology (EI-GSL) could be hindered by the limited number of comb lines generated. Hence, this thesis looks to address this issue, by exploring techniques that could be used to expand the OFCs. Two such schemes, with expansion factors >3, that are also reconfigurable are presented in chapter 3.

2.4 References

[1]   J. L. Hall, "Nobel Lecture: Defining and measuring optical frequencies," *Reviews of Modern Physics*, vol. 78, no. 4, pp. 1279–1295, Nov. 2006, DOI: 10.1103/RevModPhys.78.1279.

[2]   T. W. Hänsch, "Nobel Lecture: Passion for precision," *Reviews of Modern Physics*, vol. 78, no. 4, pp. 1297–1309, Nov. 2006, DOI: 10.1103/RevModPhys.78.1297.

[3]   M. Imran, P. M. Anandarajah, A. Kaszubowska-Anandarajah, N. Sambo, and L. Poti, "A Survey of Optical Carrier Generation Techniques for Terabit Capacity Elastic Optical Networks," *IEEE Communications Surveys and Tutorials*, vol. 20, no. 1, pp. 211–263, 2018, DOI: 10.1109/COMST.2017.2775039.

[4]   T. Fortier and E. Baumann, "20 years of developments in optical frequency comb technology and applications," *Communications Physics*, vol. 2, no. 1, pp. 153, 2019, DOI: 10.1038/s42005-019-0249-y.

[5]   A. Parriaux, K. Hammani, and G. Millot, "Electro-optic frequency combs," *Advances in Optics and Photonics*, vol. 12, no. 1, pp. 223–287, 2020, DOI: 10.1364/AOP.382052.

[6]   J. Kim and Y. Song, "Ultralow-noise mode-locked fiber lasers and frequency combs: principles, status, and applications," *Advances in Optics and Photonics*, vol. 8, no. 3, pp. 465–540, 2016, DOI: 10.1364/AOP.8.000465.

[7]   H. Hu and L. K. Oxenløwe, "Chip-based optical frequency combs for high-capacity optical communications," *Nanophotonics*, vol. 10, no. 5, pp. 1367–1385, 2021, DOI: 10.1515/nanoph-2020-0561.

[8]   R. Holzwarth, T. Udem, T. W. Hänsch, J. C. Knight, W. J. Wadsworth, and P. St. J. Russell, "Optical Frequency Synthesizer for Precision Spectroscopy," *Physical Review Letters*, vol. 85, no. 11, pp. 2264–2267, 2000, DOI: 10.1103/PhysRevLett.85.2264.

[9]   J. K. Alexander, L. Caro, M. Dernaika, S. P. Duggan, H. Yang, S. Chandran, E. P. Martin, A. A. Ruth, P. M. Anandarajah, and F. H. Peters, "Integrated dual optical frequency comb source," *Optics Express*, vol. 28, no. 11, pp. 16900–16906, 2020, DOI: 10.1364/OE.384706.

[10]   K. Minoshima and H. Matsumoto, "High-accuracy measurement of 240-m distance in an optical tunnel by use of a compact femtosecond laser," *Applied Optics*, vol. 39, no. 30, pp. 5512–5517, 2000, DOI: 10.1364/AO.39.005512.

[11]   Z. L. Newman, V. Maurice, T. Drake, J. R. Stone, T. C. Briles, D. T. Spencer, C.Fredrick, Q. Li, D. Westly, B. R. Ilic, B. Shen, M. -G. Suh, K. Y. Yang, C. Johnson, D. M. S. Johnson, L. Hollberg, K. J. Vahala, K. Srinivasan, S. A. Diddams, J. Kitching, S. B. Papp, and M. T. Hummon, "Architecture for the photonic integration of an optical atomic clock," *Optica*, vol. 6, pp. 680-685, 2019, DOI:10.1364/OPTICA.6.000680

[12]   E. Wohlgemuth, Y. Yoffe, P. N. Goki, M. Imran, F. Fresi, P. D. Lakshmijayasimha, R. Cohen, P. M. Anandarajah, L. Potì, and D. Sadot, "Stealth and secured optical coherent

transmission using a gain switched frequency comb and multi-homodyne coherent detection," *Optics Express*, vol. 29, pp. 40462-40480, 2021, DOI: 10.1364/OE.431070

[13]   G. Bosco, V. Curri, A. Carena, P. Poggiolini, and F. Forghieri, "On the Performance of Nyquist-WDM Terabit Superchannels Based on PM-BPSK, PM-QPSK, PM-8QAM or PM-16QAM Subcarriers," *Journal of Lightwave Technology*, vol. 29, no. 1, pp. 53–61, 2011, [Online]. Available: http://jlt.osa.org/abstract.cfm?URI=jlt-29-1-53

[14]   R. Zhou, T. N. Huynh, V. Vujicic, P. M. Anandarajah, and L. P. Barry, "Phase noise analysis of injected gain switched comb source for coherent communications," *Optics Express*, vol. 22, no. 7, p. 8120, 2014, DOI: 10.1364/OE.22.008120.

[15]   V. Vujicic, P. M. Anandarajah, R. Zhou, C. Browning, and L. P. Barry, "Performance Investigation of IM/DD Compatible SSB-OFDM Systems Based on Optical Multicarrier Sources," *IEEE Photonics Journal*, vol. 6, no. 5, pp. 1–10, 2014, DOI: 10.1109/JPHOT.2014.2361673.

[16]   H. Hu, F. Da Ros, M. Pu, F. Ye, K. Ingerslev, E. P. da Silva, Md. Nooruzzaman, Y. Amma, Y. Sasaki, T. Mizuno, Y. Miyamoto, L. Ottaviano, E. Semenova, P. Guan, D. Zibar, M. Galili, K. Yvind, T. Morioka, and L. K. Oxenløwe "Single-source chip-based frequency comb enabling extreme parallel data transmission," *Nature Photonics*, vol. 12, no. 8, pp. 469–473, 2018, DOI: 10.1038/s41566-018-0205-5.

[17]   T. Shao, H. Shams, P. M. Anandarajah, M. J. Fice, C. C. Renaud, F. Van Dijk, A. J. Seeds, and Liam P. Barry, "Phase Noise Investigation of Multicarrier Sub-THz Wireless Transmission System Based on an Injection-Locked Gain-Switched Laser," *IEEE Transactions on Terahertz Science and Technology*, vol. 5, no. 4, pp. 590–597, 2015, DOI: 10.1109/TTHZ.2015.2418996.

[18]   T. Shao, M. Beltrán, R. Zhou, P. M. Anandarajah, R. Llorente and L. P. Barry, "60 GHz Radio Over Fiber System Based on Gain-Switched Laser," Journal of Lightwave Technology, vol. 32, no. 20, pp. 3695–3703, 2014. DOI: 10.1109/JLT.2014.2308152.

[19]   J. Pfeifle, V. Vujicic, R. T. Watts, P. C. Schindler, C. Weimann, R. Zhou, W. Freude, L. P. Barry, and Christian Koos, "Flexible terabit/s Nyquist-WDM super-channels using a gain-switched comb source," *Optics Express*, vol. 23, no. 2, p. 724, 2015, DOI: 10.1364/oe.23.000724.

[20]   Z. Zan, M. Premaratne, and A. J. Lowery, "Laser RIN and linewidth requirements for direct detection optical OFDM," in *2008 Conference on Lasers and Electro-Optics and 2008 Conference on Quantum Electronics and Laser Science*, 2008, pp. 1–2. DOI: 10.1109/CLEO.2008.4551895.

[21]   K. Kikuchi, "Characterization of semiconductor-laser phase noise and estimation of bit-error rate performance with low-speed offline digital coherent receivers," *Optics Express*, vol. 20, no. 5, pp. 5291–5302, 2012, DOI: 10.1364/OE.20.005291.

[22] T. Pfau, S. Hoffmann, and R. Noé, "Hardware-efficient coherent digital receiver concept with feedforward carrier recovery for M QAM constellations," *Journal of Lightwave Technology*, vol. 27, no. 8, pp. 989–999, 2009, DOI: 10.1109/JLT.2008.2010511.

[23] A. D'Errico and G. Contestabile, "Next Generation Terabit Transponder," in *Optical Fiber Communication Conference*, 2016, pp. W4B.4. DOI: 10.1364/OFC.2016.W4B.4.

[24] L. Lundberg, M. Karlsson, A. Lorences-Riesgo, and M. Mazur, "Frequency Comb-Based WDM transmission systems enabling joint signal processing," *Applied Sciences*, vol. 8, no. 5, 2018, DOI: 10.3390/app8050718.

[25] W. E. Lamb, "Theory of an Optical Maser," *Physical Review*, vol. 134, no. 6A, pp. A1429–A1450, Jun. 1964, DOI: 10.1103/PhysRev.134.A1429.

[26] H. A. Haus, "Mode-locking of lasers," *IEEE Journal of Selected Topics in Quantum Electronics*, vol. 6, no. 6, pp. 1173–1185, 2000, DOI: 10.1109/2944.902165.

[27] L. E. Hargrove, R. L. Fork, and M. A. Pollack, "Locking of He–Ne laser modes induced by synchronous intracavity modulation," *Applied Physics Letters*, vol. 5, no. 1, pp. 4–5, Jul. 1964, DOI: 10.1063/1.1754025.

[28] R. G. M. P. Koumans and R. van Roijen, "Theory for passive mode-locking in semiconductor laser structures including the effects of self-phase modulation, dispersion, and pulse collisions," *IEEE Journal of Quantum Electronics*, vol. 32, no. 3, pp. 478–492, 1996, DOI: 10.1109/3.485400.

[29] F. Lelarge, B. Dagens, J. Renaudier, R. Brenot, A. Accard, F. van Dijk, D. Make, O. Le Gouezigou, J.-G. Provost, F. Poingt, J. Landreau, O. Drisse, E. Derouin, B. Rousseau, F. Pommereau, and G-H. Duan, "Recent Advances on InAs/InP Quantum Dash Based Semiconductor Lasers and Optical Amplifiers Operating at 1.55µm," *IEEE Journal of Selected Topics in Quantum Electronics*, vol. 13, no. 1, pp. 111–124, 2007, DOI: 10.1109/JSTQE.2006.887154.

[30] S. A. Diddams, "The evolving optical frequency comb [Invited]," *Journal of the Optical Society of America B*, vol. 27, no. 11, pp. B51–B62, 2010, DOI: 10.1364/JOSAB.27.000B51.

[31] M. Bagheri, C. Frez, L. A. Sterczewski, I. Gruidin, M. Fradet, I. Vurgaftman, C. L. Canedy, W. W. Bewley, C. D. Merritt, C. S. Kim, M. Kim, and J. R. Meyer, "Passively mode-locked interband cascade optical frequency combs," *Scientific Reports*, vol. 8, no. 1, pp. 1–7, 2018, DOI: 10.1038/s41598-018-21504-9.

[32] T. Habruseva, S. O. Donoghue, N. Rebrova, F. Kéfélian, S. P. Hegarty, and G. Huyet, "Optical linewidth of a passively mode-locked semiconductor laser," *Optics Letters*, vol. 34, no. 21, pp. 3307–3309, 2009.

[33] N. Rebrova, T. Habruseva, G. Huyet, and S. P. Hegarty, "Stabilization of a passively mode-locked laser by continuous wave optical injection," *Applied Physics Letters*, vol. 97, no. 10, p. 101105, Sep. 2010, DOI: 10.1063/1.3483231.

[34] J. Renaudier, G. H. Duan, P. Landais, and P. Gallion, "Phase correlation and linewidth reduction of 40 GHz self-pulsation in distributed Bragg reflector semiconductor lasers," *IEEE Journal of Quantum Electronics*, vol. 43, no. 2, pp. 147–156, 2007, DOI: 10.1109/JQE.2006.886820.

[35] M. G. Thompson, A. R. Rae, M. Xia, R. v Penty, and I. H. White, "InGaAs Quantum-Dot Mode-Locked Laser Diodes," *IEEE Journal of Selected Topics in Quantum Electronics*, vol. 15, no. 3, pp. 661–672, 2009, DOI: 10.1109/JSTQE.2008.2012265.

[36] B. R. Koch, A. W. Fang, O. Cohen, and J. E. Bowers, "Mode-locked silicon evanescent lasers," *Optics Express*, vol. 15, no. 18, pp. 11225–11233, 2007, DOI: 10.1364/OE.15.011225.

[37] J. Cetina Parra, "Passively Mode-Locked Semiconductor Lasers for All-Optical Applications," *DCU PHD Thesis*, 2014. [Online]. Available: http://doras.dcu.ie/19718/1/Thesis_JOSUE_PARRA.pdf

[38] M. L. Davenport, S. Liu, and J. E. Bowers "Integrated heterogeneous silicon / III – V mode-locked lasers," *Photonics Research*, vol. 6, no. 5, pp. 468–478, 2018.

[39] V. Vujicic, C. Calò, R. Watts, F. Lelarge, C. Browning, K. Merghem, A. Martinez, A. Ramdane and L. P. Barry, "Quantum Dash Mode-Locked Lasers for Data Centre Applications," *IEEE Journal of Selected Topics in Quantum Electronics*, vol. 21, no. 6, pp. 53–60, 2015, DOI: 10.1109/JSTQE.2015.2487884.

[40] C. Calò, V. Vujicic, R. Watts, C. Browning, K. Merghem, V. Panapakkam, F. Lelarge, A. Martinez, B. -E. Benkelfat, A. Ramdane, and L. P. Barry, "Single-section quantum well mode-locked laser for 400 Gb/s SSB-OFDM transmission," *Optics Express*, vol. 23, no. 20, pp. 26442–26449, 2015, DOI: 10.1364/OE.23.026442.

[41] C. Browning, T. Verolet, Y. Lin, G. Aubin, F. Lelarge, A. Ramdane, and L. P. Barry "56 Gb/s/λ over 13 THz frequency range and 400G DWDM PAM-4 transmission with a single quantum dash mode-locked laser source," *Optics Express*, vol. 28, no. 15, p. 22443, 2020, DOI: 10.1364/oe.397315.

[42] R. T. Watts, S. G. Murdoch, and L. P. Barry, "Spectral linewidth reduction of single-mode and mode-locked lasers using a feed-forward heterodyne detection scheme," in *CLEO: 2014*, 2014, p. STh3O.8. DOI: 10.1364/CLEO_SI.2014.STh3O.8.

[43] G. P. Agrawal, "Mode-partition noise and intensity correlation in a two-mode semiconductor laser," *Physical Review A*, vol. 37, no. 7, pp. 2488–2494, Apr. 1988, DOI: 10.1103/PhysRevA.37.2488.

[44] P. Del'Haye, A. Schliesser, O. Arcizet, T. Wilken, R. Holzwarth, and T. J. Kippenberg, "Optical frequency comb generation from a monolithic microresonator," *Nature*, vol. 450, no. 7173, pp. 1214–1217, 2007, DOI: 10.1038/nature06401.

[45] T. Herr, K. Hartinger, J. Riemensberger, C. Y. Wang, E. Gavartin, R. Holzwarth, M. L. Gorodetsky, and T. J. Kippenberg "Universal formation dynamics and noise of Kerr-

frequency combs in microresonators," *Nature Photonics*, vol. 6, no. 7, pp. 480–487, 2012, DOI: 10.1038/nphoton.2012.127.

[46] J. Pfeifle, "Terabit-Rate Transmission Using Optical Frequency Comb Sources," *KIT PHD Thesis*, 2016. [Online]. Available: https://www.semanticscholar.org/paper/Terabit-Rate-Transmission-Using-Optical-Frequency-Pfeifle/ec9d57cc6be4a3ae59bf930ac99ec12a7e5826f8

[47] J. Pfeifle, A. Coillet, R. Henriet, K. Saleh, P. Schindler, C. Weimann, W. Freude, I. V. Balakireva, L. Larger, C. Koos, and Y. K. Chembo, "Optimally Coherent Kerr Combs Generated with Crystalline Whispering Gallery Mode Resonators for Ultrahigh Capacity Fiber Communications," *Physical Review Letters*, vol. 114, no. 9, pp. 93902, Mar. 2015, DOI: 10.1103/PhysRevLett.114.093902.

[48] T. Herr, V. Brasch, J. D. Jost, C. Y. Wang, N. M. Kondratiev, M. L. Gorodetsky, and T. J. Kippenberg, "Temporal solitons in optical microresonators," *Nature Photonics*, vol. 8, no. 2, pp. 145–152, 2014, DOI: 10.1038/nphoton.2013.343.

[49] Y. K. Chembo, "Kerr optical frequency combs: Theory, applications and perspectives," *Nanophotonics*, vol. 5, no. 2, pp. 214–230, 2016, DOI: 10.1515/nanoph-2016-0013.

[50] D. K. Mefford and P. J. Reardon, "Towards a stabilized Kerr optical frequency comb with spatial interference," *Applied Optics*, vol. 59, no. 26, pp. 7930–7937, 2020, DOI: 10.1364/AO.393303.

[51] J. Pfeifle, V. Brasch, M. Lauermann, Y. Yu, D. Wegner, T. Herr, K. Hartinger, P. Schindler, J. Li, D. Hillerkuss, R. Schmogrow, C. Weimann, R. Holzwarth, W. Freude, J. Leuthold, T. J. Kippenberg, and Christian Koos, "Coherent terabit communications with microresonator Kerr frequency combs," *Nature Photonics*, vol. 8, no. 5, pp. 375–380, 2014, DOI: 10.1038/nphoton.2014.57.

[52] J. Pfeifle, A. Kordts, P. Marin, M. Karpov, M. Pfeiffer, V. Brasch, R. Rosenberger, J. Kemal, S. Wolf, W. Freude, T. J. Kippenberg, and C. Koos, "Full C and L-Band Transmission at 20 Tbit/s Using Cavity-Soliton Kerr Frequency Combs," in *CLEO 2015 Post deadline Paper Digest*, 2015, pp. JTh5C.8.

[53] L. Chang, W. Xie, H. Shu, Q. Yang, B. Shen, A. Boes, J. D. Peters, W. Jin, C. Xiang, S. Liu, G. Moille, S. P. Yu, X. Wang, K. Srinivasan, S. B. Papp, K. Vahala, and J. E. Bowers, "Ultra-efficient frequency comb generation in AlGaAs-on-insulator microresonators," *Nature Communications*, vol. 11, no. 1, pp.1331, 2020, DOI: 10.1038/s41467-020-15005-5.

[54] W. Weng, A. Kaszubowska-Anandarajah, J. He, P. D. Lakshmijayasimha, E. Lucas, J. Liu, P. M. Anandarajah, and T. J. Kippenberg, "Gain-switched semiconductor laser driven soliton microcombs," *Nature Communications*, vol. 12, no. 1, pp. 1425, 2021, DOI: 10.1038/s41467-021-21569-7.

[55] S. Ozharar, F. Quinlan, I. Ozdur, S. Gee, and P. J. Delfyett, "Ultraflat optical comb generation by phase-only modulation of continuous-wave light," *IEEE Photonics Technology Letters*, vol. 20, no. 1, pp. 36–38, 2008, DOI: 10.1109/LPT.2007.910755.

[56] D. Kwon, I. Jeon, W.-K. Lee, M.-S. Heo, and J. Kim, "Generation of multiple ultra stable optical frequency combs from an all-fiber photonic platform," *Science Advances*, vol. 6, no. 13, pp. eaax4457, Mar. 2020, DOI: 10.1126/sciadv.aax4457.

[57] R. Wu, V. R. Supradeepa, C. M. Long, D. E. Leaird, and A. M. Weiner, "Highly flat and stable optical frequency comb generation using intensity and phase modulators employing quasi-quadratic phase modulation," in *2010 IEEE International Topical Meeting on Microwave Photonics*, pp. 212–215, 2010. DOI: 10.1109/MWP.2010.5664162.

[58] V. Torres-Company and A. M. Weiner, "Optical frequency comb technology for ultra-broadband radio-frequency photonics," *Laser & Photonics Reviews*, vol. 8, no. 3, pp. 368–393, 2014, DOI: https://doi.org/10.1002/lpor.201300126.

[59] Q. Wang, L. Huo, Y. Xing, and B. Zhou, "Ultra-flat optical frequency comb generator using a single-driven dual-parallel Mach-Zehnder modulator," *Optics Letters*, vol. 39, no. 10, pp. 3050–3053, 2014, DOI: 10.1364/OL.39.003050.

[60] T. Sakamoto, T. Kawanishi, and M. Izutsu, "Asymptotic formalism for ultraflat optical frequency comb generation using a Mach-Zehnder modulator," *Optics Letters*, vol. 32, no. 11, pp. 1515–1517, 2007, DOI: 10.1364/OL.32.001515.

[61] J. Zhang, N. Chi, J. Yu, Y. Shao, J. Zhu, B. Huang, and L. Tao, "Generation of coherent and frequency-lock multi-carriers using cascaded phase modulators and recirculating frequency shifter for Tb/s optical communication," *Optics Express*, vol. 19, no. 14, pp. 12891–12902, 2011, DOI: 10.1364/OE.19.012891.

[62] A. J. Metcalf, V. Torres-Company, D. E. Leaird, and A. M. Weiner, "High-Power Broadly Tunable Electrooptic Frequency Comb Generator," *IEEE Journal of Selected Topics in Quantum Electronics*, vol. 19, no. 6, pp. 231–236, 2013, DOI: 10.1109/JSTQE.2013.2268384.

[63] S. Ozharar, F. Quinlan, I. Ozdur, S. Gee, and P. J. Delfyett, "Ultraflat Optical Comb Generation by Phase-Only Modulation of Continuous-Wave Light," *IEEE Photonics Technology Letters*, vol. 20, no. 1, pp. 36–38, 2008, DOI: 10.1109/LPT.2007.910755.

[64] T. Healy, F. C. Garcia Gunning, A. D. Ellis, and J. D. Bull, "Multi-wavelength source using low drive-voltage amplitude modulators for optical communications," *Optics Express*, vol. 15, no. 6, pp. 2981–2986, 2007, DOI: 10.1364/OE.15.002981.

[65] L. Alloatti, R. Palmer, S. Diebold, K. P. Pahl, B. Chen, R. Dinu, M. Fournier, J. -M. Fedeli, T. Zwick, W. Freude, C. Koos, and J. Leuthold "100 GHz silicon–organic hybrid modulator," *Light: Science & Applications*, vol. 3, no. 5, pp. e173–e173, 2014, DOI: 10.1038/lsa.2014.54

[66] R. Slavík, S. G. Farwell, M. J. Wale and D. J. Richardson, "Compact Optical Comb Generator Using InP Tunable Laser and Push-Pull Modulator," *IEEE Photonics Technology Letters*, vol. 27, no. 2, pp. 217-220, 2015, DOI: 10.1109/LPT.2014.2365259.

[67] K. Y. Lau, "Gain switching of semiconductor injection lasers," *Applied Physics Letters*, vol. 52, no. 4, pp. 257–259, Jan. 1988, DOI: 10.1063/1.99486.

[68] P. M. Anandarajah, S. P. O'Dúill, R. Zhou, and L. P. Barry, "Enhanced Optical Comb Generation by Gain-Switching a Single-Mode Semiconductor Laser Close to Its Relaxation Oscillation Frequency," *IEEE Journal of Selected Topics in Quantum Electronics*, vol. 21, no. 6, pp. 592–600, 2015, DOI: 10.1109/JSTQE.2015.2456751.

[69] S. P. O'Dúill, R. Zhou, P. M. Anandarajah, and L. P. Barry, "Analytical Approach to Assess the Impact of Pulse-to-Pulse Phase Coherence of Optical Frequency Combs," *IEEE Journal of Quantum Electronics*, vol. 51, no. 11, pp. 1–8, 2015, DOI: 10.1109/JQE.2015.2485228.

[70] P. M. Anandarajah, R. Maher, Y. Q. Xu, S. Latkowski, J. O'Carroll, S. G. Murdoch, R. Phelan, J. O'Gorman, and L. P. Barry, "Generation of Coherent Multicarrier Signals by Gain Switching of Discrete Mode Lasers," *IEEE Photonics Journal*, vol. 3, no. 1, pp. 112–122, 2011, DOI: 10.1109/JPHOT.2011.2105861.

[71] H. Ito, H. Yokoyama, S. Murata, and H. Inaba, "Generation of picosecond optical pulses with highly RF modulated AlGaAs DH laser," *IEEE Journal of Quantum Electronics*, vol. 17, no. 5, pp. 663–670, 1981, DOI: 10.1109/JQE.1981.1071160.

[72] R. S. Tucker, "High-speed modulation of semiconductor lasers," *IEEE Transactions on Electron Devices*, vol. 32, no. 12, pp. 2572–2584, 1985, DOI: 10.1109/T-ED.1985.22387.

[73] K. Lau and A. Yariv, "Ultra-high speed semiconductor lasers," *IEEE Journal of Quantum Electronics*, vol. 21, no. 2, pp. 121–138, 1985, DOI: 10.1109/JQE.1985.1072624.

[74] I. Fatadin, D. Ives, and M. Wicks, "Numerical simulation of intensity and phase noise from extracted parameters for CW DFB lasers," *IEEE Journal of Quantum Electronics*, vol. 42, no. 9, pp. 934–941, 2006, DOI: 10.1109/JQE.2006.880117.

[75] P. M. Anandarajah, K. Shi, J. O'Carroll, A. Kaszubowska, R. Phelan, L.P. Barry, A. D. Ellis, P.Perry, D. Reid, B. Kelly, and J. O'Gorman, "Phase shift keyed systems based on a gain switched laser transmitter," *Optics Express*, vol. 17, no. 15, pp. 12668, 2009, DOI: 10.1364/oe.17.012668.

[76] R. Zhou, S. Latkowski, J. O'Carroll, R. Phelan, L. P. Barry, and P. Anandarajah, "40nm wavelength tunable gain-switched optical comb source," *Optics Express*, vol. 19, no. 26, pp. B415–B420, 2011, DOI: 10.1364/OE.19.00B415.

[77] A. Rosado, A. Pérez-Serrano, J. M. G. Tijero, A. v Gutierrez, L. Pesquera, and I. Esquivias, "Numerical and Experimental Analysis of Optical Frequency Comb Generation in Gain-Switched Semiconductor Lasers," *IEEE Journal of Quantum Electronics*, vol. 55, no. 6, pp. 1–12, 2019, DOI: 10.1109/JQE.2019.2943482.

[78] E. K. Lau, L. J. Wong, and M. C. Wu, "Enhanced Modulation Characteristics of Optical Injection-Locked Lasers: A Tutorial," *IEEE Journal of Selected Topics in Quantum Electronics*, vol. 15, no. 3, pp. 618–633, 2009, DOI: 10.1109/JSTQE.2009.2014779.

[79] F. Mogensen, H. Olesen, and G. Jacobsen, "FM noise suppression and linewidth reduction in an injection-locked semiconductor laser," *Electronics Letters*, vol. 21, no. 16, pp. 696–697, 1985, DOI: 10.1049/el:19850492.

[80] R. Lang, "Injection locking properties of a semiconductor laser," *IEEE Journal of Quantum Electronics*, vol. 18, no. 6, pp. 976–983, 1982, DOI: 10.1109/JQE.1982.1071632.

[81] Z. Liu and R. Slavík, "Optical Injection Locking: From Principle to Applications," *Journal of Lightwave Technology*, vol. 38, no. 1, pp. 43–59, 2020, DOI: 10.1109/JLT.2019.2945718.

[82] S. P. O'Dúill, R. Zhou, P. M. Anandarajah, and L. P. Barry, "Numerical investigation into the dynamics of externally-injected, gain-switched lasers for optical comb generation," in *2014 The European Conference on Optical Communication (ECOC)*, 2014, pp. 1–3. DOI: 10.1109/ECOC.2014.6963862.

[83] F. Mogensen, H. Olesen, and G. Jacobsen, "Locking conditions and stability properties for a semiconductor laser with external light injection," *IEEE Journal of Quantum Electronics*, vol. 21, no. 7, pp. 784–793, 1985, DOI: 10.1109/JQE.1985.1072760.

[84] R. Zhou, T. Shao, M. D. Gutierrez Pascual, F. Smyth, and L. P. Barry, "Injection Locked Wavelength De-Multiplexer for Optical Comb-Based Nyquist WDM System," *IEEE Photonics Technology Letters*, vol. 27, no. 24, pp. 2595–2598, 2015, DOI: 10.1109/LPT.2015.2478791.

[85] S. T. Ahmad, P. D. Lakshmijayasimha, A. M. Kaszubowska-Anandarajah, C. Browning, and A. M. Prince, "Active demultiplexer-enabled directly modulated DMT transmission using optical frequency combs for data center interconnects," *Journal of Lightwave Technology*, p. 1, 2021, DOI: 10.1109/JLT.2021.3091959.

[86] M. D. G. Pascual, V. Vujicic, J. Braddell, F. Smyth, P. Anandarajah, and L. Barry, "Photonic Integrated Gain Switched Optical Frequency Comb for Spectrally Efficient Optical Transmission Systems," *IEEE Photonics Journal*, vol. 9, no. 3, pp. 1–8, 2017, DOI: 10.1109/JPHOT.2017.2678478.

[87] K. Hei, K. Anandarajah, E. P. Martin, G. Shi, P. M. Anandarajah, and N. Bhattacharya, "Absolute distance measurement with a gain-switched dual optical frequency comb," *Optics Express*, vol. 29, no. 6, pp. 8108–8116, 2021, DOI: 10.1364/OE.413478.

[88] C. Browning, H. Hallak Elwan, E. P. Martin, S. P. O'Duill, J. Poette, P. Sheridan, A. Farhang, B. Cabon, and L. P. Barry, "Gain-Switched Optical Frequency Combs for Future Mobile Radio-Over-Fiber Millimeter-Wave Systems," *Journal of Lightwave Technology*, vol. 36, no. 19, pp. 4602–4610, 2018.

[89] E. Prior, C. de Dios, Á. R. Criado, M. Ortsiefer, P. Meissner, and P. Acedo, "Expansion of VCSEL-Based Optical Frequency Combs in the Sub-THz Span: Comparison of Non-Linear

Techniques," *Journal of Lightwave Technology*, vol. 34, no. 17, pp. 4135–4142, 2016, DOI: 10.1109/JLT.2016.2594129.

[90]   P. M. Anandarajah, , R. Zhou, R. Maher, M. D. G. Pascual, F. Smyth, V. Vujicic and, and L. P. Barry, "Flexible optical comb source for super channel systems," *Optical Fiber Communication Conference, OFC 2013*, pp. 31–33, 2013, DOI: 10.1364/ofc.2013.oth3i.8.

[91]   A. Rosado, A. Pérez-Serrano, J. M. G. Tijero, Á. Valle, L. Pesquera, and I. Esquivias, "Enhanced optical frequency comb generation by pulsed gain-switching of optically injected semiconductor lasers," *Optics Express*, vol. 27, no. 6, p. 9155, 2019, DOI: 10.1364/oe.27.009155.

[92]   P. D. Lakshmijayasimha, P. M. Anandarajah, P. Landais, and A. Kaszubowska-Anandarajah, "Optical frequency comb expansion using mutually injection-locked gain-switched lasers," *Applied Sciences*, vol. 11, no. 15, 2021, DOI: 10.3390/app11157108.

[93]   P. M. Anandarajah, Member, S. Latkowski, C. Browning, R. Zhou, J. O'Carroll, R. Phelan, B. Kelly, J. O'Gorman, and L. P. Barry, "Integrated two-section discrete mode laser," *IEEE Photonics Journal*, vol. 4, no. 6, pp. 2085–2094, 2012, DOI: 10.1109/JPHOT.2012.2226023.

[94]   M. D. G. Pascual, V. Vujicic, J. Braddell, F. Smyth, P. Anandarajah, and L. Barry, "Photonic Integrated Gain Switched Optical Frequency Comb for Spectrally Efficient Optical Transmission Systems," *IEEE Photonics Journal*, vol. 9, no. 3, pp. 1–8, 2017, DOI: 10.1109/JPHOT.2017.2678478.

3. Expansion of Gain-Switched Optical Frequency Comb

The previous chapters presented an overview of various semiconductor-based optical frequency comb (OFC) generation techniques. Amongst them, the externally injected gain-switched laser (EI-GSL) based OFC has been chosen as the technique to be focussed on in this thesis, as it is simple, cost-effective, and open to photonic integration. More importantly, it offers flexibility and tunability in terms of the channel spacing and emission wavelength, which in turn facilitates the dynamic reconfiguration of transmission parameters, according to the network requirements. Hence, the EI-GSL based multi-carrier transmitter is an attractive candidate for deployment in next-generation reconfigurable optical networks.

While the EI-GSL delivers many advantages, its commercial application requires overcoming some shortcomings. One such deficiency is the limited number of OFC lines generated. This is due to the restricted modulation bandwidth of commercially available semiconductor lasers. To overcome this drawback, this chapter presents and experimentally demonstrates two novel OFC expansion techniques that are capable of increasing the GSL bandwidth/span at least by a factor of 3. In addition, a detailed characterisation (RIN, phase noise, phase correlation) of the expanded OFC is reported. Both expansion architectures can be photonically integrated, offer fast tuning, and

reconfigurability in terms of channel spacing, the number of comb lines and the emission wavelengths.

3.1 Introduction

As previously discussed, the use of OFC has been widely explored in numerous multi-disciplinary applications such as spectrally efficient communications systems, mmW/THz generation and radio-over-fibre systems, spectroscopy and much more. Amongst others, an EI-GSL OFC is proven to be well-served as a multi-carrier source in these applications [1]–[3]. Nevertheless, some of the shortcomings of the EI-GSL OFC still need to be addressed such as (i) a limited number of comb lines, arising from the restricted intrinsic modulation bandwidth of the laser, (ii) low comb line power and (iii) difficulty in generating low FSR (<1 GHz). The latter requires modulating the laser with short electrical pulses [4], thus increasing the complexity. In addition, in order to avoid secondary relaxation oscillations, the DC biasing of the laser must be set at or below the threshold, which leads to a severe reduction of power of the comb.

The limited number of comb lines makes the EI-GSL OFC source less attractive for various communications applications. To increase the number of generated comb lines, numerous approaches have been investigated. Zhou *et al* [5], employed an electro-optic phase modulator (PM) driven by an amplified sinewave (~$4V_\pi$) at the gain-switching frequency to expand the EI-GSL OFC by a factor of two. Another expansion technique [12], [25] includes the use of dispersion compensation fiber (DCF) followed by highly non-linear fiber (HNLF) that expands the OFC by a factor of 3. However, this approach is complex (requires very high pump power to invoke nonlinearity in the fibre), suffers from stability issues and is not suited for photonic integration. Other expansion schemes reported include the use of the dual-mode injection-locked FP laser [21], cascaded EI-GS FP lasers [9], dual-drive MZM modulators [10], and using multi-transverse modes (X and Y polarisation) in VCSEL to generate OFC [11]. However, these approaches resulted in a limited expansion and yielded comb lines with a poor OCNR. A summary of various GSL expansion approaches that have been recently reported is presented in Table 3-1.

Table 3-1 A brief survey of various broadband GSL OFC generation schemes

No.	Ref.	Key expansion component	FSR	Expansion factor	Demonstration/ comments
1	[5]	FP + Phase modulator	10	~ 2	40 nm wavelength tunability; limited expansion
2	[7]	HNLF + DCF	10.7	>3	Wide comb generation; complexity and stability issues
3	[9]	Cascaded GS FP lasers	10	~2	20 nm wavelength tunability; Limited expansion; low OCNR
4	[12]	Dual-mode injection locked FP	6.25	>2	Simple; 30 nm wavelength tunability; poor flatness; low OCNR
5	[13]	VCSEL HNLF + DCF + Modulator	5.2	~ 3	Wide comb generation; complexity; stability issues; low OCNR
6	[10]	Dual- drive MZM	9.5	>1.5	Simple; low drive voltage; limited expansion
7	[11]	VCSEL + dual mode injection locking	2.5	~2	Simple; limited expansion
8	*This work*	Mutual injection locking + phase modulator	6.25	~3	Wide comb generation; simple; FSR tunability from 390 MHz to 6.25 GHz
9	*This work*	Parallel cascaded FP + SOA	6.25	>3	Wide comb generation; amplified output power; 30 nm wavelength tunability

To overcome these drawbacks, two novel architectures to improve the expansion factor, is proposed. The first approach is based on the mutual injection locking of two GS slave lasers with a common master to generate a wider bandwidth OFC. In addition, by incorporating a PM, the same scheme facilitates further expansion and FSR tunability (GHz to MHz) via comb densification. A detailed characterisation of the expanded comb is performed, which highlights the high spectral purity attained. The second expansion

scheme is based on inducing phase correlation between two independent EI-GS Fabry Pérot (FP) using four-wave mixing (FWM) phenomena in a semiconductor optical amplifier (SOA). The broadband comb portrays an excellent phase correlation between all lines. Additionally, the experimental demonstration of 30 nm wavelength tunability of the OFC across the C band (1529 nm-1562 nm) is shown. Finally, both proposed architectures lend themselves to photonic integration, further reducing the cost, size and potentially consume less energy, making the proposed OFC generation/expansion architecture highly suitable for deployment as reconfigurable multi-carrier transmitters in next-generation optical networks.

3.2 Mutually Injection-Locked GSL-based OFCs Expansion and Densification
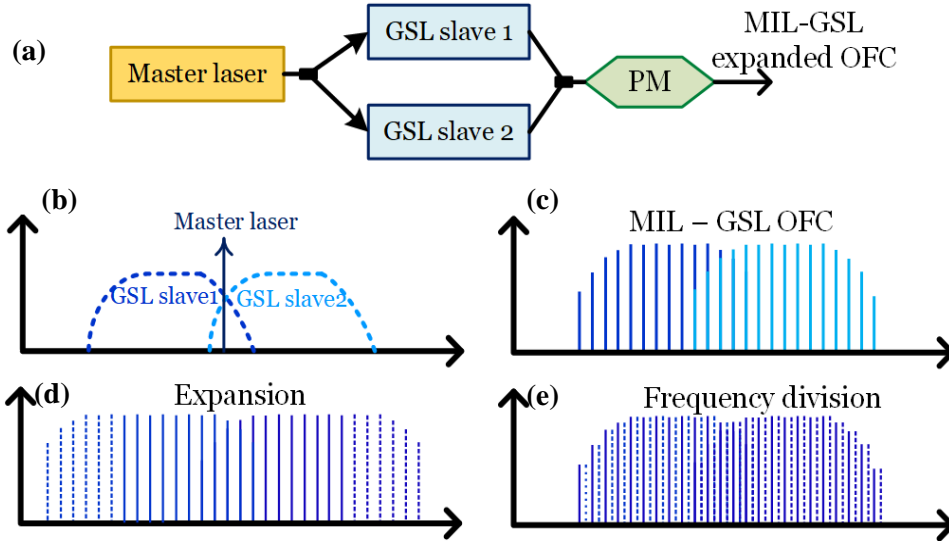
Figure 3.1 (a) Diagram of MIL-GSL OFC generation, expansion and comb densification/frequency division, and (b)-(e) the line graph showing the operational principle. Dotted lines represent newly generated tones after PM.

The first GSL expansion architecture is based on mutually injection-locked GSL (MIL-GSL) OFCs. The operational principle of the proposed scheme is as shown in Figure 3.1. It comprises two stages: (i) generation of two MIL-GSL OFCs, (ii) expansion and comb densification using a PM. Initially, two semiconductor-based single-mode lasers are

chosen as slave lasers and gain-switched (GS) using a large sinusoidal signal. The GSLs are then injection-locked by a semiconductor-based low linewidth wavelength-tunable laser, acting as a common master, as illustrated in Figure 3.1 (b). The master laser provides the frequency and phase locking to both slave lasers, resulting in two OFCs emitting comb lines with a high degree of phase correlation between them. The two OFCs are then combined, to generate a single broad OFC (Figure 3.1 (c)) and passed through a PM for further expansion.

Here, the PM can be operated in two modes: (a) expansion and (b) comb densification/frequency division. Three scenarios are investigated: (1) the MIL-GSL OFC is expanded by driving the PM with a large voltage (multiples of V_π) RF signal at the gain-switching (fundamental) frequency (f_s), as depicted in Figure 3.1 (d); (2) the PM is driven with multiples of the fundamental FSR (nf_s); (3) the PM is driven with a sinusoidal signal that is at a sub-harmonic of the fundamental frequency $\left(f_s/m\right)$ (Figure 3.1 (e)). The latter corresponds to the comb densification mode and results in the generation of a comb with an FSR that is m-times smaller than the fundamental one. In other words, the FSR of the MIL-GSL OFC can be tuned from GHz to MHz, without the need to re-optimise the GSL. Additionally, the average OFC power remains unchanged across the tuning range, thus overcoming the reduction of comb output power for low FSRs.

3.2.1 Experimental setup: MIL-GSL OFC

The experimental setup of the proposed MIL-GSL OFC generation, expansion and comb densification is shown in Figure 3.2. Here, the components with polarisation maintaining fiber (PMF) and standard single mode fiber (SSMF) are indicated by brown and grey lines, respectively. Two commercially available discrete mode (DM) lasers, from Eblana Photonics [14], [15] are chosen as the slave lasers. These are 250-µm long FP laser diodes with a slotted ridge waveguide structure that constrains the lasing in a longitudinal mode, achieving a side mode suppression ratio (SMSR) larger than 60 dB, as shown in Figure 3.3 (a). The DM lasers are encased in temperature-controlled (with the aid of thermoelectric coolers (TECs)) 7 pin butterfly packages with a k-type RF connector, to

enable high-speed modulation. The packaging does not include an optical isolator to allow external light injection. The lasers exhibit threshold currents (I_{th}) of ~10 mA and a modulation bandwidth of ~ 12 GHz, when biased at ~ 53 mA. At the same bias, slave lasers 1 and 2 emit an average power of 6 dBm and 7 dBm, respectively.
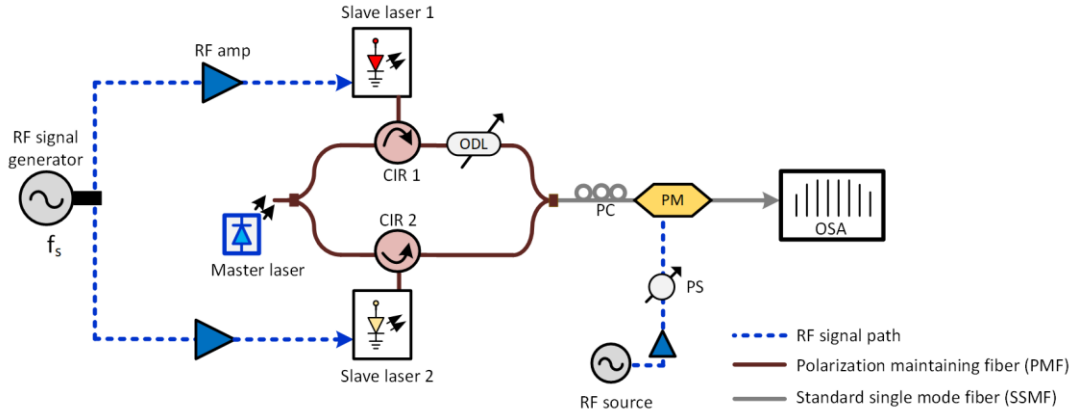
Figure 3.2 Experimental setup of the proposed MIL-GSL OFC generation. Here, RF amp: radio frequency amplifier, CIR: circulator, PS: phase shifter, ODL: optical delay line, PM: phase modulator, $\mathbf{f_s}$: free spectral range, OSA: optical spectrum analyser.

Gain switching is achieved by applying an amplified 6.25 GHz sinusoidal signal (~24 dBm) in conjunction with a 53 mA DC bias to both lasers. Subsequently, the temperature of the lasers is tuned to achieve a partial overlap of their spectra (as shown in Figure 3 (b)). Then, a narrow linewidth wavelength-tunable laser (Pure photonics PCL550), acting as a common master laser, is tuned to the overlapping wavelength region ($\lambda_{injection} = 1549.8$ nm, $P_{injection} = -3$ dBm), split using a 50: 50 splitter and injected, via 3 port circulators (CIR 1 and 2), into the two GS lasers. It is important to mention that the components used in the MIL-GSL OFC generation are pigtailed with polarisation maintaining fibre, which is aligned to the slow polarisation axis.

The two-phase correlated OFCs generated this way are then combined using a 50:50 coupler and passed through a 20 GHz PM. The modulator exhibits a V_π of ~4V (at 6.25 GHz) and is driven at ~13.5 Vpp (corresponding to $3.3V_\pi$) by a second RF source (both RF sources are synchronised using the 100 MHz reference ports). It is important to note that the same RF source could be used for the OFC generation and the phase

modulation. The expansion and spectral flattening (shaping) of the output comb, when passing through the PM, are achieved using an electrical phase shifter (PS) and an optical delay line (ODL). The PM is driven at a frequency $f = nf_s$, where $n = 1, 2$ or 3 in the expansion mode (i.e., $f = 6.35, 12.5, 18.75$ GHz) and $n = 0.5, 0.25, 0.125$ or 0.0625, in the comb densification mode ($f = 3.125, 1.5625$ GHz, 781.25 MHz, and 390.625 MHz). The resultant optical spectra are recorded using a high resolution (20 MHz) optical spectrum analyser (OSA).

3.2.2 Experimental results

3.2.2.1 *MIL-GSL OFC generation*

The continuous wave (CW) optical spectra of the two slave lasers, with SMSR > 60 dB, are shown in Figure 3.3 (a). Figure 3.3 (b) shows the overlapped spectra of the gain-switched slave 1 (blue) and 2 (red) with the FSR of 6.25 GHz and the common master laser at 1549.6 nm (black). The GS spectra in Figure 3.3 (b) illustrate the absence of discernible comb lines, indicating that there is no pulse-to-pulse phase coherence in the temporal domain [16], [17]. However, when the external injection from the master laser locks the phases of the pulses, the comb lines become clearly visible in the spectrum, as depicted in Figure 3.3 (c). The generated MIL-GSL OFC 1 and 2 feature 12 and 15 comb lines respectively (within 5 dB from spectral peak) and exhibit an OCNR >50 dB (within 20 MHz OSA resolution).

The slightly higher number of comb tones in OFC 2 is due to an enhanced modulation response of GS laser 2, which is a contribution of the injection wavelength being set to the lower wavelength end of its GS spectrum [18]–[20]. As mentioned above, injection locking with a common master laser ensures that both GSL OFCs are phase and frequency synchronised. Thus, by combining them, a single MIL-GSL OFC with 27 lines and a bandwidth of ~168.75 GHz (both within 5 dB) is generated, as illustrated in Figure 3.3 (d).
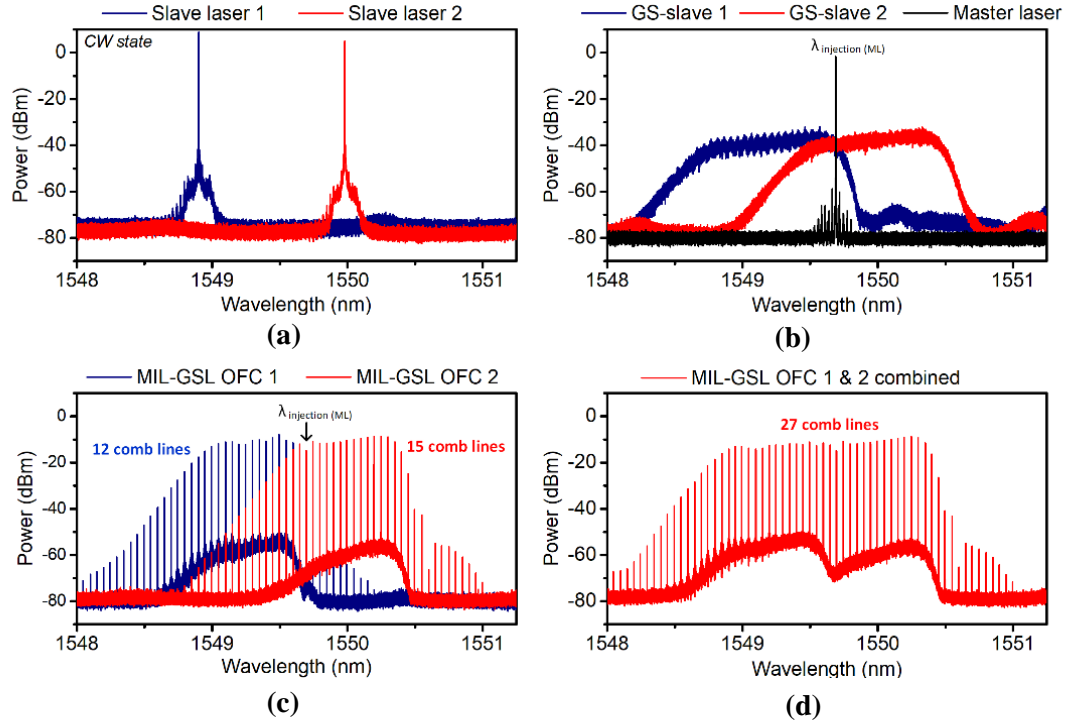
Figure 3.3 Optical spectra of (a) CW slave lasers, (b) GS slave 1, 2 and the master lasers, (c) MIL-GSL OFC 1 and 2, (d) expanded OFC (combined MIL- GSL OFC 1 and 2).

3.2.2.2 MIL-GS OFC expansion and densification

Figure 3.4 (a)-(c) illustrate the PM-induced comb expansion of the MIL-GSL OFC when the PM is driven at the fundamental and multiples of the FSR (6.25, 12.5, and 18.75 GHz). When driven at the fundamental frequency, 35 comb lines (comb 5dB bandwidth of 218.75 GHz) are generated, with an OCNR larger than 45 dB. The expansion factor is ~ 2.3 compared to the single EI-GSL OFC (red spectrum, Figure 3.3 (c)). In this case, the comb expansion is limited by the maximum allowable drive amplitude of the PM used. Therefore, to further increase the expansion, the PM is driven at multiples of f_s with the same drive voltage. The number of comb lines increases to 39 (comb 5 dB bandwidth of ~243.75 GHz) when the PM is driven at $2f_s = 12.5$ GHz and 45 (~281.25 GHz bandwidth) when driven at $3f_s = 18.75$ GHz. This could be attributed to Bessel function expansion, where every harmonic is modulated and resulting in the generation sidebands that are $2f_s$ or $3f_s$ further apart. It is worth noting that only the PM drive frequency is varied, while all other conditions, such as slave laser bias, gain-switching parameters, and PM

drive amplitude remain unchanged. Table 3-2 summarises the OFC expansion achieved. Overall, with the proposed MIL-GSL OFC technique, the number of comb lines is increased by a factor of 3 (from 15 lines, for individual EI-GSL OFC, to 45 lines for the proposed expanded OFC).
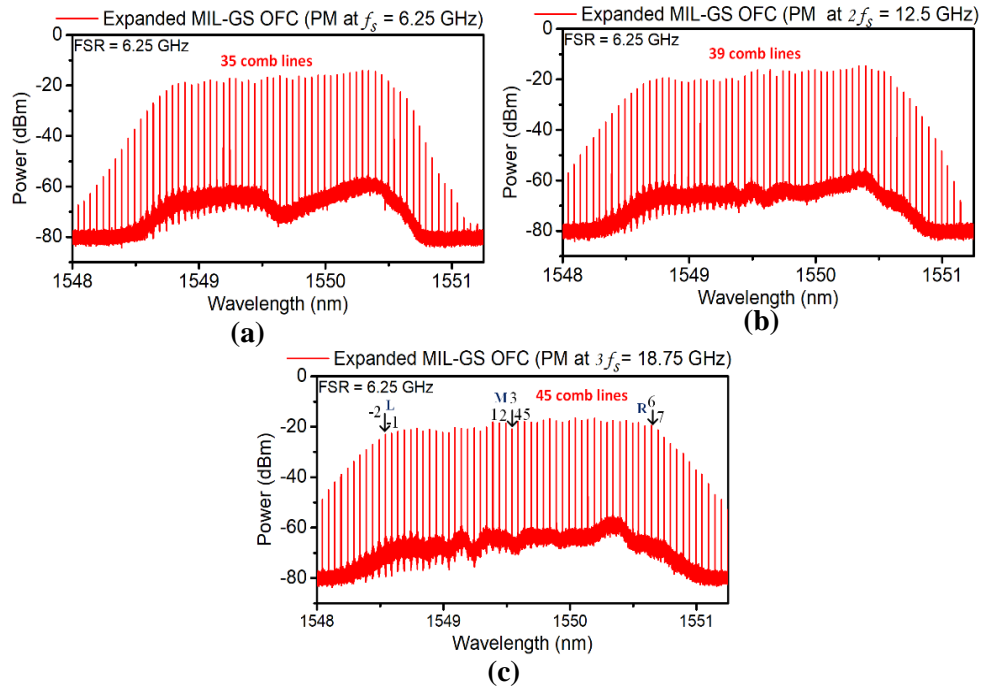
Figure 3.4 Optical spectra of expanded MIL-GSL OFC, PM driven at (a) 6.25, (b) 12.5, and (c) 18.75 GHz. The arrows (L: left, M: middle, R: right) and numbered tones are filtered for phase noise analysis.

Table 3-2 Summary of the OFC expansion

OFC	No. of lines (5 dB from peak)	Comb bandwidth (5 dB)	Expansion factor
Individual GSL OFC	15	~93.7 GHz	--
Combined MIL-GSL OFC	27	~168.75 GHz	1.8
MIL OFC + PM (at 6.25 GHz)	35	~218.75 GHz	2.3
MIL OFC + PM (at 12.5 GHz)	39	~243.75 GHz	2.6
MIL OFC + PM (at 18.75 GHz)	45	~281.25 GHz	3
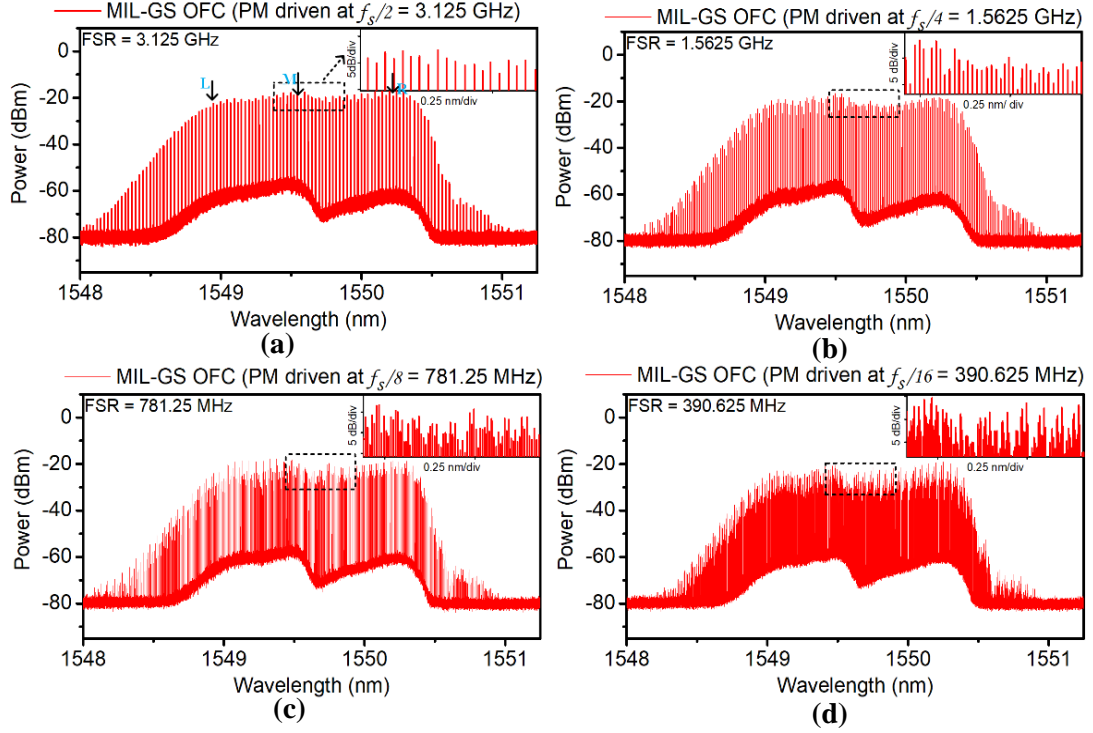
Figure 3.5 Optical spectra of the MIL-GSL OFC with an FSR of (a) 3.125 GHz, (b) 1.5625 GHz, (c) 781.25 MHz, and (d) 390.625 MHz. The insets depict a zoom-in of the dotted region.

In the comb densification mode, the PM is driven at a sub-harmonic frequency of the fundamental frequency f_s/m, where m = 2, 4, 8, and 16. The resultant combs, with an FSR of 3.125 GHz, 1.5625 GHz, 781.25 MHz, and 390.625 MHz, are shown in Figure 3.5 (a) - (d) respectively. The insets within each of these figures show a magnified dotted region. Figure 3.5 shows resolved comb tones with an OCNR ranging from ~ 30-45 dB (within 20 MHz OSA resolution) and a comb bandwidth of ~ 180 GHz over the entire tuning range. The average comb output power remains constant at ~ 9 dBm. The summary of the comb densification is presented in Table 3-3. This demonstration highlights the potential of a wide FSR tunability range, spanning from MHz to GHz, with a simplified approach and fast tuning speed. Furthermore, the fundamental FSR can also be tuned by varying the GS frequency of the slave lasers. It is important to mention that the lower FSR MIL-GS OFC could be employed in applications such as spectroscopy, gas sensing, distance measurement [2],[3], etc., where the comb flatness is not critical.

Table 3-3 Summary of the MIL-GS OFC comb densification

MIL-GS OFC FSR	OCNR (tone at ~1550 nm)	Number of lines (5 dB from peak)
6.25 GHz	50	27
3.125 GHz	45	58
1.5625 GHz	~42	~113
781.25 MHz	~38	~214
390.625 MHz	~33	~453 (within 10 dB)

3.2.2.3 MIL-GSL OFC characterisation

After the experimental demonstration of the MIL-GSL based OFC expansion or densification, the next step is to carry out a comprehensive characterisation of the expanded OFC. This includes important comb parameters such as the relative intensity noise (RIN), phase noise, and phase correlation.

(a) Relative Intensity Noise

RIN describes the random intensity fluctuations of the optical carrier (comb line) that stems from intrinsic optical phase and frequency fluctuations caused by spontaneous emission [22], [24]. It is an important transmitter parameter, particularly when employing intensity-based modulation formats and even more important when using multi-level intensity modulation formats such as pulse amplitude modulation (PAM)- 4/8. The current IEEE standard for Ethernet 802.3 specifies the stringent RIN requirement below -132 and -136 dB/Hz, for commercial deployment of 200 Gb/s (200GBASE-DR4), and 400 Gb/s (400GBASE-DR4) systems [23].

RIN can be defined as the ratio of the mean squared optical power fluctuations $\Delta P(t)$ to the squared average optical power P_o [24],

$$RIN = \frac{\left\langle \Delta P(t)^2 \right\rangle}{P_o^2} \tag{3.1}$$

The optical power fluctuations are translated into electrical power fluctuations, when detected with a photodetector and can be measured on an electrical spectrum analyser (ESA). Therefore, the corresponding RIN can be expressed as,

$$RIN = \frac{\Delta P_E}{P_{EO}} \qquad (3.2)$$

where P_{EO} is the average electrical power, ΔP_E represents overall noise comprising of laser noise (N_L), shot noise (N_q), and thermal noise (N_{th}).
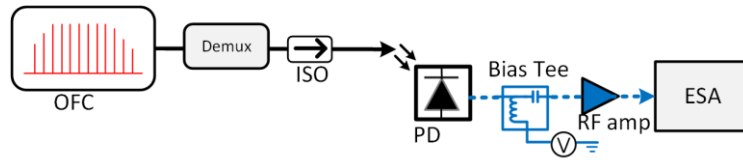
Figure 3.6 RIN measurement setup. Here, Demux: demultiplexer, ISO: isolator, PD: photodetector, ESA: electrical spectrum analyser.

The experimental setup to measure the RIN is shown in Figure 3.6. The individual OFC lines, that are marked in Figure 3.4 (c) and Figure 3.5 (a) are filtered by a filter (an active demultiplexer[1] (refer Chapter 4, Section 4.3)), passed through an isolator (to avoid any feedback reflections) and detected with a high-speed photodetector (PD) [25]. The output of the PD is passed through a bias tee to separate the DC and the AC components of the photocurrent. The AC component is amplified using an RF amplifier and captured using an ESA while the shot noise N_q, and the average electrical power P_{el} are extracted from the DC component with an aid of a multimetre. The average electrical power is given by,

$$P_{el} = \left[\left(\frac{U_{dc}}{R_{out}} \right)^2 \times R_L \right] \times V \qquad (3.3)$$

Here, V is the gain of the RF amplifier used, U_{dc} is the measured DC voltage, $R_L \ and \ R_{out}$ are the load and output resistance, respectively. Then, shot noise N_q is determined by the photocurrent, given by

---

[1] Active demultiplexer filter is used in the RIN characterisation is to have a like-to-like comparison with 3.125 and 6.25 GHz comb.

$$N_q = \left[2 \times q \times U_{dc} \left(\frac{R_L}{R_{out}} \right) \right]$$

(3.4)

To calculate the RIN, the following procedure is followed: first, the intensity noise spectrum of the detected optical signal (filtered comb line) is measured, to determine the overall noise ΔP_E. Next, the optical signal is removed, and the intensity spectrum is captured again to quantify the thermal noise N_{th}. Then, the OFC line intensity noise is retrieved using the formula $N_L = \Delta P_E - N_q - N_{th}$.
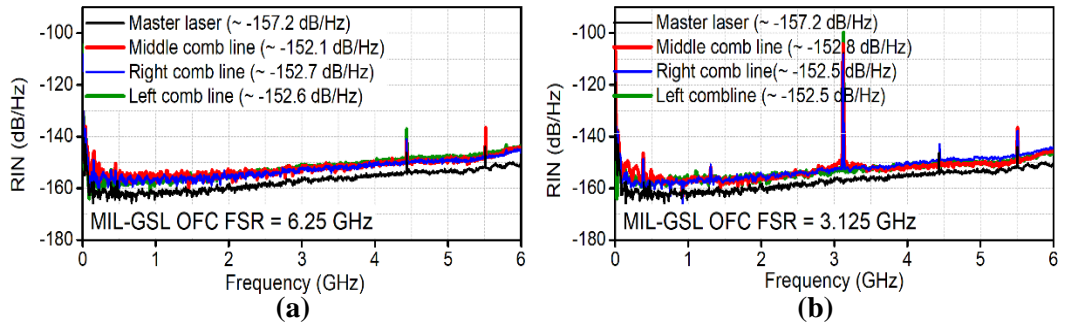
Figure 3.7 RIN measurements for MIL-GSL OFC at FSR (a) 6.25 GHz, and (b) 3.125 GHz.

The measured RIN can be expressed as a relative power spectral density, with units of dB/Hz. The resultant RIN spectra, for 6.25 GHz and 3.125 GHz FSR demultiplexed comb lines, are shown in Figure 3.7 (a) and (b), respectively. From the figures, it can be seen that all the demultiplexed comb lines exhibit a similar RIN profile, which is comparable with that of the master laser. The averaged RIN (from DC to 6 GHz) measured for 6.25 GHz and 3.125 GHz FSRs demultiplexed OFC lines are better than -152 dB/ Hz for all cases. The low RIN values can be attributed to the external injection locking from the purer master, reducing the spontaneous emission of the slave lasers, thus the associated intensity fluctuations.

(b) Phase Noise

The phase noise of the optical transmitter plays a crucial role in coherent communication systems, where modulation formats utilise both intensity and phase of the optical signal

to convey the information [26]–[29]. The phase noise of the optical carrier primarily dictates the allowable modulation type, order and baud rate that can be employed [30]. Thus, for a reconfigurable multi-carrier transmitter to be employed in a system employing higher-order modulation formats, a low phase noise is highly desirable.

The phase noise characterisation of the MIL-GSL OFC lines is performed by measuring the frequency-modulation (FM) noise spectrum using the modified delayed self-heterodyne method [31]. The FM noise spectrum $S_f(f)$, describes the power spectral density of the instantaneous frequency fluctuation originating from the phase noise. The experimental setup of FM noise measurement is as shown in Figure 3.8. The individual comb lines are filtered using a filter, passed through an isolator to avoid any reflections and sent to an FM noise measurement setup. Here, the optical signal is split into two arms using a 50:50 coupler. The upper arm is sent through 25 km of SSMF fiber (equivalent delay ~123 µs) to induce phase de-correlation between two arms. The lower arm is passed through a PM driven by an amplified 2 GHz signal, to generate second-order harmonics. Then, the two arms are recombined with a 50:50 coupler and detected on a PD. The electrical output is captured using a real-time sampling oscilloscope (RTS) operating at $1/\tau_S$ = 20 GSa/s, with a total memory points of $n = 200,000$ and the measurement time set to $(\tau_S . n)$ [26]. The recorded data is then processed offline to obtain an FM noise spectrum.
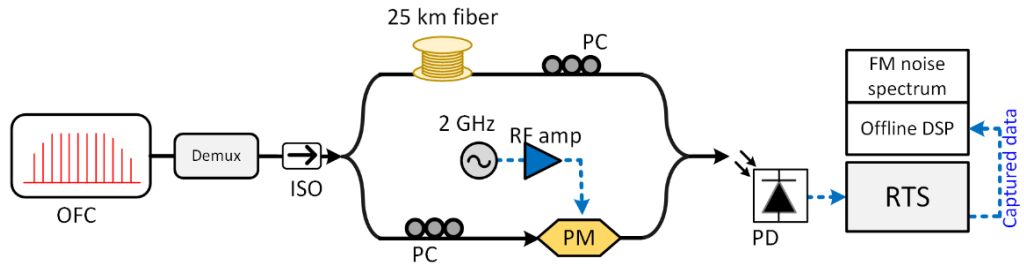
Figure 3.8 Modified delayed self-heterodyne setup for FM noise measurement [31]. Here, Demux: demultiplexer, ISO: isolator, PC: polarisation controller, PM: phase modulator, PD: photodetector, RTS: real-time oscilloscope. Demultiplexers used: optical bandpass filter [32], active demultiplexer [25] for filter 6.25 GHz and 3.125 GHz FSR OFC lines, respectively.

The FM noise spectrum ($S_f(f)$), consisting of white FM- noise, flicker (*1/f*) noise, and random-walk noise, can be written as [33],

$$S_f(\text{f}) = S_{STH}(f) + S_o\left[\frac{f_1}{f} + \left(\frac{f_2}{f}\right)^2\right]$$

(3.5)

where $f_1 = K_1/S_o$, $f_2 = \sqrt{K_2/S_o}$, f_l and f_2 are the break frequencies of the flicker noise ($^1/_f$) and random FM noise ($^1/_{f^2}$), respectively. Here, the first term represents the complete Schawlow–Townes Henry (STH) FM noise, whereas the second term is the excess FM noise. $S_{STH}(f)$ is the FM spectrum of the STH FM noise including the relaxation oscillation. The spectral shape of $S_{STH}(f)$ is determined by the carrier density relaxation oscillation in the aftermath of random spontaneous recombination and represents the linewidth broadening (α) of the lasers due to spontaneous emission, as given by [33],

$$S_{STH}(f) = \frac{S_0}{1+\alpha^2}\left(1 + \frac{\alpha^2 f_r^4}{(f_r^2 - f^2)^2 + (^{\Gamma f}/_{2\pi})^2}\right)$$

(3.6)

Where Γ and f_R, represents the damping rate and resonance frequency. More information on the origin and impact of various types of noise on the laser phase noise can be found in [33], [34].

For the phase noise analysis, three different comb lines (right (R), middle (M), and left (L)), marked by arrows in Figure 3.4 (c) and Figure 3.5 (a), are filtered and compared with the master. The resultant FM noise spectra are as shown in Figure 3.9, it can be seen that the $^1/_f$ noise dominates at frequencies < 5 MHz. Then from 5 to 30 MHz, the FM spectrum is dominated by the white noise. Beyond that, the FM noise increases until the relaxation frequency of the laser and then becomes negligible reducing to white background noise due to spontaneous emission. Hence, the digital filter applied during the offline processing, that has a cut-off frequency of 1 GHz. Therefore, the spectrum in Figure 3.9 shows a sharp drop beyond that frequency. The Lorentzian shaped optical

linewidth (δf) of the laser can be retrieved from the flat (white) FM-noise component S_o, using the relationship given by [31],

$$\delta f = S_o \times \frac{\pi}{2} \qquad (3.7)$$

Here, the factor 2 is due to the self-heterodyne nature of the measurement.
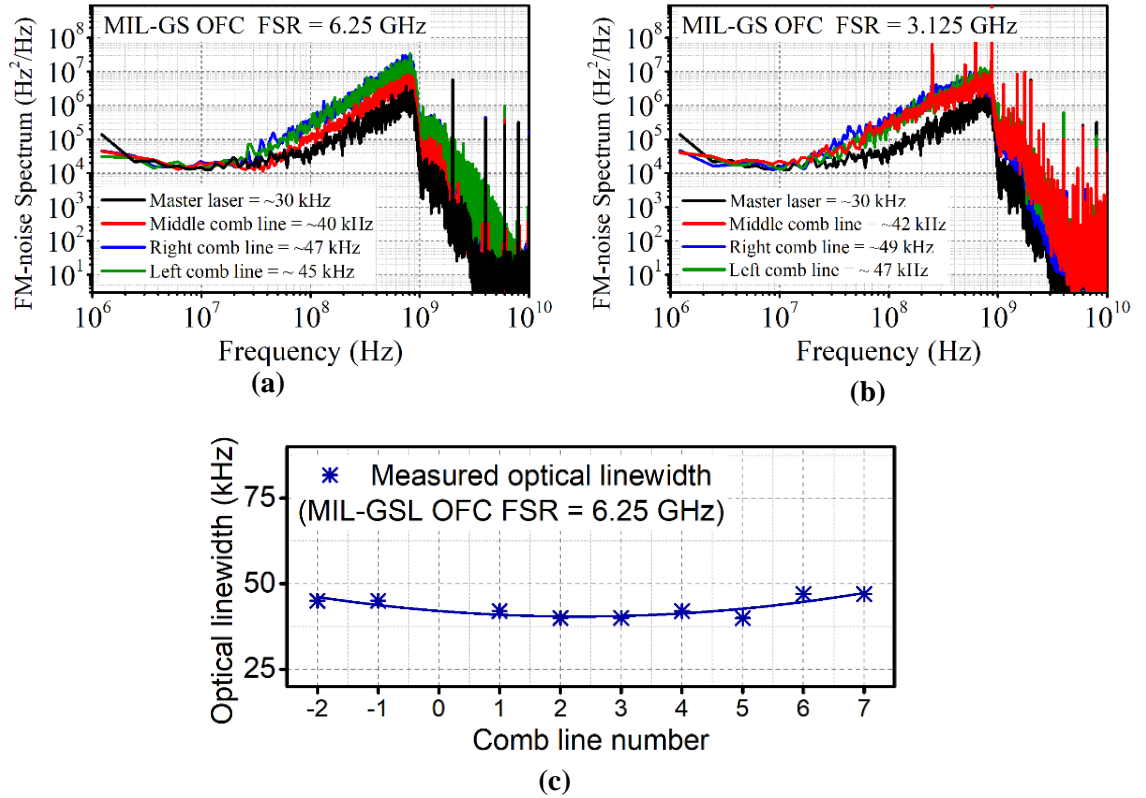
Figure 3.9 FM noise spectrum for MIL-GSL OFC lines at FSR of (a) 6.25 GHz, (b) 3.125 GHz, (c) plot of measured optical linewidths of different comb tones (FSR = 6.25 GHz).

The resultant FM noise spectrum of a 6.25 GHz comb line and the master laser is illustrated in Figure 3.9 (a). The optical linewidth of the master laser, and the middle (M), right (R), and left (L) comb lines (as in Figure 3.4(c)) are measured as ~30, ~40, ~47, and ~45 kHz, respectively. Furthermore, the optical linewidth of other comb lines is measured and found to be between 40 to 47 kHz across the entire comb, as shown in Figure 3.9 (c). Finally, the linewidth of the OFC lines with an FSR of 3.125 GHz is measured to be

~42 kHz (middle), ~49 kHz (right), and ~47 kHz (left), as shown in Figure 3.9 (b). This narrow optical linewidth in all the cases indicate the efficient transfer of phase noise from the master laser to the expanded OFC. It is important to mention that the measured linewidth fluctuates by about 10 kHz (40 to 50 kHz). This is due to the gain-switched slave lasers experiencing different injection locking conditions i.e., injection with different wavelength detuning [20]. The phase and intensity noise properties of the expanded and densified OFC lines are summarised in Table 3-4.

Table 3-4 Summary of the MIL-GSL OFC Phase noise and RIN characterization

Comb line	Phase noise		Avg. RIN (dB/Hz)	
	6.25 GHz	3.125 GHz	6.25 GHz	3.125 GHz
Master laser	~30 kHz	~30 kHz	−157.2	−157.2
Comb line (middle)	~40 kHz	~42 kHz	−152.1	−152.8
Comb line (right)	~47 kHz	~49 kHz	−152.7	−152.5
Comb line (left)	~45 kHz	~47 kHz	−152.6	−152.5

(c) Phase correlation
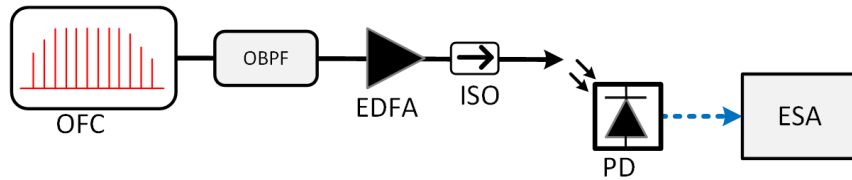
Figure 3.10 Phase correlation measurement setup. Here, ISO: isolator, OBPF: optical bandpass filter, PD: photodetector, ESA: electrical spectrum analyser.

The phase correlation between two comb lines is assessed by characterising by measuring the linewidth of their heterodyned (RF beat) tone. The measurement setup is shown in Figure 3.10. A pair of comb lines is filtered using an optical bandpass filter (OBPF), amplified by an EDFA operating in a constant gain mode (15 dB) and detected by a 50 GHz PD. The linewidth of the resultant RF beat tone is measured with a 40 GHz electrical spectrum analyser (ESA). The beat tone linewidth is determined by the phase

noise of the selected comb lines and the degree of the correlation between them. If the phase noise of the lines is not correlated, the optical linewidths of both lines add up, resulting in a broad RF beat tone. If correlated, the optical phase noise is cancelled at the PD, resulting in the generation of a spectrally pure RF signal (reflecting the purity of RF source used for the OFC generation) [34], [36].

Two neighbouring 3.125 GHz FSR comb lines are filtered and heterodyned on a 50 GHz PD to generate an RF tone, as shown in Figure 3.11 (a). As can be seen from the plot, the generated beat tone has a 3 dB line width of 33 Hz (ESA setting: VBW = 30 Hz; RBW = 30 Hz). A beat tone with a linewidth of the order of tens of Hz reflects a high degree of phase correlation between the OFC lines and the purity of the RF sources used for the OFC generation. Subsequently, the measurement is repeated for pairs of comb lines separated by multiples of FSR (up to 40 GHz due to the limited bandwidth of the ESA). Consistently, a beat linewidth of 33 Hz is measured, as shown in Figure 3.11 (b) for MIL-GSL OFC with FSR of 3.125 GHz and 6.25 GHz. The results prove a high degree of phase correlation is maintained across the entire comb, including tones that originated from two different GS lasers (OFCs 1 and 2).
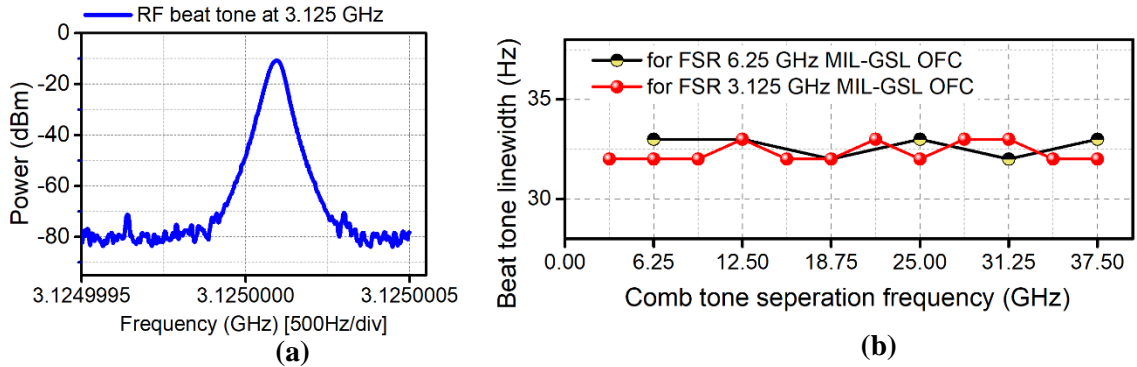
Figure 3.11 (a) An electrical spectrum of the resultant beat tone at 3.125 GHz, (b) RF beat tone linewidth for OFC with an FSR of 6.25 GHz and 3.125 GHz (ESA resolution: 30 Hz).

As the results presented in this section show, the proposed MIL-GSL scheme overcomes the bandwidth limitation of the EI-GSL OFC by expanding it by a factor of 3. It offers rapid FSR tunability from a GHz to an MHz range via the comb densification approach. The latter is attained without any optimisation of the GSL source which simplifies the

FSR tuning and more importantly offers a simple GSL OFC generation at low FSR (in MHz).

Although the MIL-GSL scheme addresses the major shortcomings of the EI-GSL, it still suffers from a low comb line power and lack of wavelength tunability. The latter is determined by the wavelength tunability of the slave lasers used in the gain-switching process. Another aspect that could be investigated for further improvement is the upper limit on the drive voltage of the PM. Driving with a larger voltage would lead to a broader comb. These minor disadvantages led to the investigation of another expansion scheme. The novel technique that employs multi-mode FP lasers, is proposed and experimentally investigated in section 3.3.

3.3 Expansion and Phase Correlation via FWM in an SOA

The second reconfigurable GSL-OFC expansion approach is based on a two-step procedure: initial expansion and then the phase correlation of several independent EI-GSL OFCs. The working principle is schematically depicted in Figure 3.12 (a). It comprises three stages: i) comb generation, ii) expansion and iii) phase correlation. The illustrative spectra of the comb at each stage are shown as insets (i)-(iii) in Figure 3.12 (b).
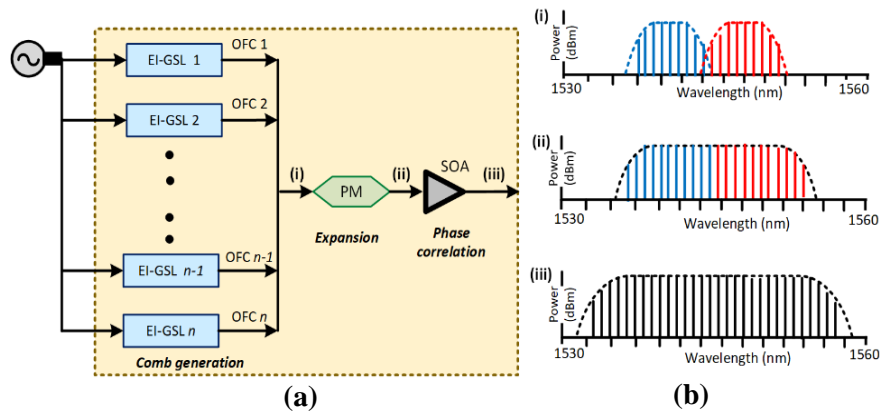
Figure 3.12 (a) Illustration of the proposed comb expansion and phase correlation technique, (b) line graphs of the spectral output at each stage: (i) individual OFCs, (ii) PM output, and (iii) SOA output.

First, the OFCs are generated using the EI-GSL technique, with each of the stages (1 to n) being operated in a master-slave (MS) configuration. Next, the OFCs outputs are passively combined and passed to the second stage, where they are expanded using a phase modulator. As each expanded comb portrays the phase noise properties of its master laser [5], combs from each of the different stages are not correlated in phase. To remedy this, all combs are sent to the third stage of the set-up: phase-correlation. Here, an SOA is used while operating in deep saturation in order to exploit its FWM-induced carrier density modulation property. The FWM between the individual OFCs introduces a phase correlation between all the comb lines, as illustrated in Figure 3.13.
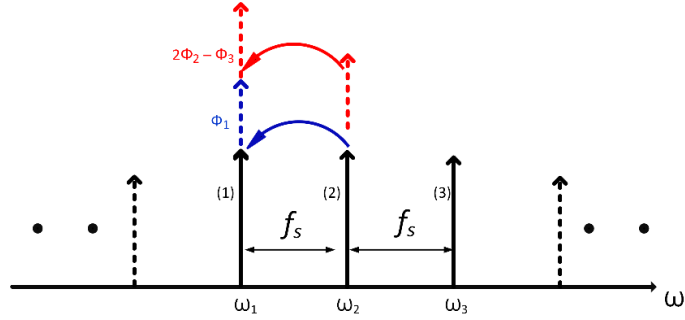
Figure 3.13 Principle of phase transfer through FWM in an SOA. Here, φ_1, φ_2, φ_3 are the phases of three comb lines, respectively and f_s denotes the FSR of the comb. The dotted lines represent newly FWM generated spectral components

When the comb lines are injected into an SOA, the beating between the different modes creates a gain and index modulation resulting in FWM through nonlinear effects such as carrier density modulation (CDM), carrier heating, spectral hole burning, two-photon absorption, and the Kerr effect [37]–[39]. However, CDM is the most significant FWM effect for FSRs below 100 GHz. Hence, this work focuses on the CDM effect.

The electric field propagating through an SOA can be written as:

$$\overrightarrow{E_i}(z,t) = A_i e^{(\omega_i t - k_i z - \varphi_i(t))} \vec{u} \tag{3.8}$$

where A_i is the magnitude, ω_i is the angular frequency, k_i is the wave vector along a given direction $\overrightarrow{u_z}$, φ_i is the phase noise of the ith comb line and $\vec{u}$ is the orientation of the electric field. The contribution of the CDM to the ith comb line is given by [38]:

$$\delta_i^{cdm} = -\frac{1}{2}(1-j\alpha)G_i\sum_{m=1}^{M}[\Delta N_m E_{i-m} + \Delta N_m^* E_{i+m}]$$

(3.9)

where α is the linewidth enhancement factor, G_i is the linear gain, ΔN_m is the mth order carrier modulation and E_i represents the electric field of ith comb line. Due to the CDM, the SOA carrier population N fluctuates around the average carrier density $\overline{N}$. ΔN_m is given by [40]:

$$\Delta N_m = -(N_0 - \overline{N})\frac{\sum_{k=m+1}^{M}\dfrac{E_k E_{k-m}^*}{P_s}}{1+\dfrac{P_t}{P_s}-jmf_s\tau_e}$$

(3.10)

where N_0 is the average carrier number, P_s is the saturation power, P_t is the total power confined in the SOA waveguide, and τ_e is the carrier spontaneous lifetime. For example, the CDM contributing to comb lines 1 and 3 are given below (for clarity, the analysis is limited to 3 comb lines).

$$\delta_1^{cdm} = \frac{1}{2}(1-j\alpha)G_1(N_0 - \overline{N})\left[\frac{|E_2|^2 E_1 + E_3^*|E_2|^2}{P_s + P_t - jf_s\tau_e P_s}\right]$$

(3.11)

$$\delta_3^{cdm} = \frac{1}{2}(1-j\alpha)G_3(N_0 - \overline{N})\left[\frac{|E_2|^2 E_3 + E_1^*|E_2|^2}{P_s + P_t - jf_s\tau_e P_s}\right]$$

(3.12)

On solving the first electric field term of δ_1^{cdm} eq. 3.11,

$$|E_2|^2 E_1 = A_2^2 A_1 e^{jw_1 - k_1 z + \varphi_1}$$

(3.13)

where $|E_2|^2 = A_2^2$ in equation. 3.13 represents the energy transfer from comb line 2 to comb line 1 and with a phase of the comb line 1 (φ_1), as represented in the blue arrow in Figure 3.13. Then, the second term of δ_1^{cdm} in equation 3.11,

$$E_3^*|E_2|^2 = A_3 A_2^2 e^{j(2w_2 t + 2\varphi_2 - w_3 t - \varphi_3)}$$

(3.14)

Equation 3.14 denotes the new FWM components at $\omega_1 = 2\omega_2 - \omega_3$ (due to the interaction of ω_2 and ω_3) but with the phase equal to $2\varphi_2(t) - \varphi_3(t)$, as corresponding

to the red arrow in Figure 3.13. This represents the transferring of the phase φ_2 and φ_3 to ω_1. Hence, the CDM contributes to the transfer of phase from comb line 2 and 3 to comb line 1. The phase noise of comb line 1 is affected by these phase transfers, a process that is similar to mode-locking [39]. Similarly, the first term of δ_3^{cdm} appears at ω_3, with the phase of comb line 3 (φ_3). The second term of δ_3^{cdm} appears at $\omega_3 = 2\omega_2 - \omega_1$, with the phase equal to $2\varphi_2(t) - \varphi_1(t)$. Thus, transfer of phase φ_2 and φ_1 to ω_3. Likewise, φ_3 is also affected by the phase transfer of φ_2 and φ_1. As a result of the phase transfer, the CDM induces a correlation between the phase of all the comb lines that are injected into an SOA. Thus, the last stage of the proposed set-up produces a single broadband and highly coherent OFC.

3.3.1   Experimental setup: expansion and phase correlation via FWM

The experimental setup of the wavelength-tunable EI-GSL OFC expansion and phase correlation technique is depicted in Figure 3.14. Two 200 µm long Fabry Pérot (FP1 and FP2) laser diodes encased in a high-speed butterfly package, are used as the slave lasers (SLs). The FPs have threshold currents (I_{th}) of 8 and 8.5 mA, are biased at $5 \times I_{th}$ and emit an output power of 7.7 dBm and 8.5 dBm, respectively. Two independent semiconductor-based tunable (master) lasers (TL1 and TL2) are used to inject light into the slave lasers via circulators (CIR 1 and CIR 2). The power of TL1 is set to 0.5 dBm and TL2 to 1.5 dBm. The external injection enables the selection of one longitudinal mode of each of the FPs, thereby achieving single-mode operation at the chosen wavelengths. Polarisation controllers (PC 1 and 2) are used to align the polarisation state of the injected light with the optical waveguides of the slave lasers. Subsequently, the FPs are gain-switched, by applying a 6.25 GHz electrical sinusoidal signal at a power of 24 dBm. The wavelengths of the TLs, used for the external injection, are tuned to lie on a 6.25 GHz frequency grid (19 × 6.25 GHz apart). This ensures that all lines of the two generated OFCs also appear on the same grid. The resulting OFCs are combined using a 50:50 optical coupler and temperature tuned to ensure a partial overlap between them. It is observed that the overlap of 3-4 comb lines is necessary for a strong phase transfer and an optimum spectral flatness of the expanded OFC.
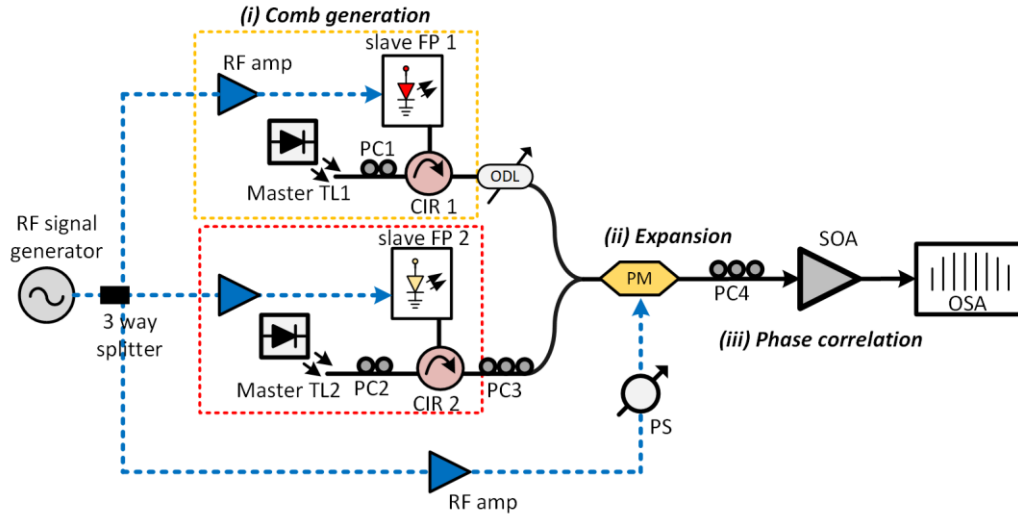
Figure 3.14 Experimental setup of the wavelength-tunable gain-switched comb expansion and phase correlation technique. Here, the dotted lines and solid lines represent the RF and optical paths, respectively. TL: tunable laser PC: polarisation controller, CIR: circulator, FP: Fabry Pérot, SOA: semiconductor optical amplifier, ODL: optical delay line, PS: phase shifter, OSA: optical spectrum analyser.

The combined OFCs are passed through a PM to increase the number of comb lines. The insertion loss of the modulator is around 2 dB and the V_π is ~4 V at 6.25 GHz. The PM is driven by the same sinusoidal signal (1 of the 3 splits) used for gain-switching. The amplitude of the sinewave is 12.5 V, which corresponds to $3.125 \times V_\pi$. The OFC expansion and flatness are optimised by aligning the gain-switched optical signal (employing an ODL) with the RF drive modulation signal (using a phase shifter). It is important to note that better expansion can be achieved by driving the PM at multiples of the gain-switching frequency, as discussed in Section 3.2. The output signal of the PM, with an average optical power of 4.5 dBm, is injected into an SOA. The SOA when DC biased at 200 mA portrays a gain of 14 dB. As the maximum output power of the SOA is 14.5 dBm, the amplifier operates in deep saturation. The injected comb lines undergo FWM resulting in the generation of new spectral components at frequencies corresponding to multiples of the FSR. The interaction of the comb lines through CDM introduces a phase correlation between all the comb tones. To enhance the FWM efficiency, the state of polarisation at the input of the SOA is optimised using a polarisation controller (PC4). The SOA output is tapped using a 90:10 coupler, with 90% of the optical signal sent to an RF beat tone

linewidth measurement setup (to verify the phase correlation between comb lines) and 10% recorded by a high resolution (20 MHz) OSA.

3.3.2 Experimental results and discussion

In this section, the experimental demonstration of OFC expansion, using the PM and the SOA, is presented. Firstly, two independent EI-GSL OFCs are generated, combined and the initial expansion performed using a PM. Next, the OFCs are injected into the SOA to further increase their bandwidth as well as to phase correlate all the lines. The degree of coherence between the OFC lines at each stage is examined with aid of an RF beat tone measurement. Finally, the wavelength tunability of the architecture is demonstrated by injection locking different longitudinal modes of the gain-switched FP lasers.

3.3.2.1 EI-GSL OFC generation and expansion

The optical spectra of the free running and injection-locked FP1 and FP2 are shown in are Figure 3.15 (a) and (b), respectively. The spacing of the longitudinal modes of FP1 and 2 are 1.4 nm and 1.7 nm, respectively. It can be seen that the external injection enables single-mode operation of the FPs, with a side-mode-suppression ratio (SMSR) > 60 dB. The spectra of the two OFCs generated by gain switching the externally injected FPs are shown in Figure 3.15 (c). The OFCs consist of 13 and 14 highly coherent lines (within a 3 dB window relative to the spectral peak) and exhibit an OCNR > 50 dB. The spectra of the combined OFCs, before and after the expansion using the PM, are shown in Figure 3.15 (d) and (e), respectively. The use of the PM increases the number of generated lines from 25 to 42, while maintaining the high OCNR (>50 dB). Inducing phase correlation between the comb lines is achieved by passing the combined and expanded OFCs through the SOA. The resultant spectrum, shown in Figure 3.15 (f), clearly shows the effect of FWM, resulting in further comb expansion over 262.5 GHz. The reduction of spectral flatness visible in the spectrum could be attributed to the SOA gain response and FWM efficiency. It is worth noting that the spectral flatness could be enhanced by optimising the entire chain (PM and SOA) rather than focusing on the output of the PM, as was done in this experiment. Improved OFC spectral flatness could also be achieved by changing the order of the devices (SOA followed by the PM).
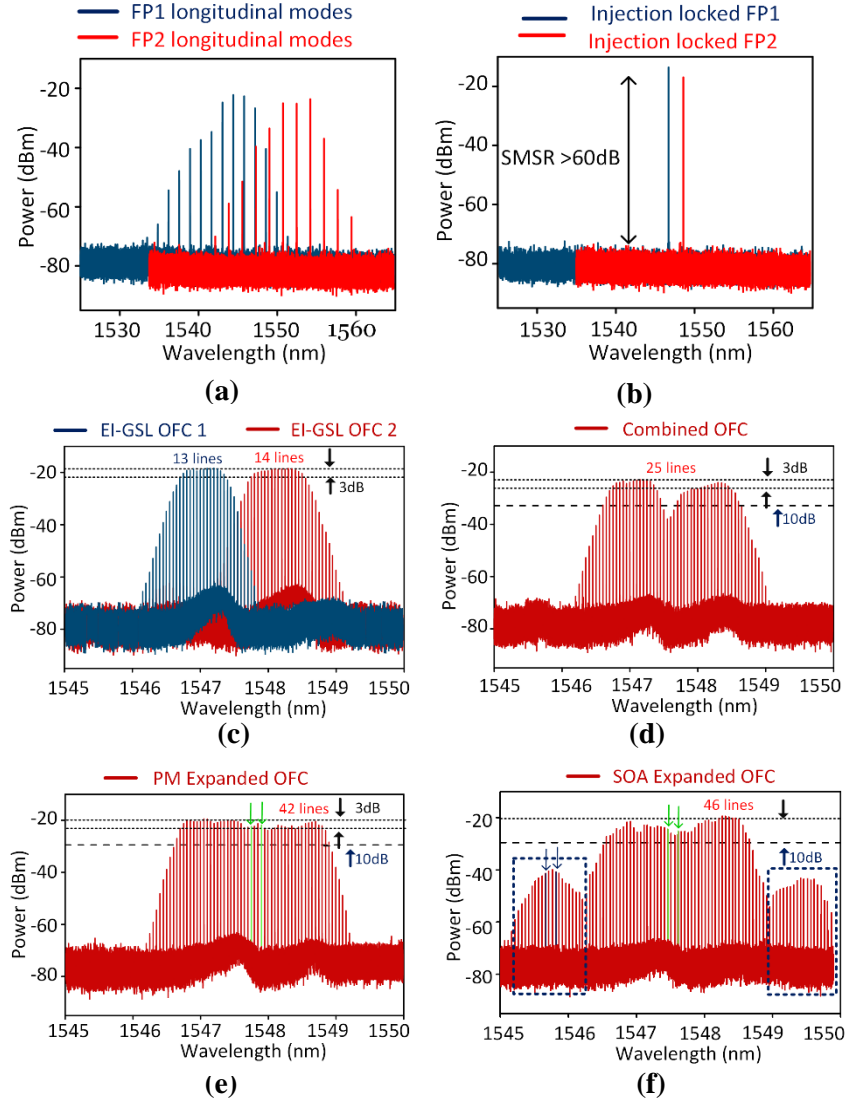
Figure 3.15 Optical spectra of (a) free running FP1 (blue) and FP2 (red), (b) externally injected FP lasers depicting single mode operation (c) individual EI-GSL OFCs showing the overlap between the combs, (d) combined EI-GSL OFCs, (e) PM output, (f) SOA output. Pairs of comb lines used for the RF beat tone measurements are marked by the green and blue arrows. OSA resolution: 20 MHz.

3.3.2.2 *Phase correlation*

The phase correlation between the comb lines is characterised using a heterodyne setup, as shown in Figure 3.10. At first, the comb lines from individual OFCs/EI-GSL stages are heterodyned on the PD and their beat tone linewidths are measured as 14 Hz (the ESA resolution set to 10 Hz), as plotted in Figure 3.16 (a). This value of a beat linewidth

indicates that there is an excellent phase correlation between the comb lines. Next, two lines from the expanded OFC (output of the PM), each originating from a different input comb, are chosen (marked by green lines in Figure 3.15 (c)). In this case, the 3 dB linewidth of the RF beat tone is measured to be ~1.1 MHz, as shown in Figure 3.16 (b). This result is a clear indication that the phase noise of the two OFCs is uncorrelated. Subsequently, by adjusting the bandwidth of the OBPF, a pair of comb lines with a frequency separation between 6.25 GHz and 37.5 GHz (the upper limit set by the ESA bandwidth) are filtered and their 3 dB beat tone linewidths are measured. The results are shown in Figure 3.16 (c) (black squares, kHz scale).
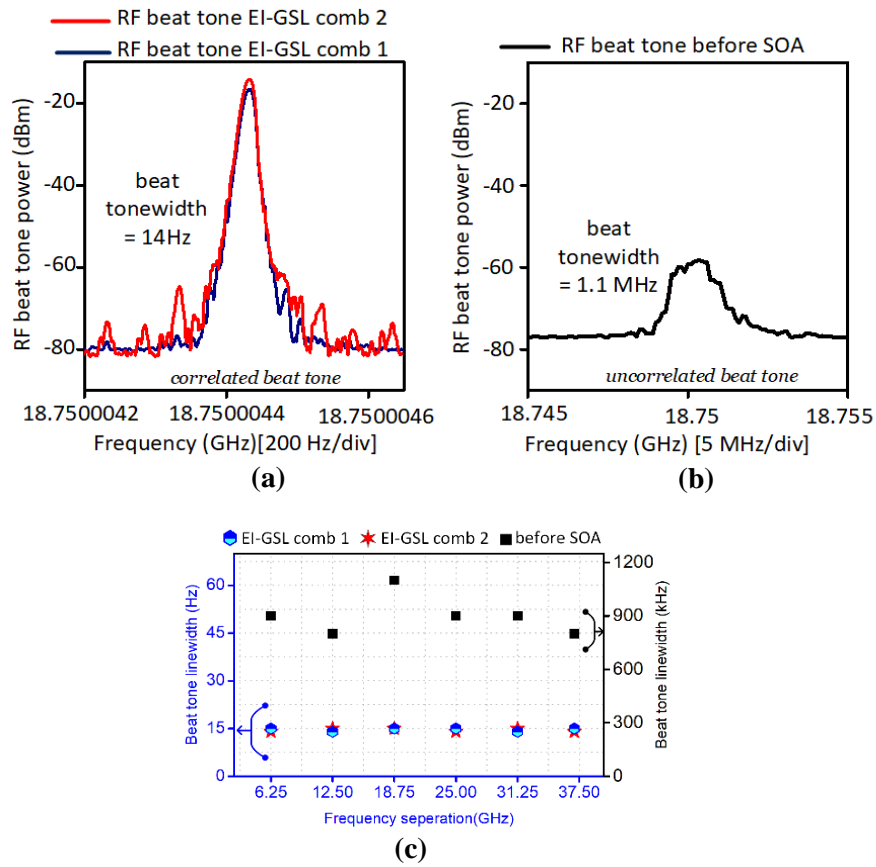
Figure 3.16 Electrical spectra of RF beat tone of (a) EI-GSL OFC 1 and OFC 2, (b) PM expanded OFC (uncorrelated), and (c) 3 dB linewidths of RF beat tones for different frequency separation: EI- GSL OFC 1 (blue), EI-GSL OFC 2 (red), in Hz scale and PM output (black square) in kHz scale.

Finally, to validate the phase correlation induced by the FWM, the RF beat tone linewidth measurement is repeated on the output signal of the SOA. For this test, comb lines from the wings of the spectrum (denoted by the dotted rectangle in Figure 3.15 (f)) that were generated by the SOA, are selected. This is to ensure that the measurement is carried out on lines originating from different combs. These spectral components arise from the FWM of the two independent OFCs in the SOA. Verification of the latter was achieved by passing one OFC at a time through the SOA. The resultant spectra (blue and red combs) are recorded and shown in Figure 3.17 (a) and (b). From the figures, it can be seen that the aforementioned wings are only present if both OFCs are passing through the SOA.
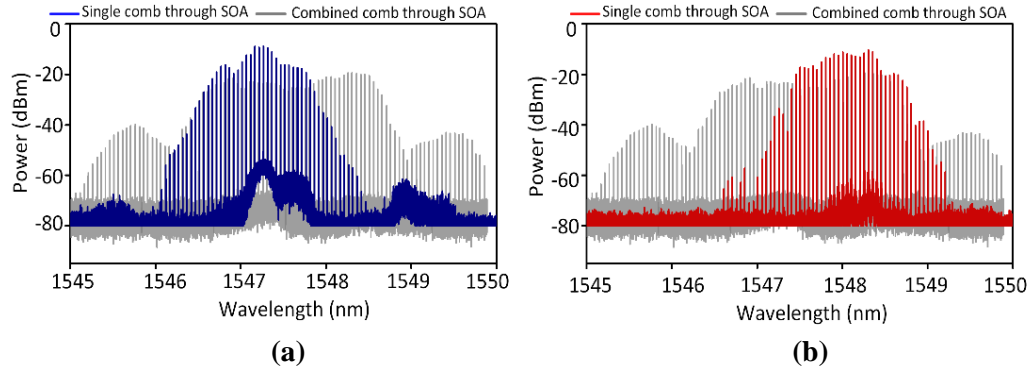
Figure 3.17 Optical spectra of the SOA output of the individual expanded OFCs: (a) OFC1 (blue) and (b) OFC2 (red). The combined expanded SOA output (grey, Figure 3.15 (f)) is superimposed for comparison.

The 3 dB RF beat tone linewidth of the FWM generated lines is measured to be ~24 Hz, as seen in Figure 3.18 (a) and (b) (neon trace). Comparing the spectra measured before (black) and after the SOA (green) in Figure 3.18 (a), reveals a significant reduction in the beat tone linewidth from 1.1 MHz to 24 Hz, due to the phase correlation induced by SOA. This value is comparable with the RF linewidth of an individual EI-GSL stage (OFC) beat tone, as illustrated in Figure 3.18 (b). The small difference in the values (24 Hz vs. 14 Hz) can be attributed to the FWM efficiency. Furthermore, the beat tones linewidths of comb lines, separated by frequencies between 6.25 GHz and 37.5 GHz, are measured and the results are plotted in Figure 3.18 (c) (green circles). The results prove that the FWM induces a phase correlation between all the comb lines.
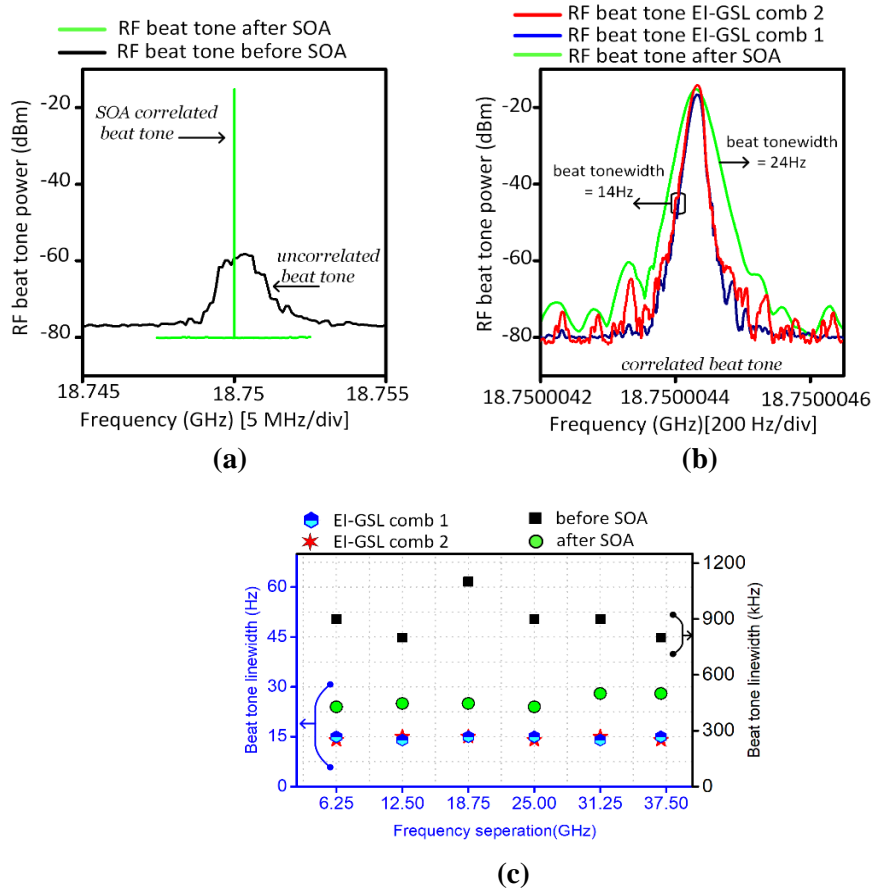
Figure 3.18 (a) Electrical spectra for RF beat tone of two comb lines: uncorrelated (SOA input, black trace), correlated (SOA output, green trace), (b) overlap of the RF beat tone of the individual input OFCs and the expanded + phase correlated OFC at the SOA output. (c) 3 dB linewidths of RF beat tones for different frequency separation: OFC 1 (blue), OFC 2 (red), SOA output (neon green) in Hz scale and PM output (black) in kHz scale.

3.3.2.3 *Central emission wavelength tunability*

The proposed comb expansion and correlation technique also offers wavelength tunability, which can be achieved by injecting light from the master laser into different longitudinal modes of each of the gain-switched slave (FP) lasers, to generate combs at different wavelengths. To demonstrate this, two additional operating points were tested. Figure 3.19 (a) shows the comb spectra, at different stages of the set-up, when the expanded comb is centred at 1560 nm, while plots Figure 3.19 (b) illustrate the spectra of the comb centred around 1530 nm. The smaller number of lines in OFC 1 and 2 at 1530, could be attributed to the gain profiles of the slave FP lasers at particular bias and

temperature conditions used. The increase in the total number of lines, due to the use of the PM, is evident: from 29 to 43 lines at 1560 nm and from 19 to 30 lines at 1531 nm. Passing these combs through the SOA results in further spectral growth but degrades the overall spectral flatness. A summary of the comb expansion across the C-band is reported in Table 3-5. Finally, the proposed scheme can be easily scaled by adding more input EI-GSL OFCs/stages in parallel. It is worth mentioning that the FSR of the proposed scheme can be tuned either by frequency division/comb densification via PM or by changing the gain-switching frequency.
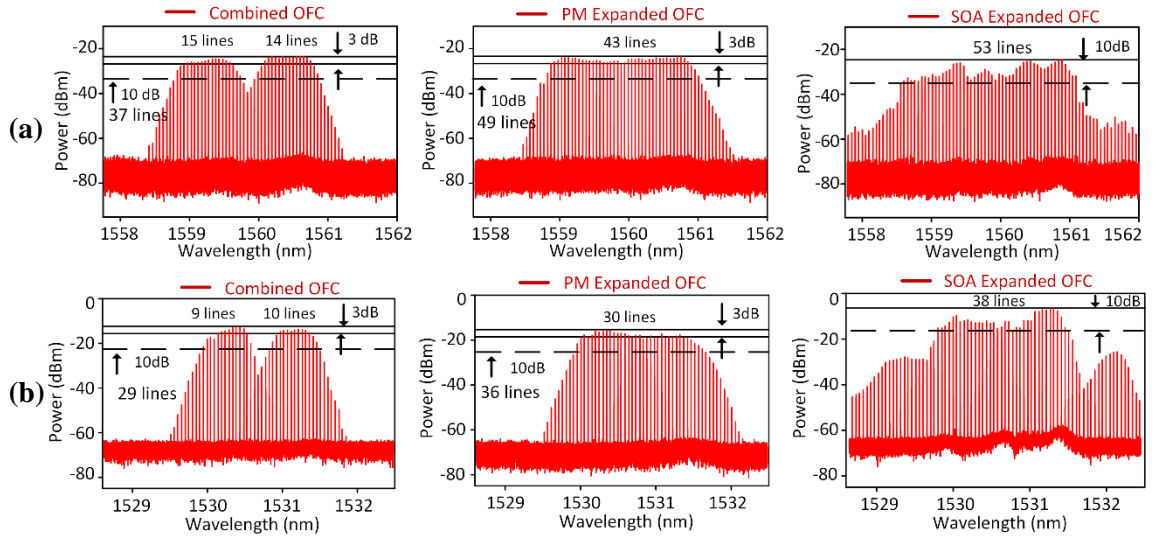
Figure 3.19 Optical spectra demonstrating wavelength tunability of the proposed configuration: (a) at 1560 nm, (b) 1530 nm.

Hence, the proposed comb expansion and phase correlation scheme can generate a broadband OFC spanning over 260 GHz bandwidth (within 10 dB from spectral peak) and offers a high degree of FSR and emission wavelength tunability (C-band). The expansion architecture can be easily scaled by stacking more OFCs in parallel according to the requirement. Furthermore, the primary aim of using the SOA is to induce the phase correlation between the OFCs, however it also results in the amplification of the OFC output power (to ~14.5 dBm), thus, addressing the issue of low OFC comb line power. However, the broadband OFC is not flat and requires optimisation. As previously mentioned, the spectral flatness could be improved by changing the order of the

components (SOA followed by PM). In addition, higher input power to the SOA could enhance the FWM process (higher saturation of the SOA), at the expense however of the total output power of the OFC.

Table 3-5 A summary of comb expansion across C-band

Comb line	1530 nm		1547 nm		1560 nm	
	No. of lines	*Exp. factor*	*No. of lines*	*Exp. factor*	*No. of lines*	*Exp. factor*
Individual EI-GSL OFC (within 3 dB)	10	--	14	--	14	--
After PM (within 3 dB)	30	~3	42	~3	43	~3
After SOA (within 10 dB)	38	~3.8	46	~3.3	53	~3.7

3.4 Conclusions

In this chapter, two novel reconfigurable EI-GSL OFC expansion schemes have been proposed and experimentally investigated. The first architecture generates highly flexible broadband OFC via mutual injection-locked GSLs. Experimental results demonstrate that by incorporating a phase modulator with a MIL-GS OFC, the comb lines can be further expanded, by more than 3 times, while achieving an OCNR > 40 dB. In addition, via comb densification, the FSR can be rapidly tuned from 6.25 GHz to 390.625 MHz. The detailed comb line characterisation reported highlights the excellent spectral purity (narrow linewidth, low RIN, and a high degree of phase correlation) of the OFC lines. The proposed scheme addresses one of the main shortcomings of the EI-GSL technique, which is the limited number of comb lines (comb span) and provides a simple and effective technique to generate an OFC with a tunable (from MHz to GHz) channel spacing. However, this expansion architecture is limited in terms of scalability and emission wavelength tunability (can be achieved if FP is used as slave laser).

Hence, a second approach, entailing a wavelength-tunable comb expansion and phase correlation via FWM, is investigated. The performed experiments demonstrate the generation of broadband OFC consisting of 42 phase correlated lines with an FSR of 6.25 GHz and with an OCNR larger than 50 dB. More importantly, the output of the expanded

OFC is amplified with the usage of an SOA. The concept of inducing phase correlation between all the comb lines through FWM has been proven by measuring the RF beat tone linewidth. The results show a two-order of magnitude reduction in the beat tone linewidth (1.1 MHz to 24 Hz) and confirm the high degree of phase correlation achieved. Furthermore, this correlation is maintained for all measured beat tone frequencies (from 6.25 GHz to 37.5 GHz). The wavelength tunability of the scheme has also been demonstrated, by generating the extended OFC at wavelengths between 1529 – 1562 nm.

Finally, both proposed architectures can be photonically integrated, which would enable the realisation of a broadband OFC at reduced cost, and form factor. Such broadband and integrated EI-GSL OFC, enabling a simple and cost-efficient generation of tones with precisely controlled channel spacing, narrow linewidth and a high degree of phase correlation, would be an asset in the realisation of the next generation terabit networks employing high spectral density modulation formats.

3.5 References

[1]   R. Zhou, P. M. Anandarajah, M. D. G. Pascual, J. O'Carroll, R. Phelan, B. Kelly, and L. P. Barry, "Monolithically Integrated 2-Section Lasers for Injection Locked Gain Switched Comb Generation," in *Optical Fiber Communication Conference*, 2014, paper Th3A.3. DOI: 10.1364/OFC.2014.Th3A.3

[2]   E. P. Martin, S. Chandran, A. Rosado, E. P. Soderholm, J. K. Alexander, F. H. Peters, A. A. Ruth, and P. M. Anandarajah, "Mutually Injection Locked Gain Switched Optical Frequency Combs for Dual Comb Spectroscopy of H2S," in Conference on Lasers and Electro-Optics, OSA Technical Digest (Optica Publishing Group, 2020), paper AM4K.2

[3]   K. Hei, K. Anandarajah, E. P. Martin, G. Shi, P. M. Anandarajah, and N. Bhattacharya, "Absolute distance measurement with a gain-switched dual optical frequency comb," Optics Express, vol. 29, no. 6, pp. 8108–8116, 2021, DOI: 10.1364/OE.413478.

[4]   A. Rosado, A. Pérez-Serrano, J. M. G. Tijero, Á. Valle, L. Pesquera, and I. Esquivias, "Enhanced optical frequency comb generation by pulsed gain-switching of optically injected semiconductor lasers*," Optics Express*, vol. 27, no. 6, pp. 9155, 2019, DOI: 10.1364/oe.27.009155.

[5]   R. Zhou, S. Latkowski, J. O'Carroll, R. Phelan, L. P. Barry, and P. Anandarajah, "40nm wavelength tunable gain-switched optical comb source," *Optics Express,* vol. 19, no. 26, pp. B415–B420, 2011, DOI: 10.1364/OE.19.00B415.

[6]   E. Prior, C. de Dios, A. R. Criado, M. Ortsiefer, P. Meissner, and P. Acedo, "Expansion of VCSEL-based optical frequency combs in the sub-THz span: Comparison of non-linear techniques," *Journal of Lightwave Technology*, vol. 34, no. 17, pp. 4135–4142, 2016, DOI: 10.1109/JLT.2016.2594129.

[7]   P. M. Anandarajah, R. Maher, Y. Q. Xu, S. Latkowski, J. O'Carroll, S. G. Murdoch, R. Phelan, J. O'Gorman, and L. P. Barry, "Generation of Coherent Multicarrier Signals by Gain Switching of Discrete Mode Lasers," *IEEE Photonics Journal*, vol. 3, no. 1, pp. 112–122, 2011, DOI: 10.1109/JPHOT.2011.2105861.

[8]   M. D. G. Pascual, R. Zhou, F. Smyth, T. Shao, P. M. Anandarajah, and L. Barry, "Dual mode injection locking of a Fabry-Pérot laser for tunable broadband gain switched comb generation," in *2015 European Conference on Optical Communication (ECOC)*, 2015, pp. 1–3. DOI: 10.1109/ECOC.2015.7341716.

[9]   M. D. G. Pascual, P. M. Anandarajah, R. Zhou, F. Smyth, S. Latkowski, and L. P. Barry, "Cascaded Fabry-Pérot lasers for coherent expansion of wavelength tunable gain switched comb," in *2014 The European Conference on Optical Communication* (ECOC), 2014, pp. 1–3. DOI: 10.1109/ECOC.2014.6964019.

[10] A. Delmade, M. Krstić, C. Browning, J. Crnjanski, D. Gvozdić, and L. Barry, "Power efficient optical frequency comb generation using laser gain switching and dual-drive

Mach-Zehnder modulator," *Optics Express,* vol. 27, no. 17, p. 24135, 2019, DOI: 10.1364/oe.27.024135.

[11] W.-Y. Yang, G. -Q. Xia, Z. -F. Jiang, T. Deng, X. -D. Lin, Y. -H. Jin, Z. -Z. Xiao, D. -Z. Yue, C. -X. Hu, B. Cui, M. Dai, and Z. -M. Wu, "Experimental Investigation on Wideband Optical Frequency Comb Generation Based on a Gain-Switched 1550 nm Multi-Transverse Mode Vertical-Cavity Surface-Emitting Laser Subject to Dual Optical Injection," *IEEE Access*, vol. 8, pp. 170203–170210, 2020, DOI: 10.1109/ACCESS.2020.3023965.

[12] M. D. G. Pascual, R. Zhou, F. Smyth, T. Shao, P. M. Anandarajah, and L. Barry, "Dual mode injection locking of a Fabry-Pérot laser for tunable broadband gain switched comb generation*," European Conference on Optical Communication, ECOC*, vol. 2015, pp. 1–3, 2015, DOI: 10.1109/ECOC.2015.7341716.

[13] E. Prior, C. de Dios, Á. R. Criado, M. Ortsiefer, P. Meissner, and P. Acedo, "Expansion of VCSEL-Based Optical Frequency Combs in the Sub-THz Span: Comparison of Non-Linear Techniques," *Journal of Lightwave* Technology, vol. 34, no. 17, pp. 4135–4142, 2016, DOI: 10.1109/JLT.2016.2594129.

[14] L. P. Barry, C. Herbert, D. Jones, A. Kaszubowska-Anandarajah, B. Kelly, J. O'Carroll, R. Phelan, P. Anandarajah, K. Shi, and J. O'Gorman, "Discrete mode lasers for communications applications," in *Proc. SPIE 7230, Novel In-Plane Semiconductor Lasers VIII*, pp. 72300N 2009, DOI:10.1117/12.810811

[15] Eblana Photonics, "Discrete Mode Laser Diodes with ultra narrow linewidth," *white paper*, 2007. [Online]. Available: https://eblanaphotonics.com/technology/ (accessed Sep. 05, 2019).

[16] S. P. Ó. Dúill, R. Zhou, P. M. Anandarajah, and L. P. Barry, "Analytical Approach to Assess the Impact of Pulse-to-Pulse Phase Coherence of Optical Frequency Combs," *IEEE Journal of Quantum Electronics*, vol. 51, no. 11, 2015, DOI: 10.1109/JQE.2015.2485228.

[17] P. M. Anandarajah, S. P. Ó Dúill, R. Zhou, and L. P. Barry, "Enhanced Optical Comb Generation by Gain-Switching a Single-Mode Semiconductor Laser Close to its Relaxation Oscillation Frequency," *IEEE Journal of Selected Topics in Quantum Electronics*, vol. 21, no. 6, pp. 592–600, 2015, DOI: 10.1109/JSTQE.2015.2456751.

[18] A. Murakami, K. Kawashima, and K. Atsuki, "Cavity Resonance Shift and Bandwidth Enhancement in Semiconductor Lasers with Strong Light Injection," *IEEE Journal of Quantum Electronics*, vol. 39, no. 11, pp. 1504, 2003, DOI: 10.1109/JQE.2003.820130.

[19] E. K. Lau, L. J. Wong, and M. C. Wu, "Enhanced Modulation Characteristics of Optical Injection-Locked Lasers: A Tutorial," *IEEE Journal of Selected Topics in Quantum Electronics*, vol. 15, no. 3, pp. 618–633, 2009, DOI: 10.1109/JSTQE.2009.2014779.

[20] R. Zhou, T. N. Huynh, V. Vujicic, P. M. Anandarajah, and L. P. Barry, "Phase noise analysis of injected gain switched comb source for coherent communications," *Optics Express*, vol. 22, no. 7, pp. 8120, 2014, DOI: 10.1364/oe.22.008120.

[21] R. Pillai, E. Garmire, and P. Menendez-Valdes, "Relative intensity noise of laser-diode arrays," *IEEE Photonics Technology Letters*, vol. 3, no. 11, pp. 968–970, 1991, DOI: 10.1109/68.97829.

[22] Z. Zan, M. Premaratne, and A. J. Lowery, "Laser RIN and linewidth requirements for direct detection optical OFDM," in *2008 Conference on Lasers and Electro-Optics and 2008 Conference on Quantum Electronics and Laser Science*, 2008, pp. 1–2. DOI: 10.1109/CLEO.2008.4551895.

[23] IEEE, IEEE Std 802.3cnTM-2019, IEEE Standard for EthernetAmendment 4: Physical Layers and Management Parameters for 50 Gb/s, 200 Gb/s, and 400 Gb/s Operation over Single-Mode Fiber, 2019. [Online]. Available: https://www.ieee802.org/3/cn/

[24] Eagleyard Photonics, "Relative Intensity Noise of Distributed Feedback Laser," *Application Note*, 2013. [Online]. Available: http://www.eagleyard.com/fileadmin/downloads/app_notes/App_Note_RIN_1-5.pdf. (accessed Jun. 1, 2019).

[25] P. D. Lakshmijayasimha, A. Kaszubowska-Anandarajah, E. P. Martin, M. N. Hammad, P. Landais, and P. M. Anandarajah, "Characterization of a multifunctional active demultiplexer for optical frequency combs," *Optics and Laser Technology*, vol. 134, pp. 106637, 2021, DOI: https://doi.org/10.1016/j.optlastec.2020.106637.

[26] K. Kikuchi and K. Igarashi, "Characterization of semiconductor-laser phase noise with digital coherent receivers," *2011 Optical Fiber Communication Conference and Exposition and the National Fiber Optic Engineers Conference*, 2011, pp. 1-3.

[27] T. N. Huynh, F. Smyth, L. Nguyen, and L. Barry, "Effects of SGDBR laser phase noise on coherent communication systems," in *European Conference on Optical Communication (ECOC)*, 2012, paper P2.09.

[28] T. N. Huynh, F. Smyth, L. Nguyen, and L. P. Barry, "Effects of phase noise of monolithic tunable laser on coherent communication systems," *Optics Express*, vol. 20, no. 26, pp. B244–B249, 2012, DOI: 10.1364/OE.20.00B244.

[29] C. Henry, "Phase noise in semiconductor lasers," *Journal of Lightwave Technology*, vol. 4, no. 3, pp. 298–311, 1986, DOI: 10.1109/JLT.1986.1074721.

[30] T. Pfau, S. Hoffmann, and R. Noé, "Hardware-efficient coherent digital receiver concept with feedforward carrier recovery for M QAM constellations," *Journal of Lightwave Technology*, vol. 27, no. 8, pp. 989–999, 2009, DOI: 10.1109/JLT.2008.2010511.

[31] T. N. Huynh, L. Nguyen, and L. P. Barry, "Phase noise characterization of SGDBR lasers using phase modulation detection method with delayed self-heterodyne measurements," *Journal of Lightwave Technology*, vol. 31, no. 8, pp. 1300–1308, 2013, DOI: 10.1109/JLT.2013.2247564.

[32]   EXFO, "XTM-50 Tunable Filter with Adjustable bandwidth," *white paper,* 2015. [Online]. Available: https://www.exfo.com/umbraco/surface/file/download/?ni=17992&cn=en-US&pi=17993. (accessed Feb. 1, 2018).

[33]   L. A. Coldren, S. W. Corzine, *Dynamic Effects* in "Diode Lasers and Photonic Integrated circuits", pp. 247-333, 9780470484128, 2012, DOI: 10.1002/9781118148167.ch5

[34]   K. Kikuchi, "Characterization of semiconductor-laser phase noise and estimation of bit-error rate performance with low-speed offline digital coherent receivers," Optics Express, vol. 20, no. 5, pp. 5291–5302, 2012, DOI: 10.1364/OE.20.005291.

[35]   K. Kikuchi, "Effect of 1/f-type FM noise on semiconductor-laser linewidth residual in high-power limit," IEEE Journal of Quantum Electronics, vol. 25, no. 4, pp. 684–688, 1989, DOI: 10.1109/3.17331.

[36]   G. Qi, J. Yao, J. Seregelyi, S. Paquet, C. Bélisle, X. Zhang, K. Wu, and R. Kashyap, "Phase-Noise Analysis of Optically Generated Millimeter-Wave Signals With External Optical Modulation Techniques," *Journal of Lightwave Technology*, vol. 24, no. 12, pp. 4861–4875, 2006, DOI: 10.1109/JLT.2006.884990.

[37]   S. Diez, C. Schmidt, R. Ludwig, H.G. Weber, K. Obermann, S. Kindt, I. Koltchanov, and K. Petermann, "Four-wave mixing in semiconductor optical amplifiers for frequency conversion and fast optical switching," *IEEE Journal on Selected Topics in Quantum Electronics*, vol. 3, no. 5, pp. 1131–1144, 1997, DOI: 10.1109/2944.658587.

[38]   G. P. Agrawal, "Population pulsations and nondegenerate four-wave mixing in semiconductor lasers and amplifiers," *Journal of the Optical Society of America B,* vol. 5, no. 1, pp. 147–159, 1988, DOI: 10.1364/JOSAB.5.000147.

[39]   K. A. Shore and W. M. Yee, "Theory of self-locking FM operation in semiconductor lasers," *IEE proceedings. Part J, Optoelectronics*, vol. 138, no. 2. pp. 91–96, 1991. DOI: 10.1049/ip-j.1991.0016.

[40]   J. Renaudier, G. H. Duan, P. Landais, and P. Gallion, "Phase correlation and linewidth reduction of 40 GHz self-pulsation in distributed Bragg reflector semiconductor lasers," *IEEE Journal of Quantum Electronics*, vol. 43, no. 2, pp. 147–156, 2007, DOI: 10.1109/JQE.2006.886820.

4. Reconfigurable OFC Demultiplexers

The previous chapters exemplify the need for reconfigurable OFC-based multi-carrier transmitters and evaluated EI-GSL OFCs suitability for the next-generation optical networks. However, the demultiplexing of closely spaced OFC carriers (<12.5 GHz), prior to modulation, poses to be a major impediment in the commercial adoption of OFCs. Thus, this chapter investigates and evaluates two potential tunable demultiplexer solutions, that can be used in next-generation OFC-based communication systems. Initial investigations focus on the use of a micro-ring resonator (MRR) after which an active demultiplexer, based on optical injection locking (OIL) is examined. Both techniques offer a high degree of flexibility (wavelength and FSR), and can be photonically integrated with the OFC sources, which makes them attractive to be employed in commercial systems.

4.1 Introduction

Despite the many advantages that OFCs provide, their employability as transmitters is hindered by the complexity and technical challenges associated with the demultiplexing individual, closely spaced OFC lines (<12.5 GHz) prior to data modulation. An OFC-based WDM system architecture based on conventional demultiplexers is depicted in Figure 4.1 (a). It comprises an OFC followed by demultiplexers (Demux) based on an

arrayed waveguide grating (AWG) [1], or wavelength selective switch (WSS) [2]. However, these devices do not possess sufficient spectral bandwidth (BW) resolution to separate comb lines with FSRs <12.5 GHz. To demonstrate this limitation, two comb tones (from an OFC with 12.5 GHz FSR) are demultiplexed using a commercially available WSS (1 x 2, from Finisar; BW > 10 GHz) [2] and an AWG (from Kylia; BW > 12.5 GHz)[1]. Figure 4.2 (a) and (b) show the optical spectra of the output of the WSS and AWG (combined two channels), respectively. From the figure, it is evident that the WSS is only able to suppress adjacent tones by 10 dB, while the AWG provides a 25 dB attenuation of the undesired frequency components. Both of these values are insufficient and would result in a severe cross-channel interference between the adjacent channels. In addition, these filtering techniques introduce a high insertion loss (>5 dB) [3] that needs to be compensated using optical amplifiers. The latter, however degrades the optical signal-to-noise ratio (OSNR) and increases the cost and complexity of the system.
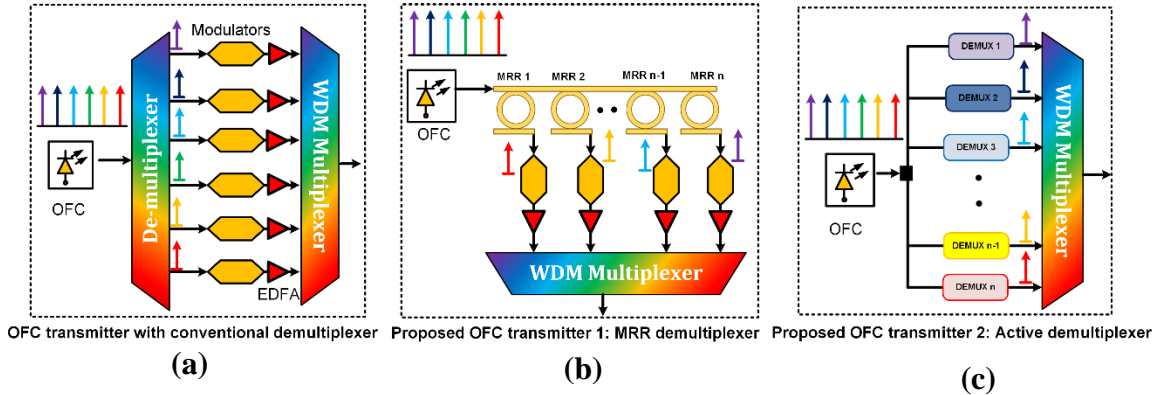
Figure 4.1 OFC-based transmitter architecture employing (a) conventional demultiplexer solutions, proposed transmitter with demultiplexer solutions: (b) MRR, (c) active demultiplexer. Here, EDFA: Erbium dope fibre amplifier, Demux: demultiplexer, MRR: microring resonators.

Furthermore, none of these techniques fulfil the necessary demultiplexing requirements for an OFC, which include small size, fine granularity, low cost, BW resolution and flexibility. Although AWG can be integrated, it operates at a fixed channel spacing and achieving channel spacing granularity below 25 GHz for such devices could be very challenging [4]. While WSSs can be expensive, bulky, and cannot be integrated along

with the transmitter. Therefore, the realisation of OFC based system operating at small/dense channel spacing of 6.25 or 12.5 GHz requires novel demultiplexing solutions.
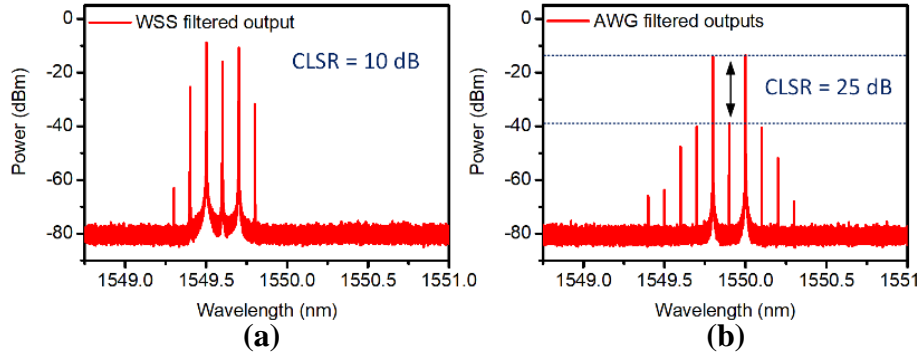
Figure 4.2 Comparison of commercially available demultiplexing solutions: optical spectra of demultiplexer output of 12.5 GHz OFC (a) WSS, (b) AWG. OSA resolution: 20 MHz.

This chapter aims to address the above-mentioned issue by investigating the two potential demultiplexing solutions such as the MRR and the active demultiplexer, as depicted in Figure 4.1 (b) and (c), respectively. A summary of recent research in the area of optical demultiplexing is given in Table 4-1.

Table 4-1 A brief survey of various OFC demultiplexer solutions. Here, IL: insertion loss, amp: optical amplifier required, OBPF: optical bandpass filter.

Ref.	Demultiplexer	Channel spacing resolution	IL/ Amp	Demonstration/ comments
[1]	AWG	>12.5 GHz	~8 dB / yes	8 channel, 12.5 GHz FSR from Kylia
[2]	WSS	15 GHz	~10 dB / yes	WSS demultiplexer from Finisar
[5]–[10]	MRR	40 GHz	--	Theoretical understanding; Box-like filter profile; Automated hitless tuning.
[11]	MRR	>20 dB	0.8 dB / No	8 channel MRR as add drop multiplexer & chip characterisation
This work	MRR	>20 GHz	0.8 dB / No	8 channel MRR, FPGA controlled static & dynamic MRR characterisation

[12]–[14]	Active Demux	250 MHz to 10 GHz	No	analytical simulation model, design & characterisation
[15]	Active Demux	20 GHz	Yes	1.2 Tb/s superchannel demonstration
[16]	Active Demux	6.25 GHz	No	OSNR robustness + DP 64- QAM
[17]–[19]	Active Demux	6.25, 10, 12.5 GHz	No	1 x 4 integrated demultiplexer; Nyquist WDM
[20]	Active Demux	12.5 GHz	No	MLL RIN reduction + PAM 4
[21]	Active Demux	6.25-25-50, 70-100 GHz	No	Asymmetric channel spacing
This work	Active Demux	390.625 MHz to 15 GHz	No	Detailed characterisation and multifunctionality demonstration

4.2   Microring Resonator as a Demultiplexer

The first demultiplexing solution entails the use of a Silicon photonics (SiP) microring resonator (MRR) as a reconfigurable demultiplexer. The MRR comprises a ring resonator coupled with two waveguides and allows the transmission (passing) or notching (dropping) of the transmitted signal based on the cavity resonance. It has been demonstrated in a diverse range of applications such as its use as wavelength-selective devices or optical filters [22], add-drop multiplexers [9], and high-speed modulators [11]. The increased interest in these devices stems from their low insertion loss, ultra-compact size, low power consumption, tunability, and CMOS compatible fabrication.

The microscopic image and the architecture of the MRR used in this work are shown in Figure 4.3 (a) and (b) respectively. It consists of eight deeply etched MRRs with a radius of 28 µm and a Q-factor varying from 6,800 to 11,100 [10]. This MRR chip is originally fabricated as an add-drop multiplexer by EpixFab, IMEC, and Integrated Photonics Laboratory, RWTH Aachen University [11]. However, in this proof-of-principle demonstration, it is used as an OFC demultiplexer. The optical spectra of the through port (upper arm) and drop port passband (R4) of the MRR is as shown in Figure 4.3 (c) and (d) respectively. The MRR has an FSR of 420 GHz and the 3 dB passband of the MRRs is around 20 GHz . The central wavelength of the passband of each of the eight rings can

be independently tuned using eight heating elements. The MRR features a low insertion loss around 0.7 dB and requires a small current of 7.6 mA to tune across the FSR.
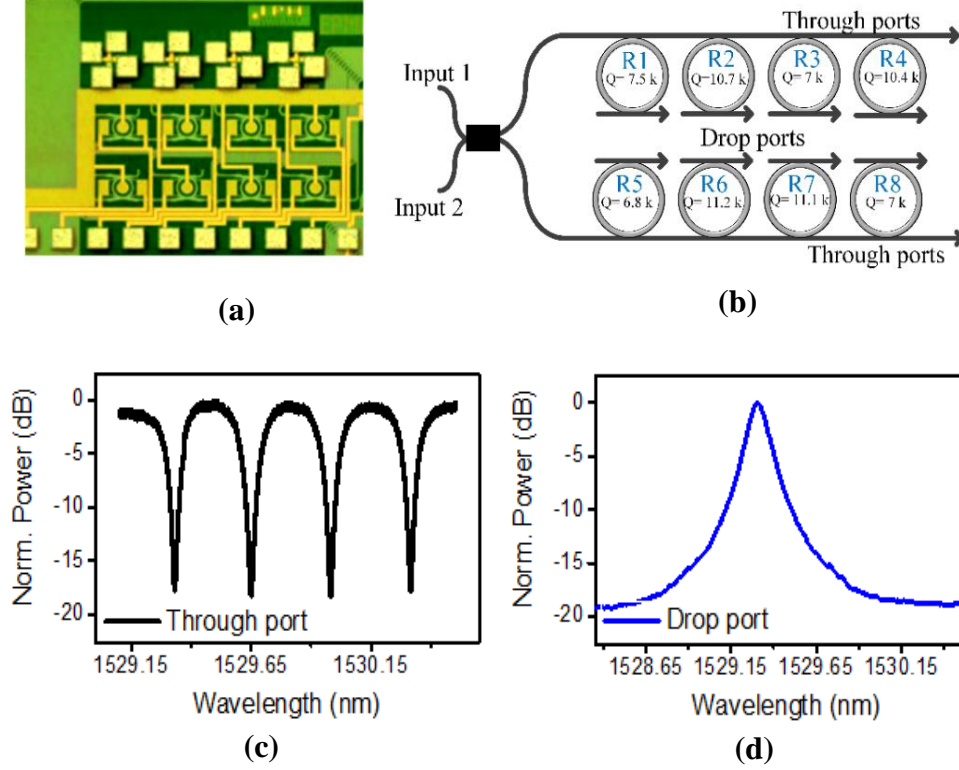
Figure 4.3 (a) Image (microscopic) of the 8 channel MRR demultiplexer chip [11], (b) schematic illustration of 8 MRRs configuration with different Q-factors, the optical spectrum of (c) through port output (d) drop port output of a single MRR.

In this chapter, the applicability of an 8 channel MRR as an OFC demultiplexer is examined. For this proof of principle experimental demonstration, a real-time FPGA programmed reconfigurable OFC-based transmitter employing MRR based demultiplexer is employed. The MRR is programmed to demultiplex different OFC lines and characterised for a scenario, where the OFC and MRR are simultaneously tuned mimicking a dynamically reconfigurable system. Finally, the MRR design challenges as well as the trade-offs between the complexity and the ability to meet the requirements of a reconfigurable demultiplexer are discussed.

4.2.1 FPGA controlled reconfigurable OFC transmitter employing an MRR based demultiplexer

As discussed in the previous chapters, to effectively scale the capacity of the optical network and cope with the dynamic traffic requirements, the optical network should evolve towards a responsive and reconfigurable optical network so as to dynamically direct capacity when and where it is needed. At the core of such a network lies a software-defined transmitter, a device allowing the operator to adjust transmission parameters according to the current requirements of the network. Hence, the FPGA-controlled real-time reconfigurable GSL OFC transmitter employing an MRR based demultiplexer is used to serve such a purpose.
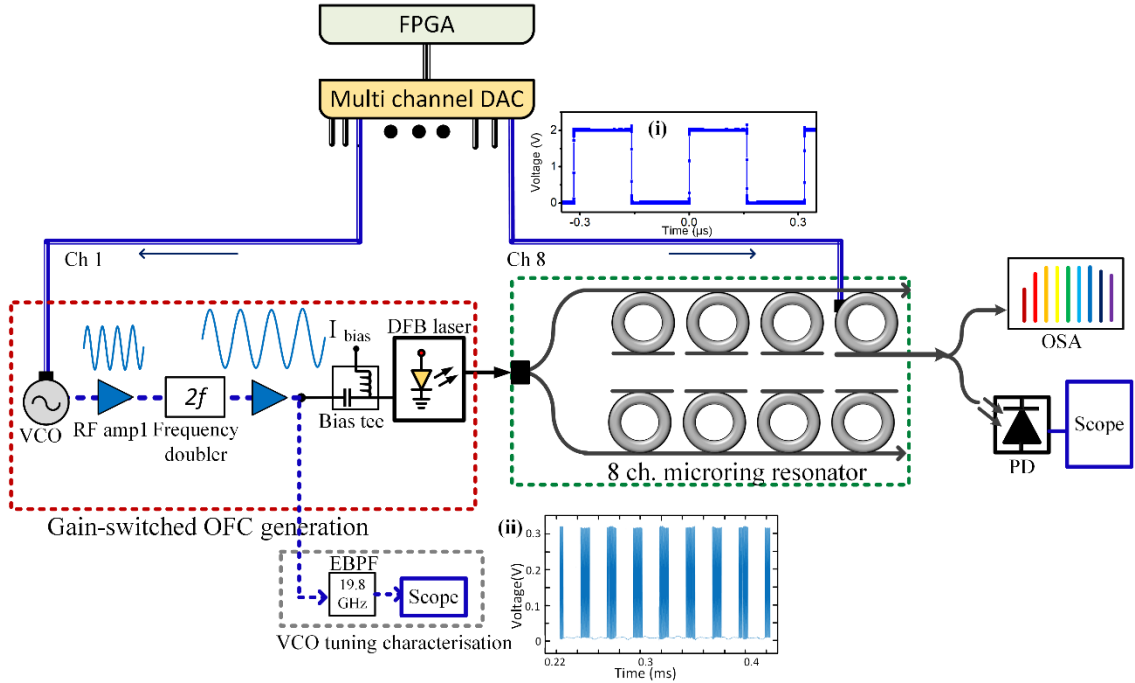
Figure 4.4 FPGA-controlled reconfigurable GSL transmitter employing an 8 channel MRR demultiplexer. Here, VCO: voltage-controlled oscillators, 2f: frequency doubler, PD: photodetector, OSA: optical spectrum analyser (300 MHz resolution). Insets: (i) DAC ch8 output, (ii) VCO characterisation: DAC ch1 after 2f output and grey block.

The experimental setup, shown in Figure 4.4 consists of two stages: (i) a reconfigurable OFC source and (ii) a demultiplexer stage. The GSL OFC includes a voltage-controlled oscillator (VCO), as a frequency synthesiser, an RF amplifier, frequency doubler (input

frequency range 9-18 GHz), and a DFB slave laser (threshold current $I_{th} = 13\ mA$). The software-controlled reconfigurable transmitter is then realised by employing an FPGA followed by a 16-channel digital-to-analog (DAC) converter, which can generate 16 different waveforms at a peak to peak voltage of 2 V$_{p-p.}$ These individual DAC channels could be used to control various OFC transmitter parameters, such as temperature and bias of the slave laser, the frequency of the RF synthesizer (thus FSR), thermal tuning of the MRR, etc.

Firstly, to demonstrate the reconfiguration of the GSL OFCs FSR, one of the DAC channels is employed to control the frequency of the VCO, which is toggled between two values. This is achieved by programming that DAC channel to generate a rectangular waveform and apply that signal voltage to the input of the VCO. The output of the VCO is then passed through a frequency doubler to obtain the final gain switching frequency (thus FSR of the OFC) of 24.9 GHz (blue) and 24.8 GHz (red), as shown in Figure 4.5 (a) and (b). It is important to mention that, in this demonstration, the OFC FSR is tuned by a small value (100 MHz), because the whole OFC drifts (as seen in Figure 4.5 (a) and (b)) due to a change in the amplitude of the VCO. However, this was sufficient to move the OFC out of the passband of the MRR. It is important to note that several distinct FSRs can be easily achieved by applying multi-level voltage signals (from the DAC) to the VCO.

To characterise the instantaneous change in the frequency generated by the VCO, the output of the frequency divider is sent through a 19.8 GHz electrical bandpass filter (EBPF), as depicted by the grey rectangle in Figure 4.4. The VCO tuning voltage is set to 4 to 4.5 V, which would result in a frequency change of ~ 5 GHz that is enough to go in and out of the passband of the EBPF. The resultant waveform is recorded as shown in inset (ii) of Figure 4.4. The 10% - 90% rise and fall tuning speed of the VCO is calculated as 148 ns and 130 ns respectively.
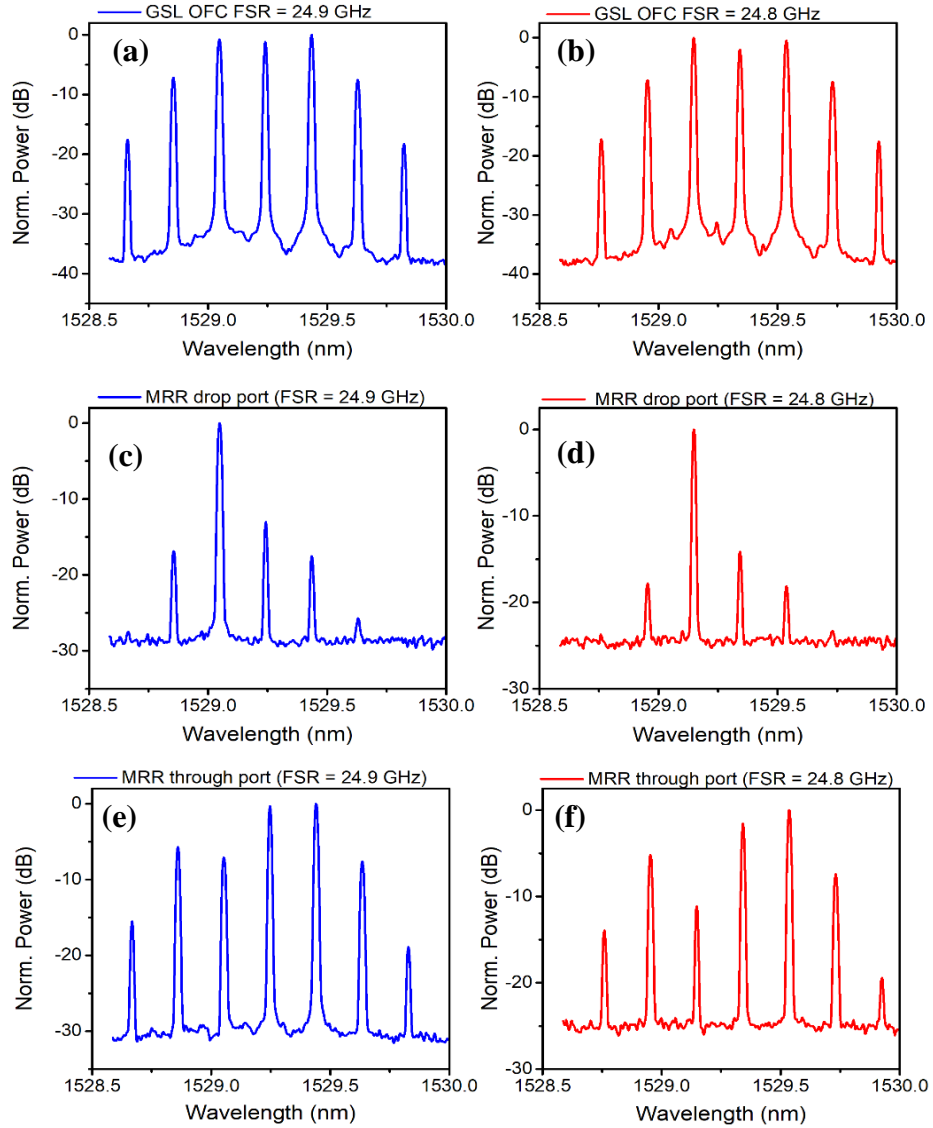
Figure 4.5 Optical spectra of the OFC with FSR (a) 24.9 GHz (blue), (b) 24.8 GHz (red), and their corresponding MRR drop/filtered ports output with a comb line suppression ratio of 15 dB in (c), (d), and through ports output in (e) and (f), respectively. OSA resolution: 300 MHz.

Next, the ability of the MRR to dynamically tune and demultiplex the desired OFC line is verified. To achieve that, another DAC channel is employed to tune the passband of the MRR. The chosen DAC channel is programmed to generate a square wave with a 3.2 μs period (as shown in the inset (i) of Figure 4.4) that is then applied to the heater of one of the rings to thermally tune its resonant frequency. The voltage levels of the signal are adjusted to ensure that the MRR passband follows the desired OFC line. The resultant

optical spectra of the MRR drop port output are shown in Figure 4.5 (c) and (d) and through port output in Figure 4.5 (e) and (f). These spectra show that the comb lines are demultiplexed with a CLSR of ~ 15 dB. The limited CLSR is attributed to the large passband of the MRR filter, as the device was not originally designed to serve as a OFC demultiplexer.

4.2.2 MRR reconfigurability
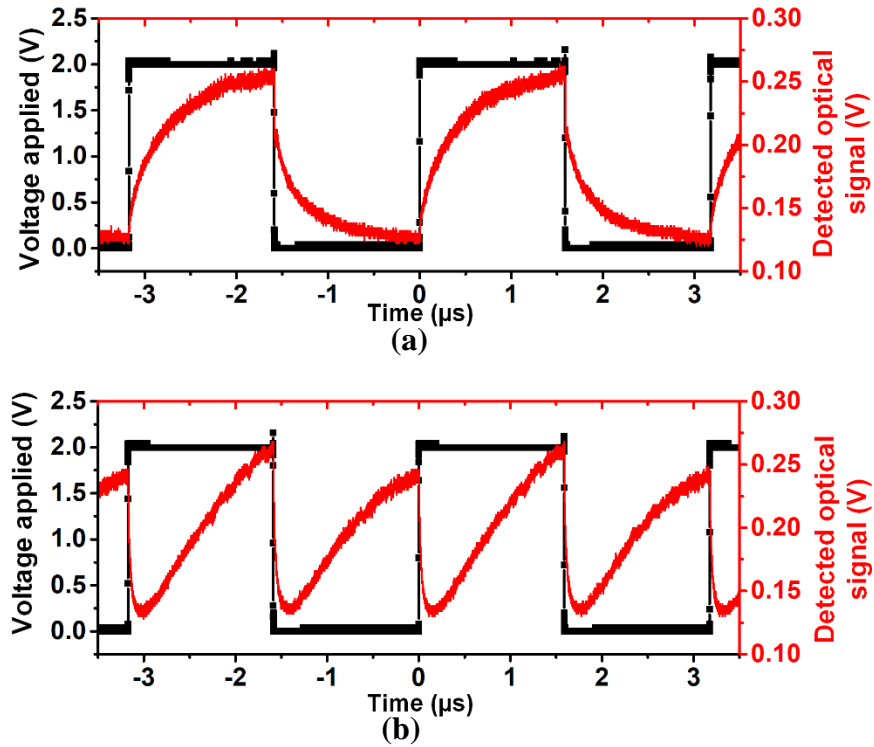
Figure 4.6 Reconfiguration characterisation: (a) where tuning voltage is applied to the MRR to demultiplex the comb lines (fixed FSR) and (b) where tuning voltages are applied to OFC and MRR.

Having proved the potential of the MRR to reconfigure its resonant frequency to demultiplex the OFC lines, the characterisation of the MRR tuning is then performed. Two tests were conducted, (i) tune the MRR with a fixed FSR to demultiplex the OFC lines and (ii) tune both the MRR and FSR of the OFC. For these tests, the output of the MRR is detected with the aid of a photodetector and recorded using a sampling oscilloscope. Figure 4.6 (a) represents the tuning of the MRR only, where the applied tuning voltage is shown in black and the detected optical signal in red. From the plot, it is

seen that the detected optical signal gradually increases and follows the applied voltage demonstrating the demultiplexing process. Also, it can be observed that tuning towards the longer wavelengths is faster than in the opposite direction. This is as expected since the former is achieved by heating (active) the MRR, while the latter requires cooling (passive), as the MRR is equipped with heaters and not temperature controllers.

Figure 4.6 (b) illustrates the scenario, where the FSR and MRR are tuned simultaneously. From the plot, it is evident that the change in the OFC FSR is faster than the tuning speed of the MRR. As a result, the comb line moves out of the MRR passband and the detected optical signal power drops rapidly. As the MRR continues to follow the change in the OFC FSR, the power increases before dropping again due to the next period in the tuning voltage (next change in FSR). This test demonstrates the potential suitability of the proposed transmitter system which can dynamically reconfigure the passband of the MRR to tune varying FSRs of an OFC.

4.2.3   MRR demultiplexer challenges

Although, MRR based demultiplexers are attractive due to their low insertion loss, ability to dynamically reconfigure and co-integrate with OFC, their deployment in a reconfigurable transmitter system could be challenging. Some of the major impediments are as follows.

(i) *Lorentzian shaped filter response:* An ideal OFC demultiplexer would exhibit a flat-top, narrow pass-band, with a steep roll-off and a high extinction ratio, to maximising the isolation between the comb lines. However, a single MRR has a Lorentzian-shape response, with a narrow peak and slow roll-off as seen in Figure 4.3 (d). The narrow peak means that there is a very limited range of wavelengths, for which the MRR exhibits the minimum insertion loss. As a result, a precise alignment between the filter and the OFC needs to be maintained, as any drift would result in a considerable drop in the power of the filtered signal. The slow roll-off reduces the selectivity/rejection of the filter, allowing adjacent wavelengths to leak into the pass-band. The steepness of the filter profile can be improved by increasing the Q factor of the resonator, as shown in Figure 4.7 (a). However, this would result in further

narrowing in the bandwidth of the filter. A more attractive solution to achieve a flat-top, steep roll-off filter profile is to use a cascade of several ring resonators [13], [29]. The cascade of 2, 3, 5 MRRs are simulated in VPI transmission maker to demonstrate flat-top filter response as shown in Figure 4.7 (b). Nevertheless, to maintain the required shape of the entire resonator, a precise control of the resonant frequency of each ring has to be performed.

(ii) *Limited tunability of the MRR bandwidth*: The pass or drop port bandwidth of a single MRR is fixed dictated by the Q-factor of the resonator cavity, as shown in Figure 4.7 (a), where the 3-dB bandwidth of the MRR is reduced from 38.5 GHz to 10 GHz by increasing the Q factor from 5,000 to 20,000. As mentioned before, such a high Q resonator would require very precise alignment between the MRR and the OFC line to avoid power loss.
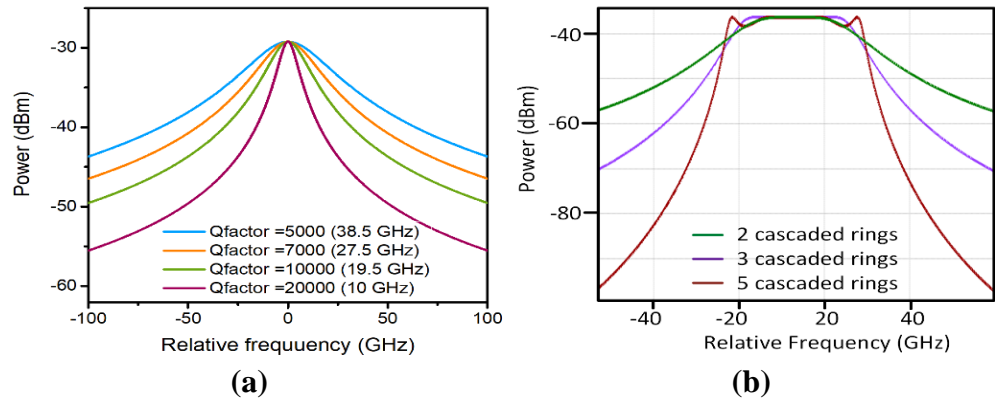
Figure 4.7 Simulation results showing the MRR frequency response as a function of (a) Q factor of a single ring and (b) number of cascaded rings.

(iii) *Slow tuning speed:* The tuning speed of the MRR can be slow limiting the overall transmitter reconfiguration time. However, tuning speeds could be improved by PN junction-based heaters, which are used in MRR based optical modulators at bitrates < 40 Gb/s [24].

Overall, the MRR is a potential OFC demultiplexer, benefiting from a low insertion loss, ability to tune, and its potential to be integrated with an OFC. The main challenge related to this technology relates to the shape of the filter, which can be addressed by employing a cascade of rings at a price of increased complexity.

4.3 Laser-Based Multifunctional Active Demultiplexers

The second solution entails the use of a laser-based active demultiplexer. It operates on the principle of optical injection locking of a semiconductor laser (acting as a demultiplexer), with the OFC line that is to be filtered [12]–[15]. An active demultiplexer enables the flexible selection of OFC lines whilst functioning as an ultra-low noise amplifier (no ASE noise added), a power equaliser, and a modulator, all in a single device. The schematic of such an active demultiplexer is shown in Figure 4.8. The demultiplexing process is achieved by injecting an OFC into an array of commercially available semiconductor lasers. The wavelength of each laser (Demux) is tuned via temperature and bias current, to match that of the desired comb tone. Consequently, the Demux is injection-locked by the tone (i.e., inherits its frequency and phase characteristics). The insets in Figure 4.8 show line graphs of the optical spectra of the OFC and the Demux before and after injection locking, demonstrating the demultiplexing process. Since the output power of the demultiplexer is much higher than that of the input tone, in addition to filtering, the selected line is also amplified. Some of the notable demonstrations include a photonically integrated 1×4 demultiplexer [18], asymmetric channel spaced WDM system [21], OSNR robustness [16], RIN reduction [26], and many more.
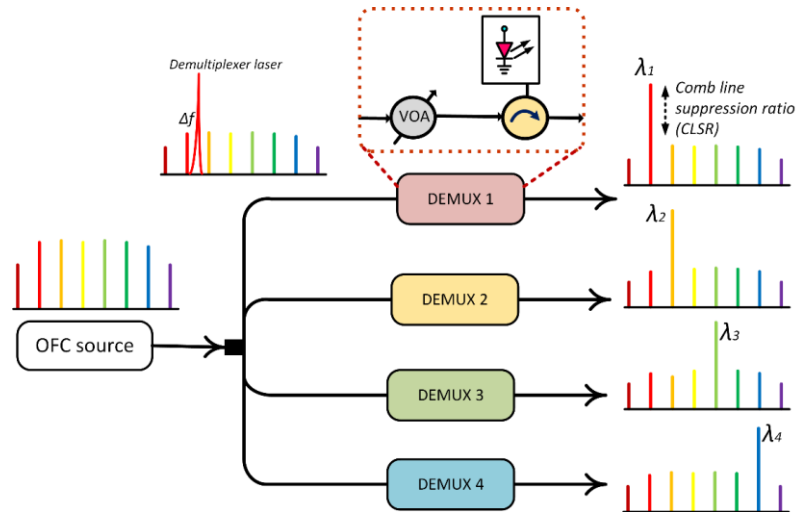
Figure 4.8 Experimental setup diagram of the semiconductor laser-based active demultiplexer (Demux). Inset: line graph illustrating the principle of operation. Here Δf: detuning frequency, VOA: variable optical attenuator.

In this work, the experimental demonstration of active demultiplexing of OFC lines is presented. This is followed by the investigation of the impact of OFC injection locking parameters, such as comb line power (CLP) and the detuning frequency (Δf), on the performance of the demultiplexer. Subsequently, the demultiplexer is characterised in terms of phase noise, RIN, and short-term beat tone stability (power, frequency, RF tonewidth) of the demultiplexed OFC lines, as these parameters dictate the overall system performance that can be achieved. Furthermore, the multi-functional operation of the active demultiplexer is examined, including the FSR tunability, ultra-low noise amplification, power equalisation, and the possibility to achieve electro-optical conversion (modulation).

4.3.1   Active demultiplexing of the OFC

The experimental setup comprises the OFC followed by an active demultiplexer (depicted in the rectangle) as shown in Figure 4.8. The realisation of an active demultiplexer using discrete components would require a variable optical attenuator (VOA), a 3-port circulator and a semiconductor laser. It is important to mention that the proposed demultiplexer technique can be used with any type of OFC [16], [18], [20], [25]. In this work, an EI-GSL OFC is chosen due to its simplicity and FSR tunability [26]–[28]. A 6.25 GHz EI-GSL OFC, consisting of 8 comb lines (within 3 dB from the spectral peak) and portraying an OCNR > 50 dB (20 MHz OSA resolution), shown in Figure 4.9 (a), is used. A commercially available DFB laser is chosen as a demultiplexer 1 (Demux 1). It exhibits a threshold current (I_{th}) of 12.5 mA and is biased at 50 mA to emit an average output power of 7.5 dBm. The optical spectrum of a free-running (DC bias with no optical injection) demultiplexer is shown in Figure 4.9 (c). The generated OFC is injected into the demultiplexer via a VOA and a circulator. The VOA is used to adjust the injected CLP. Here, the CLP is to set −32 dBm (see Figure 4.9 (b)), which is sufficient to achieve the injection locking of the demultiplexer. The output spectrum of the Demux, shown in Figure 4.9 (d), consists of the filtered line as well as the undesired comb tones. The power difference between the demultiplexed and the highest undesired tone termed as the comb line suppression ratio (CLSR), is 35 dB.
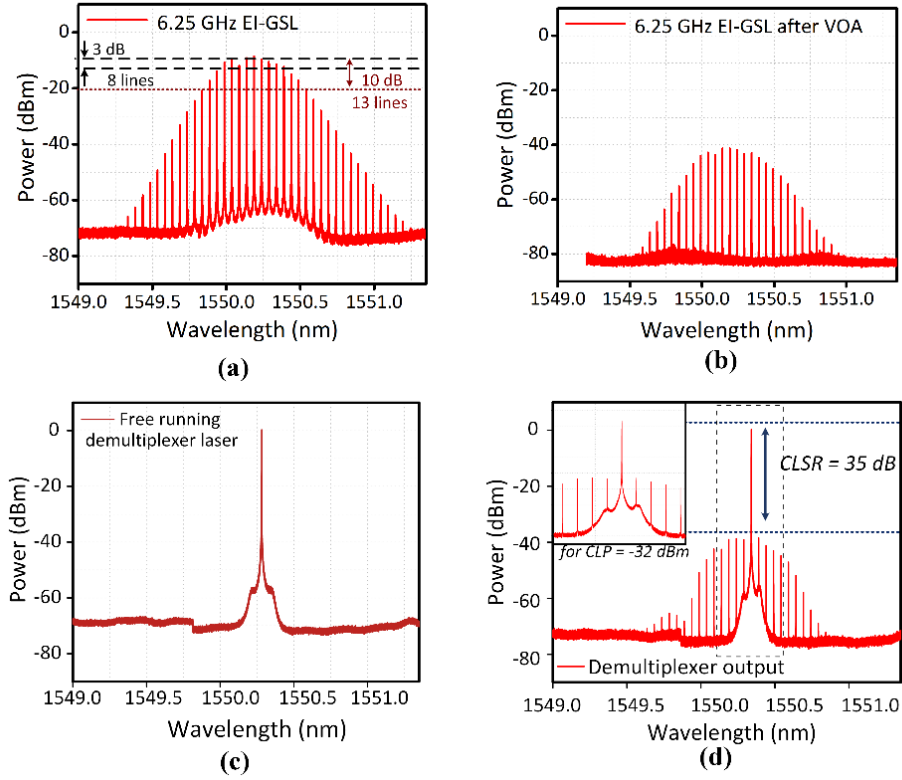
Figure 4.9 Optical spectra of (a) EI-GSL OFC with an FSR of 6.25 GHz, (b) OFC after VOA, (c) free-running demultiplexer laser (DFB), (d) injection-locked demultiplexer, the zoomed version of the dotted region is shown as the inset. OSA resolution: 20 MHz. Fixed optical attenuator on OSA: 10 dB.

4.3.1.1   CLSR dependency on CLP

The CLSR is one of the most important performance metrics of the demultiplexer. Thus a thorough investigation is carried to investigate the dependence of the CLSR on the injected CLP. To this effect, the CLP is varied from -32 to -10 dBm, with the aid of a VOA, and the equivalent CLSR noted. The optical spectra of demultiplexer output with CLSR's of 30, 22.5, and 16.5 dB achieved for the corresponding CLPs of $-27.5, -20.2,$ and -13.7 dBm is depicted in Figure 4.10 (a)-(c), respectively. Figure 4.11 (a) illustrates a plot of the CLSR as a function of the CLP. From the figure, it can be seen that the CLSR is inversely proportional to the CLP. This indicates that the CLSR is dictated by the difference between the power of the demultiplexer (free-running case) and the power of the injected comb lines.
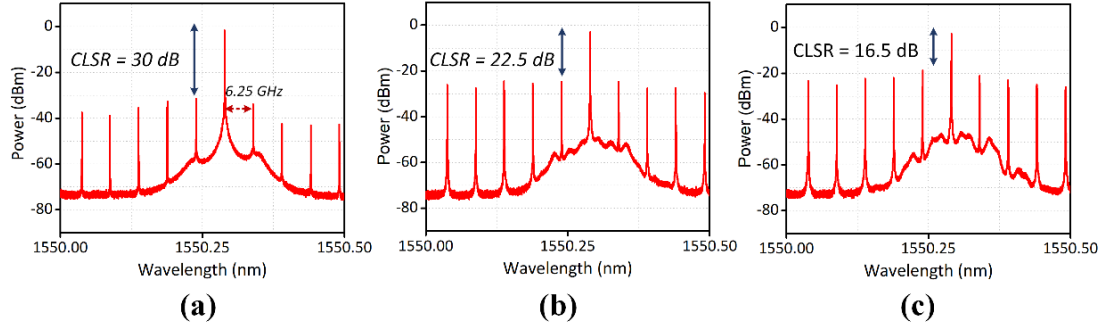
Figure 4.10 Optical spectra of active demultiplexer for various CLPs (a) CLP = −27.5 dBm, (b) CLP = −22.5 dBm, and (c) CLP = −13.7 dBm. OSA resolution 20 MHz.
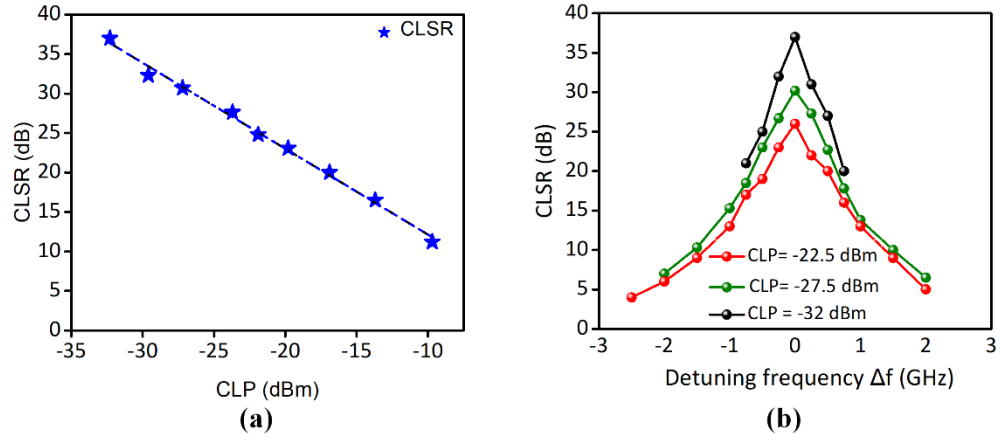
Figure 4.11 CLSR as a function of (a) CLP and (b) injection frequency detuning.

4.3.1.2 *CLSR dependency on detuning*

The previous tests were carried out, for a perfect alignment (within the 20 MHz resolution of the OSA) between the wavelength of the demultiplexer and the chosen comb line. However, it is well known that the wavelength of a semiconductor laser may drift over time. Therefore, it is important to characterise the tolerance of the demultiplexer to the detuning frequency (Δf) i.e., the difference between the injected wavelength and the emission wavelength of the demultiplexer. The stable locking range can then be obtained by varying the detuning and ensuring that the output spectrum of the slave laser remains in single-moded. The CLSR is then measured as a function of Δf for various CLPs and the results are plotted in Figure 4.11 (b). The detuning is varied from −2 to +2 GHz, in steps of 250 MHz, where the negative values indicate that the wavelength of the

demultiplexer is longer than that of the comb line. From the plot, it is evident that the CLSR degrades as the detuning increases, with the highest CLSR value achieved for the perfect alignment (zero detuning). This can be attributed to the efficiency of the injection locking. The figure also shows that the stable locking range of the demultiplexer is, as expected, injection power-dependent and increases from ±750 MHz for CLP= −32 dBm, to ± 2 GHz for CLP= −22.5 dBm.

4.3.1.3 *Phase noise analysis*

As mentioned earlier, the active demultiplexer inherits the phase and frequency characteristics of the input OFC, which is another attractive feature of the technique. As a result, the device maintains the phase correlation between the separated comb lines, which is vital for applications such as millimetre wave and THz generation, atomic clocks [29], dual-comb spectroscopy [38], [39], etc.
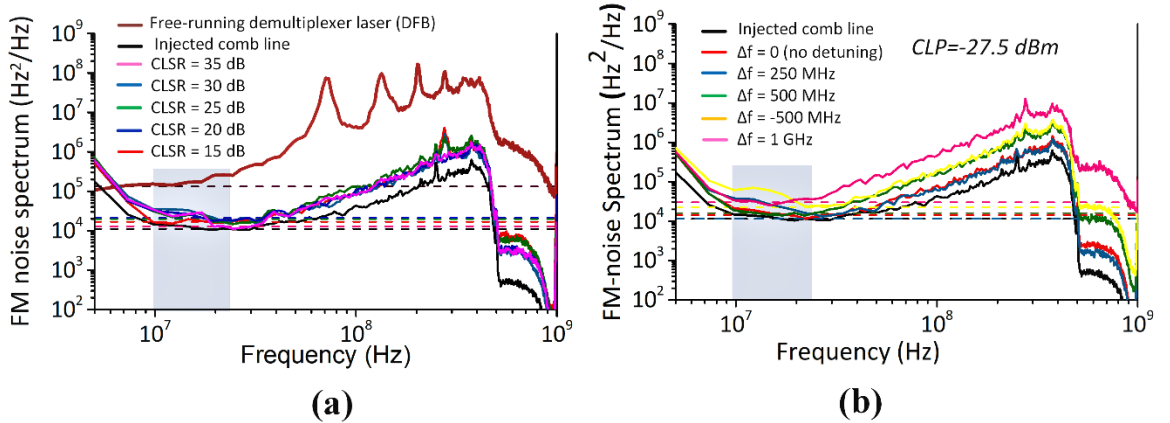
Figure 4.12 FM phase noise spectra for various (a) CLSR and (b) injection detuning frequency.

To validate the transfer of the phase characteristics from the comb to the demultiplexer, frequency modulated (FM) noise spectrum measurements are performed using a modified-delayed self-heterodyne technique, as explained in chapter 3 [32]. These tests are carried out for different values of CLP (thus CLSR) and detuning, and the results are plotted in Figure 4.12 (a) and (b), respectively. The FM noise spectrum $S_f(f)$ is the power spectral density of the instantaneous frequency fluctuation (Hz^2/Hz). The grey section in Figure 4.12 (a) and (b) is the approximate demarcation of the flat white noise part. The

Lorentzian shaped laser linewidth (δf) can be calculated, by retrieving the flat part of the FM noise spectrum using the equation $\delta f = \pi \times \frac{S_o}{2}$ [32]. The coloured dotted line in the plots mark the S_0 values that are considered for the linewidth calculations in the respective cases. The drop in the values beyond 500 MHz corresponds to the bandwidth of a digital filter used in the offline processing of the data. From the plots in Figure 4.12 (a), the measured linewidth of the free-running demultiplexer, the input OFC and the injection-locked demultiplexer (with zero detuning) are calculated to be ~2.6 MHz, 19 kHz, and 20 kHz, respectively. The three orders of magnitude reduction in the linewidth is a clear indication of the efficient phase transfer between the comb and the demultiplexer, due to stable OIL. Furthermore, the constant linewidth ~20 kHz is observed for various CLSRs (by varying CLPs) indicating the phase noise transfer is not simply dictated by the CLP, as long as a stable OIL is attained.

Next, the phase noise measurements are repeated for a constant CLP of -27.5 dBm and different values of detuning frequency. The results, presented in Figure 4.12 (b), show that the white noise part tends to increase with an increase in the detuning frequency, thus, indicating a decreasing efficiency of the phase noise transfer. In order to maintain a low linewidth of the demultiplexed comb tone, the detuning value should be kept below ±500 MHz, for the CLP used here (-27.5 dBm).

4.3.1.4 *Relative intensity noise*

The relative intensity noise (RIN) is a random amplitude fluctuation that could potentially limit the ability of the transmitter in the application of amplitude modulation formats such as on-off-keying (OOK) and multi-level formats such as PAM-4/8. It also plays a vital role in analogue modulation such as DMT systems. Thus, the RIN of the demultiplexed output is characterised as a function of CLSR. Firstly, a measurement of the RIN of an OFC line, demultiplexed using an active demultiplexer with a CLSR of 35 dB (as in Figure 4.9 (d)), is carried out [33]. The averaged RIN up to 6 GHz is measured to be – 157.7 dB/Hz. Similar RIN values are measured for CLSRs between 35- 25 dB. However, in the case of a CLSR = 20 dB, an increase in the RIN value (–152 dB/Hz) is observed. This can be attributed to the higher power levels in the suppressed tones. For comparison,

the OFC lines are filtered out using a conventional filtering technique (optical bandpass filter with an EDFA followed by an ASE removal filter). In this case, an average RIN value of –138 dB/Hz is measured. This demonstrates the measured RIN of the active demultiplexed comb tones contains contribution from both master and slave lasers depending upon the injection locking conditions.
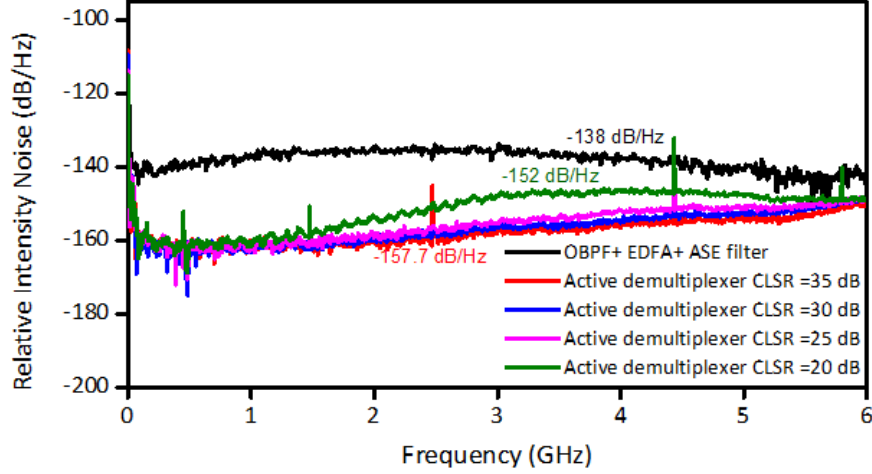
Figure 4.13 RIN spectra of the demultiplexed OFC lines using active demultiplexer (with various CLSRs) and OBPF + EDFA + ASE filter. Here, OBPF: optical bandpass filter, EDFA: Erbium-doped fibre amplifier, ASE filter: amplified spontaneous noise filter.

4.3.1.5 Stability

Finally, a stability analysis of the demultiplexer operation is carried out, using an OFC with FSR of 1.25 GHz, as shown in Figure 4.14 (a). It is important to note that the stability of the demultiplexer at such a low FSR is critical, as there is a possibility of two different comb tones falling within the injection locking range of the demultiplexer. For this test, two adjacent tones separated by 1.25 GHz are demultiplexed and combined using a 50:50 coupler. The optical spectrum of combined demultiplexed lines, is depicted in Figure 4.14 (b). The CLP used here is −32 dBm, resulting in a locking range of 1.5 GHz (from Figure 4.11 (b)).

The demultiplexer tones are then detected on a high-speed photodiode and the resultant RF beat tone is presented in Figure 4.14 (c). The power, linewidth, and frequency of the generated RF tone is monitored over 30 minutes and recorded at 5 seconds intervals.

During the test, the frequency span of the ESA is set to 1 kHz and the resolution bandwidth to 30 Hz. The plot of the frequency of the beat tone as a function of time is depicted in Figure 4.14 (d).
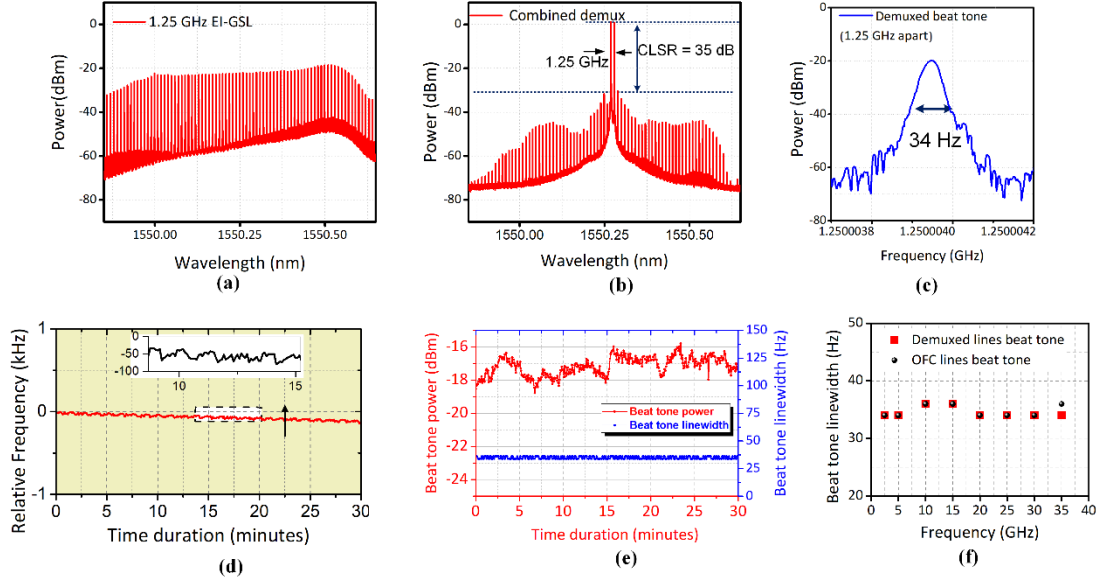
Figure 4.14 Optical spectra of (a) EI-GSL with FSR = 1.25 GHz, (b) two combined demultiplexed lines separated by 1.25 GHz, (c) electrical spectrum of the RF beat tone at 1.25 GHz. Plot of the (d) relative frequency drift, (e) beat tone power and linewidth fluctuation over 30 mins duration, and (f) beat tone linewidths for demultiplexed lines with various frequency separation.

The stability of the generated tone is better than 120 Hz, which is comparable with the stability of the RF source used for the OFC generation. Figure 4.14 (e) shows the corresponding plot of the beat tone power (red) and linewidth (blue). From the plot, it can be seen that the power fluctuation is less than 2 dB. This is caused by a variation in the polarisation and could be further reduced by using components (coupler) with polarisation maintaining fiber. The beat linewidth remains constant ~34 Hz (limited by the resolution of ESA), which reflects the high degree of phase correlation between the demultiplexed tones. This in turn, proves that stable locking is maintained throughout the duration of the test. Moreover, the phase correlation measurement is extended to the demultiplexed tones with a frequency separation between 2.5 GHz and 37.5 GHz. For all values, the 3 dB beat tone linewidth is measured as 34 Hz, as shown in Figure 4.14 (f). Overall, the results

presented in Figure 4.14 (d)-(f) demonstrate the exceptional stability of operation of the demultiplexer, even at very low FSR. Furthermore, slow feedback control techniques such as direct detection control feedback [34], OIL phase-locked loop [35], etc., could also be employed for long-term stable operation especially for low FSRs.

4.3.2 Multifunctionality of a laser-based active demultiplexer

In this section, the multifunctionality of the active demultiplexer is investigated, in particular the following aspects are evaluated:

(i) *Tunable demultiplexing*: An attractive feature of the proposed laser-based demultiplexing technique is its tunability, allowing for the selection of an arbitrary line from an OFC with an arbitrary FSR. This unique aspect makes the proposed demultiplexer an ideal candidate for application in reconfigurable optical networks (where the dynamic reconfiguration of transmitters re required). To demonstrate this feature, the device is used to select three different lines from OFCs with FSRs of 2.5 GHz (with CLP = -32 dBm); 6.25, 12.5, and 15 GHz (with CLP = -27.5 dBm). The spectra of the OFCs are shown in Figure 4.15 (a)-(d), with the selected lines marked by arrows. The corresponding output spectra of the demultiplexer, in Figure 4.15 (e)-(g), show that a CLSR >30 dB can be achieved for any line within 10 dB from the peak (line with sufficient power to achieve injection locking). This result clearly demonstrates that the proposed demultiplexer can be tuned in wavelength by 2 nm and would be able to demultiplex all lines, within that range, that possess adequate power for OIL. Furthermore, the resolution limit of the demultiplexer is examined by demultiplexing closely spaced OFC lines (FSR in the MHz range). Figure 4.16 shows the optical spectra of demultiplexed lines from OFCs with 781.25 and 390.625 MHz FSRs, achieving CLSR >20 dB. Thereby, the active demultiplexer can be used to filter lines from OFCs with FSRs ranging from MHz to GHz.

(ii) *Power equalisation:* Active demultiplexers not only can demultiplex a comb line but also acts as a power equaliser, since for any comb line demultiplexed, the output power is constant and dictated by the power of the laser (used as the demultiplexer).

As demonstrated in Figure 4.15 (e)-(h), any comb line with sufficient power to achieve stable OIL, can be demultiplexed. Therefore, even comb lines with power 10 dB less than the spectral peak, can be demultiplexed with the required CLSR. This functionality can also be used to enhance the number of comb lines available for data modulation (ordinarily defined as tones with powers within 3 dB from the spectral peak). By employing the active demultiplexer, the number of usable lines, for the OFCs shown in Figure 4.15 (a)-(d), was increased by an expansion factor of 1.7 (from 26 to 36, 8 to 13, 4 to 7, and 3 to 5 for an FSR of 2.5, 6.25, 12.5, and 15 GHz respectively). It is important to note that in each case, the efficient phase transfer (low linewidth of <35 kHz) is achieved and line output power is maintained at 7.5 dBm.
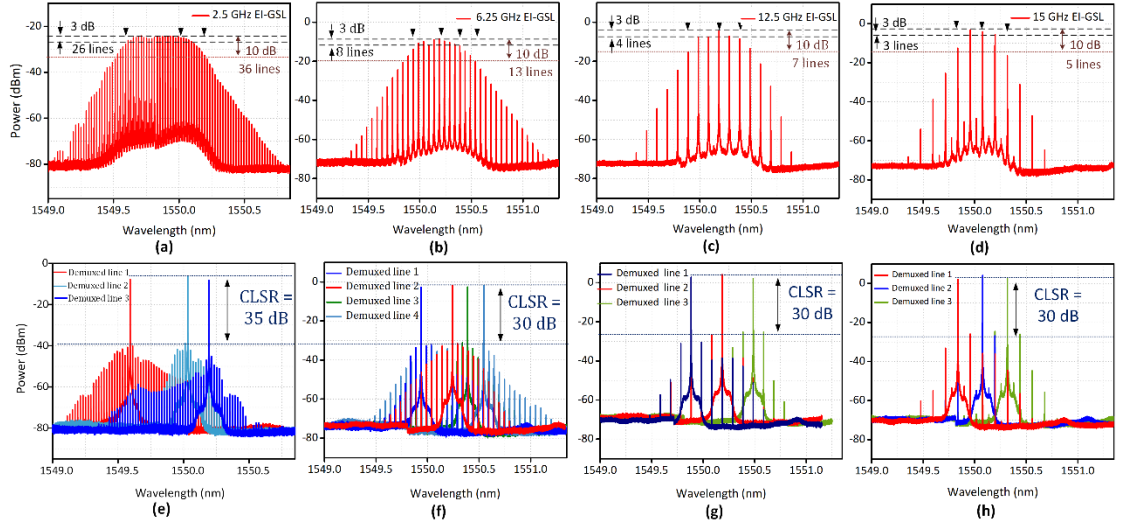
Figure 4.15 Optical spectra of EI-GSL OFC with FSR of (a) 2.5 GHz, (b) 6.25 GHz, (c) 12.5 GHz, (d) 15 GHz, and corresponding demultiplexer output (e)-(h), demonstrating the tunability, power equalisation, ultra-low noise amplification of the active demultiplexer. OSA resolution of 20 MHz.
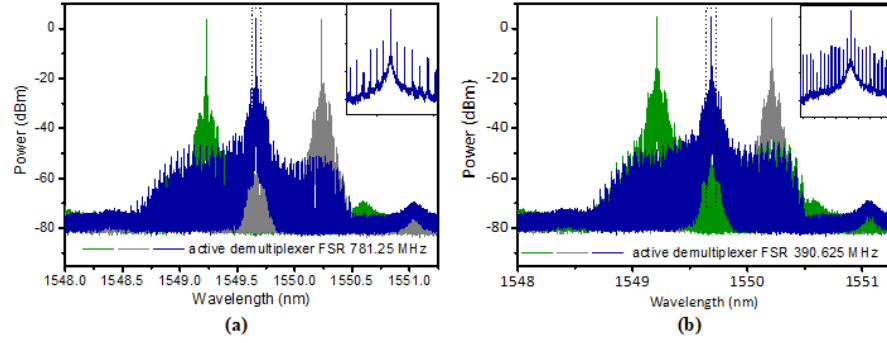
Figure 4.16 Optical spectra of active demultiplexer in MHz range (a) FSR = 781.25 MHz and (b) 390.625 MHz. OSA resolution 20 MHz.

(iii) *Ultra-low noise amplification:* Conventionally, optical amplifiers are used to overcome the insertion loss of the demultiplexer and boost the power of comb lines. However, this inevitably leads to a degraded OSNR due to the addition of ASE noise. Contrarily, in the case of the active demultiplexer, the selection of a comb line is achieved by increasing the power of a single line, while leaving the power of the remaining lines unchanged. In the experiments described in this section, a CLP of -32 dBm was used, while the power achieved at the output of the demultiplexer was 7.5 dBm (fixed). Thus, such a device provides up to 40 dB gain and can be viewed as an ultra-low noise amplifier operating in a constant power mode.

(iv) *Data modulation:* Finally, the demultiplexer is a standard semiconductor laser, which allows for the electro-optic conversion to be carried out by direct modulating the demultiplexer laser. The demonstration of the active demultiplexer as a data modulator for OOK, and 4-,16- QAM DMT formats is presented in the next chapter.

The above-mentioned multifunctionality of the active demultiplexer reduces the component count, as well as the size and complexity of the transmitter. The proposed device can be photonically integrated with the OFC source, thus further reducing the footprint, cost, and complexity of the transmitter. It is important to note that in an integrated scheme, there would not be a need for optical circulators. Hence, the active demultiplexer has been chosen as the demultiplexing solution for the system implementations investigated in the following chapters.

4.4 Conclusions

A flexible OFC demultiplexer is a key enabler of a reconfigurable OFC-based transmitter. In fact, the lack of such a solution could be considered as a limiting factor in the development and commercial employability of OFC in next-generation reconfigurable, spectrally efficient optical networks. To address these challenges, two potential demultiplexer solutions were investigated in this chapter. The first technique entails the use of MRRs, devices that exhibit a low-insertion loss, are tunable, and can be photonically integrated with the OFC source. A proof-of-principle demonstration of an FPGA-controlled OFC-based transmitter employing an MRR as a demultiplexer was presented. The dynamic reconfiguration of the GSL OFC and MRR was showcased, and the achievable tuning speed was investigated. Nevertheless, the level of flexibility that the MRR offers is limited by their passband profile, fixed bandwidth, and slow tunning speed. The second demultiplexing approach entailed the use of a semiconductor laser as an active demultiplexer. Here, the operation is based on the principle of OIL. It is extremely attractive as it not only offers tunable filtering of the comb lines, but also achieves power equalisation, ultra-low noise amplification, and data modulation, all using a single device. A comprehensive characterisation of active demultiplexer was performed, followed by an experimental demonstration of its multi-functionality. Finally, the demultiplexer can also be integrated with the GSL OFC onto a single chip, resulting in a highly reconfigurable transmitter with a reduced footprint and cost. With such excellent features, the laser-based multi-functional active demultiplexer will be attractive for employment in flexible superchannel-based optical networks.

4.5 Reference

[1] Kylia, "DWDM MUX/DEMUX," *Data sheet, 2008.* [Online]. Available:*https://kylia.com/api_website_feature/files/download/11115/datasheet-MICS-V111.pdf.* (accessed Jan. 14, 2019).

[2] Finisar, "Filter Bandwidth Definition of the WaveShaper S-series Programmable Optical Processor," *Data sheet*, 2012. [Online]. Available: https://www.exfo.com/umbraco/surface/file/download/?ni=17992&cn=en-US&pi=17993. (accessed Jan 14, 2019).

[3] EXFO, "XTM-50 Tunable Filter with Adjustable bandwidth," *Data sheet*, 2015. [Online]. Available: https://www.exfo.com/umbraco/surface/file/download/?ni=17992&cn=en-US&pi=17993, (accessed Feb 12, 2019).

[4] X. Wu, C. Liu, W. Liu, Z. Yuan, K. Wu, F. Tang, H. Chen, W. Liu, L. Yang, J. Zhang, and X. Liang, "Monolithic integrated cyclic 64-channel AWG with MZI filters and arrayed vertical reflecting mirrors for WDM-PON application," *Appl. Opt.*, vol. 58, no.30, pp. 8282-8289, 2019.

[5] W. Bogaerts, P. De Heyn, T. Van Vaerenbergh, K. De Vos, S. Kumar Selvaraja, T. Claes,P. Dumon, P. Bienstman, D. Van Thourhout, and R. Baets, "Silicon microring resonators," *Laser and Photonics Reviews*, vol. 6, no. 1, pp. 47–73, 2012, DOI: 10.1002/lpor.201100017.

[6] S. El-Sabban, A. Wageeh, and D. Khalil, "Box-like filter response using multimode single-ring microresonators," *Applied optics*, vol. 55, no. 2, pp. 408–414, 2016, DOI: 10.1364/AO.55.000408.

[7] P. Chen, S. Chen, X. Guan, Y. Shi, and D. Dai, "High-order microring resonators with bent couplers for a box-like filter response," *Optics Letters*, vol. 39, no. 21, p. 6304, 2014, DOI: 10.1364/OL.39.006304.

[8] D. Aguiar, M. Milanizadeh, E. Guglielmi, F. Zanetto, R. Ji, S. Zhou, Y. Li, X. Song, L. Zhang, M. Sampietro, F. Morichetti, and A. Melloni, "Automatic Tuning of Microring-Based Hitless Reconfigurable Add-Drop Filters," in *Optical Fiber Communication Conference*, 2018, paper W2A.41.

[9] Miloš A. Popovíc, Tymon Barwicz, Michael R. Watts, Peter T. Rakich, Luciano Socci, Erich P. Ippen, Franz X. Kärtner, and Henry I. Smith, "Multistage high-order microring-resonator add-drop filters," *Optics Letters*, vol. 31, no. 17, pp. 2571–2573, 2006, DOI: 10.1364/OL.31.002571.

[10] J. Niehusmann, A. Vörckel, P. H. Bolivar, T. Wahlbrink, and W. Henschel, "Microring Resonator," *Optics Letters*, vol. 29, no. 24, pp. 2861–2863, 2004, DOI: 10.1364/OL.29.002861.

[11] S. Sharif Azadeh, J. Müller, F. Merget, S. Romero-García, B. Shen, and J. Witzens, "Advances in silicon photonics segmented electrode Mach-Zehnder modulators and

peaking enhanced resonant devices," *Photonics North 2014*, vol. 9288, no. January 2015, p. 928817, 2014, DOI: 10.1117/12.2075836.

[12]   D. S. Wu, R. Slavik, G. Marra, and D. J. Richardson, "Direct Selection and amplification of individual narrowly spaced optical comb modes via injection locking: Design and characterization," *Journal of Lightwave Technology*, vol. 31, no. 14, pp. 2287–2295, 2013, DOI: 10.1109/JLT.2013.2262921.

[13]   S. P. Ó Duill, P. M. Anandarajah, F. Smyth, and L. P. Barry, "Injection-locking criteria for simultaneously locking single-mode lasers to optical frequency combs from gain-switched lasers," *Physics and Simulation of Optoelectronic Devices XXV*, vol. 10098, no. January, p. 100980H, 2017, DOI: 10.1117/12.2249769.

[14]   Z. Liu and R. Slavík, "Optical Injection Locking: From Principle to Applications," *Journal of Lightwave Technology*, vol. 38, no. 1, pp. 43–59, 2020, DOI: 10.1109/JLT.2019.2945718.

[15]   A. C. Bordonalli, M. J. Fice, and A. J. Seeds, "Optical injection locking to optical frequency combs for superchannel coherent detection," *Optics Express*, vol. 23, no. 2, p. 1547, 2015, DOI: 10.1364/oe.23.001547.

[16]   A. Albores-Mejia, T. Kaneko, E. Banno, K. Uesaka, H. Shoji and H. Kuwatsuka., "Optical Comb Line Selection from a Low Power / Low OSNR Comb using a Low Coherence Semiconductor Laser for Flexible Ultra Dense Short-Range Transceivers," pp. 7–9, 2015.

[17]   R. Zhou, T. Shao, M. D. Gutierrez Pascual, F. Smyth, and L. P. Barry, "Injection Locked Wavelength De-Multiplexer for Optical Comb-Based Nyquist WDM System," *IEEE Photonics Technology Letters*, vol. 27, no. 24, pp. 2595–2598, 2015, DOI: 10.1109/LPT.2015.2478791.

[18]   M. D. Gutierrez, J. Braddell, F. Smyth, and L. P. Barry, "Monolithically integrated 1x4 comb de-multiplexer based on injection locking," *European Conf. Integrated Optics*, pp. 1–2, 2016.

[19]   K. Shortiss, M. Dernaika, M. Shayesteh, and F. H. Peters, "The Effect of Relaxation Oscillations in Integrated Optical Comb Demultiplexers Based on Injection Locking," *IEEE Journal of Quantum Electronics*, vol. 55, no. 6, 2019, DOI: 10.1109/JQE.2019.2942053.

[20]   V. Vujicic, M. D. G. Pascual, J. Braddell, V. Panapakkam, C. Calò, R. Brenot, A. Ramdane, P. M. Anandarajah, F. Smyth, L. P. Barry, "Reduction of Relative Intensity Noise of Optical Multicarrier Sources Using External Injection Based Optical Demultiplexer," *European Conference on Optical Communication, ECOC*, vol. 2017-Septe, no. 4, pp. 1–3, 2017, DOI: 10.1109/ECOC.2017.8345914.

[21]   R. Zhou, M. D. Gutierrez Pascual, P. M. Anandarajah, T. Shao, F. Smyth, and L. P. Barry, "Flexible wavelength de-multiplexer for elastic optical networking," *Optics Letters*, vol. 41, no. 10, p. 2241, 2016, DOI: 10.1364/OL.41.002241.

[22] W. Bogaerts, P. Dumon, J. Brouckaert, K. de Vos, D. Taillaert, D. van Thourhout, and R. Baets, "Ultra-compact optical filters in Silicon-on-Insulator and their Applications," *2007 4th IEEE International Conference on Group IV Photonics*, pp. 1–3, 2007, DOI: 10.1109/GROUP4.2007.4347647.

[23] Y. Yanagase, S. Suzuki, Y. Kokubun, and S. T. Chu, "Box-like filter response and expansion of FSR by a vertically triple coupled microring resonator filter," *Journal of Lightwave Technology*, vol. 20, no. 8, pp. 1525–1529, 2002, DOI: 10.1109/JLT.2002.800296.

[24] F.Y. Gardes, A. Brimont, P. Sanchis, G. Rasigade, D. Marris-Morini, L. O'Faolain, F. Dong, J.M. Fedeli, P. Dumon, L. Vivien, T.F. Krauss, G.T. Reed, and J. Martí., "High-speed modulation of a compact silicon ring resonator," *IEEE International Conference on Group IV Photonics GFP*, vol. 17, no. 24, pp. 241–243, 2009, DOI: 10.1109/GROUP4.2009.5338374.

[25] K. Shortiss, M. Shayesteh, W. Cotter, A. H. Perrott, M. Dernaika, and F. H. Peters, "Mode suppression in injection locked multi-mode and single-mode lasers for optical demultiplexing," *Photonics*, vol. 6, no. 1, 2019, DOI: 10.3390/photonics6010027.

[26] P. M. Anandarajah, S. P. Ó Dúill, R. Zhou, and L. P. Barry, "Enhanced Optical Comb Generation by Gain-Switching a Single-Mode Semiconductor Laser Close to Its Relaxation Oscillation Frequency," *IEEE Journal of Selected Topics in Quantum Electronics*, vol. 21, no. 6, pp. 592–600, 2015, DOI: 10.1109/JSTQE.2015.2456751.

[27] R. Zhou, S. Latkowski, J. O'Carroll, R. Phelan, L. P. Barry, and P. Anandarajah, "40nm wavelength tunable gain-switched optical comb source," *Optics Express*, vol. 19, no. 26, pp. B415–B420, 2011, DOI: 10.1364/OE.19.00B415.

[28] P. M. Anandarajah, R. Maher, Y. Q. Xu, S. Latkowski, J. O'Carroll, S. G. Murdoch, R. Phelan, J. O'Gorman, and L. P. Barry, "Generation of Coherent Multicarrier Signals by Gain Switching of Discrete Mode Lasers," *IEEE Photonics Journal*, vol. 3, no. 1, pp. 112–122, 2011, DOI: 10.1109/JPHOT.2011.2105861.

[29] S. A. Diddams, "The evolving optical frequency comb [Invited]," *Journal of the Optical Society of America B*, vol. 27, no. 11, pp. B51–B62, 2010, DOI: 10.1364/JOSAB.27.000B51.

[30] R. Holzwarth, Th. Udem, T. W. Hänsch, J. C. Knight, W. J. Wadsworth, and P. St. J. Russell, "Optical Frequency Synthesizer for Precision Spectroscopy," *Physical Review Letters*, vol. 85, no. 11, pp. 2264–2267, Sep. 2000, DOI: 10.1103/PhysRevLett.85.2264.

[31] Q. Yang, M. Suh, K. Y. Yang, X. Yi, and K. J. Vahala, "Microresonator Soliton Dual-Comb Spectroscopy," *Science*, vol. 354, no. 6312, 2017. DOI: 10.1126/science.aah6516

[32] T. N. Huynh, L. Nguyen, and L. P. Barry, "Phase noise characterization of SGDBR lasers using phase modulation detection method with delayed self-heterodyne measurements," *Journal of Lightwave Technology*, vol. 31, no. 8, pp. 1300–1308, 2013, DOI: 10.1109/JLT.2013.2247564.

[33]   Eagle Yard Photonics, "Relative Intensity Noise of Distributed Feedback Laser," *Application Note*, 2013. [Online]. Available: http://www.eagleyard.com/fileadmin/downloads/app_notes/App_Note_RIN_1-5.pdf (accessed Oct. 18, 2019).

[34]   A. Bordonalli, C. Walton, and A. J. Seeds, "High-performance phase locking of wide linewidth semiconductor lasers by combined use of optical injection locking and optical phase-lock loop," *Journal of Lightwave Technology*, vol. 17, no. 2, p. 328, Feb. 1999.

[35]   E. K. Lau, L. J. Wong, and M. C. Wu, "Enhanced modulation characteristics of optical injection-locked lasers: A tutorial," *IEEE Journal of Selected Topics Quantum Electronics*, vol. 15, no. 3, pp. 618–633, May-Jun. 2009

5. Compact OFC Transmitters for Data Centre Interconnects and Short-Reach Applications

A compact OFC transmitter can facilitate the dense packing of channels and achieve a high spectral efficiency (by reducing the guard bands between channels), whilst also accomplishing low cost and reduced energy consumption (compared to other OFC based system). However, the realisation of such a densely spaced communications system with the utilisation of an OFC, requires a high-resolution demultiplexer to select individual lines before data modulation. In the previous chapter, a simple laser-based multi-functional active demultiplexer was investigated and its multi-functionality (tunable filter, amplifier, and power equaliser) was experimentally characterised. In this chapter, the active demultiplexer functionality is extended to that of a data modulator, and a compact OFC based multicarrier transmitter best suited for short-reach and data centre applications is demonstrated.

5.1 Introduction

Modern datacentres enable disruptive technologies such as cloud computing, hyperconvergence, and many other applications and services, which handle extremely large data [1]. The $3/4^{th}$ of the global data traffic is carried in and out of data centres and

is driving the data centre communications towards the so-called "Zettabyte Era" [2], [3]. To accommodate such extreme traffic volumes, data centre networks (DCNs) require scalable datacentre interconnects (DCI) offering high-speed, and high-throughput connectivity, while maintaining a low energy consumption [4]–[7]. The latter is essential to ensure a return of investment (economic benefit), as these mega data centres will contain hundreds of thousands of servers. Recently, there have been considerable efforts in both academia and industry to enhance the performance of DCIs by employing new photonic architecture to enable (i) high-bandwidth-density links, and (ii) effective utilisation of resources [6]–[11].

To achieve high-capacity optical interconnects, a coherent-detection-based transmission can be employed [7], [12]. However, it brings significant system complexity and cost, which could prove to be prohibitive. A viable alternative is to use intensity modulation and direct detection (IM/DD) based techniques, such as four-level pulse amplitude modulation (PAM4) and discrete multi-tone (DMT) modulation. Currently, 100 Gb/s and 400 Gb/s transceivers, based on quad small form-factor pluggable (QSFP28), and QSFP-double density (QSPF-DD) are deployed in short-reach applications such as intra-DC links [13], [14]. QSFP28 consists of 4 channels, each modulated with a 25 Gb/s NRZ signal (IEEE 802.3ba 100GBASE), whereas the QSFP-DD consists of 8 or 4 channels of 53 Gb/s (IEEE 400GBASEFR8), and 106 Gb/s PAM 4 (IEEE 400GBASE-DR4) signals, respectively [13], [15]. Some of the recent notable demonstrations include 2×56 Gb/s PAM4 [16], [17] and 4×50 Gb/s DMT signal transmission for short-reach networks [18]. While continual efforts are made to achieve higher capacity DCIs, it is important to consider the effective utilisation of the resources to overcome DC resource fragmentation scenarios, where resources are mismatched with the traffic requirements. In large-scale DCs, even a small improvement in performance or resource utilisation will have a significant impact on the overall network [4], [19]. Therefore, flexible optical transceivers, which facilitate the reassignment of the DCI bandwidth to better match the traffic patterns and enable effective utilisation of the resources through network disaggregation, are crucial [8], [20].

A state-of-the-art DCI transmitter solution employs an array of laser sources (VCSEL's or DFB's), utilises large channel spacing or guard band (spectrally inefficient) and does not exhibit wavelength tunability [8], [9]. A promising candidate to serve as a flexible optical transceiver, in DCIs, is an OFC (multi-carrier) source. The use of a reconfigurable OFC enables a simple and cost-efficient generation of carriers that exhibit precise wavelength spacing. The precise spacing allows the reduction of the size of the frequency guard bands thereby offering better SE [21]–[23]. However, the OFC-based DCI would require a tunable demultiplexer that selects the individual comb line before encoding the data. The architecture of an OFC-based DCIs employing a conventional demultiplexer (such as WSSs, AWGs[24], [25]) is shown in Figure 4.1 (a). However, these demultiplexing solutions are limited in spectral resolution and introduce a large insertion loss and requires EDFAs.
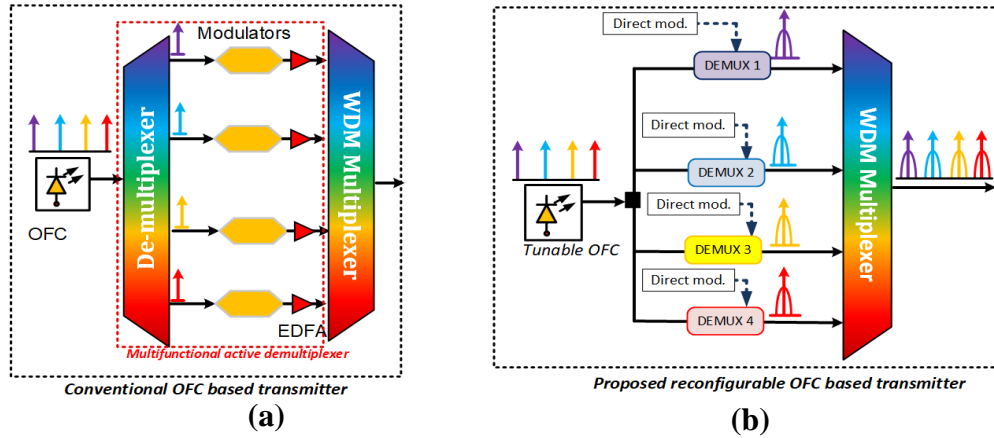
Figure 5.1 OFC-based transmitter architecture employing (a) conventional WSS/AWG demultiplexer and (b) proposed active demultiplexer. AWG: arrayed waveguide grating, WSS: wavelength selective switch, EDFA: Erbium-doped fibre amplifier, Demux: active demultiplexer.

An attractive alternative is to employ a multi-functional active demultiplexer based on optical injection locking (OIL) [26]–[29]. As explained in the previous chapter, such a device selects a comb tone by injecting the OFC into a demultiplexer laser and aligning the wavelength of this laser with the desired comb line. Since the demultiplexer is a semiconductor laser, it can be directly modulated with the data that needs to be transmitted, thus realising the functionality of a data modulator. The architecture of the

proposed OFC-based transmitter employing an active demultiplexer for short reach (due to direct modulation) applications is as shown in Figure 5.1 (b). It can be seen that in the proposed transmitter that a single demultiplexer laser replaces a filter (AWG/WSS), an optical amplifier, and an external modulator. One of the immediate positive impacts that the OIL-based demultiplexer brings is the reduction in the number of components required (when compared to other OFC based transmitter), ensuring the similar SE. In addition, the fact that such a demultiplexer can be integrated with the rest of the transmitter introduces simplicity, reduces the footprint and improves the energy efficiency [30],[31].

In this chapter, a novel OFC-based transmitter architecture employing a multifunctional active demultiplexer is proposed. Firstly, as a proof-of-concept validation, a two-channel active demultiplexer directly modulated with a 10.7 Gb/s on-off keyed (OOK) signal is presented. The modulated signal is then transmitted, error-free, over 3 km of SSMF. Then, a VPI simulation is performed to investigate the impact of injection of the comb line on the chirp induced by the direct modulation of the demultiplexer. Furthermore, the proposed transmitter is verified with multi-level modulation formats such as 4- and 16-QAM DMT. By utilising a unique gain equaliser property of the active demultiplexer, OFC lines within 20 dB from the spectral peak are demultiplexed and directly modulated to achieve an aggregate data rate of 100 Gb/s (8×12.5 Gb/s) for 4 QAM DMT and 200 Gb/s (8×25 Gb/s) for 16 QAM DMT modulated system. Then, a 4 channel DWDM system (channel spacing of 12.5 GHz), employing a direct modulation and carrying 4 QAM DMT data, is realised and the impact of cross-channel interference on the system performance is investigated. Finally, a brief comparison of the proposed transmitter with some of the current DCI technologies is presented, proving the suitability of the proposed OFC and active demultiplexer based transmitter for short-reach applications.

5.2 Performance Evaluation of a Directly Modulated 10.7 Gb/s OOK System Employing Active Demultiplexers

5.2.1 Two-channel 10.7 Gb/s OOK system

The experimental setup of the proposed OFC-based OOK transmitter system is shown in Figure 5.2. It comprises an OFC source, followed by a two-channel demultiplexer. The OFC is based on an EI-GSL with an FSR of 12.5 GHz. The generated comb is split using a 50:50 coupler and injected into two commercially available distributed feedback (DFB) lasers, each acting as an active demultiplexer (Demux). Both Demux lasers exhibit a threshold current (I_{th}) of 12.5 mA and a 3-dB modulation bandwidth of 14 GHz. When biased at $4 \times I_{th}$, the average optical power emitted is 8.5 dBm (Demux 1) and 9 dBm (Demux 2). The wavelength of each demultiplexer is then temperature tuned to match that of the chosen comb line. The injected comb line power (CLP) is optimised by inline VOAs. The CLP is a crucial parameter as it affects both the locking range (higher power leads to a larger locking range) and the CLSR (an increase in CLP reduces the CLSR) [28]. Thus, the injected power level is a compromise between achieving stable injection locking of the demultiplexer and the required CLSR. Here, the CLP is set to -31 dBm to achieve a CLSR of 37 dB as shown in Figure 5.3 (b).
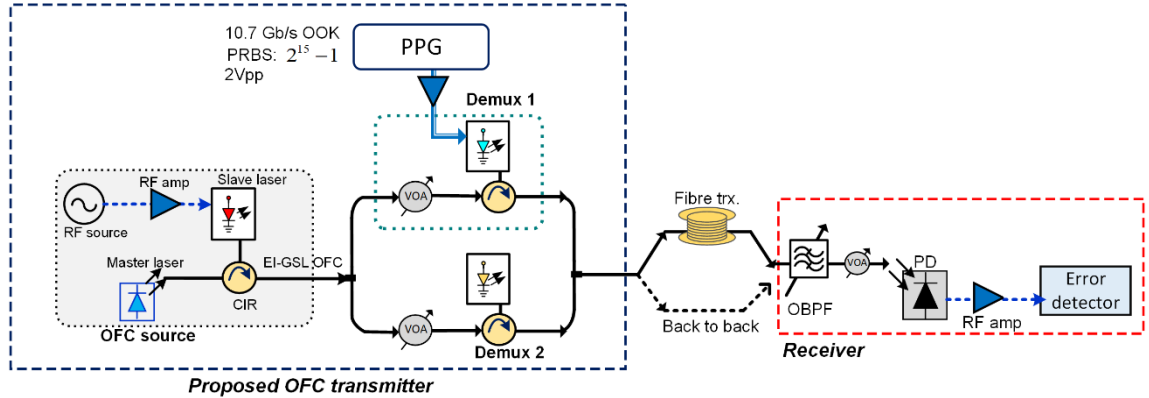
Figure 5.2 Experimental setup of the two-channel OOK system employing the OFC and active demultiplexer based transmitter. Here, VOA: variable optical attenuator, CIR: circulator, Demux: demultiplexer laser, PPG: pulse pattern generator, OBPF: optical bandpass filter, PD: photodetector.

Next, the data is modulated onto Demux 1 by driving it directly (direct modulation) with a 10.7 Gb/s PRBS signal with a length of 2^{15}-1 and a 1 V amplitude. Due to equipment constraints, only one of the demultiplexers is modulated. Subsequently, the two channels are multiplexed together using another 50:50 coupler. The combined channels are then transmitted over 3 km of standard single-mode fibre (SSMF). At the receiver, the modulated signal is filtered using an optical bandpass filter (OBPF) and detected using a 20 GHz photodetector (PD). The electrical signal is then amplified, by a low-noise amplifier, and the bit error ratio (BER) is measured using an error detector. The eye diagrams are recorded using a 50 GHz sampling oscilloscope.

5.2.2 Results and discussion
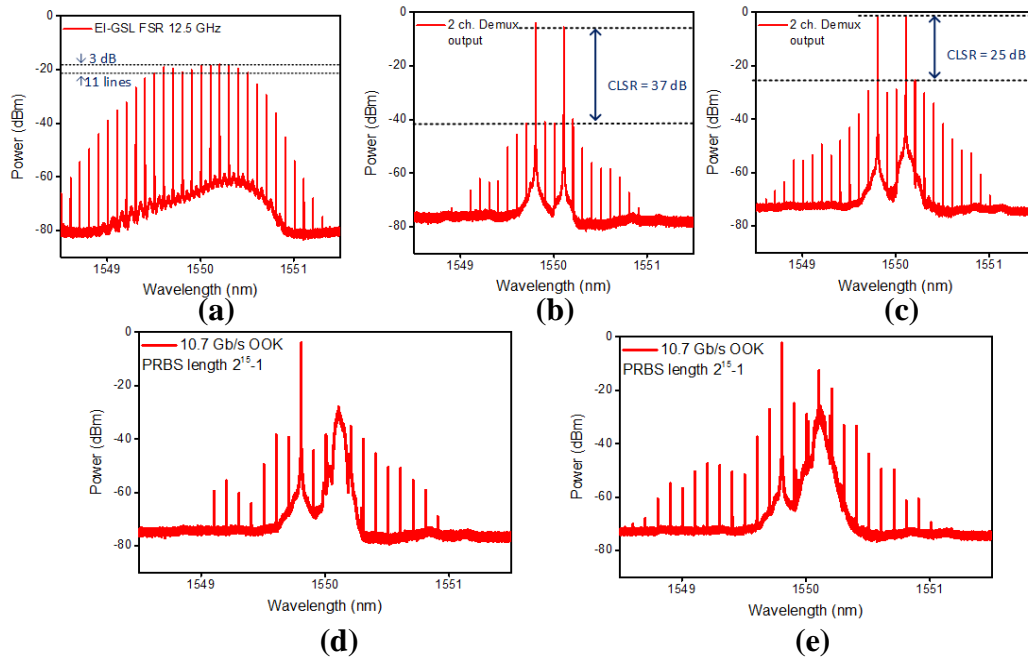
Figure 5.3 Optical spectra of (a) EI-GSL OFC with FSR of 12.5 GHz, combined two-channel active demultiplexer output with CLSR of (b) 37 dB, (c) 25 dB, combined demultiplexers output with modulated Demux 1, when the CLSR is (d) 37 dB, and (e) 25 dB. OSA resolution: 20 MHz, spectra are recorded with 5 dB attenuation before the OSA.

The optical spectrum of the EI-GSL OFC is shown in Figure 5.3 (a). It consists of 11 lines (within 3 dB from the spectral peak), with an FSR of 12.5 GHz and an OCNR >50 dB (within 20 MHz OSA resolution). The combined optical spectrum of the two

demultiplexed comb lines, separated by 37.5 GHz, is shown in Figure 5.3 (b). This channel spacing is specifically chosen to avoid any interference between the adjacent WDM channels that are directly modulated (double sideband) with the 10.7 Gb/s OOK signal. To investigate the impact of the CLSR on the system performance, the CLP is set to −31 dBm and −27.5 dBm, to achieve a Demux output with a CLSR of 37 and 25 dB, respectively, as shown in Figure 5.3 (b) and (c). It is important to note that as the output power of the demultiplexer is much higher than that of the injected comb tone, the demultiplexer can be considered to amplify (~40 dB gain) the selected comb line. The optical spectra of the combined output of the demultiplexers, where Demux 1 is modulated with the data, are depicted in Figure 5.3 (d) and (e).
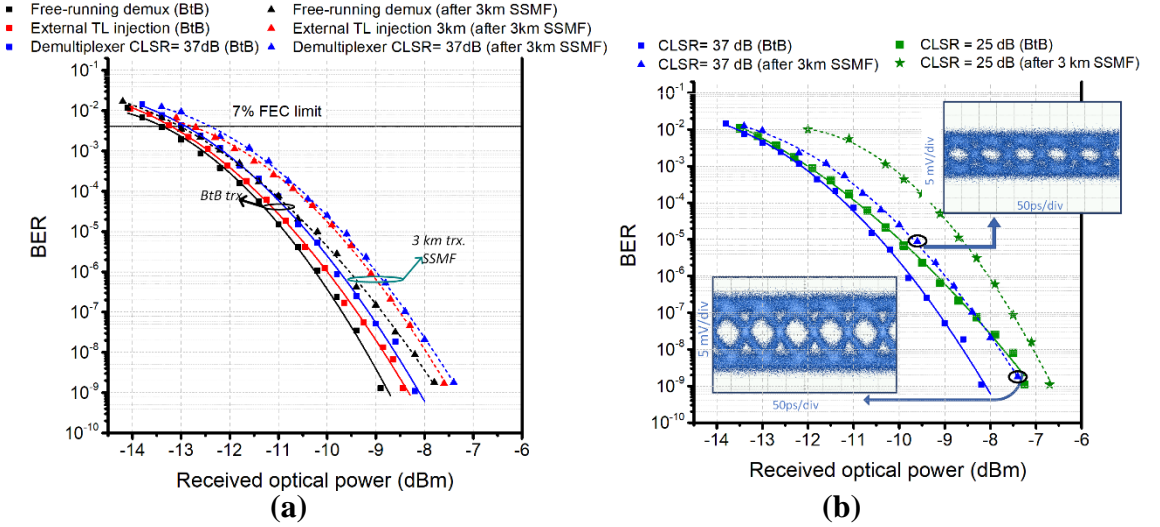
Figure 5.4 Plot of BER vs received optical power for (a) three test scenarios, (b) comparison between CLSR of 37 and 25 dB. Insets are the recorded eye diagrams at the indicated points. Here, BtB: back-to-back, SSMF: standard single mode fibre.

The system performance is then evaluated, by measuring the BER vs. received optical power (ROP) for the back-to-back (BtB) case and after 3 km fibre transmission. Four different scenarios are investigated: a directly modulated Demux (1) with no injection (free-running DFB laser), (2) externally injected with a tunable laser (TL) with a power of −31 dBm, externally injected with an OFC with a (3) CLP of −31 dBm (CLSR= 37 dB), and a (4) CLP of −27.5 dBm (CLSR = 25 dB). The first scenario serves as a

benchmark, the second provides an insight into the impact of external injection on the performance of a directly modulated laser, while the third and fourth configurations allow us to quantify the effect of the spurious (unsuppressed) comb tones on the performance of the OFC-based transmitter for two different values of CLSR. The BER plots for all four cases are plotted in Figure 5.4 (a) and (b). Figure 5.4 (b) illustrates the performance comparison between two CLSR of 37 and 25 dB cases. The insets show the received eye diagrams of the OFC-based transmitter at a BER of $1e^{-5}$ and $1e^{-9}$. The summary of the system performance is presented in Table 5-1.

Table 5-1 Summary of the system performance for various configurations

Case	Demultiplexer	Receiver sensitivity (BER $1e^{-9}$)	Power penalty for 3 km SSMF trx. (compared to its BtB)
1	Free-running DFB	−8.8 dBm	1.2 dB
2	Injection locked with TL at −31 dBm	−7.6 dBm	0.8 dB
3	OFC injection locked Demux CLP= −31 dBm	−7.4 dBm	0.7 dB
4	OFC injection locked Demux CLP= −27.5 dBm	−6.7 dBm	0.55 dB

From the BER plots, it can be seen that the stand-alone demultiplexer (configuration (1)) performs best in the BtB case, having a receiver sensitivity of −8.8 dBm. Nevertheless, it suffers from the highest penalty of 1.2 dB (at a BER of $1e^{-9}$), when transmitted over the 3 km SSMF link. This stems from the large frequency chirp induced by direct modulation, which exacerbates the effect of chromatic dispersion, leading to a large penalty. On comparing the BtB cases, for configurations (2), (3), and (4) there is a 0.5, 0.8, and 1.65 dB power penalty (incurred at a BER of $1e^{-9}$), with respect to the the reference configuration (1). This is a consequence of a reduction in the extinction ratio caused by the external injection. However, the additional penalty due to the fibre transmission is smaller for these cases and equals 0.8 dB, 0.7 dB, and 0.55 dB for configuration (2), (3) and (4) respectively (compared to their respective BtB cases). This improved resilience to the transmission impairments can be credited to the reduction in chirp due to external

injection. It is expected that for longer transmission distances, the impact of the limited CLSR will become more pronounced. This is due to all the spectral components, passing through the demultiplexer, being modulated with the same data. As they traverse sufficiently long transmission distances, chromatic dispersion will introduce a phase mismatch between the different signals, causing them to interfere destructively at the receiver.

5.2.3   Simulation analysis and discussion
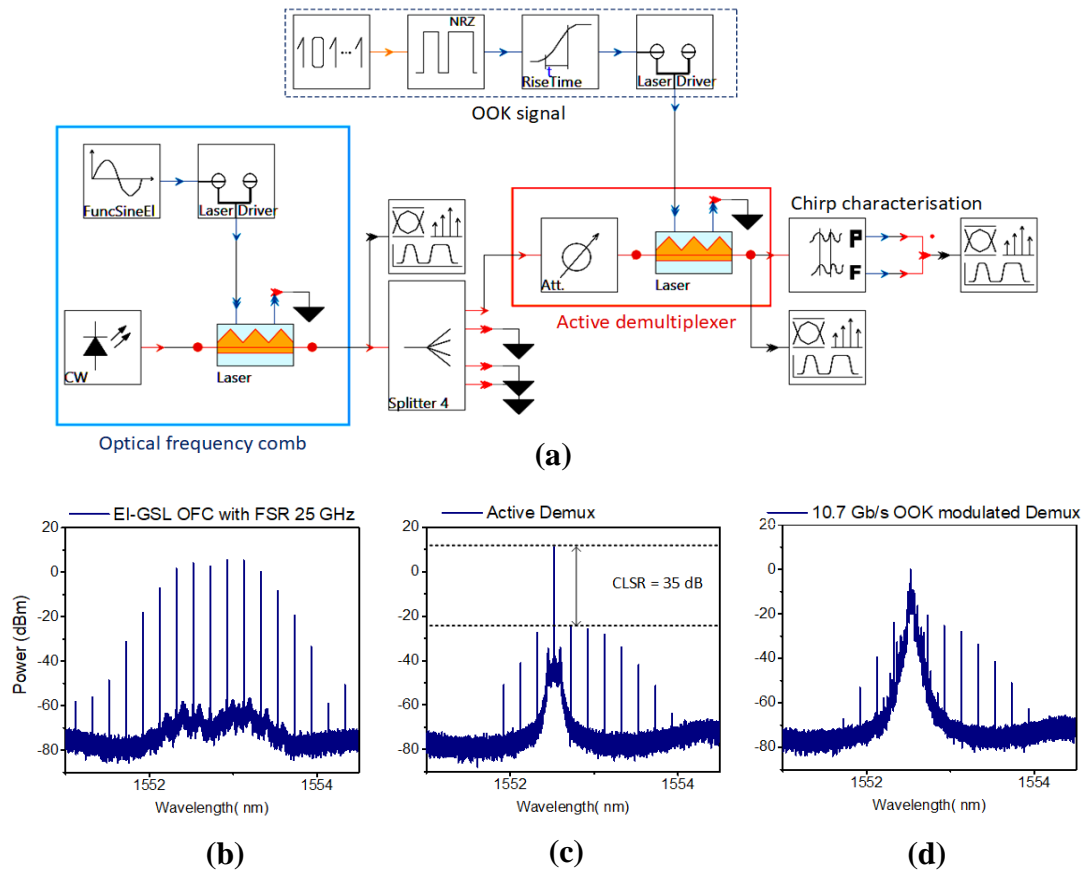
Figure 5.5 Simulation: (a) VPI schematic of the proposed OFC transmitter employing active demultiplexer. Optical spectra of (b) EI-GSL with FSR 25 GHz, (c) active demultiplexer CLSR of 35 dB, and (d) directly modulated 10.7 Gb/s OOK demultiplexer output. Simulation resolution: 20 MHz.

In order to carry out a more thorough investigation into the impact of the CLP and to understand the effect of the weak injection on the chirp (of the demux), a VPI photonics

simulation model is built. The schematic of this simulation model is shown in Figure 5.5 (a). An EI-GSL OFC with an FSR of 25 GHz is generated as shown in Figure 5.5 (b). The demultiplexer laser exhibits an I_{th} of 12 mA and portrays a modulation bandwidth of 14 GHz and emits a power of ~11 dBm when biased at 60 mA. It is important to note that the VPI model's laser alpha parameter is not matched with the laser used in the experiment. The CLP is adjusted to achieve a CLSR of 35 dB (Figure 5.5 (c)). Subsequently, the demux is directly modulated with a 10.7 Gb/s OOK data signal (Figure 5.5 (d)) and the induced chirp is characterised using a "time-resolved frequency and power analyser" module, which calculates the instantaneous power and frequency of an optical signal.

The chirp due to direct modulation is examined for the following Demux configurations (i) free-running, and injection locked by the OFC with a CLSR of (ii) 35 dB and (iii) 25 dB. The plots of the chirp (orange) and intensity (blue) are shown in Figure 5.6 (a)-(c), while the optical spectra of the directly modulated Demux for these cases are depicted in Figure 5.6 (d)-(f), respectively. Firstly, a free-running DFB laser is characterised as a reference. As a consequence of the direct modulation, a strong adiabatic and transient chirp can be seen in Figure 5.6 (a) [32]-[34]. When the Demux is injection locked with CLP of −27 dBm (CLSR 35 dB), no significant chirp reduction is observed, as shown in Figure 5.6 (b). This can be attributed to low injection power (weak injection locking regime) [33]. In configuration (iii), the CLP is increased to −20 dBm (CLSR 25 dB), which induces a strong ringing in both the intensity and chirp (Figure 5.6 (c)). This can be attributed to the beating of emission mode and the injected mode (with frequency detuned). Such a phenomenon is similar to a chaotic behaviour (self-pulsation) of the slave when subjected to a moderate injection locking power regime [33],[35].

Next, the Demux is injection-locked by a tunable laser (TL) and the injection power is swept from −20 dBm to +10 dBm to observe the chirp. In this case, a strong laser ringing dominated by damped oscillations is observed up to TL = 0 dBm, as shown in Figure 5.7 (a). For TL > 3 dBm, chaotic behaviour disappears, and a chirp cancellation is observed, as depicted in Figure 5.7 (b) [33]. It should be noted that the VPI analyser is restricted in

terms of its dynamic range, thus the chirp reduction is not observed but only cancellation. Due to which (along with different alpha parameter), the results are not aligned with the experimental but shows the general trend of the chirp behaviour.
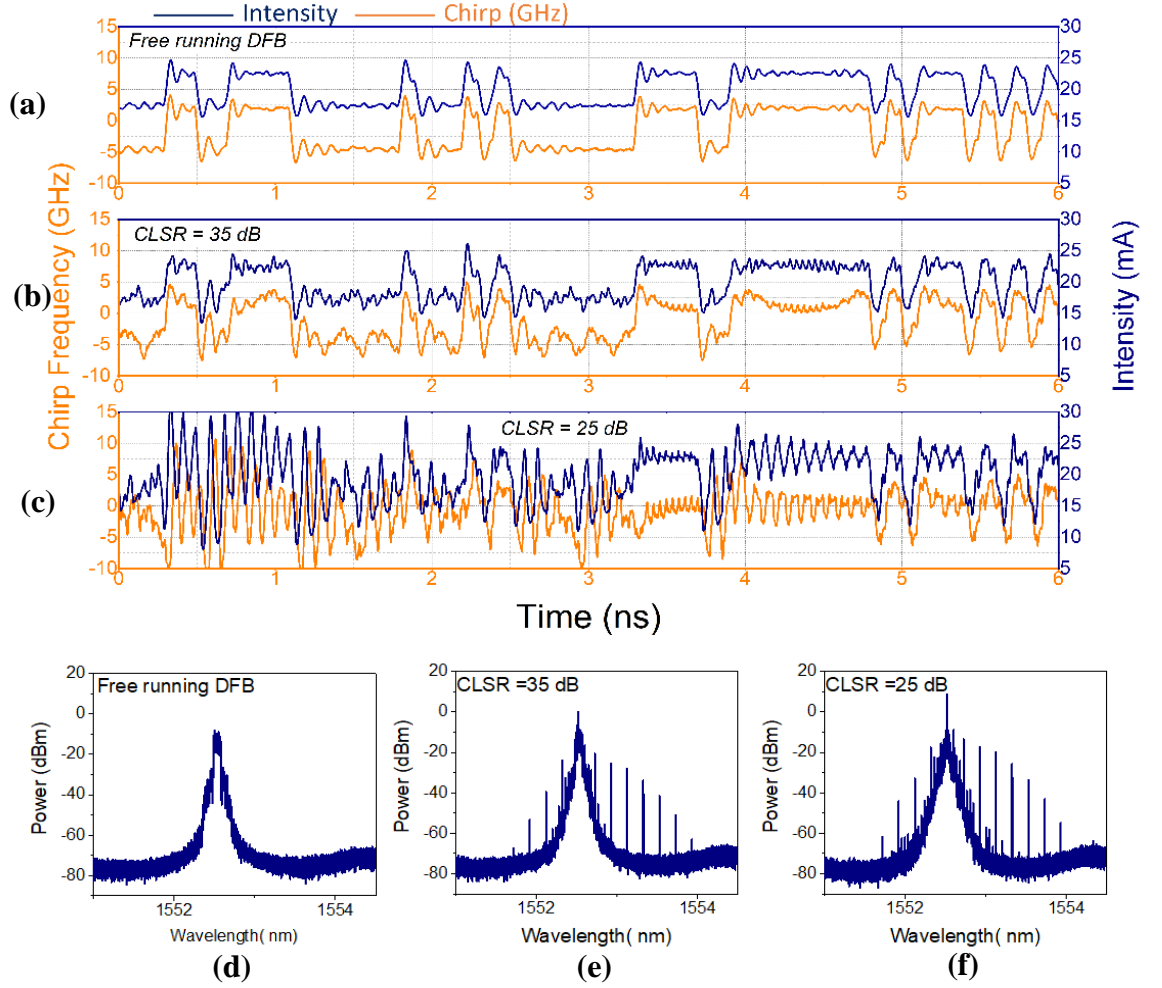
Figure 5.6 Analysis of chirp for various scenarios (a) free-running DFB, active demultiplexer with CLSR of (b) 35 dB, (c) 25 dB, simulated optical spectra of directly modulated DFB laser with (d) no injection, injection locked with CLSR of (e) 35 dB, and (f) 25 dB. Simulation resolution: 20 MHz.

However, such a high CLP could not be achieved employing the proposed active demultiplexer, as the increase in CLP decreases the CLSR (deleterious for system performance). To overcome this drawback and reap the benefits of OIL such as chirp reduction and enhancement of modulation bandwidth, a novel dual-stage active

demultiplexer is proposed. The VPI simulation schematic of the proposed approach, shown in Figure 5.8 (a), comprises two active demuxes in cascade, where Demux 1 acts as a filter and an amplifier (boost the injection power into the next stage) and Demux 2 is used as a modulator. The output of Demux 1 with an average power of 11 dBm is injected into the directly modulated Demux 2, which yields a significant reduction of the chirp, as shown in Figure 5.7 (c). The corresponding optical spectrum of the directly modulated dual-stage Demux is depicted in Figure 5.8 (d).
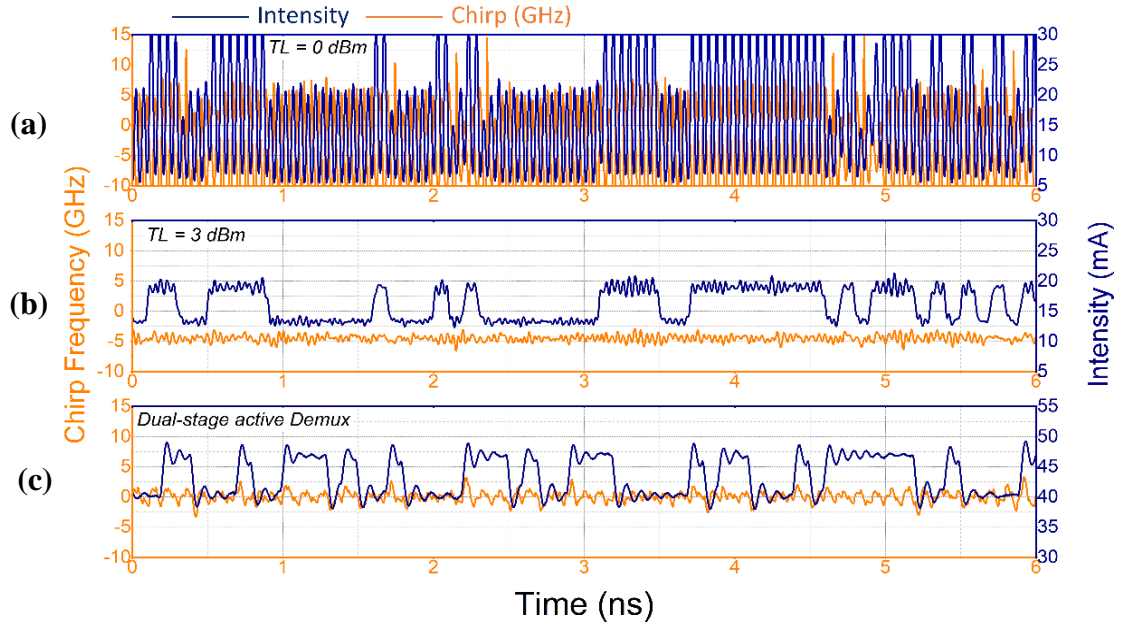
Figure 5.7 Analysis of chirp for various scenarios (a) TL locked Demux P =0 dBm, (b) TL locked Demux P = 3 dBm, (c) proposed dual-stage active Demux.

Additionally, the dual-stage active demultiplexer can be employed to improve/increase the CLSR. By adjusting the power of Demux 1 injected into Demux 2 as well as the frequency detuning between the two lasers (to avoid nonlinear phenomena such as spatial hole burning or carrier heating [36]), the final CLSR can be optimised. Figure 5.8 (c), shows the optical spectrum of the Demux 2, when the signal from Demux 1 (CLSR of 32 dB) is attenuated by 15 dB before being injected into Demux 2. From the figure, it can be seen that the cascade of demultiplexers can enhance the CLSR by 15 dB. The results prove

that by employing two active demultiplexers, both conflicting (opposing) requirements of low (reduced) chirp and high (improved) CLSR could be attained.

(a)

(b) **(c)** **(d)**
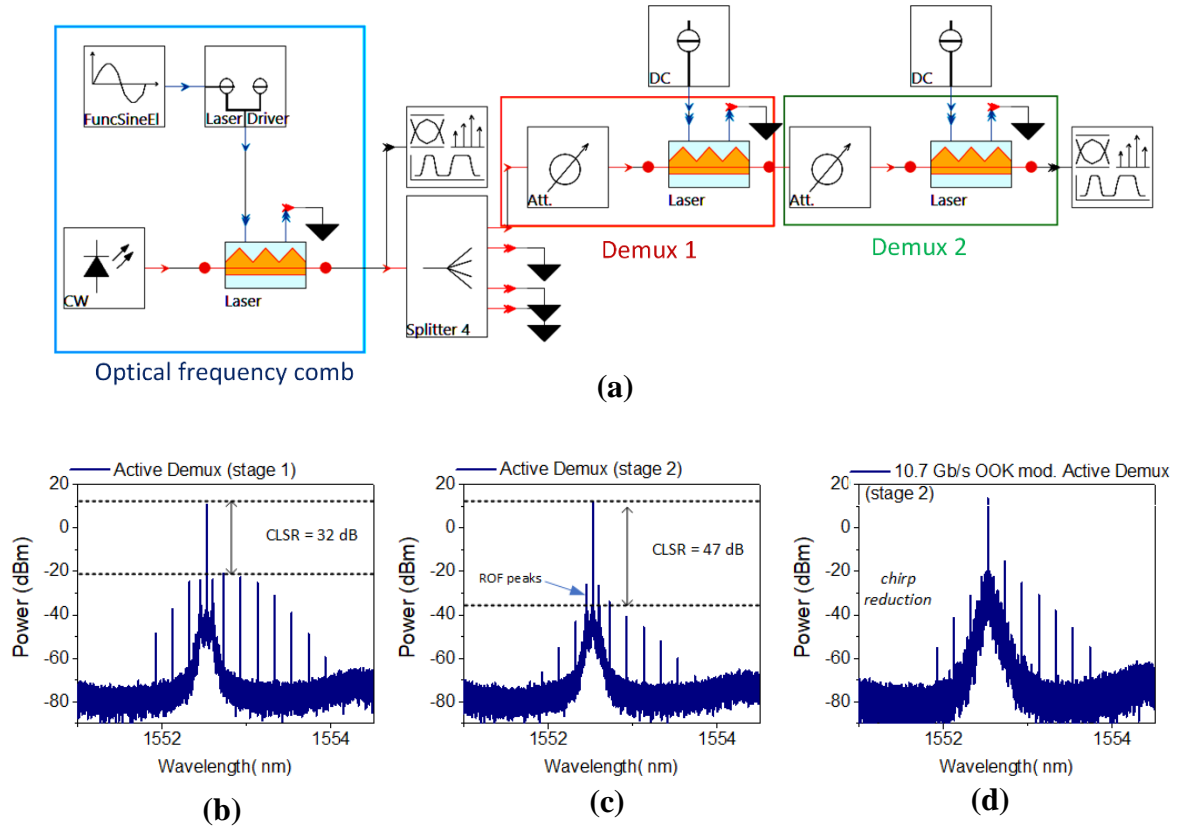
Figure 5.8 Simulation: (a) VPI schematic of the proposed OFC transmitter employing dual-stage active demultiplexer. Simulation results (b) Demux 1 with CLSR of 32 dB, (c) Demux 2 with CLSR of 47 dB, and (d) directly modulated 10.7 Gb/s OOK Demux 2 output. Simulation resolution: 20 MHz.

5.3 Performance Evaluation of a 200 Gb/s Directly Modulated DMT System Employing Active Demultiplexers

5.3.1 Two-channel 4- and 16-QAM DMT system
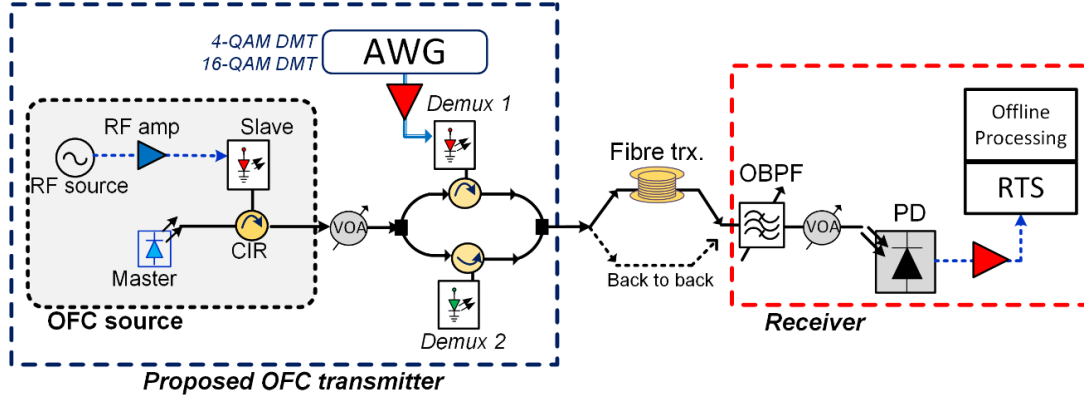
Figure 5.9 Experimental set-up of the proposed OFC based two-channel DMT transmitter employing an active demultiplexer. Here, CIR: circulator, AWG: arbitrary waveform generator, OBPF: optical bandpass filter, VOA: variable optical attenuator, PD: photodiode, RTS: real-time oscilloscope.

The proposed transmitter system, shown in Figure 5.9, is similar to the previously demonstrated OOK system except that the Demux 1 is directly modulated with a QAM DMT signal[2]. At the transmitter, an EI-GSL generates an OFC with an average power of 6 dBm and an FSR of 12.5 GHz, as shown in Figure 5.10 (a). It consists of 12 and 24 comb tones within 3 dB and 20 dB from the spectral peak, respectively. Conventionally, while using passive demultiplexers, only 12 tones with powers within 3 dB from the spectral peak would be used for data transmission. This ensures a near-uniform performance across all the channels. However, with the active multiplexer, data can be successfully transmitted using comb lines (~23) that are 20 dB below the spectral peak whilst ensuring near-uniform performance. This stems from the fact that as long as the comb tone has sufficient power to achieve a stable injection locking of the demultiplexer, the power of the filtered tone at the output of the demultiplexer will remain constant (equal

---

[2] 4- and 16-QAM DMT signal generation code was developed by Dr. Syed Tajmmul Ahmad (DCU).

to the output power of the demultiplexing laser). Thus, the number of channels available from a given OFC is enhanced, resulting in a significant reduction of the per-channel cost and power consumption of the transmitter.

The output of the OFC is split using a 50:50 coupler and injected, via circulators, into two active demultiplexers. The injected CLP is set, using inline VOA, to -27 dBm (for lines within 3 dB from the spectral peak) and -35 dBm (for lines 20 dB below the spectral peak), to yield a CLSR of 35 dB, as depicted in Figure 5.10 (c). Since the proposed demultiplexing technique is based on the passive splitting of the comb output, the attenuation values at the inline VOAs: 28 dB (for tones 3 dB from the spectral peak) and 20 dB (tones 20 dB below the spectral peak) can be considered as the power budget determining the maximum split ratio. Hence, with an attenuation of 28 dB and 20 dB, a split ratio of 1:512 and 1:64 could be realised [37], whilst ensuring that stable injection locking and an optimum CLSR are attained. Thus, the same comb could be used as an input to many demultiplexers within the system, ensuring a reduction in cost and complexity.

The filtered lines are recombined using a 3 dB coupler and transmitted over different link lengths of SSMF (an average optical launch power of 8.6 dBm). At the receiver, the modulated signal is filtered using an OBPF with a 3-dB bandwidth of 28 GHz. A VOA is used to vary the received optical power falling on a 20 GHz PD. Subsequently, the signal is electrically amplified and then captured using a real-time oscilloscope operating at 100 GSa/s. Finally, offline processing (re-sampling, timing synchronization, phase estimation, and BER measurements) is performed in MATLAB. To evaluate the system performance, BER measurements versus ROP are carried out for three different transmission cases: i) back-to-back (BtB), ii) 25 km, and iii) 40 km SSMF transmission for Ch. 1 (middle comb line) and Ch. 4 (comb line with power 20 dB below the spectral peak of the OFC).
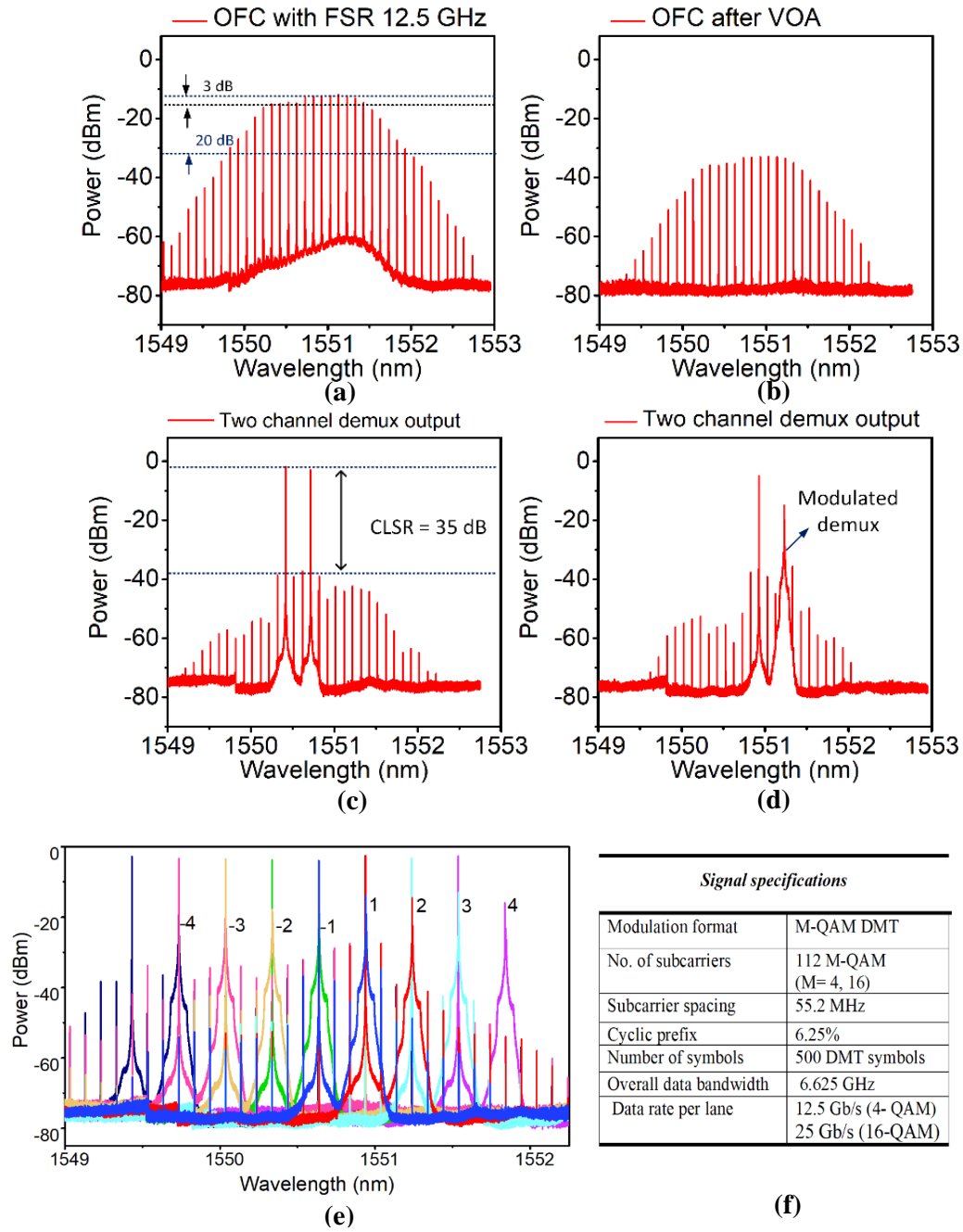
Figure 5.10 Optical spectra of (a) EI-GSL OFC with FSR of 12.5 GHz, (b) OFC after VOA, (c) combined two demultiplexed channel with CLSR of 35 dB, (d) combined demultiplexers output with Demux 1 modulated with M-QAM DMT signal, (e) overlapped 8 demultiplexed channels within a bandwidth of 2.4 nm, each modulated with M-QAM DMT signals, and (f) DMT signal specifications. OSA resolution: 20 MHz, fixed optical attenuation at the input of the OSA: 10 dB.

5.3.1.1   4 QAM DMT System
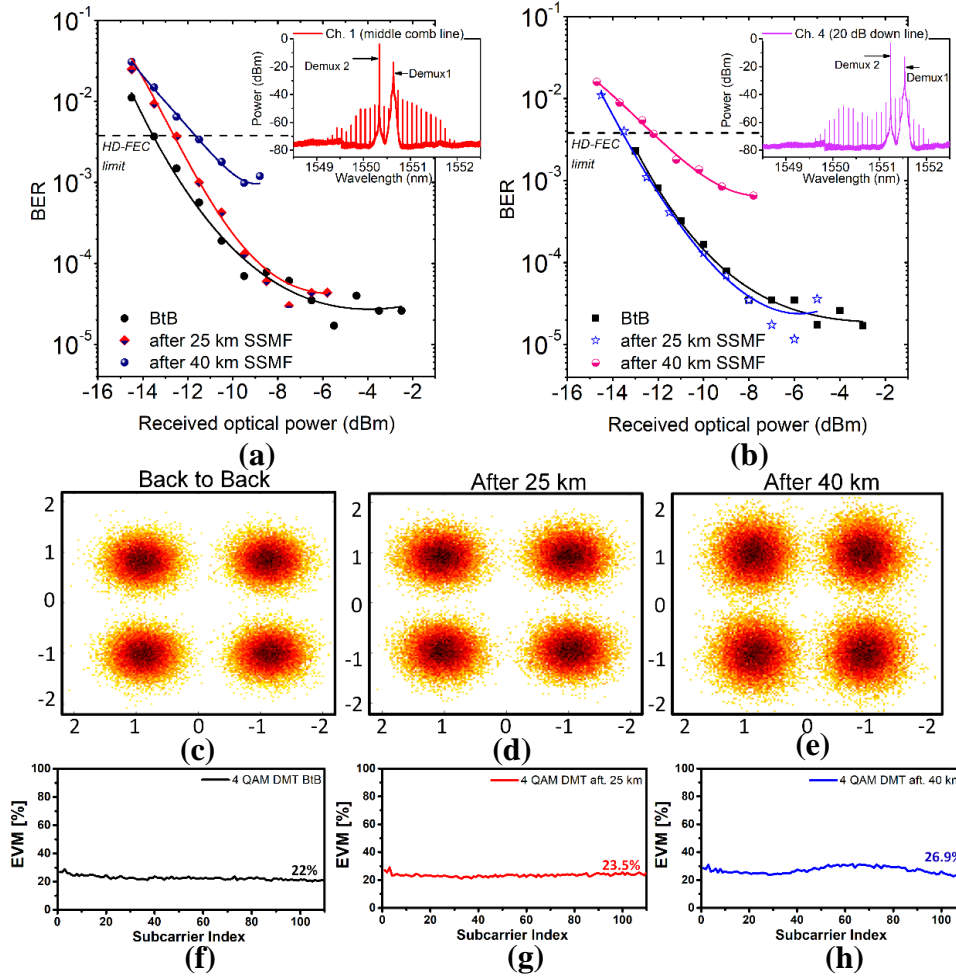
Figure 5.11 BER vs received optical power of (a) Ch. 1, (b) Ch. 4 (20 dB below spectral peak) for back-to-back (BtB), 25 km, and 40 km of fibre transmission The insets show the spectrum of the directly modulated Ch. 1 and Ch. 4 combined with a second demultiplexed line separated by 37.5 GHz. Constellation diagrams of Ch. 1 at received optical power of −9.5 dBm for (c) back-to-back and after (d) 25 km, and (e) 40 km fibre transmission and corresponding EVM plots for (f) back-to-back and after (g) 25 km, and (h) 40 km fibre transmission

The BER vs ROP plots for the three transmission cases (BtB, 25 and 40 km) for Ch. 1 and Ch. 4, are shown in Figure 5.11 (a) and (b). The insets depict the combined output spectra of Ch. 1 modulated with data (Demux 1) and an unmodulated line (Demux 2). The performance evaluation for the 4-QAM DMT system is summarised in Table 5-2. An improvement in the BER with an increase of the ROP is observed for the BtB and 25 km

transmission cases until it reaches −6 dBm. Beyond that value, the PD saturates, and nonlinearities start to degrade the performance of the system.

From Figure 5.11 (a) it can be seen that, at the HD-FEC limit, the fibre transmission introduces a power penalty (relative to the BtB case) of 0.8 and 2 dB for 25 and 40 km transmission respectively. This can be attributed to the interference caused by the unsuppressed comb tones, which are also modulated with the data as they pass through Demux 1. As a result, both the demultiplexed tone and the unsuppressed lines are modulated with the same DMT signals. When transmitted over fibre, chromatic dispersion causes a phase mismatch between these data signals. The further degradation after 40 km can be attributed to the insufficient cyclic prefix in DMT signal. At the receiver, the unsuppressed tones are detected on the PD, and may interfere with the in-band desired data signal. Figure 5.11 (c) - (e) and (f) – (g) show the constellation diagrams and EVM plots for the 4 QAM DMT system, at an ROP of −9.5 dBm, for the BtB, 25 km, and 40 km fibre transmission scenarios respectively. From the constellation diagrams, it is clear that a significant amount of noise is present in the symbols when the signal is transmitted over the 40 km SSMF link.

Similarly, the BER performance of the directly modulated Ch. 4 is also evaluated and illustrated in Figure 5.11 (b). The plot shows a negligible power penalty, at the HD-FEC limit, for the 25 km transmission case. For the 40 km transmission case, a penalty of 1.6 dB is recorded, which is slightly lower than in the case of Ch. 1. This can be attributed to the reduced interference from adjacent channels, as the power of the unsuppressed tones that pass through the receiver OBPF is much lower in this case, leading to a lower level of interference.

Table 5-2 4-QAM DMT system performance summary for Ch. 1 and Ch. 4

Channel	Receiver sensitivity (HD-FEC)		Power penalty (HD-FEC)	
	25 km	40 km	25 km	40 km
Ch. 1	−12.5 dBm	−11.5 dBm	0.8 dB	2 dB
Ch. 4	−13.5 dB,	−12.25 dBm	0 dB	1.6 dB

5.3.1.2 16 QAM DMT System
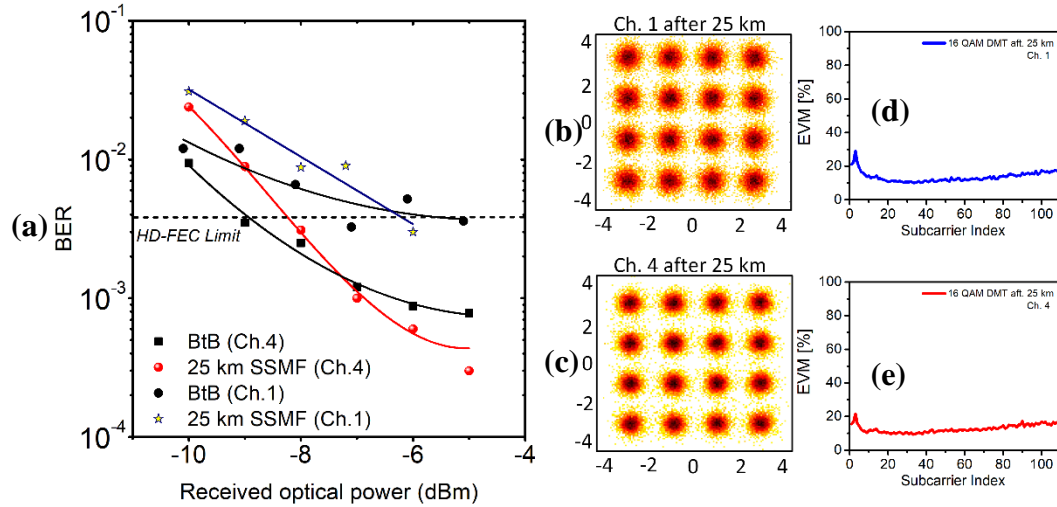
Figure 5.12 (a) plot of BER vs received optical power for BtB and 25 km fibre transmission of Ch. 1 and Ch. 4 modulated with 16-QAM DMT signal. 16-QAM DMT constellation diagrams at an ROP of −6 dBm and after 25 km SSMF transmission with (b) Ch. 1 and (c) Ch. 4 and corresponding EVM's for (d) Ch. 1, (e) Ch. 4

In order to further increase the data rates, the Demux's are then modulated with 16-QAM DMT signal and the performance of Ch. 1 and Ch. 4 are examined. Figure 5.12 (a) shows the plot of the BER versus ROP of both channels, for the BtB and 25 km SSMF transmission scenarios. For both cases, a BER below the HD-FEC limit is achieved after 25 km. At the FEC limit, a power penalty of 2 dB is observed for Ch. 1 relative to Ch. 4. As discussed earlier, this penalty is due to the higher power of the unsuppressed comb tones. Figure 5.12 (b) and (c) show the constellation diagrams of 16-QAM DMT signals and corresponding EVMs plots in Figure 5.12 (d) and (e) for Ch. 1 and Ch. 4 respectively, at an ROP of −6 dBm. From the constellation diagrams, a large spread in all the symbols can be observed with Ch. 1 (middle channels) due to interference, when compared to Ch. 4 (20 dB below the spectral peak channels). It is important to mention that 25 km transmission case does not outperform the BtB case (for Ch. 4). This can be attributed to measurement error, as the noise process in the BtB is quite different from the transmission case.

The results above demonstrate the successful transmission of 12.5 Gb/s/λ 4-QAM and 25 Gb/s/λ 16-QAM DMT signals over 40 km and 25 km, respectively. Furthermore, by employing all 8 comb lines, the system can potentially achieve an aggregate data rate of 100 Gb/s (8×12.5 Gb/s) for 4-QAM DMT and 200 Gb/s (8×25 Gb/s) for 16-QAM DMT over 40 km and 25 km of fibre transmission respectively.

5.3.2 Four-channel 4 QAM DMT DWDM system
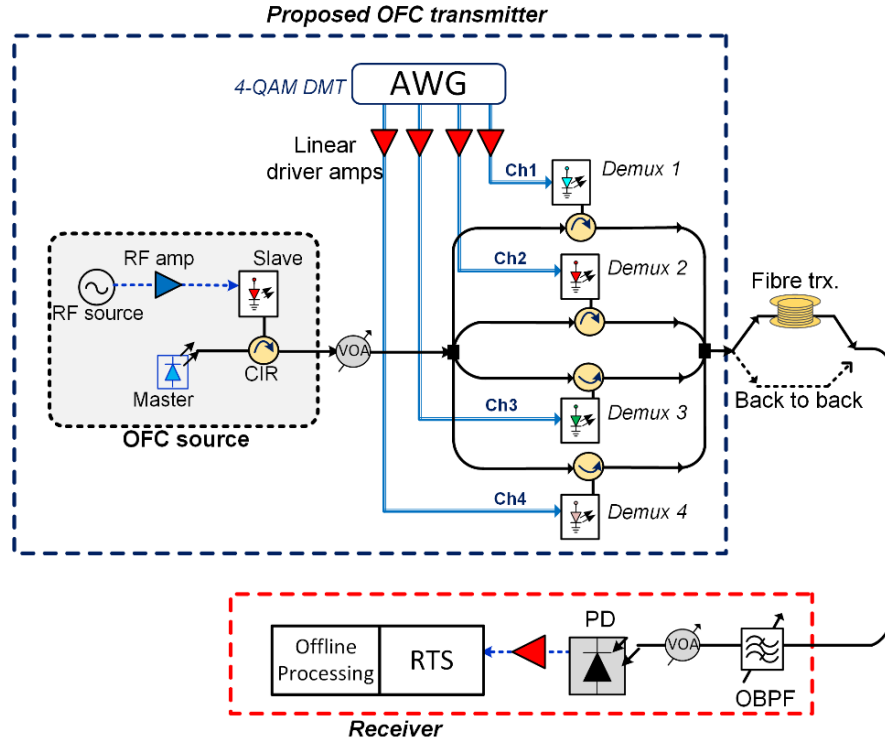
Figure 5.13 Experimental setup of the proposed DWDM 4-QAM DMT transmission system using an OFC and an active demultiplexer. Here: AWG: arbitrary waveform generator, VOA: variable optical attenuator; CIR: circulator, OBPF: optical bandpass filter, PD: photodiode, RTS: real-time oscilloscope.

In the previous demonstrations, a frequency separation of 37.5 GHz between the two channels has been used to avoid inter-channel interference. This results in a poor SE and wastage of potential carriers (OFC lines). To improve the efficiency of the system, a 4 channel DWDM DMT transmitter is experimentally demonstrated, where the data/signal bandwidth is optimised taking into account the FSR of the comb and allowing the use of

all the available OFC lines within 20 dB from the spectral peak. The experimental setup of the proposed DWDM transmitter is shown in Figure 5.13. An OFC with an FSR of 12.5 GHz (as shown in Figure 5.14 (a)) is split using a 1:4 splitter and injected into 4 demultiplexers. The CLP, (after 1:4 splitter) is adjusted to −22.5 dBm to achieve the demultiplexing of the OFC lines with a CLSR of 30 dB at each Demux output. The optical spectra of the 4 channel demultiplexed and subsequently combined signal are depicted in Figure 5.14 (b). Three different sets of 4 channels, across the entire comb, are selected to demonstrate the ability of the demultiplexer to utilise OFC tones within 20 dB from the spectral peak.

The 4-QAM DMT signal bandwidth is set to 4.375 GHz (to fit OFC FSR of 12.5 GHz), thus giving a raw (actual) data rate of 8.75 Gb/s (8.25 Gb/s) per channel. Four DMT signals are generated, combined with the bias current and used to directly modulate all four Demux lasers. The outputs of the demultiplexer are then combined, using a 4x1 optical coupler, to form a DWDM signal with an average power of 7.6 dBm. Figure 5.14 (c), shows the overlapped optical spectra of the directly modulated channels that were tested (12 in total). The combined DWDM signal is then transmitted over a 25 km SSMF and the performance of each channel is evaluated by measuring the BER as a function of the received optical power. A BER below the HD-FEC limit for all 12 channels is achieved after transmission over a 25 km SSMF link. Using the numbering scheme from Figure 5.14 (c), it can be seen that Ch. 1-4 refer to OFC lines within 3 dB, while Ch. −4 to −1 and Ch. 5 to 8 are the lower power OFC lines. To understand the impact of adjacent channel interference in the DWDM system, the performance of the following channels are compared: (i) Ch. 1, which experiences interference mainly from the modulated Ch. 2 and unmodulated unsuppressed OFC lines, (ii) Ch. 2, which is affected by the interference from two modulated channels 2 and 4, (iii) Ch. −4, for which the interference source is Ch. −3 and low power OFC lines (unmodulated). Finally, the performance of Ch. −4 is compared with a free-running laser (with no OFC injection). The plot of the BER vs ROP for the above-mentioned cases is shown in Figure 5.15 (a)-(d). The insets (i)-(iii) show the spectrum at the output of the OBPF filter, when the received signal is on

(red line) and off (black line), the latter showing the interference affecting different channels.
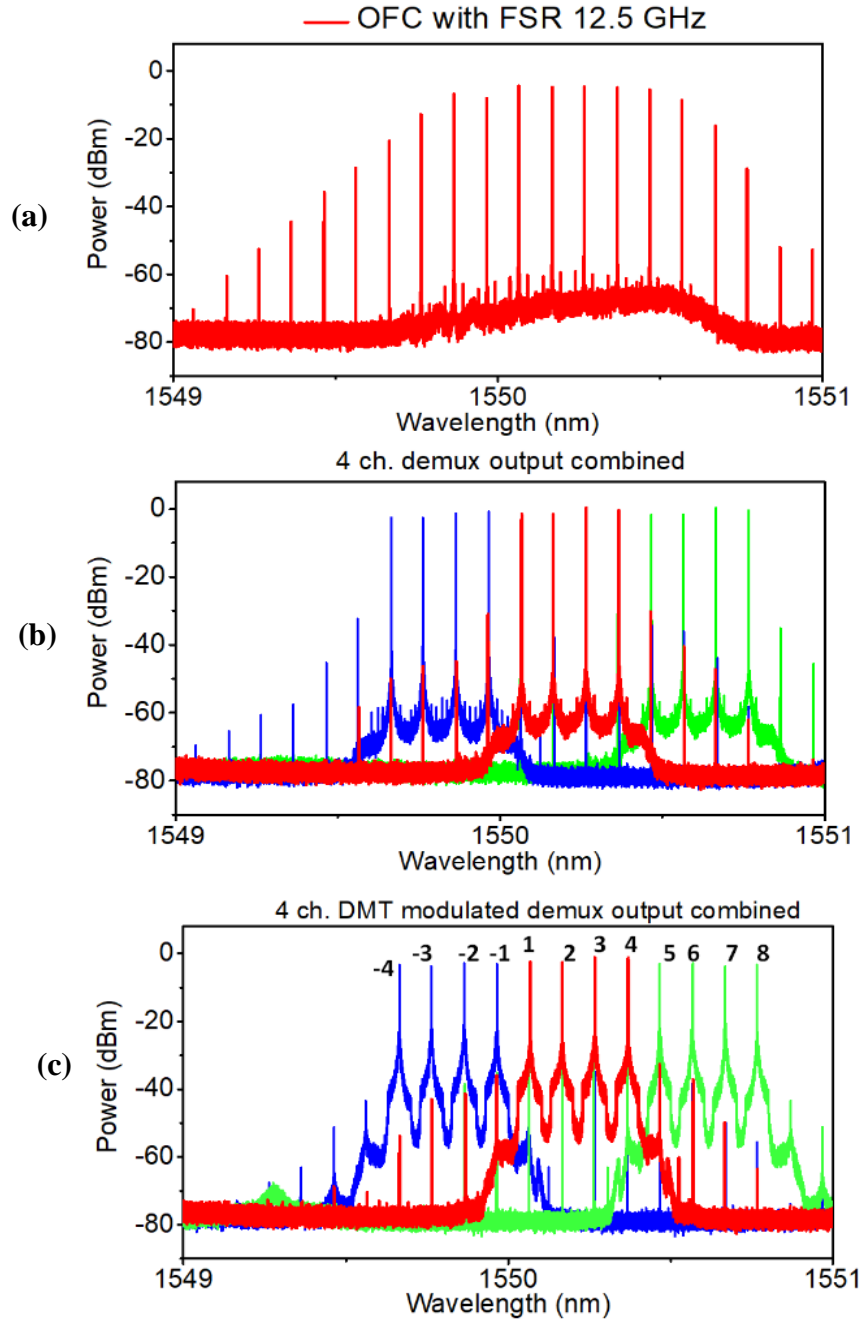
Figure 5.14 Optical spectra of (a) EI-GSL OFC with FSR of 12.5 GHz, the 12 channels under test (b) unmodulated, (c) modulated with the DMT data signal. OSA resolution: 20 MHz.
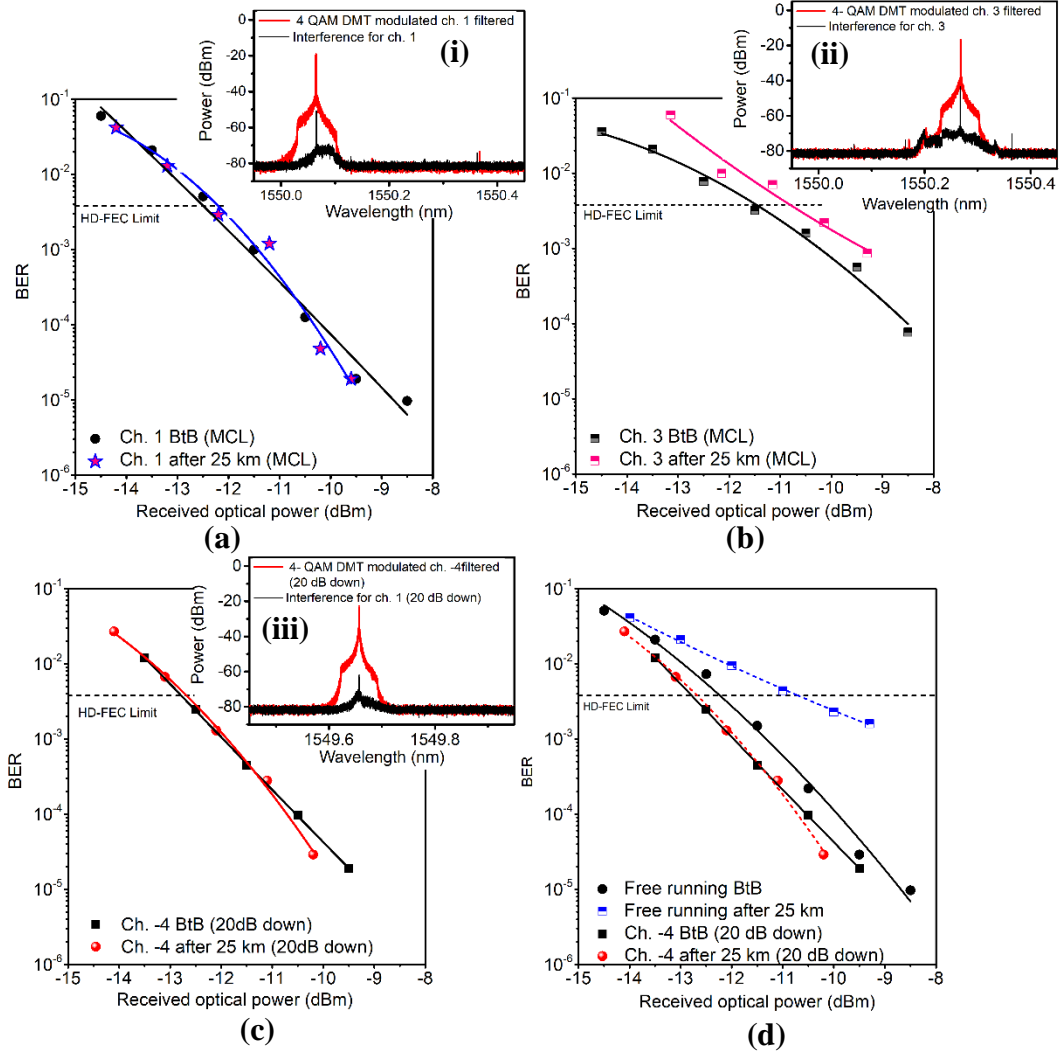
Figure 5.15 Plot of BER vs received optical power for BtB and 25 km fibre transmission of (a) Ch. 1, (b) Ch. 3, (c) Ch. −4, (d) comparison between free running case and Ch −4. Insets (i)-(iii) show the optical spectra of OBPF output with the received signal on (red) and off (black trace).

From Figure 5.15, it can be seen that Ch. −4 performs best amongst all the channels. It portrays a receiver sensitivity of −12.7 dBm (at HD-FEC) and a negligible power penalty when the signal is transmitted over 25 km of SSMF. On the other hand, Ch. 3 shows a receiver sensitivity of −10.8 dBm and incurs a power penalty of 0.7 dB due to the fibre transmission (compared to its BtB). This is due to strong cross-channel interference from neighbouring channels as depicted in the inset (ii) of Figure 5.15 (b). Similarly, for Ch. 1 the fibre transmission introduces a minimal penalty of 0.2 dB, because in this case, only one of the adjacent channels is modulated, limiting the amount of interference. It is also

important to note that Ch. −4 (benefiting from OIL of the OFC) outperforms the free-running Demux laser by ~ 2 dB as shown in Figure 5.15 (d). This also highlights the unique property of the active demultiplexer, which is that the initial low power of the comb tone has no bearing on the final performance of the demultiplexed channel. A summary of the performance evaluation is summarised in Table 5-3.

Table 5-3 Performance evaluation for various interference scenarios

Channel	Receiver sensitivity (at HD-FEC)		Power penalty (HD-FEC)	
	BtB	25 km trx.	Compared to its BtB	Ch. −4
Ch. −4	−12.7 dBm	−12.7 dBm	0	--
Ch. 1	−12.4 dBm	−12.2 dBm	0.2 dB	0.5 dB
Ch. 3	−11.5 dBm	−10.8 dBm	0.7 dB	2 dB
Free-running	−10.8 dBm	−12 dBm	1.2 dB	2 dB

Finally, the proposed OFC transmitter with the multifunctional active demultiplexer is compared with some of the currently used data centre technologies. Table 5-4 shows the comparison of key performance indicators (KPIs) associated with some currently used technologies in datacentres [4], [5], [14], [15] and and the proposed scheme. It demonstrates the benefits of the proposed transmitter and highlights the potential improvements that if implemented, would make the proposed transmitter a highly attractive solution for deployment in data centres and other short-reach applications.

Table 5-4 Comparison of KPIs associated with some currently used technologies and the proposed scheme. Here, DMLs: directly modulated lasers, EML: externally modulated lasers, DFB: distributed feedback laser, SOA: semiconductor optical amplifier, APD: avalanche photodiode

Parameters	100G-LR4	100G-ER4	400G-LR4/8	OFC + active demultiplexer
Data rate	25 Gb/s	25 Gb/s	100/50 Gb/s	12.5/25 Gb/s
Lane count	4	4	4/8	8 [1]
Signal rate/lane	25.78 GBd	25 GBd	106/53 GBd	12.5 / 25 GBd [2]

Centre wavelength	1310 nm	1310 nm	1550 nm	1550 nm [3]
Modulation format	OOK / NRZ	PAM4	PAM4	4/16-QAM DMT
Laser source	4 DMLs	4 EMLs	4/8 DFBs	OFC + DFB/ lane [4]
Channel spacing	~4.5 nm	~4.5 nm	20 nm	12.5 / 37.5 GHz
TEC	250 mW / lane	300 mW / lane	Required	Not a strict req. OFC provides fixed channel spacing [5]
Reach	10 km	40 km	40 km	25 / 40 km (DWDM)
Optical amplifier	Yes	Yes	Yes	No
Receiver	PIN	(SOA + PIN)	APD	PIN
Receiver sensitivity	-8.6 dBm	-21.6 dBm	< -9.1 dBm	-10.8 dBm [6]
Power budget	30 dB	32 dB	21.9 dB	28 dB [6]
Cost	Low	Medium	High	Medium [7]

[1] Can be further increased through optimisation of the FSR and channel bandwidth.

[2] Can be increased by increasing the signal bandwidth.

[3] Can also be realised in 1310 nm to extend the reach.

[4] Enables dense channel spacing.

[5] When integrated, temperature variation affects OFC and demultiplexer in a similar way.

[6] Proof of concept result (after 25 km) can be improved significantly.

[7] Integration and commercial production will reduce the cost.

5.4 Conclusions

In this chapter, a novel flexible optical transmitter for data centre and short-reach application is proposed and experimentally demonstrated. It entails the use of an OFC followed by an active demultiplexer. The latter is a single device able to simultaneously perform functionalities of demultiplexing, ultra-low noise optical amplification, power equalisation, and data modulation. The potential of the proposed method has been verified by successfully demultiplexing a 12.5 GHz spaced OFC line, modulating it with 10.7 Gb/s

data, and achieving error-free operation, when transmitted over 3 km of SSMF. Then, the impact of the injection of an OFC tone on the frequency chirp (induced by direct modulation of the Demux) is investigated through VPI simulations.

Furthermore, the proposed transmitter system is examined with advanced multi-level amplitude modulation formats such as 4-, 16-QAM DMT system. The power equalisation property of the active demultiplexer provides an enhanced channel count, as any comb tone with sufficient power to achieve a stable locking of the demultiplexer, can be used for the data modulation (within 20 dB from spectral peak). Thus, using the proposed transmitter, an aggregate data rate of 100 Gb/s (12.5 Gb/s/λ) using 4-QAM and 200 Gb/s (25 Gb/s/λ) using 16-QAM system is realised. The implemented system experimentally demonstrates error-free (below HD-FEC limit) transmission over 40 km and 25 km (for 4- and 16-QAM signals respectively). A four-channel DWDM DMT system is then released by utilising all the OFC lines (FSR of 12.5 GHz) available for data modulation to increase the overall data rate and spectral efficiency of the transmitter. The performance of various channels and the impact of cross-channel interference were evaluated.

As the proposed architecture is entirely based on direct modulation (for both comb generation and data modulation) it is simple and cost-efficient. Additionally, the multifunctionality of the active demultiplexers significantly reduces the number of components (by replacing the need for external modulators and amplifiers) and increases the number of carriers available for data modulation. This in turn increases the energy efficiency and reliability, while reducing the cost and footprint of the transmitter. Finally, the entire transmitter can be integrated onto a single chip, offering a further reduction in the transmitter footprint, cost, and energy consumption. Hence, the proposed technique is well suited for next-generation short-reach and specifically intra data centre networks.

5.5 References

[1] J. Fruhlinger and Z. Kerravala, "What are data centers? How they work and how they are changing in size and scope", *Network World*, 2020. [Online]. Available: https://www.networkworld.com/article/3599213/what-are-data-centers-how-they-work-and-how-they-are-changing-in-size-and-scope.html (accessed Oct. 08, 2021).

[2] CISCO 2017, "The Zettabyte Era: Trends and Analysis," 2017. [Online]. Available: http://www.hit.bme.hu/~jakab/edu/HTI18/Litr/Cisco_The_Zettabyte_Era_2017June__v ni-hyperconnectivity-wp.pdf. (accessed Jan. 5, 2020).

[3] A. Ghiasi, "Large data centers interconnect bottlenecks," *Optics Express*, vol. 23, no. 3, pp. 2085, 2015, DOI: 10.1364/oe.23.002085.

[4] C. Lam, H. Liu, B. Koley, X. Zhao, V. Kamalov, and V. Gill, "Fiber optic communication technologies: What's needed for datacenter network operations," *IEEE Communications Magazine*, vol. 48, no. 7, pp. 32–39, 2010, DOI: 10.1109/MCOM.2010.5496876.

[5] Q. Cheng, M. Bahadori, M. Glick, S. Rumley, and K. Bergman, "Recent advances in optical technologies for data centers: a review," *Optica*, vol. 5, no. 11, p. 1354, 2018, DOI: 10.1364/optica.5.001354.

[6] X. Zhou, H. Liu, and R. Urata, "Datacenter optics: requirements, technologies, and trends (Invited Paper)," *Chinese Optics Letters*, vol. 15, no. 5, pp. 120008, 2017, [Online]. Available: http://www.osapublishing.org/col/abstract.cfm?URI=col-15-5-120008

[7] M. Morsy-Osman and D. V. Plant, "A comparative study of technology options for next generation intra-and inter-datacenter interconnects," in *Optical Fiber Communications Conference and Exposition, OFC 2018 - Proceedings*, 2018, pp. 1–3.

[8] Y. Shen, A. Gazman, Z. Zhu, M. Y. Teh, M. Hattink, S. Rumley, P. Samadi, and K. Bergman, "Autonomous dynamic bandwidth steering with silicon photonic-based wavelength and spatial switching for datacom networks," *Optical Fiber Communications Conference and Exposition, OFC 2018 - Proceedings*, pp. 1–3, 2018.

[9] Q. Cheng, S. Rumley, M. Bahadori, and K. Bergman, "Photonic switching in high performance datacenters [Invited]," *Optics Express*, vol. 26, no. 12, pp. 16022, 2018, DOI: 10.1364/oe.26.016022.

[10] H. Liu, C. F. Lam, and C. Johnson, "Scaling optical interconnects in datacenter networks: Opportunities and challenges for WDM," *Proceedings - 18th IEEE Symposium on High Performance Interconnects, HOTI 2010*, pp. 113–116, 2010, DOI: 10.1109/HOTI.2010.15.

[11] S. Gringeri, E. B. Basch, and T. J. Xia, "Technical considerations for supporting data rates beyond 100 Gb/s," *IEEE Communications Magazine*, vol. 50, no. 2, pp. 21–30, 2012, DOI: 10.1109/MCOM.2012.6146482.

[12]   X. Zhou, R. Urata, and H. Liu, "Beyond 1 Tb/s Intra-Data Center Interconnect Technology: IM-DD or Coherent?," *Journal of Lightwave Technology*, vol. 38, no. 2, pp. 475–484, 2020, DOI: 10.1109/JLT.2019.2956779.

[13]   T. Rokkas, I. Neokosmidis, B. Shariati, and I. Tomkos, "Techno-Economic Evaluations of 400G Optical Interconnect Implementations for Datacenter Networks," in *Optical Fiber Communication Conference*, 2018, p. M1A.1. DOI: 10.1364/OFC.2018.M1A.1.

[14]   IEEE, "IEEE Standard for Ethernet - Amendment 10: Media Access Control Parameters, Physical Layers, and Management Parameters for 200 Gb/s and 400 Gb/s Operation," *IEEE Std 802.3bs-2017*. pp. 1–372, 2017. DOI: 10.1109/IEEESTD.2017.8207825.

[15]   QSFP-DD, "Accelerating 400GbE Adoption with QSFP-DD," 2017. [Online]. Available: http://www.qsfp-dd.com/wp-content/uploads/2017/03/QSFP-DD-whitepaper-15.pdf (accessed Feb. 20, 2020).

[16]   R. Nagarajan, M. Filer, Y. Fu, M. Kato, T. Rope, and J. Stewart, "Silicon Photonics-Based 100Gbit/s, PAM4, DWDM Data Center Interconnects," *Journal of Optical Communications and Networking*, vol. 10, no. 7, pp. B25–B36, 2018, DOI: 10.1364/JOCN.10.000B25.

[17]   S. Zhou, X. Li, L. Yi, Q. Yang, and S. Fu, "Transmission of 2 × 56 Gb/s PAM-4 signal over 100 km SSMF using 18 GHz DMLs," *Optics Letters*, vol. 41, no. 8, pp. 1805–1808, 2016, DOI: 10.1364/OL.41.001805.

[18]   F. Li, X. Xiao, J. Yu, X. Li, S. Shi, C. Ge, Y. Xia, and Y. Chen, "Real-time reception of four channels 50 Gb/s class high-level QAM-DMT signal in short reach," in *2016 Optical Fiber Communications Conference and Exhibition, OFC 2016*, 2016, pp. 7–9. DOI: 10.1364/ofc.2016.th2a.3.

[19]   T. Benson, A. Akella, and D. A. Maltz, "Network traffic characteristics of data centers in the wild," *Proceedings of the ACM SIGCOMM Internet Measurement Conference, IMC*, pp. 267–280, 2010, DOI: 10.1145/1879141.1879175.

[20]   G. Zervas, H. Yuan, A. Saljoghei, Q. Chen, and V. Mishra, "Optically disaggregated data centers with minimal remote memory latency: Technologies, architectures, and resource allocation [Invited]," *IEEE/OSA Journal of Optical Communications and Networking*, vol. 10, no. 2, pp. A270–A285, 2018, DOI: 10.1364/JOCN.10.00A270.

[21]   A. R. C. Serrano, C. de Dios Fernandez, E. P. Cano, M. Ortsiefer, P. Meissner, and P. Acedo, "VCSEL-based optical frequency combs: Toward efficient single-device comb generation," *IEEE Photonics Technology Letters*, vol. 25, no. 20, pp. 1981–1984, 2013, DOI: 10.1109/LPT.2013.2280700.

[22]   T. Fortier and E. Baumann, "20 years of developments in optical frequency comb technology and applications," *Communications Physics*, vol. 2, no. 1, p. 153, 2019, DOI: 10.1038/s42005-019-0249-y.

[23]   M. Imran, P. M. Anandarajah, A. Kaszubowska-Anandarajah, N. Sambo, and L. Poti, "A Survey of Optical Carrier Generation Techniques for Terabit Capacity Elastic Optical

Networks," *IEEE Communications Surveys and Tutorials*, vol. 20, no. 1, pp. 211–263, 2018, DOI: 10.1109/COMST.2017.2775039.

[24]   Kylia, "DWDM MUX/DEMUX," *Data sheet, 2008*. [Online]. Available: https://kylia.com/api_website_feature/files/download/11115/datasheet-MICS-V111.pdf (accessed Jul. 10, 2020).

[25]   Finisar, "Filter Bandwidth Definition of the WaveShaper S-series Programmable Optical Processor," *Data sheet,* 2012. [Online]. Available: https://teracomm.com/newsite/wp-content/uploads/2015/02/WaveShaper_Filter_Bandwidth_Defn.pdf. (accessed Jul. 10, 2020).

[26]   S. Fukushima, C. F. C. Silva, Y. Muramoto, and A. J. Seeds, "Optoelectronic millimeter-wave synthesis using an optical frequency comb generator, optically injection locked lasers, and a unitraveling-carrier photodiode," *Journal of Lightwave Technology*, vol. 21, no. 12, pp. 3043–3051, 2003, DOI: 10.1109/JLT.2003.822250.

[27]   A. C. Bordonalli, M. J. Fice, and A. J. Seeds, "Optical injection locking to optical frequency combs for superchannel coherent detection," *Optics Express*, vol. 23, no. 2, p. 1547, 2015, DOI: 10.1364/oe.23.001547.

[28]   P. D. Lakshmijayasimha, A. Kaszubowska-anandarajah, E. P. Martin, M. N. Hammad, P. Landais, and P. M. Anandarajah, "Characterization of a multifunctional active demultiplexer for optical frequency combs," *Optics and Laser Technology*, vol. 134, no. October 2020, pp. 4–8, 2021.

[29]   D. S. Wu, R. Slavik, G. Marra, and D. J. Richardson, "Direct Selection and amplification of individual narrowly spaced optical comb modes via injection locking: Design and characterization," *Journal of Lightwave Technology*, vol. 31, no. 14, pp. 2287–2295, 2013, DOI: 10.1109/JLT.2013.2262921.

[30]   M. Deseada Gutierrez Pascual, Vidak Vujicic, Jules Braddell, Frank Smyth, Prince M. Anandarajah, and Liam P. Barry, "InP photonic integrated externally injected gain switched optical frequency comb," in *Optics Letters*, vol. 42, no. , pp. 555-558, 2017.

[31]   M. D. G. Pascual, J. Braddell, F. Smith, and L. P. Barry, "Monolithically Integrated 1x4 Comb De-multiplexer Based on Injection Locking", in *18ᵗʰ European Conference on Integrated Optics*, 2016, pp. 37.

[32]   I. Garcés, A. Villafranca, and J. Lasobras, "Characterization of the chirp behavior of integrated laser modulators (ILM) by measurements of its optical spectrum," in *Semiconductor Lasers and Laser Dynamics III*, vol. 6997, 2008. DOI: 10.1117/12.781222.

[33]   S. Mohrdiek, H. Burkhard, and H. Walter, "Chirp Reduction of Directly Modulated Semiconductor Lasers at 10 Gb/s by Strong CW Light Injection," *Journal of Lightwave Technology*, vol. 12, no. 3, pp. 418–424, 1994, DOI: 10.1109/50.285323.

[34]   K. Sato, S. Kuwahara, and Y. Miyamoto, "Chirp characteristics of 40-Gb/s directly modulated distributed-feedback laser diodes," *Journal of Lightwave Technology*, vol. 23, no. 11, pp. 3790–3797, 2005, DOI: 10.1109/JLT.2005.857753.

[35]   S. Nishikawa, M. Gotoda, T. Nishimura, and Y. Tokuda, "Self-pulsation and sub-harmonic optical injection locking beyond 200 GHz using multi-electrode DFB lasers," in *Optical Amplifiers and Their Applications/Integrated Photonics Research*, 2004, paper IThD1.

[36]   A. D'Ottavi, E. Iannone, A. Mecozzi, S. Scotti, and P. Spano, "Investigation of carrier heating and spectral hole burning in semiconductor amplifiers by highly nondegenerate four-wave mixing," *Applied Physics Letters*, vol. 64, no. 19, pp. 2492–2494, 1994, DOI: 10.1063/1.111576.

[37]   M. Hajduczenia, S. Networks, and S. A. S. Pato, "Channel insertion loss for 1x64 and 1x128 split EPONs Task 1 – ad hoc on high split EPON systems," 2006. [Online] Available: https://www.ieee802.org/3/av/public/2006_11/3av_0611_hajduczenia_1.pdf (accessed April. 13, 2020).

6. Tunable Millimetre Wave Generation and A-RoF Distribution Employing OFC and Active demultiplexers

The emphasis of the previous chapter was on the suitability of the OFCs as multicarrier transmitters in high-capacity communication systems. In this chapter, applications of such transmitters in wireless/mobile telecommunication systems are explored. As wireless communication systems evolve towards the 5th generation and beyond (5G+), they are expected to offer higher capacity high data rate (up to 10 Gb/s), and low latency (< 1 ms) Fulfilment of such stringent requirements requires careful design of the mobile front- and backhaul network [1]-[3]. From a fronthaul perspective, photonically generated millimetre waves (mmW) with analog radio-over fibre (A-RoF) distribution can provide an efficient solution for future 5G+. In such systems, coherent heterodyning of two mutually coherent tones generated by an OFC source serves as a simple and cost-effective solution.

Nevertheless, the OFC-based A-RoF system suffers from challenges associated with the demultiplexing process, which could deteriorate the phase of the resultant mmW signal

and in turn affect the overall system performance. Hence, this chapter presents two OFC based A-RoF systems employing an active demultiplexer employed in different configurations. The first scheme examines the generation of an mmW whilst focussing on the multifunctionality of the active demultiplexers as a way of simplifying the transmitter. The second scheme concentrates on the tolerance of the active demultiplexer to the optical linewidth of the source. In summary, this chapter presents a comprehensive experimental characterisation of generated mmW signals, followed by its implementation in an A-RoF distribution system.

6.1 Introduction

Wireless networks are progressing towards 5G and beyond, which will provide the necessary infrastructure for next-generation bandwidth-hungry services such as autonomous vehicles, augmented- reality, tele-surgery, smart cities, industry 4.0, etc. [3]. Due to spectral congestion in the microwave band (300 MHz to 3 GHz), the transmission of ultra-broad bandwidth data will utilise new millimetre-wave (mmW) frequencies, 26 GHz and above, where large bands of un-allocated spectrum are available. In particular, the bands around 28, 38, 60 and 73 GHz have been recommended by ITU-R for future 5G implementations [4].

To reap the benefits of this new paradigm, network operators need to build an infrastructure capable of supporting the stringent transmission requirements (large bandwidth, low latency, high reliability), in both the wired and wireless domains. Thus, 5G+ could employ a centralised or cloud radio access network (C-RAN) [5], consisting of a pool of baseband processing units (BBUs), connected to the antenna sites or remote radio units (RRUs) by an optical fibre (as depicted in Figure 6.1) or an mmW link. The data exchange between the BBU and the RRU can be realised in either the digital or analog domain [6]. The latter, termed as analog radio over fibre (A-RoF), delivers improved spectral efficiency and simplifies the RRU architecture, by shifting the high-speed digital signal processing from the RRU to the BBU [7], [8].

An A-RoF system relies on the generation of mmW signals by heterodyning: two coherent optical tones (one of which is modulated with data), separated by the desired mmW frequency, are generated in the BBU and transmitted over fibre to the RRU [9], [10]. The tones mix on a photodiode (PD), at the RRU, effectively upconverting the data signal to the mmW band. The quality of the generated signal is dependent on the linewidth and phase correlation of the optical modes. If the two tones are correlated, optical phase noise cancellation takes place at the PD, resulting in a high-quality RF output [11]. Over the years, several approaches to the generation of coherent optical tones have been investigated, including the use of OFCs [12]–[19], frequency doubling using external modulators [20], dual-mode lasers [21], dual-wavelength fibre lasers [22], etc. Among these, the use of an OFC enables a simple and flexible way of generating correlated tones with excellent frequency stability.
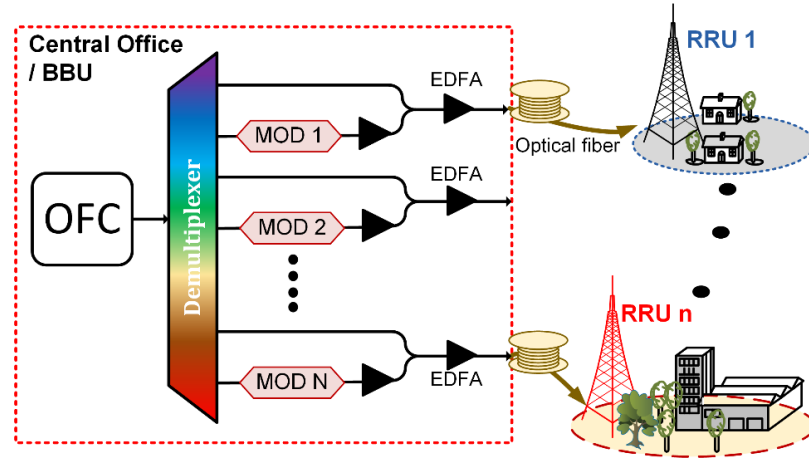
Figure 6.1 Generic architecture of the OFC-based A-RoF distribution system. Here, BBU: baseband processing unit, RRU: remote radio unit, OFC: optical frequency comb, EDFA: Erbium-doped fibre amplifier, MOD: modulator.

A conventional OFC-based A-RoF system is shown in Figure 6.1. It comprises an OFC source, a demultiplexer that filters two comb tones separated by the desired frequency, and an external modulator. The most common implementation reported in research work entails the use of arrayed waveguide gratings (AWGs) and wavelength selective switches (WSSs) as the demultiplexers [15], [17]. As discussed in chapters 4 and 5, they suffer

from high insertion losses (~ 6-10 dB), large footprint and limited finesse and requires optical amplifiers to boost the power. While the above-mentioned techniques are effective, using them in a photonically integrated circuit is challenging. Moreover, all these approaches are based on a split-select-recombine principle, where comb lines are split, and the desired tones are selected employing a demultiplexer prior to being re-combined using a coupler (as in Figure 6.1). This would result in a difference in length between the paths traversed by the two tones. This path length mismatch results in a phase walk-off between the two tones, which in turn degrades the quality of the generated mmW signal. The issue is exacerbated when an external modulator is used for data modulation, as it introduces a significant imbalance between the two path lengths. In [16], an experimental demonstration of the phase walk-off, as a function of the time delay between two optical tones, and its impact on the performance of a 12.5 Gbaud QPSK signal was presented. The results highlight the importance of matching the path lengths, which can be achieved by adding a length of the fibre or a tunable optical delay line (ODL) [16], [19]. Furthermore, the negative impact of the phase walk-off increases with the increased optical linewidth of the tones (source) [15]. This introduces a stringent requirement on the purity (low linewidth) of the optical tones used for the mmW generation, thus increasing the overall cost of the transmitter.

To overcome these shortcomings, a laser-based active demultiplexer poses as an attractive solution to select two OFC lines for the heterodyne process [22]–[27]. Therefore, in this chapter, two novel architectures, employing the active demultiplexer, to generate high-quality mmW signals are proposed and their application in an A-RoF system is evaluated. In the first configuration, OFC lines are filtered using two active demultiplexers in parallel (split-select-recombine approach). The work carried out shows that such an architecture benefits from the multiple functionalities of the active demultiplexer, which include filtering, amplification and data modulation. In comparison with conventional OFC-based A-RoF system [15], [16], the BBU of the system proposed, does not require an external modulator (reduced insertion loss), Erbium-doped fibre amplifiers (EDFAs) or ASE removal filters. Thus, the active demultiplexer solution can overcome most of the shortcomings associated with the AWG or WSS-based solutions.

However, a major issue that remains unaddressed relates to the mismatch of the path lengths traversed. Hence, a second approach is proposed, which includes the use of a novel dual-stage active demultiplexer – active demultiplexers in a series configuration. The main benefit of this new architecture stems from the fact that both tones travel the same path, which alleviates the path length compensation challenges. The latter renders the system highly tolerant to the optical linewidth of the source (OFC). Furthermore, as the method is based on an active demultiplexer, it benefits from its multifunctionality, eliminating the need for an external modulator and optical amplifier. Finally, a splitter or re-combiner is not required thereby reducing the insertion losses incurred at the transmitter. All the above mentioned advantages and the fact that the entire transmitter can be photonically integrated leads to a simple architecture with a reduced footprint, cost and energy consumption.

In this chapter, a 61 GHz unamplified A-RoF distribution system employing an OFC and an active demultiplexer in parallel, is experimentally demonstrated. Two tones separated by 56 GHz are selected by utilising a pair of active demultiplexers and then an A-RoF distribution is realised, by directly modulating one of the demultiplexers with a 64- QAM universal filtered orthogonal frequency division multiplexed (UF-OFDM) signal that is transmitted over 25 km SSMF link. A BER of 2.4 e^{-3} (below HD-FEC limit) is achieved with only a 0.5 dB power penalty (compared to its BtB) after transmission over 25 km of SSMF thereby verifying the suitability of employment of active demultiplexers in A-RoF systems. Subsequently, the second approach employing a dual-stage active demultiplexer is investigated. The principle of operation of the dual-stage active demultiplexer based transmitter, as well as a detailed characterisation of the generated mmW signal, is presented. The first step in this process consisted of demonstrating the generation of mmW signals, at 25.5, 34, and 59.5 GHz, with high purity and exceptional stability. The latter is confirmed, by measuring the beat tone linewidth and power fluctuations over 80 minutes. The signal sideband phase noise analysis (SSB) is performed to verify the purity of the generated mmW signals. Subsequently, an A-ROF distribution is realised by transmitting a 64-QAM UF-OFDM data signal at 29.5 and 38 GHz, over 10 and 25 km of SSMF. In all the cases, the BER was recorded to be below the HD-FEC limit.

Furthermore, the impact of path length mismatch and optical source linewidth on the quality of the resultant mmW signal is examined with aid of SSB phase noise measurements. To this effect, two OFC sources are used (i) a gain-switched laser (GSL) and (ii) an externally injected GSL (EI-GSL) with optical tone linewidths of 3.1 MHz, and 30 kHz, respectively. In addition, to compare the performance of the parallel scheme with the cascaded scheme, the performance of an A-RoF system employing the dual-stage active demultiplexer is examined as a function of the OFC linewidths. Using the dual-stage demultiplexer, identical system performance for both OFC sources is achieved, which demonstrates its high tolerance to the source linewidth. Finally, a case study of an A-RoF distribution system is presented, to illustrate the benefits of the proposed schemes, in terms of power budget and the number of RRU's that can be served using a single OFC.

6.2   A mmW A-RoF System Employing an Active Demultiplexer

6.2.1   Principle of operation: active demultiplexer based mmW signal generation

The operational principle of the mmW signal generation employing an OFC and active demultiplexers in parallel is as shown in Figure 6.6Figure 6.2. The set-up consists of an OFC generation stage followed by two semiconductor-based active demultiplexers (Demux) to select the desired OFC tones. The principle operation of the active demultiplexer is the same as described in chapters 4 and 5. First, the output of the OFC is split and injected into two demultiplexers. Demux 1, whose wavelength (λ_{D1}) is tuned, using the bias current and the temperature, to match the wavelength of the desired comb tone ($\lambda_{desired\ tone\ 1}$). Once these two are within the injection locking range Δf, i.e.: $\lambda_{\text{D}1} = \lambda_{desired\ tone\ 1} \pm \Delta f$, Demux 1 is injection-locked by the desired comb tone. Consequently, Demux 1 inherits the frequency and phase characteristics of the OFC, while providing amplification to the chosen tone. Likewise, the OFC is injected into Demux 2 and injection-locked by a comb tone that is separated, by the desired mmW signal frequency (f_{mmW}), from Demux 1. The output of the two demultiplexers are then combined to constitute two amplified correlated comb tones and are detected on the PD to generate a mmW signal at f_{mmW}.
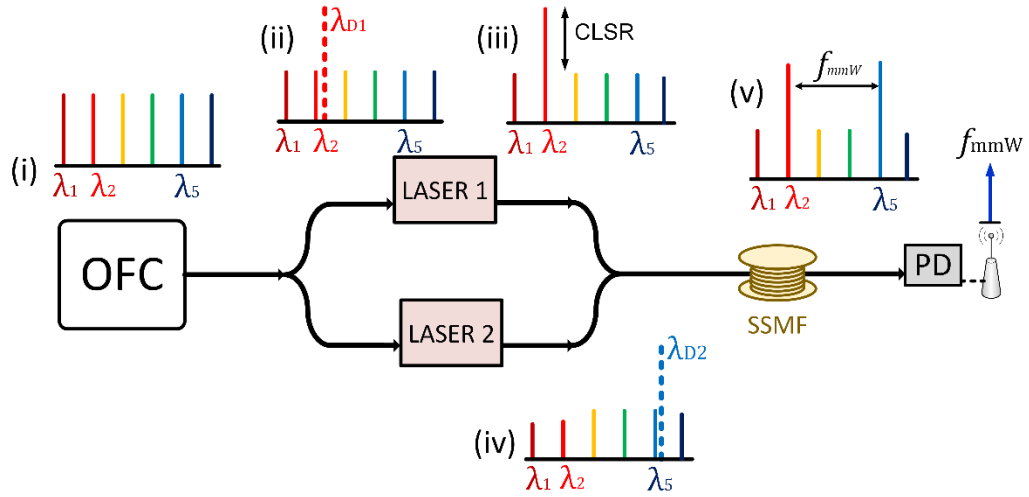
Figure 6.2. Schematic diagram of mmW signal generation and distribution employing OFC and active demultiplexers. Here SSMF: standard single-mode fibre, CLSR: comb line suppression ratio. Insets (i)-(v) are line graphs illustrating the operational principle. The solid and dotted lines show the OFC tone and free running demultiplexers respectively.

6.2.2 Experimental demonstration of the A-RoF system based on active demultiplexers in parallel

The experimental setup of the mmW signal generation and A-RoF distribution system employing an OFC and active demultiplexers is as shown in Figure 6.3. The setup emulates the BBU and RRU connected by a length of fibre and the electrical signal is transmitted to the user wirelessly or over a length of RF cable. In the BBU, an EI-GSL generates an OFC with an FSR of 14 GHz portraying an optical carrier to noise ratio (OCNR) > 55 dB (20 MHz bandwidth resolution), as shown in Figure 6.4 (a). The OFC is split using a 50:50 coupler and then injected, through optical circulators, to two commercially available DFB lasers that serve as the active demultiplexers. The lasers are biased at about ~ 5.5 × threshold current (I_{th}) and emit approximately 9 dBm of average optical power. The wavelengths of the demultiplexers are tuned to match two comb tones separated by 56 GHz (4 times the FSR). The power of the injected comb tones is adjusted, using a variable optical attenuator (VOA), to achieve an unsuppressed comb line suppression ratio (CLSR) of 30 dB, as seen in Figure 6.4 (b).
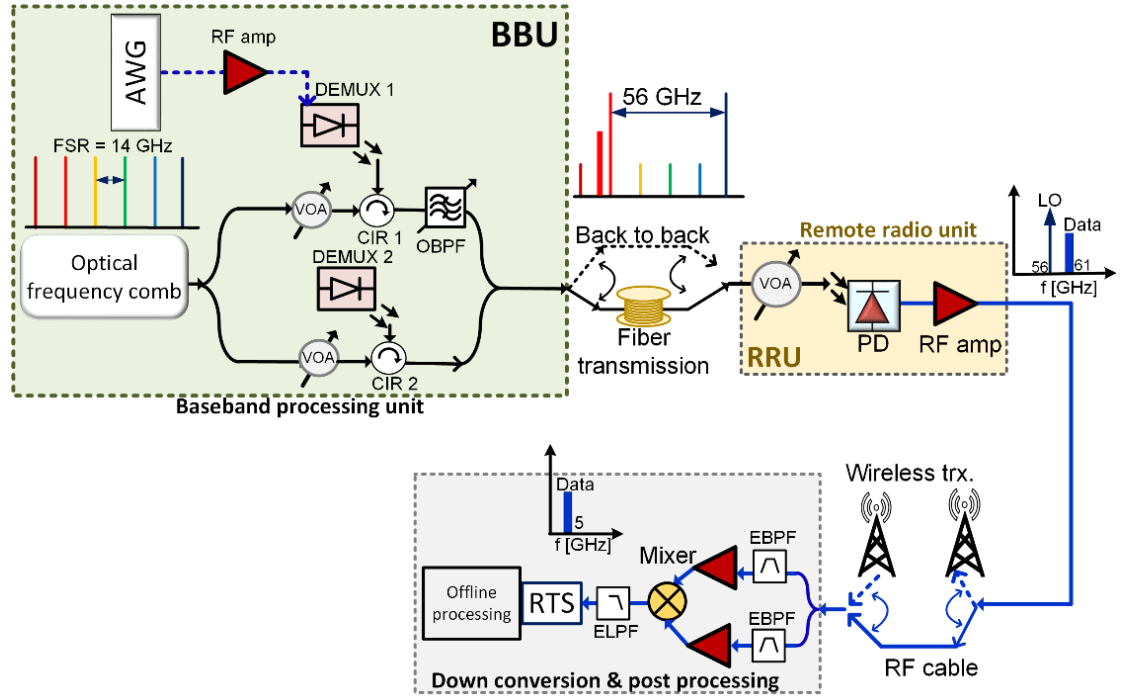
Figure 6.3 Experimental setup of the A-RoF system employing OFC and active demultiplexers in parallel. Here, BBU: baseband processing unit; RRU: remote radio unit; VOA: variable optical attenuator; AWG: arbitrary waveform generator; CIR: circulator; PD: photodetector; EHPF: electrical high pass filter; EBPF: electrical bandpass filter; LO: local oscillator; RTS: real-time oscilloscope.

Subsequently to realise an A-ROF system, one of the two demultiplexed tones is directly modulated with a 64- QAM UF-OFDM data signal [28], [29]. To achieve this, a 40 mA peak to peak downlink data signal is combined with a 51 mA DC bias current and applied to Demux 1. The data signal used is a single sideband (SSB) UF-OFDM signal[3] generated by a Tektronix arbitrary waveform generator operating at 20 GSa/s. The signal is centred at an intermediate frequency (IF) of 5 GHz and consists of 76 64-QAM subcarriers, each at 1.95 MBaud, resulting in a total (raw) data rate of 0.89 Gb/s and occupying a bandwidth of 148.5 MHz. The directly modulated output of Demux 1 is then converted to an SSB signal by filtering out one sideband using an optical bandpass filter (OBPF) with a

---

[3] The UF-OFDM code was developed by Dr. Colm Browning (DCU) and Dr. Armang Farhang (Maynooth University)

bandwidth of 6 GHz (as shown in Figure 6.4 (c)). The filtering also aids in adjusting the power in the carrier, to match the (total) power of the sideband, to ensure optimal efficiency of the heterodyning process at the photodetector. The signals from both demultiplexers are combined together and transmitted over SSMF to the RRU. The launched average optical power into the fibre is measured to be 6 dBm.
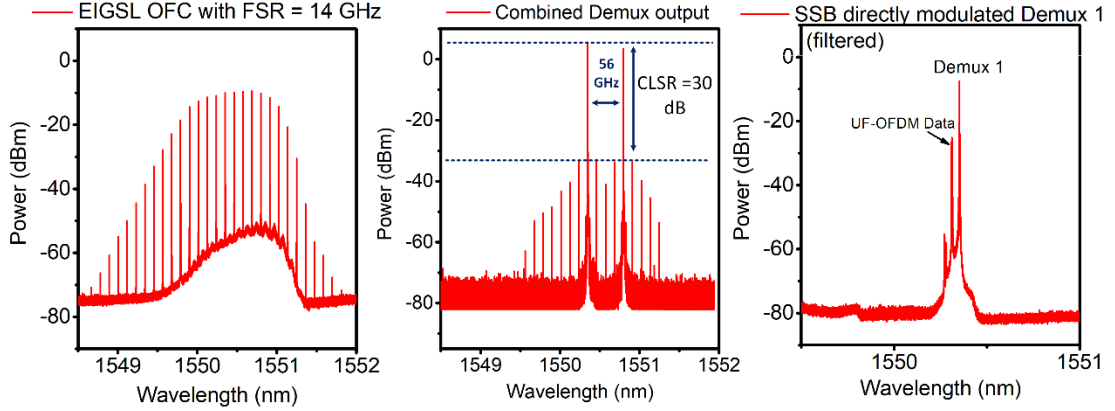
Figure 6.4 Optical spectral of (a) EI-GSL OFC with an FSR of 14 GHz, (b) combined output of demultiplexer with two OFC lines separated by 56 GHz, (c) Demux 1 output depicting a directly modulated UF-OFDM signal after OBPF filter (carrier and SSB signal).

At the RRU, the optical signals consisting of the unmodulated carrier from Demux 2 and the modulated signal (carrier and the SSB data) from Demux 1, are detected using a 70 GHz PD. A VOA is used to vary the optical power falling onto the PD. The three spectral components beat together to produce two RF signals of interest: the downlink data upconverted to 61 GHz and an unmodulated carrier of 56 GHz. As this work mainly concentrates on the optical part of the A-RoF system, the wireless connection is replaced by an RF cable (1 m). These signals are then amplified and separated using an RF splitter and two electrical BPFs with centre frequencies (bandwidth) of 62 GHz (6 GHz) and 56 GHz (500 MHz) respectively [30]. The 56 GHz signal is used as a local oscillator (LO) to downconvert the downlink UF-OFDM data signal back to an IF. The IF data is filtered and then captured using a real-time oscilloscope (RTS) operating at 50 GSa/s. Offline processing, including re-sampling, channel estimation and equalization, BER and EVM calculations, are performed using MATLAB. .

6.2.3 Performance evaluation of the A-RoF system employing active demultiplexers in parallel
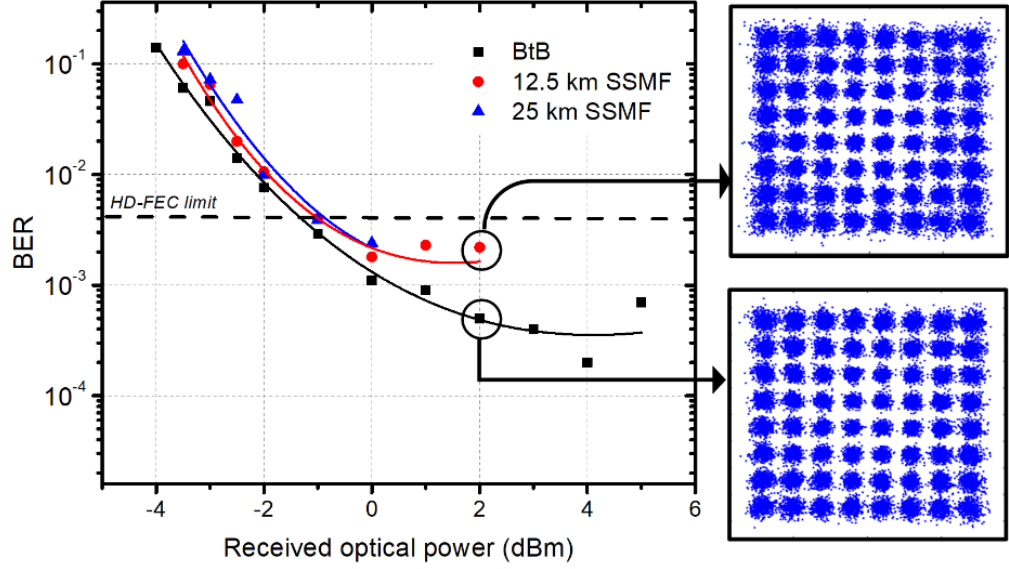
Figure 6.5 BER vs received optical power for back-to-back (BtB), after 12.5 km fiber transmission and after 25 km of fiber transmission. Inset shows the 64-QAM constellations at a received optical power of 2 dBm for the BtB and the 12.5 km SSMF.

To verify the performance of the active demultiplexer-based mmW A-RoF distribution system, the BER as a function of the received optical power (ROP) is measured. Three transmission scenarios were carried out: (i) back-to-back (BtB), and where the BBU and RRU are connected with a 1m optical patch cord, (ii) 12.5 km of SSMF spool, and (iii) 25 km of SSMF spool. From Figure 6.5, it can be seen that a BER below the HD-FEC limit can be achieved for all three cases at a received optical power > 0 dBm. For the BtB transmission, the BER improves with an increase in the optical power until it reaches 4 dBm. Beyond that power, the PD saturates, and the nonlinearities start to degrade the quality of the received signal. In the case of fibre transmission, at the FEC limit, a power penalty of approximately 0.5 dB is recorded with respect to the BtB case. By comparing the constellation diagrams for the BtB and the 12.5 km fibre transmission (at an ROP of 2 dBm), it can be seen that there is significantly more noise present in the outer points of the constellation. As these correspond to parts of the signal with the highest power, it

suggests that the degradation in the signal quality is caused by fibre nonlinearities [32]. For the 25 km transmission case, only a very small additional penalty (0.1 dB) can be observed (w.r.t the 12 km). This is due to the received power being limited to 0 dBm as a result of the transmission loss. At this power level, the performance of the system is mainly determined by the receiver noise. Nevertheless, the system performance is below the HD-FEC limit and more importantly, such performance is achieved without requiring EDFAs or SOAs. Moreover, the system's power budget can be further improved by optimising the receiver by various means such as using a narrow bandwidth detector (which has better responsivity at a given frequency), linear amplifiers, directional antennae, etc.

Despite all these benefits, the demonstrated architecture may suffer from random phase walk-off due to a path length mismatch, which could have a severe impact on the system performance especially if operating with large OFC (source) linewidths. Hence, the second architecture is proposed in the next section, which uniquely features a single optical path for both tones used for the mmW generation, thus eliminating the challenges related to the mismatch of path lengths whilst maintaining all the other benefits.

6.3 Dual-Stage Active Demultiplexer

6.3.1 Principle operation: dual-stage active demultiplexer
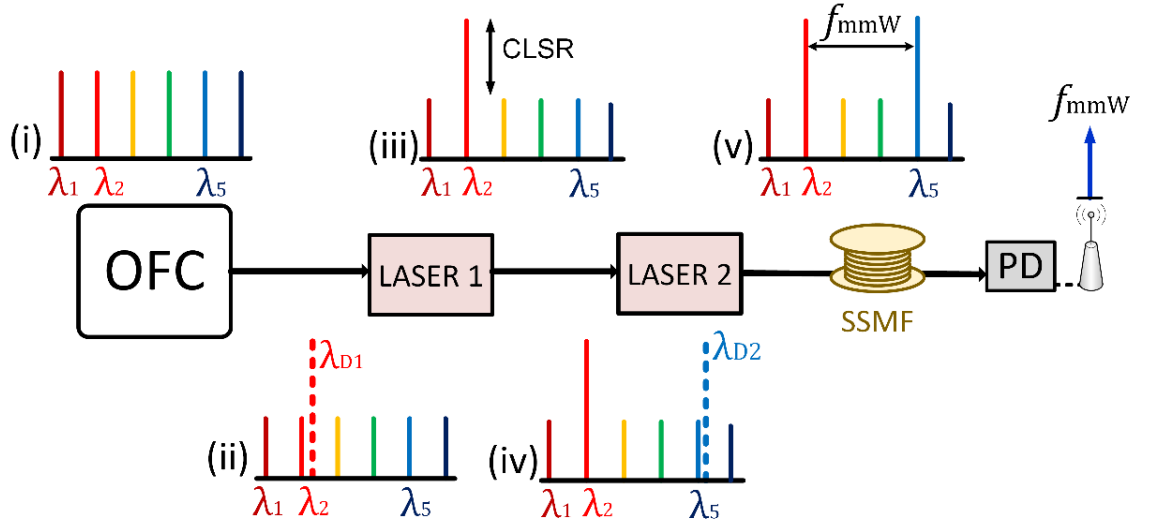
Figure 6.6 Schematic diagram of the dual-stage active demultiplexer based mmW generation and distribution. Here SSMF: standard single-mode fibre. Insets (i)-(v) are line graphs illustrating the operational principle. The solid and dotted lines show the OFC tone and free running demultiplexers respectively.

The idea of employing a dual-stage active demultiplexer for mmW signal generation stems from the simulations results presented in Chapter 5. In the simulation, it was employed to achieve either CLSR improvement or chirp reduction (when the active demultiplexer was directly modulated (Section 5.2.3)). The operational principle of the mmW generation scheme employing a dual-stage active demultiplexer is depicted in Figure 6.6. The set-up consists of an OFC followed by a dual-stage active demultiplexer, enabling the selection or filtering of two of the comb tones, separated by the desired mmW frequency. The output of the OFC is injected into the first demultiplexer (Demux 1), and injection-locked by the chosen OFC line. Consequently, the frequency and phase characteristics of the OFC are transferred to Demux 1, while de-facto amplifying the chosen OFC line. The remaining OFC tones pass through the Demux 1 without any amplification. While the power levels of the unsuppressed tones at the output of the Demux 1 are low, they are sufficient to achieve stable injection locking of the second stage demultiplexer. Thus, the output of Demux 1 is injected into Demux 2, whose

wavelength (λ_{D2}) is tuned to match an unsuppressed comb tone, separated from the tone filtered by Demux 1, by the desired f_{mmW}. Once injection-locked, Demux 2 also acquires the OFC's characteristics, while amplifying the selected tone. Therefore, the output of Demux 2 consists of two coherent tones that can be used to generate a high-quality mmW signal at the desired f_{mmW}.

6.3.2   Generation of the mmW signal

The experimental setup, used to verify the performance of the dual-stage active demultiplexer based mmW generation scheme, is shown in Figure 6.7 (a). The EI-GSL produces 11 highly coherent tones (within 3 dB from the spectral peak) with an FSR of 8.5 GHz and an OCNR > 55 dB (20 MHz bandwidth resolution). The entire OFC spans about 1 nm, as shown in Figure 6.7 (c). Next, two commercially available discrete-mode (DM) lasers from Eblana Photonics [33] are used as the active demultiplexers. These lasers, with a cavity length of 250 µm, are encased in a TEC-controlled 7-pin high-speed butterfly package with an RF connector that enables high-speed direct modulation. They both exhibit a I_{th} of ~10 mA and a modulation bandwidth of ~ 12 GHz. Demux 1 and 2, when biased at ~ 5.5 x I_{th}, emit an average output power of 7.5 dBm and 8 dBm, respectively. It is also important to note that a single laser with multiple integrated sections could be used as a dual-stage active demultiplexer.

The OFC is injected into Demux 1 via an optical circulator. The injected CLP is adjusted to −25 dBm with the aid of an inline VOA (as shown in Figure 6.7 (d)). Figure 6.7 (e) depicts the output of Demux 1 with a CLSR of 30 dB and output power of 7.5 dBm. The power of the unsuppressed tones is around −30 dBm, which is sufficient to injection lock Demux 2 [25]. The wavelength of Demux 2 is tuned to select the unsuppressed tone 34 GHz (4 × FSR) away from Demux 1. As a result, the output of Demux 2 consists of two tones with a CLSR of 35 dB, as shown in Figure 6.7 (f). This two-tone signal is then heterodyned on a high-speed 50 GHz photodetector. The resultant beat tone at 34 GHz is recorded on a 40 GHz electrical spectrum analyser (ESA) and shown as in Figure 6.7 (b). The phase correlation between the two tones at the output of Demux 2 results in the cancelation of the optical phase noise and the generation of a high purity RF beat tone

with a 3 dB linewidth of 13 Hz (ESA resolution: VBW= 10 Hz; RBW: 10 Hz). The Hz level beat tone indicates the excellent phase correlation between the comb lines and reflects the purity of the RF source used for OFC generation.
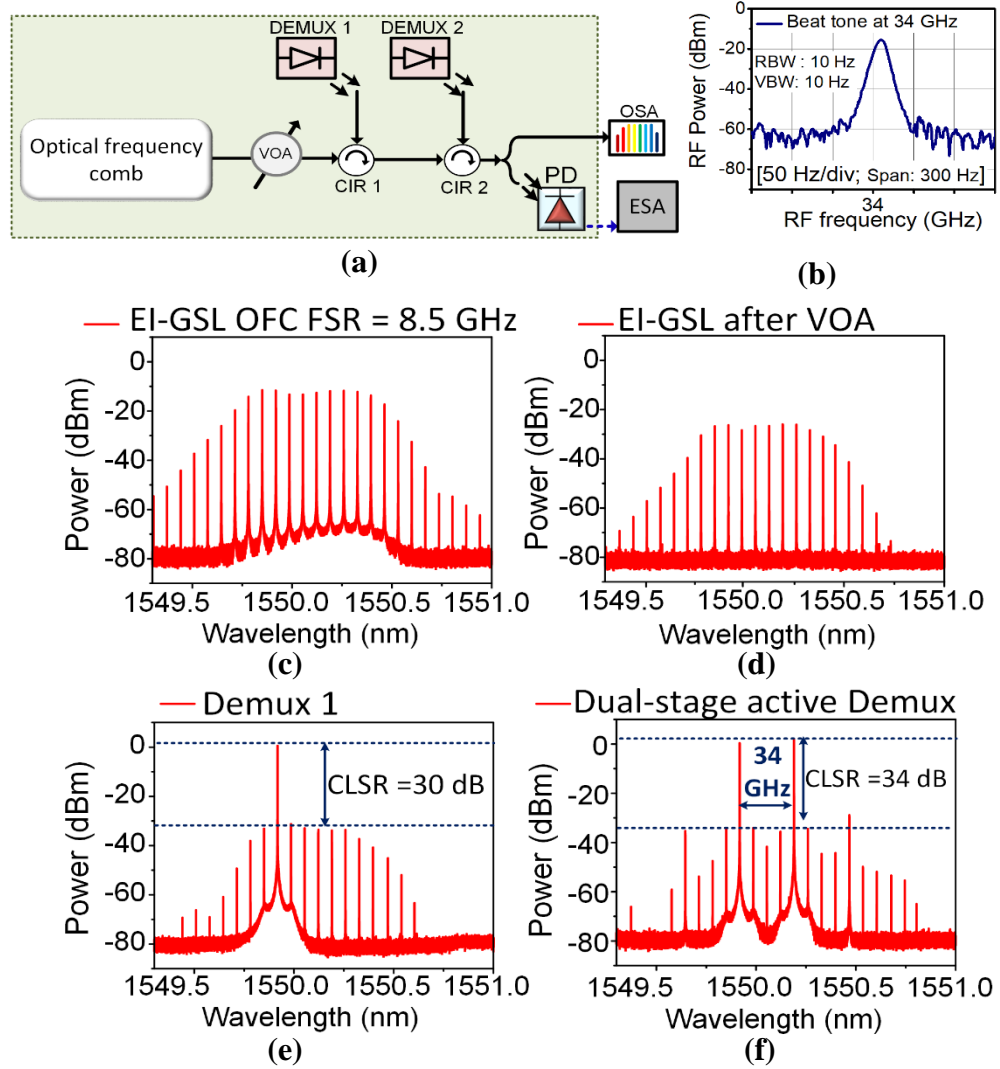
Figure 6.7 (a) Experimental setup of dual-stage active demultiplexer based mmW generation. (b) an electrical spectrum of the resultant RF beat tone at 34 GHz. Optical spectra of (c) EI-GSL OFC with an FSR of 8.5 GHz, (d) OFC after the VOA (CLP = −25 dBm), (e) Demux 1 output, and (f) Demux 2 output. Optical spectra are captured with a fixed (7 dB) optical attenuator before the OSA (20 MHz resolution). ESA resolution set to RBW: 10 Hz, VBW: 10 Hz.

One of the attractive features of the dual-stage active demultiplexer is the frequency tunability of the generated mmW signal (by multiples of the OFC's FSR). This can be

achieved by simply tuning the wavelength of Demux 2 to match a different unsuppressed tone. This is demonstrated in Figure 6.8, where tones separated by 25.5 GHz (3 × FSR), 34 GHz (4 × FSR), and 59.5 GHz (7 × FSR) are demultiplexed. Figure 6.8 also shows that two new frequency components are generated in the cavity of Demux 2. These are products of four-wave mixing (FWM) between the two demultiplexed modes.
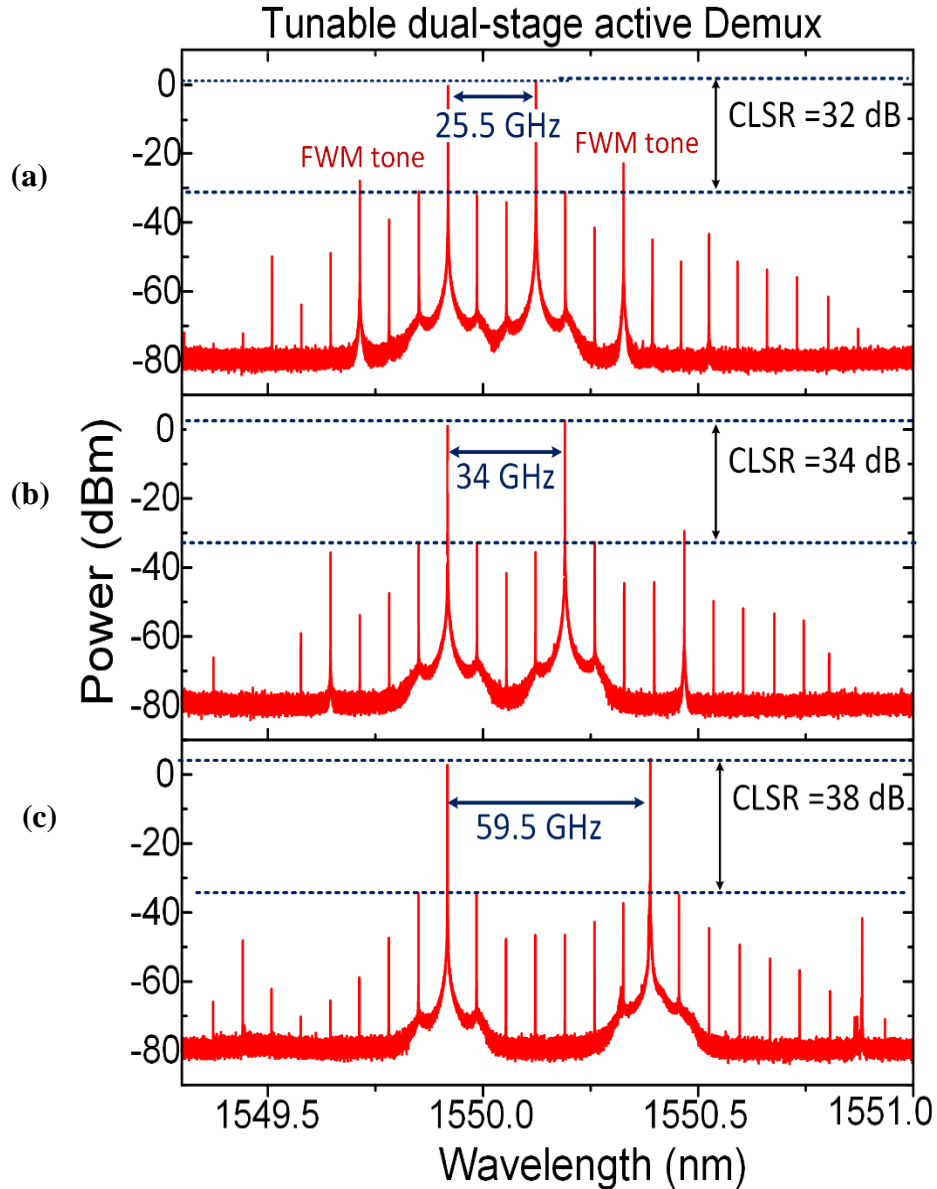
Figure 6.8 Optical spectra of the dual-stage active demultiplexer (Demux 2 output) configured to filter tones separated by (a) 25.5 GHz, (b) 34 GHz, and (c) 59.5 GHz. Optical

spectra are captured with fixed optical attenuation of 7 dB before the OSA (20 MHz resolution).
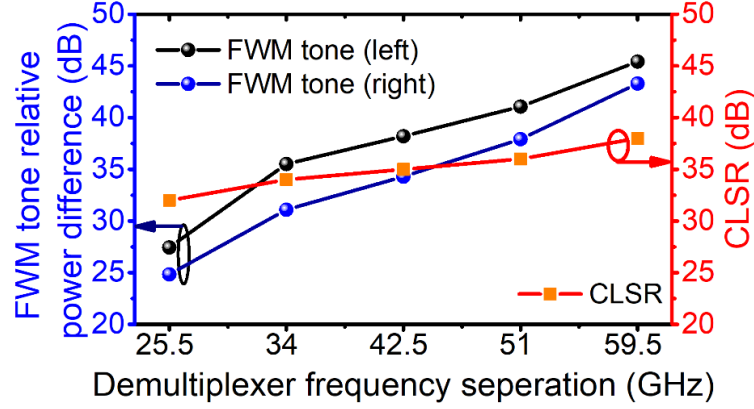
Figure 6.9 Relative power difference (ΔP_{FWM}) between the FWM tones and the demultiplexer output (blue and black) and CLSR (red) as a function of frequency separation.

Unsurprisingly, the strength of the FWM tones reduces as the separation between the tones increases [34],[35]. To quantify this trend, the relative power difference (ΔP_{FWM}), between the demultiplexed tones and the FWM products, as a function of the frequency separation, is measured and plotted in Figure 6.9. As the demultiplexed tones are moved further apart (from 25.5 to 59.5 GHz), ΔP_{FWM} increases from 25 to 42.5 dB (longer wavelength FWM tone) and from 27.5 to 45 dB (shorter wavelength FWM tone). This can be attributed to the reduced FWM efficiency, as the carrier density modulation decreases with an increase in the frequency separation [34]. It can also be seen that the CLSR at the output of Demux 2 increases (from 32 to 38 dB, Figure 6.9 (red line)) with the increased separation between the tones. This can also be credited to the lower FWM efficiency, which leads to more power left in the desired tones and thereby a higher CLSR. Thus, the performance of the dual-stage active demultiplexer improves with an increase in the frequency of the mmW signal, rendering it a suitable candidate for sub / THz generation (in conjunction with a sufficiently broad OFC).

6.3.3 Characterisation of the mmW signal

(a) Transfer of the optical phase noise in a dual-stage active demultiplexer:

The generation of a high-quality mmW signal requires a high degree of phase correlation between the two optical tones. In the active demultiplexer based scheme, coherent OFC lines transfer its phase characteristics to the demultiplexed tones. To verify this, the phase noise of the dual-stage active demultiplexer is characterised by measuring the FM noise spectrum, using a modified delayed self-heterodyned technique [36]. The measured FM noise spectrum $S_F(f)$, describes the power spectral density (PSD) of the instantaneous frequency fluctuations. The Lorentzian shaped optical linewidth (δf) can be retrieved from the flat portion of the spectrum, corresponding to the white noise component (S_0), using the formula $\delta f = \pi \times S_0/2$ [36]. Figure 6.10 shows the measured FM noise spectra for several cases.
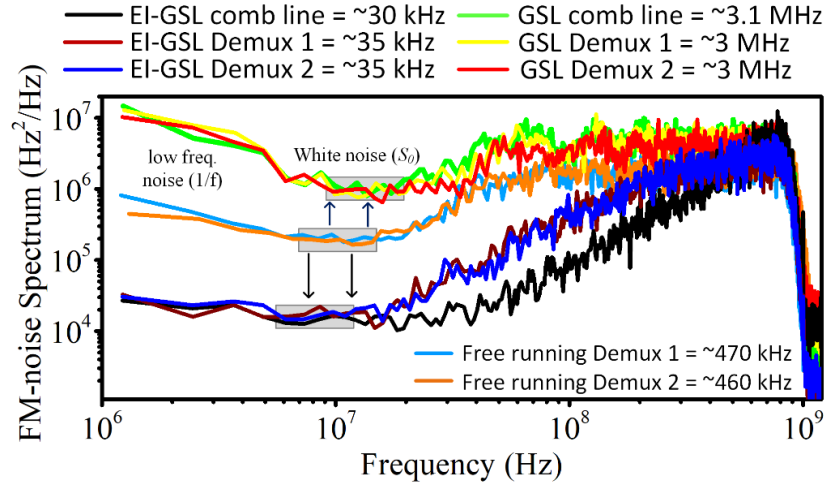
Figure 6.10 FM-noise spectra of the dual-stage active demultiplexer for various scenarios.

Firstly, the phase noise for the EI-GSL comb line and free-running (FR) Demux 1 & 2 are characterised. The optical linewidths are measured as 30 kHz (EI-GSL line), 460 kHz (FR Demux 1) and 470 kHz (FR Demux 2). Subsequently, two OFC tones, separated by 34 GHz are demultiplexed, using the dual-stage active demultiplexer. The optical linewidth of the injection-locked Demux 1 and 2 is measured to be ~35 kHz, reflecting

the linewidth of the EI-GSL lines. Similarly, to investigate the impact of OFC linewidths on the quality of the mmW signal, which will be discussed later in section 6.4, a gain-switched OFC (no external injection) is also considered (as depicted in Figure 6.16). Here as well, the optical linewidths of the OFC, as well as two tones (demultiplexed using the dual-stage active demultiplexer and separated by 34 GHz), are characterised as shown in Figure 6.10. The obtained values for all three measurements are 3 MHz. These results clearly show that OIL allows an efficient transfer of the phase noise characteristics of the comb to the demultiplexer, leading to either improvement (in case of the EI-GSL) or degradation (in case of the GSL) of the optical linewidth of the free-running demultiplexer.

(b) Phase noise of resultant mmW signal:
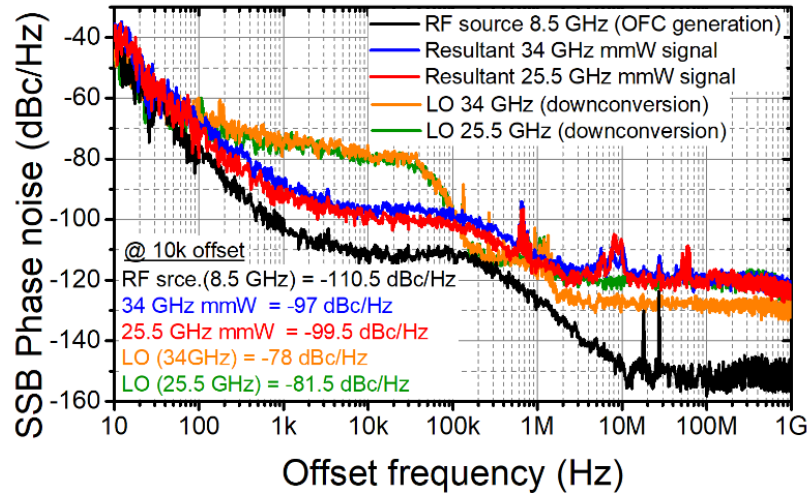
Figure 6.11 Single sideband phase noise of the generated mmW signal

Next, the phase noise of the resultant mmW signal is examined, by measuring the SSB phase noise of the generated 25.5 and 34 GHz mmW signal and comparing it with that of the external signal generator (Rohde & Schwarz SMB100A) used for the EI-GSL OFC generation. The obtained results are as shown in Figure 6.11. At an offset frequency of 10 kHz, the measured SSB phase noise of the generated 25.5 and 34 GHz carrier, and the 8.5 GHz RF signal used for the OFC generation, is -99.5 dBc/Hz (red trace), -97

dBc/Hz (blue trace), and -110.5 dBc/Hz (black trace), respectively. The low phase noise measured validates that a high degree of phase correlation between the comb tones is maintained during the demultiplexing process. The phase noise degradation of the mmW signals is as expected, given that linear frequency multiplication would result in a quadratic change in phase noise power, as described by $20\ log_{10}N$, (where N is the order of comb tone; here, N = 3 & 4, for 25.5 and 34 GHz) [10],[37]. Moreover, the achieved mmW signal phase noise is better than the external signal generator (later used as LO for downconversion at the user site) at 25.5 GHz (-81.5 dBc/Hz, green trace, at 10 kHz offset) and 34 GHz (-78 dBc/Hz, orange trace, at 10 kHz offset).

(c) Stability analysis:
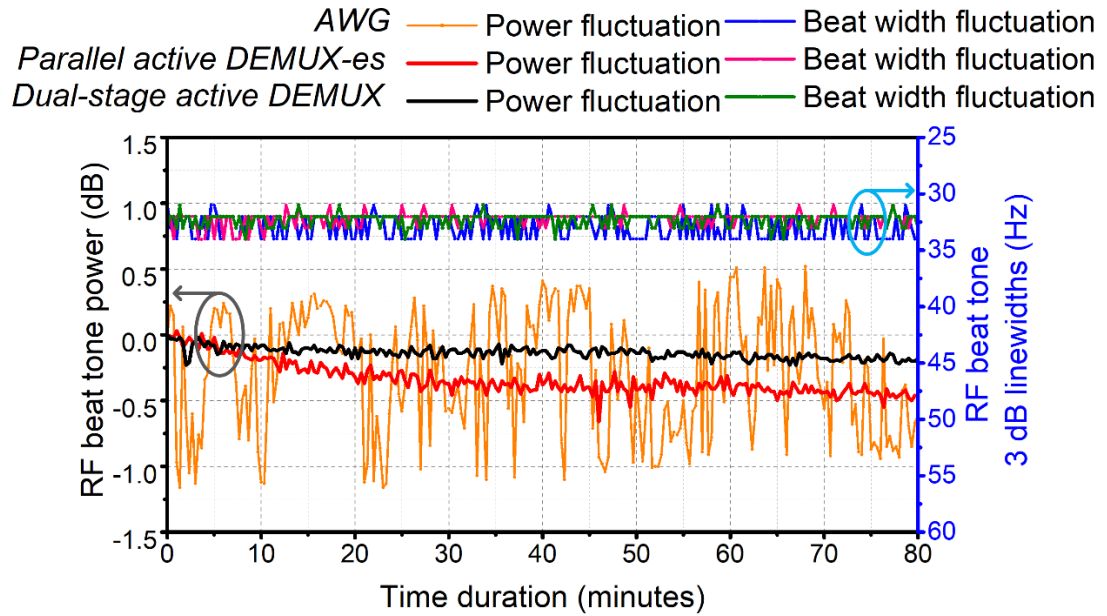
Figure 6.12 RF beat tone power and linewidth measurements for tones demultiplexed using an AWG, an active demultiplexer in parallel, and a dual-stage active demultiplexer.

The stability analysis of the dual-stage demultiplexer is then carried out. To this effect, two tones from the output of Demux 2 (separated by 25.5 GHz) are heterodyned on the high-speed PD. The resultant mmW signal power and 3 dB linewidth are recorded every 10 seconds over a duration of 80 minutes. To reduce the sweep time for the stability

measurements, the ESA resolution and video bandwidth (RBW, VBW) were set to 30 Hz and the frequency span to 1 kHz. For comparison, the same stability test is performed on a signal generated by tones demultiplexed using two other techniques i.e. the parallel active demultiplexer and a commercially available AWG from Kylia [38]. As the AWG had an FSR of 12.5 GHz, for this test, the FSR of the OFC is changed to 12.5 GHz. As shown in Figure 6.12, the dual-stage demultiplexer exhibits a maximum beat tone power fluctuation of 0.26 dB (Figure 6.12, black trace). The 3 dB beat tone linewidth is measured to be ~ 33 Hz (limited by the ESA resolution set to 30 Hz) indicating the high degree of phase correlation between the two tones. In the case of the active demultiplexer in a parallel configuration, the power fluctuation and the linewidth are measured to be 0.8 dB and 33 Hz, respectively. Finally, when using the AWG, the power fluctuation and linewidth of the beat tone are measured to be 1.6 dB and 33 Hz, respectively. This large power variation stems from the frequency drift of the OFC, which is translated to power variations, as the tones experience different attenuation when passing through the narrow passband of the AWG. The summary of the measurement results is shown in Table 5-2, which clearly shows that amongst the tested techniques, the dual-stage active demultiplexer offers the best stability. This is because both optical tones traverse the same path (no splitting or recombining), thus are not susceptible to differing polarisation or phase variations.

Table 6-1 Stability analysis: RF beat tone fluctuation over 80 minutes

	Dual-stage active demultiplexer	*Active demultiplexer in parallel*	*AWG*
Power fluctuation (dB)	~0.26	~0.8	~1.6
Beat tone linewidth (Hz)	~33	~33	~33

6.3.4 Experimental demonstration of the A-RoF system based on dual-stage active demultiplexer
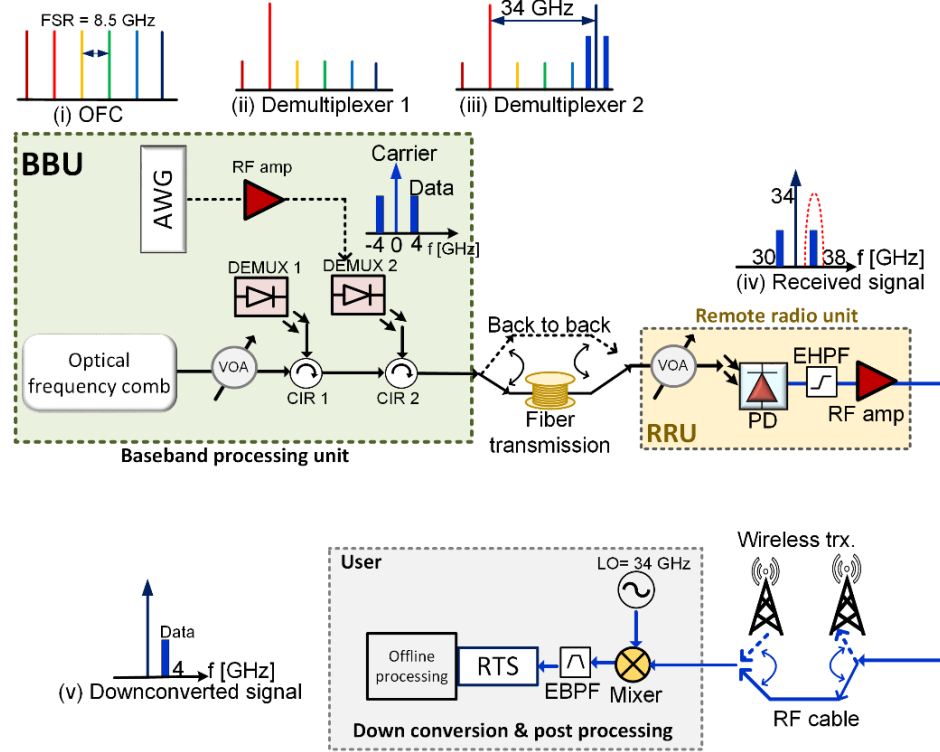
Figure 6.13 Experimental setup of the OFC-based A-RoF system employing dual-stage active demultiplexer. The insets (i)-(v) illustrate the principle of operation. Here, BBU: baseband processing unit; RRU: remote radio unit; VOA: variable optical attenuator; AWG: arbitrary waveform generator; CIR: circulator, PD: photodetector; EHPF: electrical high pass filter; EBPF: electrical bandpass filter; LO: local oscillator; RTS: real-time oscilloscope.

In the previous section, the viability of the dual-stage active demultiplexer to generate a high-quality mmW signal was proved. In this section, the application of the dual-stage active demultiplexer in a simple A-RoF transmission system is demonstrated. The experimental setup, shown in Figure 6.13, is similar to Figure 6.3. The BBU consists of an OFC followed by a dual-stage active demultiplexer, while the RRU comprises a PD, followed by an electrical high-pass filter and an RF amplifier. In this experiment, the traditional down conversion stage is used at the user site, where the mmW signal is downconverted to an IF, by mixing it with a signal from an external local oscillator.

178

Finally, after passing through an EBPF, the signal is sampled using an RTS and processed offline

At the BBU, the selection of the two OFC tones, separated by the desired mmW frequency, is carried out as described in section 6.3.2. Next, Demux 2 is directly modulated with the data to be transmitted. A single band 64-QAM UF-OFDM signal is generated using a Micram arbitrary waveform generator operating at 25 GSa/s and with properties listed in Table 6-2. A 1.2 Vp-p signal is applied to Demux 2 in conjunction with a DC bias current of 58 mA (~ 5.5 x I_{th}). The optical spectra of the directly modulated demultiplexer, with tones separated by 25.5, 34, and 59.5 GHz, are shown in Figure 6.14 (a) - (c). The inset in Figure 6.14 (c) displays the enlarged portion of the spectrum, showing Demux 2 and the two modulation sidebands at an IF of 4 GHz. The output of Demux 2 (with an average power of 9.5 dBm) is connected to the RRU through an optical fibre and detected on a PD.

The beating of the tones shown in Figure 6.14 (a) - (c), results in the generation of three main frequency components: an unmodulated carrier (at 25.5, 34, and 59.5 GHz) plus two data signals upconverted to mm frequencies (carrier frequency $\pm$ IF). The line graph of the mmW generation, for the optical tones separated by 34 GHz, is shown in Figure 6.13. In this case, the output of the PD consists of an unmodulated carrier at 34 GHz and two upconverted data signals at 30 and 38 GHz, with the higher frequency data being the signal of interest.

Table 6-2 UF-OFDM data signal properties (for dual-stage active demultiplexer)

Property	Value
Modulation format	64 QAM
Number of subcarriers	36
Subcarrier upconverted frequency	4 GHz
Subcarrier baud rate	1.4 Mbaud
Total data bandwidth	112 MHz
Total data rate	0.67 Gb/s
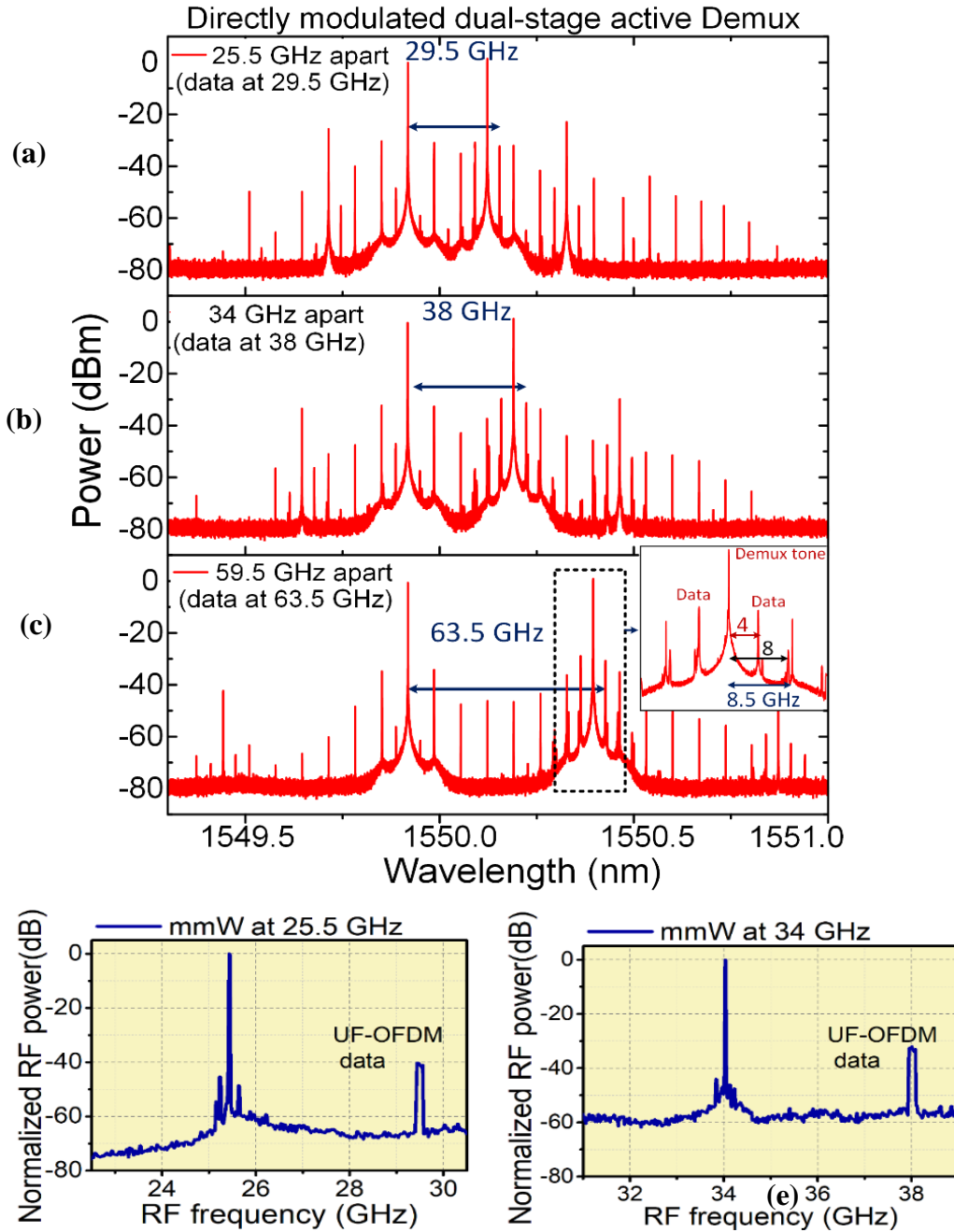
Figure 6.14 Optical spectra of Demux 2, directly modulated with a UF-OFDM signal, for a tone separation of (a) 25.5 GHz, (b) 34 GHz, (c) 59.5 GHz. The inset in (c) shows the enlarged portion of the dotted area. The RF spectra of the generated mmW signal (carrier and the upper sideband only) at (d) 29.5 GHz, and (e) 38 GHz. Optical spectra: resolution of 20 MHz, 7 dB attenuation at the input of the OSA; ESA resolution: 10 kHz (RBW, VBW).

Figure 6.14 (d) and (e) show the RF spectra of the generated unmodulated carrier and the upper sideband at 29.5 and 38 GHz, respectively. In the complete system, the upper sideband (data upconverted to a mmW) would be transmitted wirelessly to the end-user. As mentioned earlier, in this set-up the wireless link is replaced by an RF cable, after which the data signal is downconverted to an IF of 4 GHz, using a mixer and a signal from an LO. The 4 GHz signal is then filtered using an EBPF and captured using a 20 GHz LeCroy Teledyne RTS operating at 40 GSa/s. Finally, the captured data is processed offline using MATLAB and the EVM and BER calculations are carried out. It is worth mentioning that the 63.5 GHz signal is not analysed in this work, due to the limited bandwidth of the photodetector (50 GHz).

6.3.5 Performance evaluation of the A-RoF system employing the dual-stage active demultiplexer

In this section, the performance of the tunable A-RoF system employing the dual-stage active demultiplexer is evaluated, by measuring the BER as a function of the received optical power, for 3 cases: (i) BtB (ii) 10 km and (iii) 25 km SSMF link between the BBU and RRU. To demonstrate the flexibility of the A-RoF system, the aforementioned tests are carried out at 29.5 GHz and 38 GHz. The results are plotted in Figure 6.15 (a). Here, the solid and dotted lines represent the BER curve for 29.5 GHz and 38 GHz signals respectively. The recorded constellation diagrams, for BtB, 10 km, and 25 km fibre transmission, are shown in Figure 6.15 (b) for the 29.5 GHz signal and Figure 6.15 (c) for the 38 GHz signal. Figure 6.15 (d) shows the RF spectra of the received data downconverted to IF for BtB (black) and 25 km fibre transmission (for 38 GHz, red trace; for 29.5 GHz, blue trace).

The performance of this UF-OFDM A-RoF system is summarised in Table 6-3. Figure 6.15 (a) clearly shows that for both carrier frequencies, the system performs similarly, achieving BER values below the HD-FEC limit ($3.8\ e^{-3}$ corresponding to an EVM $< 8\%$) for all the cases. Examining the power required to attain the FEC limit, a small penalty of
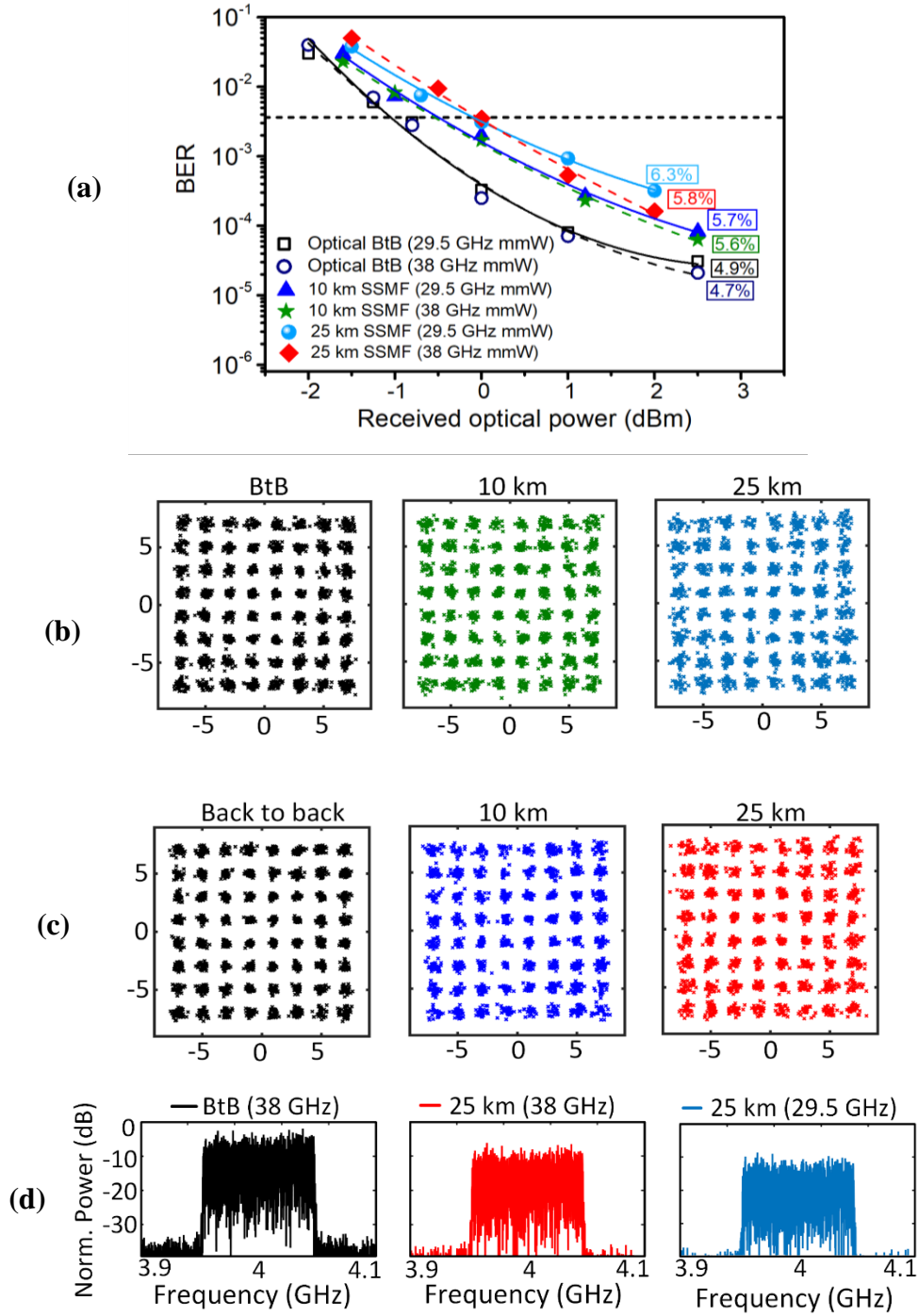
Figure 6.15 (a) BER vs. received optical power (EVM's are mentioned for respective cases within a rectangle); constellation diagrams for (b) 29.5 GHz, and (c) 38 GHz signal for the various transmission cases, (d) electrical spectra of the received data downconverted to 4 GHz for BtB (black) and after 25 km of SSMF transmission (red: 38 GHz; blue: 29.5 GHz signal).

~ 0.5 dB and ~ 1 dB can be seen while transmitting for 10 km and 25 km SSMF respectively when compared to their BtB performance. The error floor in the plots is due to the saturation of the PD at power levels >3 dBm. From Figure 6.15 (d) it can be seen that the power of the downconverted data for 29.5 GHz is lower than in the case of the 38 GHz carrier. This can be attributed to the power of the FWM components increasing with the reduction of the mmW frequency, which in turn reduces the power of the demultiplexed tones. It is important to mention that this excellent system performance is achieved without employing dedicated optical amplifiers. Thus, the dual-stage active demultiplexer method provides a simple and cost-efficient way of generating and distributing high-quality mmW signals.

Table 6-3 Dual-stage active demultiplexer based A-RoF system performance with UF-OFDM signal

	Data at 29.5 GHz			Data at 38 GHz		
	BtB	*10 km*	*25 km*	*BtB*	*10 km*	*25 km*
BER	3.1 e^{-5}	8.3 e^{-5}	3.2 e^{-4}	2.1 e^{-5}	6.3 e^{-5}	1.6 e^{-4}
EVM	4.9%	5.7%	6.3%	4.7%	5.6%	5.8%

6.4 Impact of OFC Linewidth on the Generated mmW Signal and the A-RoF System Performance

In this section, the investigation of the dual-stage active demultiplexer performance in the A-RoF system is expanded to include the impact of the OFC (source) linewidth. To this effect, a single-mode DFB laser (threshold current I_{th} of ~12 mA) is gain-switched by driving the laser with an amplified (~21 dBm) 8.5 GHz sinusoidal signal in conjunction with a DC bias of 51 mA. The optical spectrum of the generated GSL OFC with an FSR of 8.5 GHz, is shown in Figure 6.16 (a). It consists of 6 tones within 3 dB from the spectral peak and exhibits an OCNR of 50 dB (within 20 MHz OSA bandwidth resolution). The generated OFC lines exhibit optical linewidths of ~3.1 MHz, as verified in Figure 6.10 (green plot). The OFC is then attenuated to achieve a CLP of −25 dBm (as in Figure 6.16

(b)) and the demultiplexing of the two tones, separated by 34 GHz, is carried out using the dual-stage active demultiplexer, as illustrated in Figure 6.16 (c) and (d).
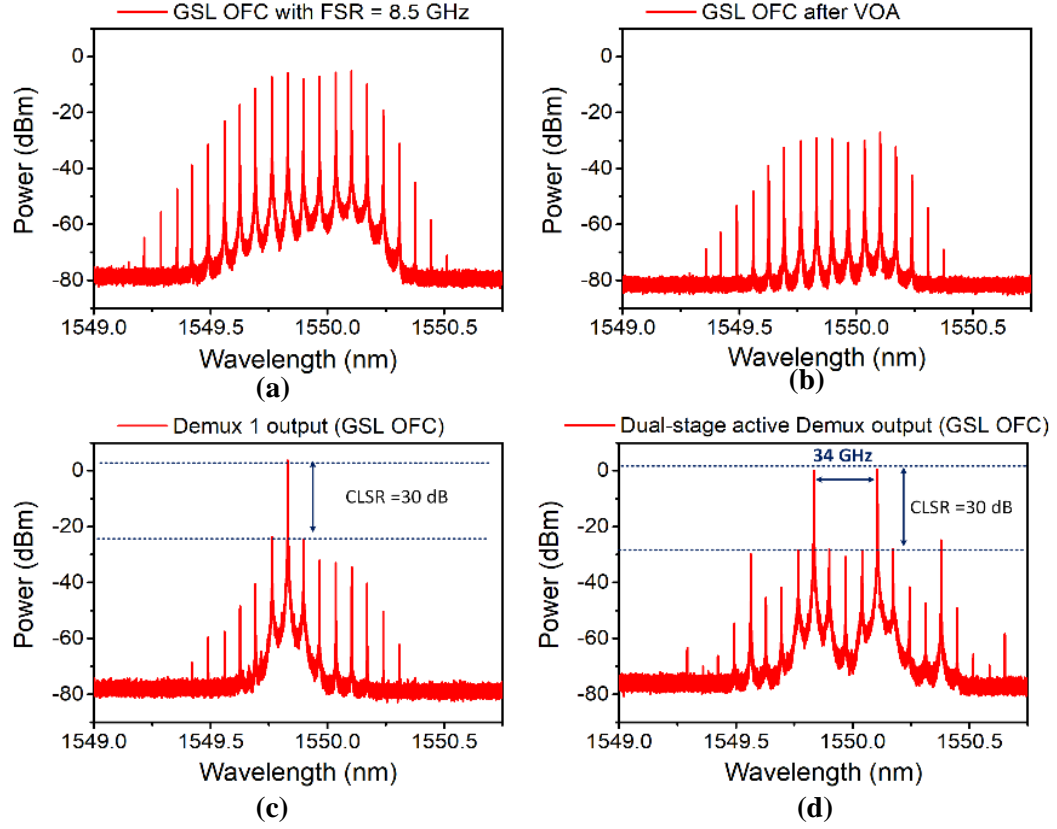
Figure 6.16 Optical spectra of (a) GSL OFC with FSR of 8.5 GHz, (b) GSL OFC after VOA, (c) Demux 1 output, and (d) Demux 2 output consisting of two tones separated by 34 GHz. OSA resolution: 20 MHz.

6.4.1 Impact of OFC linewidth and pathlength mismatch on the phase noise of the mmW signal

To investigate the impact of linewidth (δf) and path length mismatch on the phase noise of the generated 34 GHz mmW signal, two OFCs with different linewidths are considered; (i) GSL OFC (δf = 3.1 MHz) and EI-GSL OFC (δf = 30 kHz). In addition, two demultiplexing solutions are used to select the tones for the generation of the mmW signal i.e, parallel active demultiplexer and dual-stage active demultiplexer. The phase noise analysis of the generated mmW signals is performed by measuring their SSB phase noise, as shown in Figure 6.17. Firstly, the GSL OFC (δf ~3.1 MHz) lines are filtered employing

parallel active demultiplexers to generate the mmW carrier. The SSB phase noise measured, at an offset frequency of 10 kHz, is -83.5 dBc/Hz as shown as the red trace in Figure 6.17. Subsequently, a 0.5 m (time delay, $\tau_d = 2.5$ ns) and 1 m (5 ns) fibre is introduced in one arm and the measurements are repeated. The results are depicted by the green (-83.5 dBc/Hz) and black traces (-73.5 dBc/Hz) in Figure 6.17. In the case of the 1m fibre length, the phase noise deteriorates by 10 dB/Hz (compared to when there is no added fibre). This degradation can be attributed to the random phase walk-off induced by the path length mismatch between the two arms. Next, the same procedure is repeated with the EI-GSL OFC ($\delta f \sim 30$ kHz). As seen in Figure 6.17 (blue trace), in this case, increasing the path length mismatch (1 m) results in an SSB phase noise of -95.5 dBc/Hz (at 10 kHz offset). This clearly shows that the effect of the delay is less significant with narrow linewidths. On comparing the GSL with the EI-GSL (no added fibre), a phase noise degradation can be seen, which can be attributed to the fact that the larger linewidth tones (from the GSL) have shorter coherence length, thus a worse tolerance to a mismatch in path length (and vice versa). The above findings attest to the stringent linewidth requirements of the mmW signal generation schemes that use tones that traverse different paths. It is worth noting that, in the first mmW generation approach (section 6.2), the OFC linewidth is in kHz. Hence, less prone to phase walk-off due to pathlength mismatch.
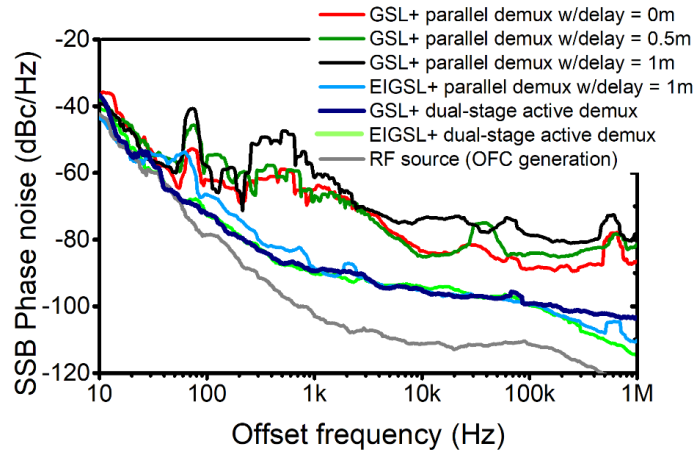
Figure 6.17 SSB phase noise analysis of mmW signals generated with various demultiplexing techniques. Note: 1% smoothing is applied to the ESA traces to observe the general trend of the phase noise.

Finally, the GSL OFC (δf ~3.1 MHz) with the dual-stage active demultiplexer is considered. The SSB phase noise of the resultant 34 GHz mmW signal, at offset frequency of 10 kHz is measured as -95.5 dBc/Hz, as illustrated by the navy-blue trace in Figure 6.17. The measured mmW phase noise is comparable to the RF source (-110 dBc/Hz, at RF of 8.5 GHz)) used for OFC generation. The low phase noise signifies that the excellent phase correlation, between the tones, is maintained during demultiplexing and the mmW generation process. This is because both filtered tones traverse the same path and do not experience any phase walk-off. Thus, the dual-stage active demultiplexer scheme provides a high tolerance to the OFC linewidth and alleviates any path matching challenges, while generating a high purity mmW signal.

6.4.2 Impact of the OFC linewidth on the 64-QAM DMT A-RoF system performance

Here, the impact of the OFC linewidth on the performance of the A-RoF system is evaluated by comparing the system performance achieved by two OFC sources with different linewidths. In section 0, the A-ROF demonstration is verified with the UF-OFDM signal. Here, a dual-stage active demultiplexer scheme is tested with a 64-QAM discrete multitone (DMT) signal. A single band 64 QAM DMT signal[4] is generated using a Micram arbitrary waveform generator operating at 25 GSa/s. It consists of 36 subcarriers (96 symbols/subcarriers) upconverted to 3.5 GHz, with a total bandwidth of 480 MHz. The subcarrier baud rate is set to 12.5 MBaud, resulting in a raw data rate of 1.32 Gb/s. This data signal, at 1.8 Vp-p, is used to directly modulate Demux 2 that is DC-biased at 51 mA. The optical spectrum of the directly modulated dual-stage active demultiplexer is as shown in Figure 6.18. An enlarged view of the dotted area shows the optical carrier and the double sideband DMT data at an intermediate frequency (IF) of 3.5 GHz. The

---

[4] The DMT signal code was developed by Dr. Syed Tajammul Ahmad (DCU)

output of the Demux 2 is sent to the RRU through an optical fibre. The receiver section remains the same as in section 0.
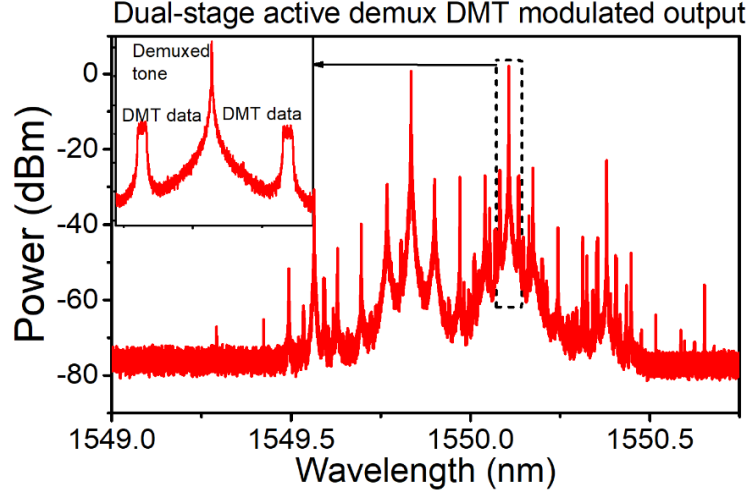
Figure 6.18 Optical spectrum of the 64-QAM DMT directly modulated dual-stage demultiplexer. Inset is the enlarged view of the dotted area.

To evaluate the impact of the OFC linewidth on the performance of the A-RoF system, the BER is measured as a function of the ROP for the 64 QAM DMT signals at 37.5 GHz, in a BtB scenario and after fibre transmission over 25 km. The above-mentioned tests were performed for OFC linewidths of 30 kHz, and 3.1 MHz. From Figure 6.19, it is evident that the BER is less than the 7% HD-FEC limit for all the cases. A summary of A-ROF system performance is shown in Table 6-4. After 25 km transmission (at an ROP of 1 dBm), a small BER degradation is observed in the case of larger linewidth. This can be attributed to the chromatic dispersion in the fibre (time delay = ~135 ps, for 37.5 GHz separation). In the 25 km SSMF transmission case, a penalty of ~0.5 dB and ~0.6 dB (reference taken at the FEC limit and compared to the corresponding BtB values) can be observed for linewidths of 30 kHz and 3.1 MHz, respectively. Hence, it can be said that both OFC sources deliver similar system performance. The fact that the larger linewidth does not result in a significant penalty highlights the linewidth tolerance of this A-RoF system. This will enable network operators to employ a cheaper OFC with MHz linewidths (instead of expensive kHz linewidth sources) without compromising the purity

of generated mmW signal. However, it is important to note that fibre dispersion would hinder longer transmission distances even though the 5G front haul requirements should not exceed 25 km due to its latency requirement [2],[3].
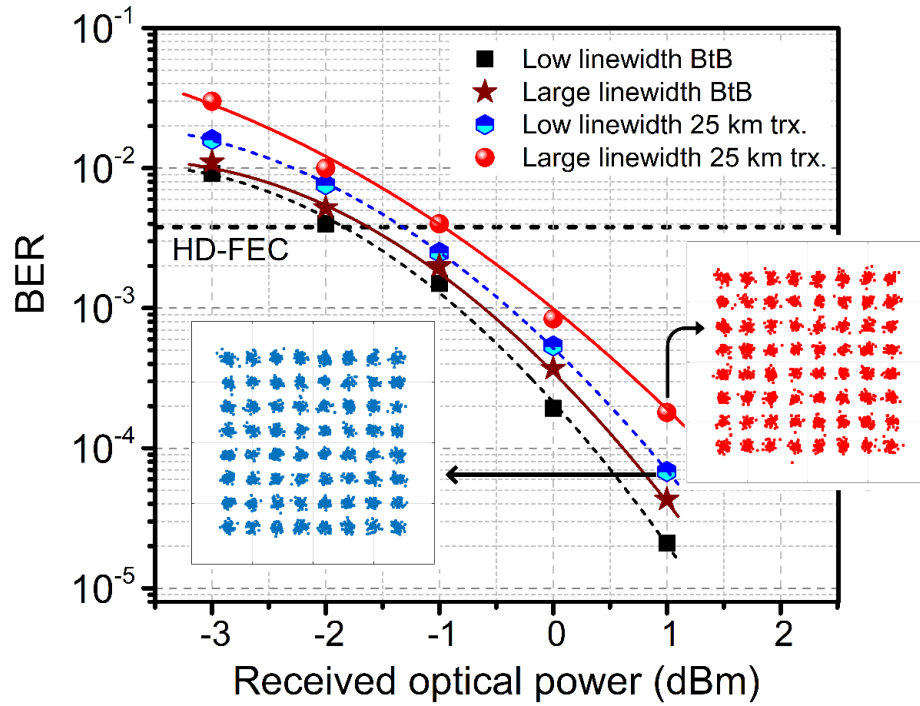
Figure 6.19 BER vs ROP for BtB and 25 km transmission. Insets: the constellations at the ROP of 1 dBm. Here, the solid and dotted curves are for OFC with 3.1 MHz and 30 kHz linewidth, respectively.

Table 6-4 Dual-stage active demultiplexer based A-RoF system performance with DMT signal as a function of OFC linewidths

OFC linewidth	Data at 37.5 GHz		Power penalty after 25 km trx.(at HD-FEC)
	BtB	25 km	
δf = 30 kHz	2.1 e-5	6.8 e-5	0.5 dB
δf = 3.1 MHz	4.3 e-5	1.8 e-4	0.6 dB

6.5 System Deployment Scenarios
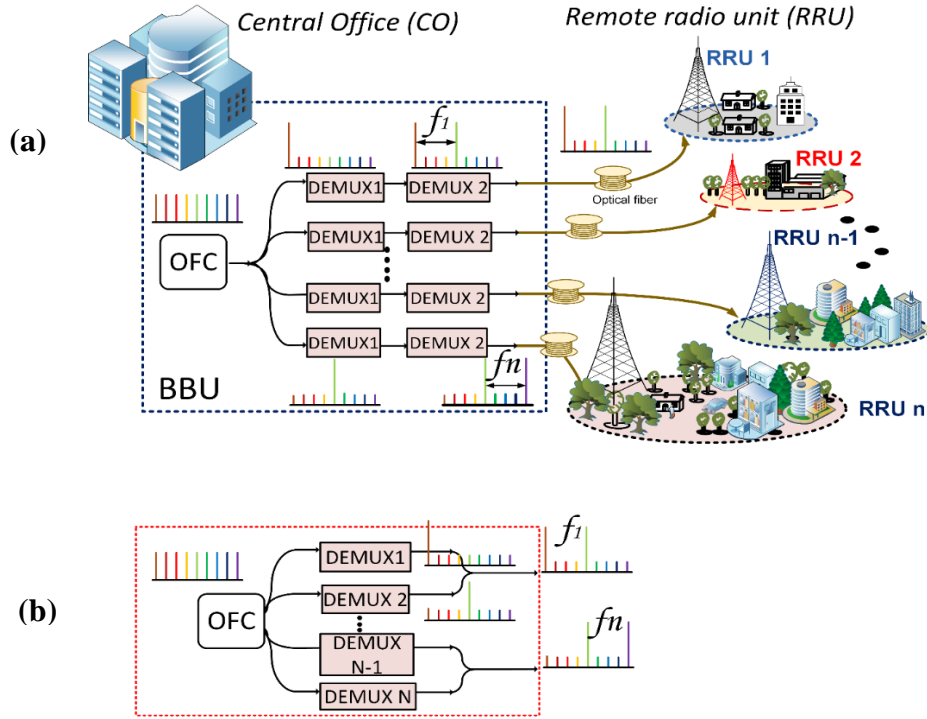
Figure 6.20 An OFC-based A-RoF system, comprising a BBU connected to several RRUs by a length of SSMF. Demultiplexing solution: (a) dual-stage active and (b) active demultiplexers in parallel

This section looks at the implementation constraints of an OFC-based A-RoF system employing one of the three demultiplexing solutions. Specifically, a system operating at 38 GHz is considered, employing an OFC that portrays the same parameters as that used in the experiments described above (FSR = 8.5 GHz, 11 and 14 tones within 3 dB and 10 dB from the spectral peak, and 6 dBm total output power). For each of the scenarios, the limits of the system, in terms of the power budget and the number of RRU's that can be served using a single OFC, are investigated. Here, it is assumed that each RRU uses a single mmW frequency that can be modulated with multiple IF data signals to serve multiple end-users. The demultiplexing scenarios under consideration are (i) an AWG/WSS solution as shown in Figure 4.1, and the (ii) parallel and (iii) dual-stage active demultiplexer architectures, as shown in Figure 6.20.

Case (i): AWG/WSS filter:

In this case, to maintain a uniform performance across all the channels, only 11 OFC tones (EI-GSL, within 3 dB from the peak) are used for the mmW generation. As a result, a single OFC can provide 4 pairs of tones separated by 34 GHz ($4 \times FSR$). Assuming that each pair feeds a single RRU, 4 RRU's can be serviced using one OFC. Due to the insertion loss of the demultiplexer and the split/recombine losses that are part of the system architecture, optical amplification stages will be required. Also, optical delay lines would be required to compensate for any path length mismatches, as the two tones travel different paths.

Case (ii): Parallel active demultiplexer :

Here a system based on the parallel active demultiplexers (the first proposed architecture), as shown in Figure 6.20 (b) (red rectangle), is considered. Due to the inherent amplification and power equalisation property of the active demultiplexer [27], 14 tones (within 10 dB from the spectral peak) can be successfully demultiplexed. However, for this study, only the 11 strongest lines will be considered in order to simplify the power budget and the comparison between the different schemes. When using a parallel configuration, the comb needs to be split, before being injected into the active demultiplexer, and the filtered tones recombined, after the data modulation. This introduces a minimum of 6 dB loss for each generated mmW signal. For the OFC used in this study (with an average power of 6 dBm), an attenuation of 21 dB is needed to achieve an output CLSR of 30 dB (CLP of -25 dBm). This level of attenuation means that the OFC output can be split 128 times (minimum insertion loss of 21 dB). Out of this power budget, a minimum of 6 dB must be used for the mmW generation process (splitting and recombining of the tones). Thus, in this scenario, a BBU using a parallel active demultiplexer could support 32 RRU's. However, with 11 comb lines available from our OFC, 4 distinct wavelength pairs (separated by 34 GHz) can be created. These pairs can be transmitted using WDM, over a single fibre. If multiple fibre feeds are in place, the total number of RRU's (N_{RRU}) that the system can serve:

$$N_{RRU} = max\{4 \cdot N_{fiber}, 32\} \tag{6.1}$$

where N_{fiber} is the number of fibre feeds between the BBU and RRU.

Case (iii): Dual-stage active demultiplexer:

The A-RoF system employing a dual-stage demultiplexer, as illustrated in Figure 6.20 (a) (blue rectangle), is the subject of study here. As this demultiplexing method does not require splitting or recombining the tones, the system has a 6 dB higher power budget than the one employing a parallel active demultiplexer. As a result, theoretically, it can serve 128 RRU's using a single OFC. As in the previous case, the OFC provides 4 distinct tone pairs (separated by 34 GHz), limiting the number of RRU's that can be served, using a single fibre, to 4. However, if multiple fibre feeds are in place, the number of RRU's that can be served:

$$N_{RRU} = max\{4 \cdot N_{fiber}, 128\} \tag{6.2}$$

As mentioned earlier, when using an active demultiplexer, the number of comb tones that can be demultiplexed is 14, giving 6 distinct tone pairs. However, as the power of these extra tones can be up to 10 dB lower than the strongest lines, the number of possible splits would be lower than that calculated above. Table 6-5 summarises the differences between the three system methods. From the table, it is clear that the dual-stage demultiplexer provides a significant reduction in cost and complexity, while at the same time increasing the power budget of the system. The latter can be used to serve multiple RRU's using a single OFC or to increase the reach of the system, without the need for an external amplifier. Furthermore, the architecture can be easily scaled by employing a wider comb.

Table 6-5 A-RoF system demonstration case study comparison

Case	Split & recombine	Path matching	Optical amplifiers	Split budget	$N_{RRU(Max)}$
(i)	Yes	Yes	Yes	--	4
(ii)	Yes	Yes	No	15 dB	32
(iii)	No	No	No	21 dB	128

6.6 Conclusion

In this chapter, two photonic schemes to generate mmW signals, based on the active demultiplexing of an OFC, are proposed. The first scheme demonstrates the use of a multifunctional active demultiplexer in parallel to generate a high-quality mmW signal. Employing such a scheme, a 61 GHz A-RoF distribution is realised that enables the transmission (with a BER below FEC limit) of 64- QAM UF-OFDM signal over 25 km SSMF. The second configuration, where two active demultiplexers are placed in series to reap a unique benefit where two demultiplexed tones traverse a common optical path. Thus, this scheme alleviates the path length matching challenges and reduces the requirements on the purity of the OFC used. A comprehensive characterisation and beat tone stability analysis is performed. Both approaches perform exceptionally well compared to the AWG-based solution. However, a complete characterisation (comparison) shows that the dual-stage active demultiplexer generates mmW signal with very high spectral purity as well as superior power stability. Next, the influence of the linewidth and the path length variations (relative time delay) between the optical tones are analysed with aid of SSB phase noise measurements.

Subsequently, a dual-stage active demultiplexer based A-RoF distribution system is realised, and its performance evaluated using two data formats: 64 QAM UF-OFDM and 64-QAM DMT, as well as two different OFCs, with optical linewidths of 30 kHz and 3 MHz. A BER below HD-FEC limit, after 25 km SSMF transmission, is achieved for all the cases. Moreover, the two order of magnitude increase in optical linewidth of the source introduces a minimal penalty of 0.1 dB at the HD-FEC limit, verifying the linewidth tolerance of the proposed system. As a result, a cheap OFC with MHz linewidth can be used instead of an expensive high purity OFC source with kHz linewidths. Finally, a case study of the A-RoF distribution system, employing three different demultiplexing solutions, is presented. The analysis clearly shows that the dual-stage demultiplexer provides a larger power budget (> 6 dB) in comparison to the other techniques. This additional budget can be used to extend the system reach and/or to increase the number of RRU's served using a single comb.

An active demultiplexer based solution benefits from a lower component count. As outlined in the first scheme, the use of optical amplifiers, ASE filters and external modulators can be eliminated. In addition, the second approach does not require splitters and re-combiners, and path length matching fibres or a tunable delay lines. Overall, the benefits of the proposed methods, coupled with the possibility of photonic integration of the entire transmitter, can deliver a significant reduction in the cost, complexity, footprint, and energy consumption of the systems, paving a way for rapid deployment of the future 5G+ deployments.

6.7 References

[1]   J. G. Andrews, S. Buzzi, W. Choi, S. V. Hanly, A. Lozano, A. C. K. Soong, J. C. Zhang, "What Will 5G Be ?," *IEEE Journal on Selected Areas in Communications*, vol. 32, no. 6, pp. 1065–1082, 2014.

[2]   D. Choudhury, "5G wireless and millimeter wave technology evolution: An overview," *2015 IEEE MTT-S International Microwave Symposium*, 2015, pp. 1-4, DOI: 10.1109/MWSYM.2015.7167093.

[3]   IEEE 5G, "IEEE 5G and beyond technology roadmap," *IEEE white paper*, 2017. [Online] Available: https://futurenetworks.ieee.org/roadmap/roadmap-white-paper. (accessed on 21-02-2020).

[4]   ITU-R, "Technical feasibility of IMT in bands above 6 GHz," *IEEE Future Networks,* 2015.[Online] Available: https://www.itu.int/pub/R-REP-M.2376 (accessed on 25-02-2020).

[5]   A. Checko, H. L. Christiansen, Y. Yan, L. Scolari, G. Kardaras, M. S. Berger, L. Dittmann, "Cloud RAN for Mobile Networks — A Technology Overview," *IEEE Communications Surveys & Tutorials*, vol. 17, no. 1, pp. 405–426, 2015.

[6]   E. Wong and A. Nirmalathas, "5G C-RAN With Optical Fronthaul : An Analysis From a Deployment Perspective," *Journal of Lightwave Technology*, vol. 36, no. 11, pp. 2059–2068, 2018.

[7]   S. Cho, J. Kim, J. K. Lee, J. H. Lee, and T. Paper, "Demonstration of IFoF-Based Mobile Fronthaul in 5G Prototype With 28-GHz Millimeter wave," *Journal of Lightwave Technology*, vol. 36, no. 2, pp. 601–609, 2018.

[8]   C. Lim and N. Ampalavanapillai, "Radio -over-Fiber Technology: Present and Future," *Journal of Lightwave Technology*, vol. 8724, no. c, pp. 5–12, 2020, DOI: 10.1109/JLT.2020.3024916.

[9]   U. Gliese, T.N. Nielsen, M. Bruun, E. Lintz Christensen, K.E. Stubkjaer, S. Lindgren, and B. Broberg, "A Wideband Heterodyne Optical Phase-Locked Loop for Generation of 3-18 GHz Microwave Carriers," *Photonics Technology Letters,* vol. 4, no. 8, pp. 936–938, 1992.

[10]   I. Aldaya, A. Arag, and G. Campuzano, "Millimeter-Wave Frequency Radio over Fiber Systems : A Survey," *IEEE Communications Surveys & Tutorials*, vol. 15, no. 4, pp. 1593–1619, 2013.

[11]   G. Qi, G. Qi, J. Yao, J. Seregelyi, S. Paquet, C. Belisle, X. Zhang, K. Wu, and R. Kashyap, "Phase-Noise Analysis of Optically Generated Millimeter-Wave Signals With External Optical Modulation Techniques," *Journal of Lightwave Technology*, vol. 24, no. 12, pp. 4861–4875, 2006, DOI: 10.1109/JLT.2006.884990.

[12] E. P. Martin, T. Shao, V. Vujicic, P. M. Anandarajah, C. Browning, R. Llorente, and L. P. Barry, "25-Gb/s OFDM 60-GHz Radio Over Fiber System Based on a Gain Switched Laser," *Journal of Lightwave Technology*, vol. 33, no. 8, pp. 1635–1643, 2015.

[13] C. Browning, H. H. Elwan, E. P. Martin, S. O'Duill, J. Poette, P. Sheridan, A. Farhang, B. Cabon, and L.P. Barry, "Gain-Switched Optical Frequency Combs for Future Mobile Radio-Over-Fiber Millimeter-Wave Systems," *Journal of Lightwave Technology*, vol. 36, no. 19, pp. 4602–4610, 2018.

[14] Y. Tian, K. Lee, C. Lim, and A. Nirmalathas, "Experimental Comparison of DSB-SC & OSSB based 60 GHz Radio-over-Fiber Fronthaul Links," in *2016 IEEE International Topical Meeting on Microwave Photonics (MWP)*, 2016, vol. 18, pp. 141–144. DOI: 10.1109/MWP.2016.7791299.

[15] T. Shao, M. Beltrán, R.Zhou, P. M. Anandarajah, R. Llorente, and L. P. Barry, "60 GHz Radio Over Fiber System Based on Gain-Switched Laser," *Journal of Lightwave Technology*, vol. 32, no. 20, pp. 3695–3703, 2014.

[16] T. Shao, H. Shams, P. M. Anandarajah, M. J. Fice, C. C. Renaud, F. van Dijk, A. J. Seeds, and L. P. Barry, "Phase Noise Investigation of Multicarrier Sub-THz Wireless Transmission System Based on Gain-switched Laser," *IEEE Transactions on Terahertz Science and Technology*, vol. 5, no. 4, pp. 590–597, 2015.

[17] S. T. Ahmad, P. D. Lakshmijayasimha, C. Browning, P. M. Anandarajah, A. Delmade, L. P. Barry, and A. Kaszubowska-Anandarajah, "Active demultiplexer enabled mmW ARoF transmission of directly modulated 64-QAM UF-OFDM signals," *Optics Letters*, vol. 45, no. 18, pp. 5246–5249, 2020.

[18] A. Kanno, A. Kanno, P. Tien Dat, N. Sekine, I. Hosako, N. Yamamoto, Y. Yoshida, K. Kitayama, and T. Kawanishi, "Seamless Fiber-Wireless Bridge in the Millimeter- and Terahertz-Wave Bands," *Journal of Lightwave Technology*, vol. 34, no. 20, pp. 4794–4801, 2016.

[19] G. K. M. Hasanuzzaman, H. Shams, C. C. Renaud, J. Mitchell, A. J. Seeds and S. Iezekiel, "Tunable THz Signal Generation and Radio-Over-Fiber Link Based on an Optoelectronic Oscillator-Driven Optical Frequency Comb," *Journal of Lightwave Technology*, vol. 38, no. 19, pp. 5240–5247, 2020.

[20] C. Yin, B. Li, J. Li, C. Yin, J. Dai, F. Yin, Y. Dai, and K. Xu, "Microwave Photonic Frequency Up-Convertor With Frequency Doubling and Compensation of Chromatic-Dispersion-Induced Power Fading," *IEEE Photonics Journal*, vol. 9, no. 3, pp. 1–7, 2017, DOI: 10.1109/JPHOT.2017.2706518.

[21] H. Chen, Y. Chi, and G. Lin, "Remote heterodyne millimeter-wave over fiber based OFDM-PON with master-to-slave injected dual-mode colorless FPLD pair," *Optics Express*, vol. 23, no. 17, pp. 22691–22705, 2015, DOI: 10.1364/OE.23.022691.

[22]   H. Ahmad, F. D. Muhammad, C. H. Pua, and K. Thambiratnam, "Dual-Wavelength Fiber Lasers for the Optical Generation of Microwave and Terahertz Radiation," *IEEE Journal of Selected Topics in Quantum Electronics*, vol. 20, no. 5, 2014.

[22]   D. S. Wu, R. Slavík, S. Member, G. Marra, and D. J. Richardson, "Direct Selection and Amplification of Individual Narrowly Spaced Optical Comb Modes Via Injection Locking : Design and Characterization," *Journal of Lightwave Technology*, vol. 31, no. 14, pp. 2287–2295, 2013, DOI: 10.1109/JLT.2013.2262921.

[23]   A. C. Bordonalli, M. J. Fice, and A. J. Seeds, "Optical injection locking to optical frequency combs for superchannel coherent detection," *Optics Express*, vol. 23, no. 2, pp. 1547–1557, 2015, DOI: 10.1364/OE.23.001547.

[24]   A. J. S. S. Fukushima, C.F.C Silva, and Y. Muramoto, "Optoelectronic Millimeter-Wave Synthesis Using an Optical Frequency Comb Generator, Optically Injection Locked Lasers, and a Unitraveling-Carrier Photodiode," *Journal of Lightwave Technology*, vol. 21, no. 12, pp. 3043–3051, 2003.

[25]   P. D. Lakshmijayasimha, A. Kaszubowska-anandarajah, E. P. Martin, M. N. Hammad, P. Landais, and P. M. Anandarajah, "Characterization of a multifunctional active demultiplexer for optical frequency combs," *Optics and Laser Technology*, vol. 134, no. 106637, pp. 4–8, 2021.

[26]   Z. Liu, S. Member, S. Member, R. Slavík, S. Member, and I. Tutorial, "Optical Injection Locking : From Principle to Applications," *Journal of Lightwave Technology*, vol. 38, no. 1, pp. 43–59, 2020.

[27]   P. D. Lakshmijayasimha, A. Kaszubowska-Anandarajah, P. Landais, and P. M. Anandarajah, "Performance evaluation of a comb-based transmission system employing multi-functional active demultiplexers," in *Optical Fiber Communication Conference (OFC) 2020,* paper. W2A.10. DOI: 10.1364/OFC-2020-W2A.10.

[28]   C. Browning, A. Farhang, A. Saljoghei, N. Marchetti, V. Vujicic, L. E. Doyle, and L. P. Barry, "5G wireless and wired convergence in a passive optical network using UF-OFDM and GFDM," in *2017 IEEE International Conference on Communications Workshops, ICC Workshops 2017*, 2017, pp. 386–392. DOI: 10.1109/ICCW.2017.7962688.

[29]   B. Farhang-boroujeny and H. Moradi, "OFDM Inspired Waveforms for 5G," *IEEE Communications Surveys & Tutorials*, vol. 18, no. 4, pp. 2474–2492, 2016.

[30]   C. Browning, A. Delmade, Y. Lin, J. Poette, H. H. Elwan and L. P. Barry, "Phase noise robust optical heterodyne system for reduced complexity millimeter-wave analog radio-over-fibre," 45th European *Conference on Optical Communication (ECOC 2019)*, 2019, pp. 1-4, DOI: 10.1049/cp.2019.0779.

[31]   A. Kaszubowska-Anandarajah, A. Delmade, E. Martin, P. Anandarajah, L. Barry, and C. Browning, "Bidirectional fiber transmission of mmW signals using remote downconversion and wavelength reuse," in *Conference on Lasers and Electro-Optics*, 2019, paper SM4G.2

[32] Hu, A. Kaszubowska, and L. P. Barry, "Investigation of stimulated Brillouin scattering effects in radio-over-fiber distribution systems," *Optics Communication,* vol. 255, no. 4, pp. 253- 60, 2005.

[33] L. P. Barry, C. Herbert, D. Jones, A. Kaszubowska-Anandarajah, B. Kelly, J. O'Carroll, R. Phelan, P. Anandarajah, K. Shi, and J. O'Gorman, "Discrete mod*e lasers for communications applications,"* in *Proc.SPIE Novel In-Plane Semiconductor Lasers VIII*, Feb. 2009, vol. 7230. DOI: 10.1117/12.810811

[34] G. P. Agrawal, "Highly nondegenerate four-wave mixing in semiconductor lasers due to spectral hole burning," *Applied Physics Letters*, vol. 51, no. 5. pp. 302–304, 1987. DOI: 10.1063/1.98450.

[35] G. P. Agrawal, "Four-wave mixing and phase conjugation in semiconductor laser media," *Optics Letters*, vol. 12, no. 4, pp. 260–262, 1987, DOI: 10.1364/OL.12.000260.

[36] T. N. Huynh, L. Nguyen, and L. P. Barry, "Phase noise characterization of SGDBR lasers using phase modulation detection method with delayed self-heterodyne measurements," *Journal of Lightwave Technology*, vol. 31, no. 8, pp. 1300–1308, 2013, DOI: 10.1109/JLT.2013.2247564.

[37] M. S. McCorquodale, J. D. O'Day, S. M. Pernia, G. A. Carichner, S. Kubba and R. B. Brown, "A Monolithic and Self-Referenced RF LC Clock Generator Compliant With USB 2.0," *IEEE Journal of Solid-State Circuits*, vol. 42, no. 2, pp. 385-399, 2007, DOI: 10.1109/JSSC.2006.883337.

[38] Kylia, "DWDM MUX/DEMUX," *Datasheet*, 2008. [Online] Available: https://kylia.com/api_website_feature/files/download/11115/datasheet-MICS-V111.pdf (accessed 10-07-2020).

7. Conclusions and Future work

Within the framework of this thesis, several notable investigations and advancements of the state of the art, towards the realisation of a reconfigurable OFC-based multicarrier transmitter, have been presented. In particular, the EI-GSL technique has been the focus of this work, due to its simplicity, cost-effectiveness, excellent spectral characteristics and flexibility.

An extensive experimental investigation has been presented, addressing various physical layer OFC implementational challenges, with emphasis placed on the application of EI-GSL in access (including A-RoF distribution systems) and data centre networks. This chapter summarises the research outcomes from these studies and introduces potential future research pathways/roadmaps.

7.1   Contribution to the State-of-the-art and Research Outcomes

- *Development of reconfigurable OFC source*

  Chapter 3 focuses on the development of a simple and flexible EI-GSL OFC. The generated OFC is shown possess excellent noise properties and dynamic reconfiguration (FSR and emission wavelength) capability. Initial work entailed surmounting a major shortcoming of EI-GSLs, which is the limited OFC bandwidth. This was addressed by experimentally demonstrating two novel reconfigurable OFC

expansion architectures which generates a broadband OFC with an expansion factor of 3 (with respect to the standard EI-GSL).

i. The first expansion technique proposed was a novel MIL-GSL approach. A 6.25 GHz FSR broadband OFC consisting of 45 lines (spanning over 281.25 GHz), with an expansion factor > 3, is demonstrated. Using the above-mentioned technique, comb densification was demonstrated by tuning the FSR (by subharmonics of the gain switching frequency) from 6.25 GHz to 390.625 MHz. The latter results facilitate EI-GSL OFC generation with a very low FSR and higher average power (in comparison to previously reported techniques). Finally, the OFC line characterisation validates the generation of an OFC with optimum characteristics; OFC exhibits excellent noise properties, with RIN better than -152 dB/Hz, optical linewidth of ~35 kHz, and a high degree of phase correlation between OFC lines (beat tone linewidth of 33 Hz). A couple of disadvantages with the MIL-GSL approach are the limited scalability and the restricted wavelength tunability.

ii. The second expansion architecture investigated entails the use of multiple independent EI-GS Fabry-Perot lasers. Phase correlation between the independently generated OFCs is then introduced via FWM in an SOA. As a proof of principle, two independent OFCs with an FSR of 6.25 GHz are employed in this scheme resulting in the generation of 42 mutually coherent lines spanning over 262.5 GHz (within 10 dB). The expansion can be scaled up by using multiple EI-GSL stages in parallel. The concept of inducing phase correlation via FWM in an SOA is verified by heterodyning two tones originating from different input combs and validated by achieving a reduction, by five-orders of magnitude, in the beat tone linewidth (from 1.1 MHz to 24 Hz). An added benefit achieved by the employment of the SOA in the architecture is amplification, which boosts the comb average power from 4.5 to 14.5 dBm. Finally, by using FP GSLs, the architecture is shown to be capable of tuning the central wavelength of the comb by 30 nm.

- *Investigation of demultiplexer solutions*

  As discussed in chapter 4, the implementation of an OFC in a reconfigurable optical network could be impeded by the complexity associated with the demultiplexing of individual comb lines prior to data modulation. To overcome this issue, two potential demultiplexer solutions: (i) a microring resonator, and (ii) a laser baser active demultiplexer were investigated.

  i.   To best our knowledge, we demonstrate for the first time an FPGA-controlled GSL OFC transmitter enabled by an 8 channel MRR demultiplexer. The ability of the GSL OFC and MRR to handle dynamic requirements is verified by reconfiguring, the FSR of the OFC and the MRR, in real-time. The results validate the potential of a software-defined (FPGA-controlled) GSL OFC transmitter. However, the MRR device used in this test was originally not designed as an OFC demultiplexer (passband of >20 GHz). Therefore, the desired MRR demultiplexer specifications, such as the Q-factor and number of rings per output port, are investigated through VPI simulations. The simulations and experiements led us to draw a conclusion that to achieve precise, fast, and independent tuning of individual MRRs, heating elements should be replaced by a PN junction embedded within the ring.

  ii.   A second demultiplexer solution based on a semiconductor laser-based active demultiplexer is investigated. A detailed examination/characterisation of its multifunctionalities such as wavelength-tunable demultiplexing, ultra-low noise amplification, power equalisation, and direct data modulation, is carried out. Both demultiplexers solutions that were investigated can be integrated with the EI-GSL OFC into a single chip to gain techno-economic benefits. It is important to mention that the studies presented in chapter 4 are not limited to EI-GSL but are compatible with any OFC.

- *Implementation of a novel OFC based transmitter for short-reach application*

Chapter 5 presents a demonstration of a novel simple OFC-based transmitter system employing an active demultiplexer (filter-amplifier-modulator) for data centres and short-reach applications. Some highlights of the results achieved;

i. Demonstration of an OFC based short reach transmission system. This involved a directly modulated two-channel 10.7 Gb/s on-off keyed system with a SSMF link of 3 km yielding error-free transmission.

ii. The impact of OFC injection on chirp (induced by direct modulation) is examined using simulations carried out in VPI. This led to the proposal of a novel dual-stage active demultiplexer that is demonstrated to enhance the CLSR and reduce the chirp.

iii. Performance verification of the proposed transmitter in a system employing advanced modulation formats such as 4-QAM DMT and 16-QAM DMT to realise aggregate data rates of 100 Gb/s (8×12.5 Gb/s) and 200 Gb/s (8×25 Gb/s), respectively. A BER below the HD-FEC limit is achieved for all channels (including channels with powers less than 20 dB from the spectral peak) for transmission over 40 (4-QAM DMT) and 25 km (16-QAM DMT) of SSMF.

iv. Demonstration of a 4 channel (4-QAM DMT) DWDM transmitter, which utilises all available OFC lines to improve spectral efficiency. The impact of cross channel interference due to closely spaced adjacent channels is also investigated.

- *Linewidth tolerant mmW generation and A-RoF distribution system*

In chapter 6, two novel mmW signal generation and A-RoF distribution schemes are proposed. The two configurations entail the employment of active demultiplexers in a parallel and cascaded configuration The proposed schemes provide significant benefits in comparison to the state-of-the-art solutions. The main results achieved are outlined;

i. Multifunctionality of the active demultiplexer (filter-amplifier-modulator): which overcomes many drawbacks such as (i) large insertion loss of the filter and external modulator (ii) need for external optical amplifiers such as EDFA or

SOA (to compensate losses), and (iii) OSNR degradation (stems from the use of amplifiers).

ii. Generation of a tunable mmW signal and the realisation of an A-RoF distribution system:

- Demonstration of mmW signal generation at multiple frequencies; 29.5, 38, 63.5 GHz and a detailed characterisation of the generated mmW signals.

- Demonstration of an A-RoF distribution system enabled by the direct modulation of the active demultiplexer with 64-QAM UF-OFDM, and -DMT signals. 25 km SSMF transmission shows system performance ac below HD-FEC limit after.

iii. Tolerance to a large optical linewidth (cascaded scheme).

- Verification of linewidth tolerance by characterising SSB phase noise for two OFC sources with linewidths of 3.1 MHz and 30 kHz.

- Evaluation of system performance as a function of linewidths: two orders of magnitude increase in OFC linewidth introduces a negligible performance penalty of 0.1 dB (at HD-FEC limit), highlighting the linewidth tolerance of the proposed scheme.

iv. Reduced loss: split ratio reduced by a factor of two in comparison to the standard architecture (cascaded scheme).

v. Reduced component count and potential photonic integration: further reducing cost, footprint and energy.

Overall, the successful development of a reconfigurable OFC-based transmitter system enabled by a multi-functional active demultiplexer is presented in this thesis. It overcomes most of the implementational challenges and facilitates the tunability of transmission parameters according to incoming traffic requirements and conditions. The scientific advancements and investigation presented in this thesis, may play a vital role in the

realisation of a cost-effective transmitter to be employed in future high-capacity data transmission systems.

7.2   Future Work and Potential Research Directions
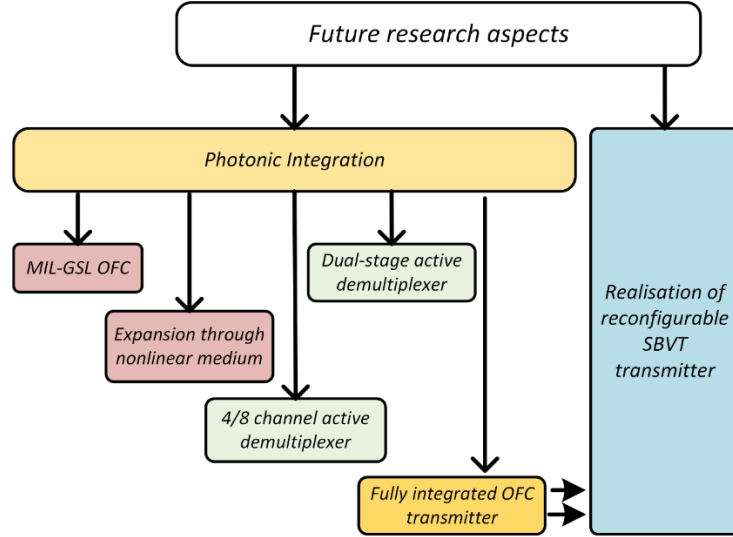

Figure 7.1 Future work in the area of an OFC-based reconfigurable transmitter.

While the research work presented in this thesis has provided technical solutions (and the science behind it) to several challenges, there is still a large body of work that can be carried out to further the science and to pave the way towards the realisation of a commercial OFC-based reconfigurable transmitter. Figure 7.1 outlines some of the future work, including the photonic integration of the proposed schemes that have been investigated in this thesis. In addition, advancements can be made by implementing software-controlled reconfigurable sliceable bandwidth variable transmitters (SBVT) and fully characterising their performance.

- *OFC expansion:* The work on the OFC expansion described in chapter 3 can be extended by investigating ways of realising the proposed scheme in a photonic integrated circuit (PIC). Some progress has been made on this, where the first batch of PICs based on the MIL-GSLs have been fabricated by Pilot Photonics Ltd. The schematic of the PIC is shown in Figure 7.2. It comprises a 4-section master laser followed by two 2-section slave DFB lasers. A phase tuner is placed on one arm to

compensate for any delay/path difference between the two arms. Spot-size converters (SSC) are used for all-optical inputs and outputs. An optional SSC is provided to allow external optical injection if needed. A detailed characterisation of such a MIL-GSLs would be an obvious next step in the realisation of simple, compact, cost-effective, energy-efficient OFC. Future design iterations may also include a phase modulator and an SOA at the output of MIL-GSL to enhanced the tunability of the FSR and amplify the OFC power.
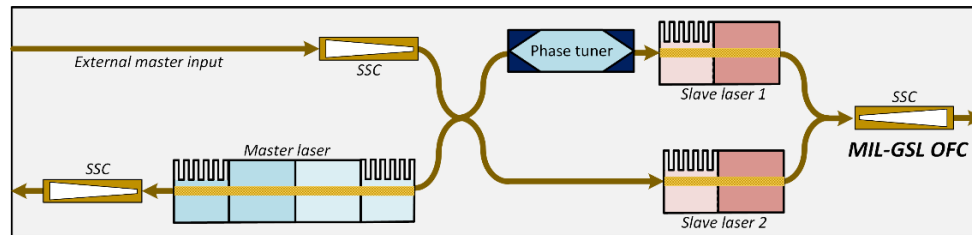
Figure 7.2 PIC architecture of MIL-GSL-based OFC generation.
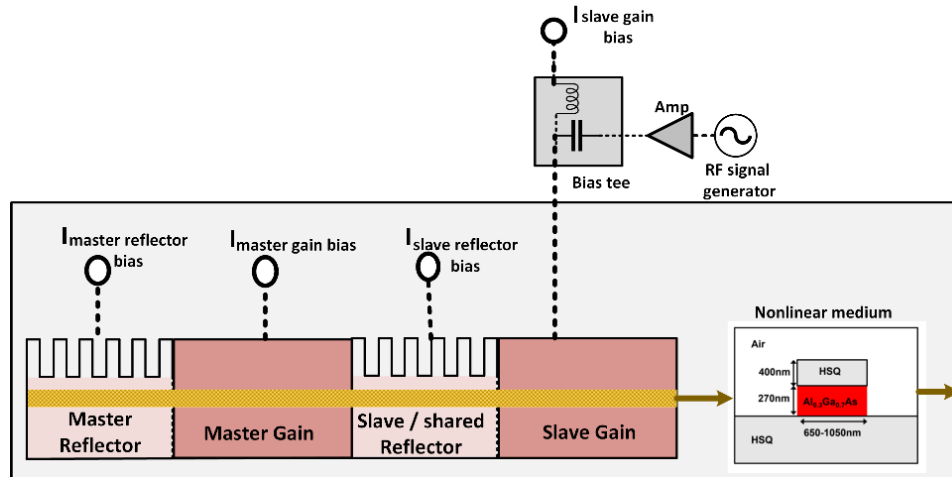
Figure 7.3 Schematic of a potential OFC expansion architecture employing AlGaAs-on-insulator waveguide.

- *Expansion via integrated nonlinear medium:* Another possible OFC expansion scheme is to integrate the OFC with a nonlinear medium. However, the main drawback of such scheme was the fabrication challenges to integrate with OFC and would result in high propagation losses. However, the recent development of heterogeneous integration of *AlGaAs-on-insulator (AlGaAs-OI)* could overcome

these difficulties and allow the fabrication of sub-micron scale nonlinear waveguides. Hence, an OFC could be effectively expanded by employing a dispersion-engineered *AlGaAs-OI* nonlinear medium, as depicted in Figure 7.3. The OFC shown is generated using a 4-section integrated EI-GSL and subsequently expanded using an *AlGaAs-OI* nonlinear waveguide. Hence, the investigation of such waveguides to induce a nonlinear expansion of an OFC would be an interesting topic for future research.
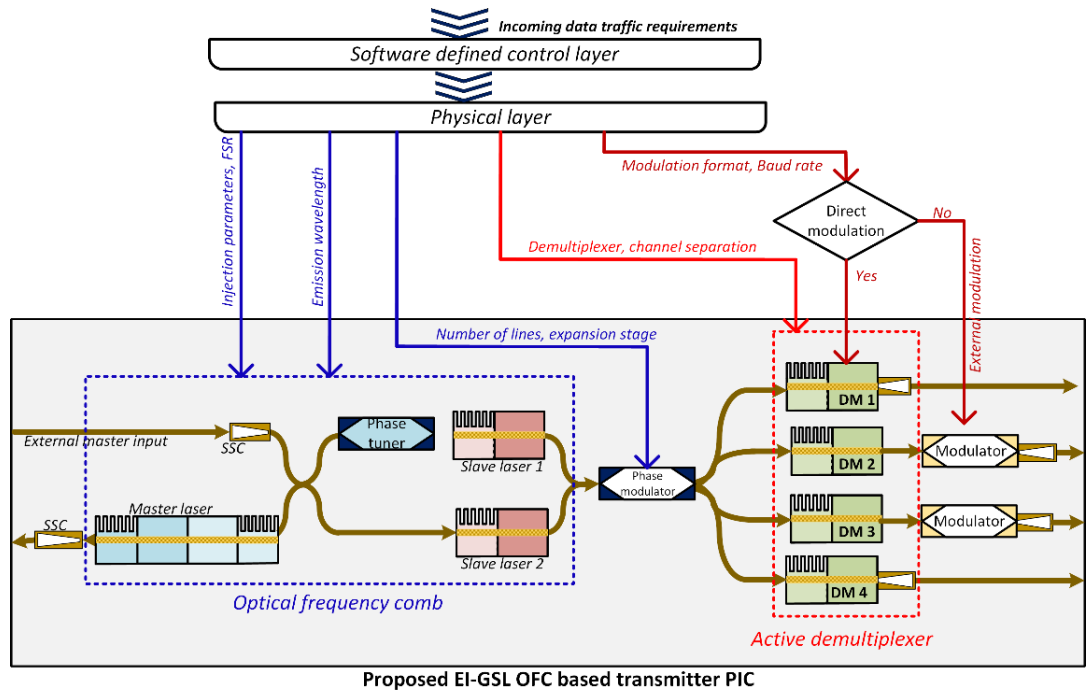
Figure 7.4 Schematic of a PIC-based architecture of an EI-GSL-based OFC transmitter (OFC + 1 x 4 active demultiplexer).

- *Realisation of a fully integrated EI-GSL-based OFC transmitter:* The work on the reconfigurable multi-carrier transmitter, described in chapters 3 and 4, can be furthered by integrating the OFC and demultiplexer on a single chip, as shown in Figure 7.4. The broadband OFC can be generated by employing a MIL-GSL (as in Figure 7.2) and could include an electro-optic phase modulator to further expand or provide FSR tunability, depending upon the application. The demultiplexing and amplification of the OFC lines could be performed using a 1 x 4 active demultiplexer. The chip may include an integrated data modulator after the demultiplexer to enable

modulations of individual carriers with advanced modulation formats for long-haul communications. Furthermore, the dual-stage active demultiplexing proposed in chapter 5, can also be included for CLSR improvement and/or chirp reduction in case of direct modulation (short reach applications). The chip-level realisation of the fully integrated reconfigurable OFC transmitter would be a vital advancement in the field, facilitating commercial deployment of OFC-based transmitters.

- *Realisation of software-defined SBVTs:* The research work carried out in this thesis work, is aimed at the realisation of software-defined SBVT to facilitate network adaptability to dynamic traffic conditions. Future work may include a software-defined control layer that translates the incoming data plane commands into the SBVT configuration settings. The schematic of such an OFC-based scheme is depicted in Figure 7.4. The main building block of such an architecture is a reconfigurable OFC source, that could be based on the architecture presented in chapter 3. A phase modulator could follow the proposed OFC to control the number of lines generated and allow a swift tuning of the FSR. This block can be followed by a 1×4 *or* 1×8 active demultiplexer, as described in chapter 4, which performs wavelength-tunable demultiplexing, ultra-low amplification and power equalisation. Furthermore, depending upon the traffic requirements, the demultiplexed tone can be directly or externally modulated with the data using a given format and data rate.

- Potential future work could also include exploring other applications that can benefit from the use of an OFC such as dual-comb spectroscopy, steganography, distance measurements, soliton generation, etc.

APPENDIX

List of Publications

The following is the list of publications yielded from this work.

Refereed Journal Papers

J.1   **Prajwal. D. Lakshmijayasimha,** Aleksandra Kaszubowska-Anandarajah, Syed T. Ahmad, Eamonn P. Martin, and Prince M. Anandarajah, "*Optical linewidth tolerant mmW generation employing a dual-stage active demultiplexer*," in *Photonics Technology Letters,* vol. 34, no. 9, pp. 451-454, 2022, DOI: 10.1109/LPT.2022.3166254.

J.2   **Prajwal. D. Lakshmijayasimha,** Syed T. Ahmad, Eamonn P. Martin, Prince M. Anandarajah and Aleksandra Kaszubowska-Anandarajah, "*Tunable mm-wave A-RoF transmission scheme employing an optical frequency comb and dual-stage active demultiplexer*," in *Journal of Lightwave Technology*, vol. 39, no. 24, pp. 7771-7780, 2021. DOI: 10.1109/JLT.2021.3098949.

J.3   Syed T. Ahmad, **Prajwal. D. Lakshmijayasimha,** Aleksandra Kaszubowska-Anandarajah, Colm Browning and Prince M. Anandarajah, "*Active Demultiplexer-enabled Directly Modulated DMT Transmission Using Optical Frequency Combs for Data Center*

Interconnects," in *Journal of Lightwave Technology*, vol. 39, no. 17, pp. 5468-5473, 2021. DOI: 10.1109/JLT.2021.3091959.

J.4 Wenle Weng, Aleksandra Kaszubowska-Anandarajah, Jijun He, **Prajwal D. Lakshmijayasimha**, Erwan Lucas, Junqiu Liu, Prince M. Anandarajah, and Tobias J. Kippenberg, "*Gain-switched semiconductor laser driven soliton microcombs",* in *Nature Communications*, vol. 12, no. 1425, 2021. DOI: *10.1038/s41467-021-21569-7.*

J.5 **Prajwal D. Lakshmijayasimha,** Prince M. Anandarajah, Pascal Landais and Aleksandra Kaszubowska-Anandarajah, "*Optical Frequency Comb Expansion Using Mutually Injection-Locked Gain-Switched Lasers,*" in *Applied Sciences*, vol. 11, no. 7108, 2021, DOI: 10.3390/app11157108.

J.6 **Prajwal D. Lakshmijayasimha**, Aleksandra Kaszubowska-Anandarajah, Eamonn P. Martin, Mohab N. Hammad, Pascal Landais and Prince M. Anandarajah, "*Characterization of a multifunctional active demultiplexer for optical frequency combs,*" in *Journal of Optics & Laser Technology*, vol. 134, no. 106637, 2021. DOI: 10.1016/j.optlastec.2020.106637.

J.7 Eyal Wohlgemuth, Yaron Yoffe, Pantea N. Goki, Muhammad Imran, Francesco Fresi, **Prajwal D. Lakshmijayasimha**, Roi J. Cohen, Prince M. Anandarajah, Luca Poti, and Dan Sadot, "*Stealth and secured optical coherent transmission using a gain switched frequency comb and multi-homodyne coherent detection",* in *Optics Express,* vol. 29, no 28, pp. 40462-40480, 2021. DOI: 1*0.1364/OE.431070.*

J.8 Mohab N. Hammad, **Prajwal D. Lakshmijayasimha**, Aleksandra Kaszubowska-Anandarajah, and Prince M. Anandarajah, "*Photonically integrated gain-switched lasers for optical frequency comb generation,*" in *Microwave and Optical Technology Letters*, vol. 63, pp. 2219-2226, 2021. DOI: 10.1002/mop.32880.

J.9 Syed T. Ahmad, **Prajwal D. Lakshmijayasimha**, C. Browning, Prince M. Anandarajah, Amol Delmade, Liam P. Barry, and Aleksandra Kaszubowska-Anandarajah, "*Active demultiplexer enabled mmW A-RoF transmission of directly modulated 64-QAM UF-OFDM signals,*" in *Optics Letters*, vol. 45, pp. 5246-5249, 2020. DOI: 10.1364/OL.399418.

J.10 Mohab N. Hammad, Aleksandra Kaszubowska-Anandarajah, Deseada G. Pascual, Pascal Landais, **Prajwal D. Lakshmijayasimha**, Gaurav Jain, and Prince M. Anandarajah,

"*Characterization and Direct Modulation of a Multi-Section PIC Suited for Short Reach Optical Communication Systems*", in *Photonics*, vol. 7, no. 3, 2020. DOI: 10.3390/photonics7030055.

J.11 **Prajwal D. Lakshmijayasimha**, Aleksandra Kaszubowska-Anandarajah, Eamonn P. Martin, Pascal Landais and Prince M. Anandarajah, "*Expansion and phase correlation of a wavelength tunable gain-switched optical frequency comb*," in *Optics Express*, vol. 27, no. 12, pp. 16560-16570, 2019. DOI: 10.1364/OE.27.016560.

Refereed Conference Papers

C.1 Syed T. Ahmad, **Prajwal D. Lakshmijayasimha**, C. Browning, Prince M. Anandarajah, Liam P. Barry, and Aleksandra Kaszubowska-Anandarajah, "*Optical Frequency Comb and Active Demultiplexer-enabled 60 GHz mmW ARoF Transmission using Directly Modulated 64-QAM UF-OFDM signals*" in *Conference on Lasers and Electro-Optics Europe & European Quantum Electronics Conference (CLEO/Europe-EQEC)*, 2021. DOI: 10.1109/CLEO/Europe-EQEC52157.2021.9541846.

C.2 Syed T. Ahmad, **Prajwal D. Lakshmijayasimha**, Aleksandra Kaszubowska-Anandarajah, and Prince M. Anandarajah, "*Active Demultiplexer-enabled 300G 16-QAM SSB-DMT Transmission using Optical Frequency Combs*", in *Conference on Lasers and Electro-Optics, (CLEO)*, 2021, pp. STh1I.4. DOI:10.1364/CLEO_SI.2021.STh1I.4

C.3 Wenle Weng, Aleksandra Kaszubowska-Anandarajah, Jijun He, **Prajwal D. Lakshmijayasimha**, Erwan Lucas, Junqiu Liu, Prince M. Anandarajah, and Tobias J. Kippenberg, "*Gain-switched semiconductor laser driven soliton microcombs,*" in *Conference on Lasers and Electro-Optics (CLEO),* 2021, pp. SW2H.1. DOI: 10.1364/CLEO_SI.2021. SW2H.1.

C.4 **Prajwal. D. Lakshmijayasimha**, Syed. T. Ahmad, Eamonn. P. Martin, Prince. M. Anandarajah and Aleksandra Kaszubowska-Anandarajah, "*A Novel mmW A-RoF Transmission Scheme Employing Dual-stage Active Demultiplexing of an Optical Frequency Comb*," in *European Conference on Optical Communications (ECOC)*, 2020, pp. Th1G-4, DOI: 10.1109/ECOC48923.2020.9333254.

C.5   **Prajwal. D. Lakshmijayasimha,** Aleksandra Kaszubowska-Anandarajah, Pascal Landais, and Prince. M. Anandarajah, "*Performance evaluation of a comb-based transmission system employing multi-functional active demultiplexers*," in *Optical Fiber Communication Conference (OFC),* 2020, pp. W2A.10. DOI: 10.1364/OFC.2020.W2A.10

C.6   Syed T. Ahmad, **Prajwal D. Lakshmijayasimha**, Aleksandra Kaszubowska-Anandarajah, and Prince M. Anandarajah, "*200 Gb/s Short Reach Transmitters Based on Optical Frequency Combs,*" in in *22nd International Conference on Transparent Optical Networks (ICTON)*, 2020, DOI: 10.1109/ICTON51198.2020.9203281.

C.7   Aleksandra Kaszubowska-Anandarajah, **Prajwal D. Lakshmijayasimha**, Syed T. Ahmad, and Prince M. Anandarajah, "*A multifunctional demultiplexer for optical frequency combs in broadband access networks*," in *Photonics West*, *Broadband Access Communication Technologies XIV*, vol. 11307. SPIE, pp. 69–74, 2020. DOI:10.1117/12.2545750

C.8   **Prajwal. D. Lakshmijayasimha,** Aleksandra Kaszubowska-Anandarajah, Pascal Landais, and Prince. M. Anandarajah, "*Tunable Active De-Multiplexer for Optical Frequency Combs,*" in *21st International Conference on Transparent Optical Networks (ICTON)*, 2019, DOI: 10.1109/ICTON.2019.8840491.

C.9   **Prajwal. D. Lakshmijayasimha,** Prince. M. Anandarajah, Deseada G. Pascual, Gaurav Jain, Jules Braddell, Pascal Landais, and Aleksandra Kaszubowska-Anandarajah "*Optical Generation of mmW and THz Signals Using PICs*," in *21st International Conference on Transparent Optical Networks (ICTON)*, 2019, DOI: 10.1109/ICTON.2019.8840557.

C.10   **Prajwal. D. Lakshmijayasimha,** Eamonn P. Martin, Sean P. O'Duill, Pascal Landais, Prince. M. Anandarajah, and Aleksandra Kaszubowska-Anandarajah, "*Performance of an injection-locked active demultiplexer for FSR-tunable optical frequency combs*," in *Conference on Lasers and Electro-Optics (CLEO),* 2019, pp. STU4N.5. DOI: 10.1364/CLEO_SI.2019.STu4N.5

C.11   **Prajwal. D. Lakshmijayasimha,** Aleksandra Kaszubowska-Anandarajah, Eamonn P. Martin, Pascal Landais, and Prince. M. Anandarajah, "*Expansion and phase correlation of gain-switched optical frequency combs through FWM in an SOA*," in *Optical Fiber Communication Conference (OFC),* 2019, pp. W1B.2. DOI: 10.1364/OFC.2019.W1B.2

C.12 Mohab N. Hammad, Eamonn P. Marin, **Prajwal D. Lakshmijayasimha**, Aleksandra Kaszubowska-Anandarajah, Pascal Landais, and Prince M. Anandarajah, "*Optimum optical frequency comb generation via externally injection of a gain switched VCSEL",* in *Conference on Lasers and Electro-Optics (CLEO),* 2019, pp. SM4N.6. DOI: 10.1364/CLEO_SI.2019.SM4N.6.

C.13 **Prajwal. D. Lakshmijayasimha,** Mohab N. Hamad, Christian Bluemm, Alvaro Moscoso-Mártir, Florian Merget, Jeremy Witzens, J. van de Belt, Prince. M. Anandarajah, and Aleksandra Kaszubowska-Anandarajah, "*Reconfigurable Microring Resonator-Based Optical Transmitter for Elastic Optical Networks,"* in *20th International Conference on Transparent Optical Networks (ICTON)*, 2018. DOI: 10.1109/ICTON.2018.8473998.

Patents

P.1 **Prajwal D. Lakshmijayasimha**, Aleksandra Kaszubowska-Anandarajah, Prince M. Anandarajah, Syed T. Ahmad, "*Optical linewidth independent high purity mmw/THz generator employing cascaded demultiplexing,*" pending, GB2016809.2, filed on 22-10-2020.